Exotic ground states and excitations in quantum magnets

by

Samuel Patrick Michael Curley

Thesis

Submitted to the University of Warwick

for the degree of

Doctor of Philosophy

Department of Physics

August 2021

Contents

List of Tables

List of Figures

Acknowledgments

Firstly I would like to thank my supervisor Paul Goddard for his time, support and guidance throughout my PhD. In addition, I thank him for his seemingly limitless patience as I bumbled my way through various projects; it was much appreciated. I thank Martin Lees for continued assistance throughout my PhD with experimental work, as well as Ali Julian, Patrick Ruddy and Tom Orton for all the support with experimental equipment they provided. The entire Superconductivity and Magnetism group at Warwick have been excellent during my time, and I thank them all warmly.

I have been fortunate enough to have exceedingly kind and inspiring postdocs, who fast became good friends, throughout my PhD and wish to extend my deepest gratitude to Robert Williams, Kathrin Götze, William Blackmore and Matthew Coak for the many invaluable lessons they have imparted. To my office mates Sam Holt, Matthew Pearse, Lunci Xiang, Beth Hampshire, Amelia Hall and David Jonas, I'm not sure I'd have held things together as well without our communal whinges, tea breaks and snack trips. Special thanks are owed to Jamie Manson and all his team for providing the myriad of interesting materials in this thesis, as well as John Singleton, Dave Graf and David Voneshen for showing me the ropes at their respective user facilities. I must also thank Dave Walker, Rebecca Scatena, Roger Johnson, Jere Tidey and Guy Clarkson for their assistance in all things crystallography.

I'm grateful to all the friends I've made whilst studying for my PhD and living in Birmingham, who, I am blessed to say, are far too numerous to mention here individually. All of you have made the four years of my PhD more fun and enriching than I could have possibly hoped for; I can't thank you all enough. A special shout goes out to the VeloBoiz Tomi Russell, Matthew Nijsen, Jack Foord and Copper Lewis who all aspire to the ‘incline life’; my childhood friends Alex Baker and Ellen Masters for always being there, here’s to many more rounds of Helan Går at Swedish Christmas; and the Cademan Climbing Crew, who taught me work stress is easily forgotten when you’re on a rope 40 feet in the air. A huge thanks to my house mates Tomi Russell, Katie Briggs and Kitty Allsop with whom I spent nearly a year isolating with during the covid-19 pandemic; the extravagant dinners parties, and thinking up increasingly cunning schemes to get Tomi away from his turntables during the early hours, will be sorely missed. To my little brothers Harry, Jack and Daniel, I’m forever grateful for the support you’ve all given, despite the fact physics is, according to each of you, ‘for nerds’. Finally, a huge thanks to my parents Jane Wych and Michael Curley, this work would not have come to fruition without all of the love and encouragement you have given me.

Declarations

This thesis is submitted in support of my application for the degree of Doctor of Philosophy. The work presented in this thesis has been undertaken by myself except in the cases explicitly stated below.

Samples were grown by a variety of collaborators, with single-crystals of Co(NCS)$_2$(thiourea)$_2$, CuVOF$_4$(H$_2$O)$_6$·H$_2$O, NiI$_2$(3,5-lutidine)$_4$ and [Cu(pyrazine)$_{0.5}$(glycine)]ClO$_4$ synthesized by Jacqueline Villa, Danielle Villa, Melissa Rhodehouse, Zachary Manson and Jamie Manson of East Washington University, USA, as were polycrystalline powder samples of Ni(NCS)$_2$(thiourea)$_2$ and NiI$_2$(3,5-lutidine)$_4$.

Structural data for Ni(NCS)$_2$(thiourea)$_2$ and Co(NCS)$_2$(thiourea)$_2$ was collected and refined by P. Macchi and R. Scatena at The University of Bern, Switzerland. Single-crystal heat capacity data for Co(NCS)$_2$(thiourea)$_2$ was collected by J. Eckert and E. Krenkel of Harvey-Mudd College, CA, USA. Analysis of the data was performed by myself. Zero-field positive-muon-spin-relaxation data for Ni(NCS)$_2$(thiourea)$_2$ and Co(NCS)$_2$(thiourea)$_2$ was collected and analysed by T. Hicken, B. Huddart, T. Lancaster, S. Blundell and F. Xiao using the GPS instrument at Swiss Muon Source, Paul Scherrer Institut. Charge and spin-density calculations were performed by R. Scatena and P. Macchi whilst at the University of Bern, Switzerland.

For NiI$_2$(3,5-lutidine)$_4$ the structure was determined by D. Villa, J. Schlueter and J. Manson at ChemMatCARS 15-ID-B beamline of the Advanced Photon Source at Argonne National Laboratory. Powder SQUID magnetometry data was collected by W. Blackmore at The University of Warwick whilst powder pulsed-field measurements were performed by J. Singleton at The National High Magnetic Field Laboratory (NHMFL-LANL), USA. I was involved in the analyses of both data. Inelastic neutron scattering data collection was performed with the assistance of local contact D. Voneshen. Analyses was performed by myself and R. Williams. Positive-muon-spin-relaxation measurements were completed by T. Lancaster, B. Huddart, T. Hicken, S. Blundell and F. Xiao on the LTF and GPS instruments at the Swiss Muon Source, Paul Scherrer Institut, Switzerland. Electron-spin resonance measurements were performed by A. Ozarowski using a home built spectrometer at the EMR facility, National High Magnetic Field Laboratory, Tallahassee, Florida, USA.

Refinement of the ambient single-crystal x-ray diffraction data for $CuVOF_4(H_2O)_6{\cdot}H_2O$ was performed with the assistance of J. Tidey at the University of Warwick. Electron-spin resonance data was collected and analysed by D. Kamenskyi at Augsburg University. I was heavily involved with the discussion of the results. Spin-polarised density functional theory calculations for $CuVOF_4(H_2O)_6{\cdot}H_2O$ were undertaken by B. Huddart and T. Lancaster at Durham University, UK. I was heavily involved with the discussion of the results. Experimental set-up of the Guertin piston-cylinder cells for high-pressure magnetometry measurements of $CuVOF_4(H_2O)_6{\cdot}H_2O$ and $[Cu(pyrazine)_{0.5}(glycine)]ClO_4$ are the NHMFL, USA was done with the assistance of local contact D. Graf.

This thesis has been composed by myself and has not been submitted to any other institution for the award of a degree.

Below is a list of publications obtained during my PhD:

- **S. P. M. Curley**, B. M. Huddart, D. Kamenskyi, M. J. Coak, R. C. Williams, S. Ghannadzadeh, A. Schneider, S. Okubo, T. Sakurai, H. Ohta, J. P. Tidey, D. Graf, S. J. Clark, S. J. Blundell, F. L. Pratt, M. T. F. Telling, T. Lancaster, J. L. Manson, and P. A. Goddard, *Anomalous magnetic exchange in a dimerized quantum magnet composed of unlike spin species*, Phys. Rev. B 104, 214435 (2021). - Chapter 5

- J.L. Manson, **S. P. M. Curley**, R. C. Williams, D. Walker, P. A. Goddard, A. Ozarowski, R. D. Johnson, A. M. Vibhakar, D. Y. Villa, M. L. Rhodehouse,

S. M. Birnbaum, and J. Singleton, *Controlling Magnetic Anisotropy in a Zero-Dimensional $S = 1$ Magnet Using Isotropic Cation Substitution*, J. Am. Chem. Soc. 143, 4633 (2021).

- **S. P. M. Curley**, R. Scatena, R. C. Williams, P. A. Goddard, P. Macchi, T. J. Hicken, T. Lancaster, F. Xiao, S. J. Blundell, V. Zapf, J. C. Eckert, E. H. Krenkel, J. A. Villa, M. L. Rhodehouse, and J. L. Manson, *Magnetic ground state of the one-dimensional ferromagnetic chain compounds $M(NCS)_2(thiourea)_2$ (M = Ni , Co)*, Phys. Rev. Mater. 5, 34401 (2021). - Chapter 3

- J. L. Manson, Z. E. Manson, A. Sargent, D. Y. Villa, N. L. Etten, W. J. A. Blackmore, **S. P. M. Curley**, R. C. Williams, J. Brambleby, P. A. Goddard, A. Ozarowski, M. N. Wilson, B. M. Huddart, T. Lancaster, R. D. Johnson, S. J. Blundell, J. Bendix, K. A. Wheeler, S. H. Lapidus, F. Xiao, S. Birnbaum, and J. Singleton, *Enhancing easy-plane anisotropy in bespoke Ni(II) quantum magnets*, Polyhedron 180, 114379 (2020).

- R. C. Williams, W. J. A. Blackmore, **S. P. M. Curley**, M. R. Lees, S. M. Birnbaum, J. Singleton, B. M. Huddart, T. J. Hicken, T. Lancaster, S. J. Blundell, F. Xiao, A. Ozarowski, F. L. Pratt, D. J. Voneshen, Z. Guguchia, C. Baines, J. A. Schlueter, D. Y. Villa, J. L. Manson, and P. A. Goddard, *Near-ideal molecule-based Haldane spin chain*, Phys. Rev. Res. 2, 1 (2020).

Work in this thesis was presented at the following conferences as poster presentations:

- Magnetism 2018, *"Towards control of uniaxial anisotropy in $S = 1$ magnetic systems"*, University of Manchester, (2018).

- Magnetism 2019, *"Thermodynamic and magnetic measurements of the ferromagnetic chain materials $M(NCS)_2(thiourea)_2$; M = Co, Ni."*, University of Leeds, (2019).

- The 13th International Symposium on Crystalline Organic Metals, Superconductors and Magnets, *“Halide substitution as a tool in moving toward control of the magnetic properties in* $S = 1$ *Ni chains”*, Tomar, Portugal, (2019).

and in the form of an oral presentation at:

- American Physical Society March Meeting 2021, *“Pressure evolution of an asymmetric* $S = 1/2$ *dimer magnet”*, Virtual Conference, (2021).

Abstract

Within this thesis I will outline experimental and theoretical investigations on five quantum magnets, which are primarily composed of lattices of transition-metal ions joined via molecular linkers. The first study compares the two isostructural quasi-one-dimensional ferromagnetic chain compounds $M(\mathrm{NCS})_2(\mathrm{thiourea})_2$ where $M = \mathrm{Ni(II)}$, Co(II) and thiourea $= \mathrm{SC(NH_2)_2}$. Experimental measurements reveal a large difference in the strength of the intrachain exchange coupling in each material, with $J_{\mathrm{Ni}} \sim 100$ K and $J_{\mathrm{Co}} \approx 4$ K, despite the highly similar exchange pathways in the two compounds. Charge density calculations reveal that the changes in the electronic structure, caused by substitution of the spin-species, are the underlying cause for the large difference in the two exchange energies. The work highlights the important role of the spin-species in effectively mediating magnetic exchange interactions.

Secondly, multiple measurement techniques were used to determine the magnetic ground-state of the coordination polymer $\mathrm{NiI_2(3,5\text{-lutidine})_4}$, where 3,5-lutidine $= \mathrm{C_7H_9N}$. Owing to a minimal Ising-like anisotropy $D = -1.2(1)$ K compared to the intrachain coupling $J = 17.5(2)$ K and vanishingly small interchain coupling, the system was found to reside deep within the Haldane phase of the zero-field phase diagram for quasi-one-dimensional $S = 1$ antiferromagnets. Magnetometry data combined with inelastic neutron scattering studies show that the anisotropic critical fields for field parallel $\mu_0 H_{\mathrm{c}}^{\parallel} = 5.3(1)$ T and perpendicular $\mu_0 H_{\mathrm{c}}^{\perp} = 4.3(1)$ T to the chain axis were best described by a quantum-field-theoretical ‘fermion’ model, previously posited to only be applicable to easy-plane Haldane systems. Furthermore, in-field inelastic neutron scattering studies reveal a novel excitation in the system above 2 T, attributable to spin-half end-chains predicted to exist in Haldane systems. High-pressure magnetometry studies on this compound also demonstrate it is exceedingly amenable to pressure being used as an external tuning parameter to alter the strength of the magnetic exchange interactions in the system.

Lastly, the magnetic ground-state of the asymmetric $S = 1/2$ antiferromagnetic dimer $\mathrm{CuVOF_4(H_2O)_6{\cdot}H_2O}$ was characterised using magnetometetry, electron-spin resonance and density functional theory calculations. The work highlights that the Jahn-Teller distortion of the Cu(II) octahedral environment is not only responsible for the unique structure, but also the low-dimensional magnetism in this compound. A study of the pressure-evolution of the magnetic and structural properties of $CuVOF_4(H_2O)_6 \cdot H_2O$ was performed and compared to a parallel pressure study on the symmetric dimer compound $[Cu(pyrazine)_{0.5}(glycine)]ClO_4$ (where pyrazine = $C_4H_4N_2$ and glycine = $C_2H_5NO_2$). The behaviour of each compound under applied hydrostatic pressure was found to radically different, with the quantum-disordered ground-state of $CuVOF_4(H_2O)_6 \cdot H_2O$ being made more robust with increasing pressure whilst, in contrast, pressure serves to close the singlet-triplet energy gap in $[Cu(pyrazine)_{0.5}(glycine)]ClO_4$ as the system is driven through a pressure-induced quantum critical point around 16.5(3) kbar.

Abbreviations

1D = One-dimensional

2D = Two-dimensional

3D = Three-dimensional

3,5-lut = 3,5-lutidine

AFM = Antiferromagnetic

a.u. = Arbitrary units

BEC = Bose-Einstein condensate

CEF = Crystal electric field

DAC = Diamond anvil cell

DFT = Density functional theory

DMI = Dzyaloshinskii-Moriya interaction

DPPH = 2,2-Diphenyl-1-picrylhydrazyl

ESR = Electron-spin resonance

FM = Ferromagnetic

gly = glycine

INS = Inelastic neutron scattering

JT = Jahn-Teller

LANL = Los-Alamos National Laboratory

MCE = Magnetocaloric effect

MM = Multipolar model

NHMFL = National High Magnetic Field Laboratory

PCC = Piston cylinder cell

PDO = Proximity-diode oscillator

PPMS = Physical properties measurement system

PTCFE = Polychlorotrifluoroethylene

pyz = pyrazine

Q1D = Quasi-one-dimensional

Q2D = Quasi-two-dimensional

QCP = Quantum critical point

QD = Quantum disorder

QD-MPMS = Quantum design$^{\text{TM}}$ magnetic property measurement system

QPT = Quantum-phase-transition

RF = Radio-frequency

SIA = Single-ion anisotropy

SQUID = Superconducting quantum interferometer device

TDO = Tunnel-diode oscillator

TLL = Tomonaga-Luttinger liquid

ZF = Zero-field

ZFS = Zero-field splitting

μ^+**SR** = positive-muon-spin-relaxation

Chapter 1

Introduction

1.1 A historical introduction to magnetism

Magnetic materials have long been a prevalent, and yet often overlooked, proponent of technological advancement throughout history. Whilst the ancient Greeks initially recognised magnetism within lodestone (a naturally occurring iron-oxide containing mineral) circa 500 BC, the Chinese were the first to use lodestone for navigation purposes, pioneering the early compasses during the 11^{th} century Song dynasty 980-1279 AD [1]. This innovation was deemed so significant that, to this day, the invention of the compass is held up in China as being one of the 'four great inventions' that signified notable advances in science and technology (the other three being gunpowder, paper-making and printing). Magnetism continues to permeate our society even now, with magnetic devices forming the salient components of many modern technologies, such as smartphones, power generators and computer hard drives.

Whilst magnetism has been documented for over a thousand years, it wasn't until relatively recently, around the 1800s, that the early theories behind the phenomena began to take shape. An intrinsic link between magnetism and electricity had been long-held, with early sailors noting the sudden reversal in the polarity of compass needles when aboard ships struck by lightning [2] and, in 1819, Danish physicist Hans Christian Ørsted observed the deflection of a compass needle when held close to a current carrying wire. This link was solidified in 1864 by Scottish-born mathematician James Clerk Maxwell, who demonstrated that an oscillating electrical field sustains an oscillating magnetic field, and visa versa, verifying that electricity and magnetism were indeed two sides of the same coin [3]. In 1895, Pierre Curie observed that heating permanent magnets served to destroy their ability to attract other magnetisable objects, showing that magnetic behaviour spontaneously developed below a critical temperature [4]. This was expanded upon by Pierre Weiss in 1907, who formulated the theory that the individual magnetic moment on each atom would naturally align itself with the mean-field produced by all the other atoms in the system, giving the first microscopic explanation for the macroscopic behaviour of ferromagnetic materials [5].

1.2 An overview of magnetism

1.2.1 The magnetic moment

Classically, magnetism is due to the co-alignment of individual magnetic moments, where an individual magnetic moment $\boldsymbol{\mu}$ arises due to the motion of a charged particle around a closed current loop, as in Figure 1.1(a), with the direction of the magnetic moment being perpendicular to the plane of that loop. The orbital motion of an electron around the nucleus of an atom can be considered within this simplified picture, and therefore has a magnetic moment associated with this motion. This moment is directly proportional to the orbital angular momentum of the electron $\boldsymbol{\mu} = \gamma\mathbf{L}$ (but in the opposite direction owing to the negative charge on the electron), where γ is called the gyromagnetic ratio [6, 7]. In real atoms, the orbital component of the angular momentum is dependent upon the suborbital electronic state occupied by the electron, described in terms of the orbital angular momentum quantum number l. A free ion harbours $2l+1$ degenerate suborbital states, with each state labelled by m_l, where m_l can take integer values within the range $l \leq m_l \leq -l$ $(l, l-1, ..., -l)$ [6]. In addition to the orbital component of the angular momentum, the electron also possesses an intrinsic angular momentum named spin $\mathbf{S}$. (This is because for a time electrons were thought to spin about their own axis, however, as electrons are point particles, this is rather hard to imagine, but the name stuck). The spin is defined in terms of the spin quantum number s, which for an electron has a value $s = \frac{1}{2}$. The component of the spin angular momentum along a fixed axis (typically labelled z) is m_s, which can take $2s+1$ possible values within the range $s \leq m_s \leq -s$ in steps of one. As electrons have $s = 1/2$, there are only two possible values of $m_s = \pm\frac{1}{2}$. In a magnetic field B the energy E of the electron is

$$E = g\mu_{\mathrm{B}} m_s B \tag{1.1}$$

meaning that an increasing magnetic field will drive the energy levels of the electron apart in a process known as Zeeman splitting [8], see Figure 1.1(b), with the degree of splitting dependent upon m_s. The value of g is a constant called the g-factor and

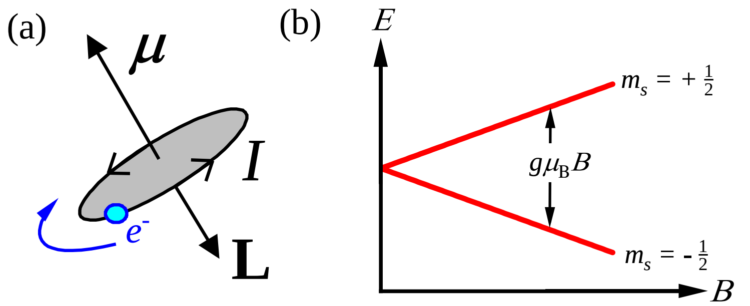

Figure 1.1: (a) Sketch of an elementary magnetic moment $\boldsymbol{\mu}$ due to the circular orbit of an electron which forms a closed current-loop I with angular momentum $\mathbf{L}$ labelled, as adapted from [7]. (b) Zeeman splitting of the energy (E) levels of a spin-half magnetic moment upon increasing magnetic field (B) as adapted from [6].

μ_B is named the Bohr magneton ($\mu_\mathrm{B} = \frac{e\hbar}{2m_e} \approx 9.274 \times 10^{-24}$ J T^{-1}).

The full magnetic moment of an electron derives from a combination of the orbital $\mathbf{L}$ and spin $\mathbf{S}$ components of the angular momentum, which sum to make the total angular momentum $\mathbf{J}$ [6],

$$\mathbf{J} = \mathbf{L} + \mathbf{S}. \tag{1.2}$$

Typically, atoms contain many electrons which fill the suborbital electron shells. If a shell is unfilled, then unpaired electrons in that shell can combine to give non-zero components of the spin and orbital angular momentum. For a free electron $\mathbf{S}$ and $\mathbf{L}$ can be considered separately, however, when confined to an orbital these two components do in fact weakly couple to each other through what is known as spin-orbit coupling [9]. This leads to $\mathbf{L}$ and $\mathbf{S}$ not being separately conserved, whilst the total angular momentum $\mathbf{J}$ is. Subsequently, there are many possible combinations of angular spin and momentum quantum number that may exist within a single system. To navigate all these possible combinations and determine the actual ground-state (lowest energy electronic configuration) for a particular ion, one must observe Hund's rules. These are:

i) The value of $\mathbf{S}$ must be maximised to prevent electrons with parallel spins occupying the same state, in accordance with the Pauli exclusion principle, which in turn minimises the Coulombic repulsion between electrons.

ii) The value of $\mathbf{L}$ must therefore be maximised. This can be thought of as ensuring electrons orbit in the same direction, thus reducing the Coulombic repulsion between them.

iii) $\mathbf{J} = |\mathbf{L} - \mathbf{S}|$ for a shell less than half full and $\mathbf{J} = |\mathbf{L} + \mathbf{S}|$ if a shell is more than half full, which minimises the spin-orbit energy.

There are however exceptions to Hund's rules, most notably for electrons that occupy the $3d^5$ to $3d^{10}$ electronic states, such as in the transition metal Co(II), Ni(II) and Cu(II) ions discussed in this thesis.

1.2.2 Transition-metal ions in octahedral environments

The five $3d$ orbitals each have a unique spatial distribution as outlined in Figure 1.2(a), where, for a free ion, the energy of the orbitals is degenerate in zero-field. The orbitals fall into two classes: the e_g orbitals which point along the x, y, z axes, encompassing the d_{z^2} and $d_{x^2-y^2}$ orbitals; and the t_{2g} orbitals, which point between axes, which includes the d_{xy}, d_{xz} and d_{yz} orbitals. The local crystalline environment an ion resides in introduces a crystal-electric-field CEF that interacts with the central transition-metal ion. For $3d$ transition-metal ions in a six-coordinate octahedral environment, as depicted in Figure 1.2(b), the CEF mainly arises due to the electrostatic repulsion between the central $3d$ metal-ion [blue sphere, Figure 1.2(b)] and the six coordinating ligands [red spheres, Figure 1.2(b)]. The effect of the CEF here is to lower the energy of the t_{2g} levels and raise the energy of the e_g levels. This is because the t_{2g} orbitals, which point between the principle axes, will have less orbital overlap with the six coordinating ligands and thus experience a lower electrostatic repulsion compared to the e_g orbitals, which point along the principle axes. For $3d$ transition metals in octahedral environments, the energy of the CEF, which lifts the degeneracy of the energy-levels, is much greater than the energy of the spin-orbit interaction within the system. Therefore, Hund's third rule does not hold and the orbital component of the angular momentum $\mathbf{L}$ is quenched, meaning that the angular momentum of the $3d$ transition-metal ions can be represented solely by the spin angular momentum, $\mathbf{J} = \mathbf{S}$.

Hund's rules can still be used to determine the ground-state of transition-metal ions, with the effect of the CEF from an octahedral environment on the energy-levels of Cu(II), Ni(II) and Co(II) ions shown in Figure 1.2(c), 1.2(d) and 1.2(e), respectively [10]. For Cu(II) ($3d^9$), Hund's rules dictate that a single electron occupies the $d_{x^2-y^2}$ orbital. The e_g levels split further due to a spontaneous axial-elongation of the octahedra known as a Jahn-Teller (JT) distortion [11]. This arises as it is energetically favourable to distort the octahedra, due to a reduction in the electrostatic repulsion within the doubly occupied d_{z^2} orbital. For Ni(II), one electron occupies the $d_{x^2-y^2}$ orbital and one the d_{z^2} orbital, and no JT distortion occurs. Co(II) allows for two possible spin configurations. The high-spin configura-

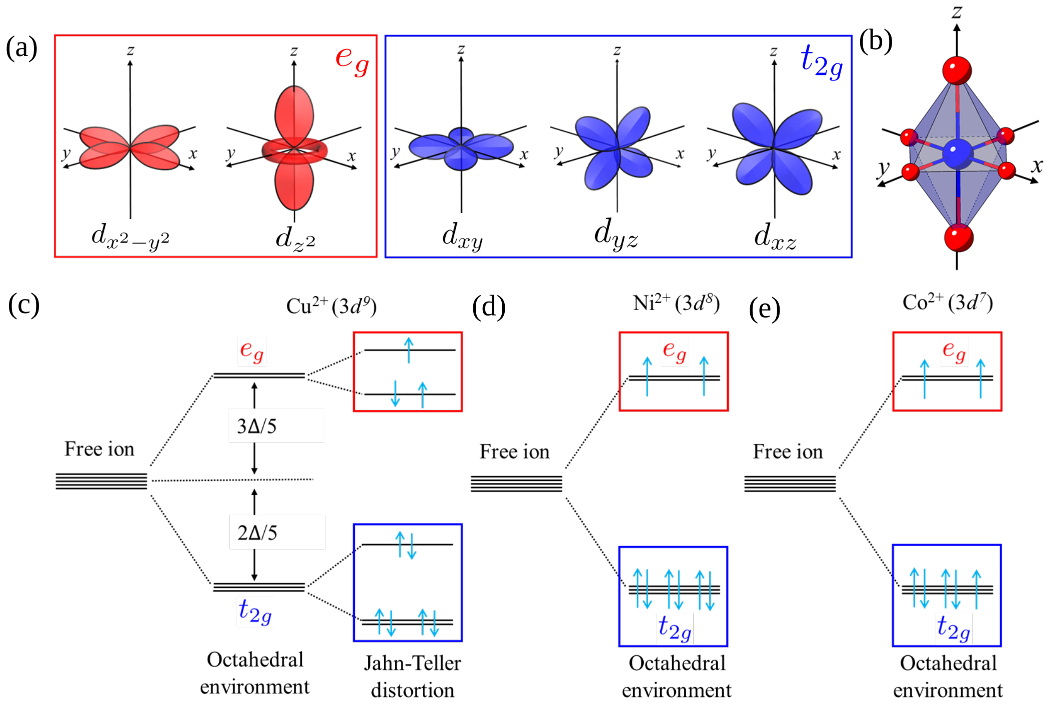

Figure 1.2: (a) Sketches of the spatial distribution of the five atomic d-suborbitals where the e_g orbitals point along, and the t_{2g} orbitals point between, the x, y and z axes, with the coordinate axes defined by the octahedral environment as depicted in (b). The effect of an octahedral environment on the energy levels of (c) Cu(II), (d) Ni(II) and (e) Co(II) ions, with Co(II) being in the high-spin $S = 3/2$ state.

tion, as in Figure 1.2(e), where two co-linear spins occupy the e_g state to give a total spin $S = 3/2$, and the low-spin state, where a single spin occupies the e_g level, such that the resultant spin of the system is $S = 1/2$.

For Ni(II) and Co(II), where $S > 1/2$, the crystal field can further split the m_s energy-levels to give a preferred orientation of the spin within the local environment, this is known as the zero-field splitting (ZFS) [12]. The ZFS for a $S > 1/2$ ion can be described by the Hamiltonian [12],

$$\mathcal{H} = D\sum_i (\hat{\mathbf{S}}_i^z)^2 + E\sum_i [(\hat{\mathbf{S}}_i^x)^2 + \hat{\mathbf{S}}_i^y)^2], \tag{1.3}$$

where D is the axial single-ion anisotropy (SIA) parameter and E describes the equatorial SIA often called the rhombic anisotropy. Here, D is the energy difference between the $m_s = \pm 1$ states and the $m_s = 0$ state. The E-term is only present in systems where there is an energy difference between the $m_s = +1$ and $m_s = -1$ states, owing to distortions within the equatorial-plane of the octahedra [13]. For

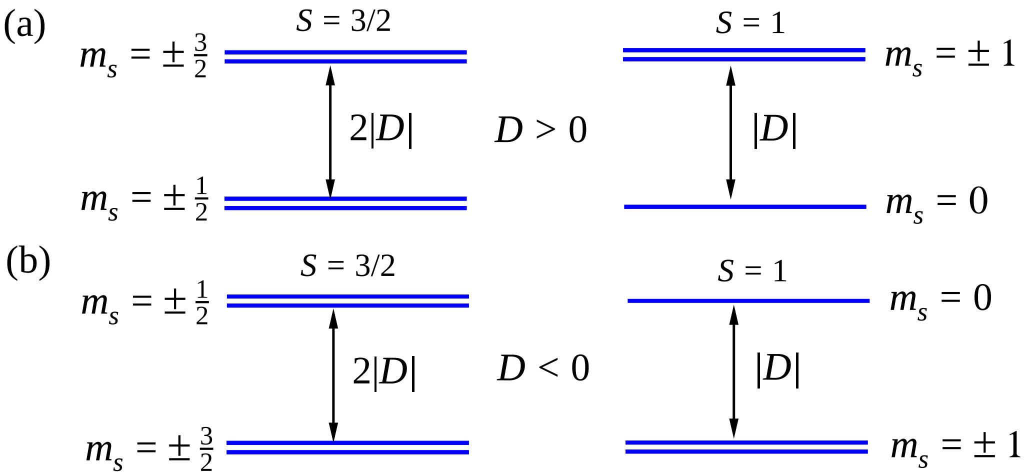

Figure 1.3: Cartoon energy-level diagrams for a $S = 1$ and $S = 3/2$ ion in zero-field with $D \neq 0$ and $E = 0$ for both the easy-plane ($D > 0$) and easy-axis ($D < 0$) anisotropy case.

systems with $S = 1$ [Ni(II)] where $E = 0$, the sign of D determines the magnetic ground-state of the system. For $D > 0$, the $m_s = 0$ singlet is the ground-state of the system, whilst for $D < 0$ the $m_s = \pm 1$ doublet is [14, 15]. For $S = 3/2$ systems, such as Co(II), a positive D results in an $m_s = \pm 1/2$ ground-state doublet and $m_s = \pm 3/2$ doublet excited-state; visa-versa for negative D [16].

The zero-field arrangement of the energy levels for non-zero D with $E = 0$ is outlined in Figure 1.3 for a $S = 3/2$ Co(II) ion and $S = 1$ Ni(II) ion. Where $D > 0$, systems are referred to as easy-plane as the magnetic moment prefers to lie within the xy-plane of the local octahedra. Conversely, $D < 0$ systems are dubbed easy-axis (or said to have Ising-like anisotropy) as the magnetic moment prefers to align along the z-axis of the octahedra. For $S = 1$ Ni(II) octahedra, easy-plane anisotropy is often preferred for an axially elongated octahedra whilst axial compression typically promotes easy-axis anisotropy [14]. However, recent work in reference [17] has also highlighted the important role that the electronegativity of the coordinating ligands has on determining the sign of D in six-coordinate Ni(II) complexes. For Co(II) complexes, axial compression is common and often results in easy-axis anisotropy with large values of $|D|$ [16].

1.2.3 Interacting magnetic moments

Individual magnetic moments interact via the magnetic exchange interaction which arises due to the direct spatial overlap of the wavefunctions of two electrons. When this occurs, there is a finite probability that the two interacting electrons are exchanged, which results in the spin angular momentum of the two electrons aligning co-linearly [18]. In reality, there is often insufficient orbital overlap for this direct exchange interaction to occur [6]. Typically, the magnetic exchange is mediated via an intermediary non-magnetic ion, or molecule, which links the two interacting magnetic ions and permits the wavefunctions of each to delocalise over the whole system [19]. This form of exchange is called the superexchange interaction, and all of the materials discussed in this thesis interact via this mechanism (all subsequent references to the exchange interaction refer to superexchange).

If the superexchange invokes a parallel arrangement between adjacent spins then the result is ferromagetic (FM) ordering, where the system has a net magnetic moment [5]. For an anti-parallel arrangement, the ground-state is one of antiferromagnetic (AFM) order, where the moments on the two spins cancel each other out, resulting in zero net magnetic moment [20]. For a system to enter into an AFM or FM long-range ordered state, the temperature must be low enough to ensure the exchange interactions are the dominant energy scale of the system, otherwise individual spins are uncorrelated and the system becomes paramagnetic [6]. In general, the exchange interaction between a number of interacting magnetic ions can be summarised by the spin Hamiltonian,

$$\mathcal{H} = J \sum_{<i,j>} \hat{\mathbf{S}}_i \cdot \hat{\mathbf{S}}_j \tag{1.4}$$

where J is the magnetic exchange energy between the spins $\mathbf{S}_{i,j}$ and $< i, j >$ denotes sums over unique pairs of nearest neighbour spins in the system; $J < 0$ and $J > 0$ describe FM and AFM exchange interactions, respectively. The above describes what is known as the Heisenberg model, where the interacting spins can point in whatever direction they like, as long as they remain co-linear to each other. This is, however, not always the case. In addition, within real systems the strength of the exchange is not necessarily the same along all crystallographic directions.

The latter is called spatial exchange anisotropy. Here, one can imagine a three-dimensional lattice built of octahedra, as in Figure 1.2(c), where the exchange between the magnetic-ions within the xy-plane J is not the same as that along the z-axis J', leading to the Hamiltonian,

$$\mathcal{H} = J \sum_{<i,j>} \hat{\mathbf{S}}_i \cdot \hat{\mathbf{S}}_j + J' \sum_{<i,j'>} \hat{\mathbf{S}}_i \cdot \hat{\mathbf{S}}_{j'} \tag{1.5}$$

where $< i, j >$ denotes sums over unique pairs of spins within the xy-plane and $< i, j' >$ denotes sums over unique pairs of spins along the z-direction, with J' being the strength of the exchange along z. For this situation, and $J/J' >> 1$, the spin-system will exhibit quasi-two-dimensional (Q2D) behaviour, with the predominant exchange interactions occurring between co-planar spins. Conversely, the situation where $J'/J >> 1$ describes a quasi-one-dimensional (Q1D) chain-like system, where the primary exchange interactions occurs along z, with adjacent chains being weakly coupled within the xy-plane.

The other form is spin-exchange anisotropy, where the exchange is non-Heisenberg and consequently adjacent spins prefer to orientate themselves either along a unique-axis, known as the Ising model, or within a plane, known as the XY-model. This modifies the components of the spins in Eq. 1.5 by $\hat{\mathbf{S}}_i, \hat{\mathbf{S}}_j \longrightarrow \hat{S}_i^z, \hat{S}_j^z$ for the Ising model and $\hat{\mathbf{S}}_i, \hat{\mathbf{S}}_j \longrightarrow \hat{S}_i^{xy}, \hat{S}_j^{xy}$ for the XY-model; the orientation of adjacent spins relative to each other also contains contributions from single-ion effects as discussed above.

1.3 Low-dimensional coordination polymers magnets

It is clear that modifying the exchange anisotropy in real magnetic systems can produce spin-networks which operate in reduced dimensions, such as Q1D or Q2D systems. This field of research is known as low-dimensional magnetism and has long been of interest from a theoretical and experimental perspective [21]. From a fundamental physics standpoint, this is due to the array of exotic quantum ground-states and quantum-critical points (QCPs; zero-temperature phase-transitions involving a reorganisation of a material's ground-state which is driven, not by thermal, but quantum fluctuations of the system [22]) on offer within low-dimensional magnets. These include: Bose-Einstein condensation (BEC) in $S = 1/2$ AFM dimers [23, 24]; the gapped Haldane ground-state in $S = 1$ Q1D Heisenberg AFMs [25–27]; Berezinskii–Kosterlitz–Thouless phase-transitions in Q2D XY-like spin systems [28–30]; and the transverse-field Ising model in $S = 1/2$ Q1D FM coupled chains, which is the simplest theoretical model of a QCP phase-transition [22, 31, 32]. Low-dimensional magnets are also of interest from a technological perspective. Square-lattice Q2D networks of $S = 1/2$ Cu(II) ions with AFM Heisenberg exchange coupling are the fundamental building blocks of the the high-temperature superconducting cuprate family [33]. Alongside this, the symmetry protected edge-states present within Q1D Haldane spins-chains have possible applications within quantum computation [34].

Investigating the quantum phenomena and possible technological advancements on offer in low-dimensional magnets relies heavily on building a solid understanding of the underlying physics within these systems. Experimentally, determining the factors which govern the sign and strength of both the exchange interactions and single-ion anisotropy within a system is paramount to classifying the magnetic ground-state. In addition, the interplay between these interactions dictates whether any QCP behaviour may exist within a system upon application of an external tuning parameter, such as magnetic field or pressure. Understanding these factors would allow research to begin to move toward constructing bespoke magnetic systems whose properties could be chemically tuned from the point of synthesis. Whilst the structural simplicity of inorganic systems has lead to many productive research efforts in this regard, the strength of the exchange interactions in these systems is often large, meaning pushing such systems through field or pressure induced QCPs is often difficult [35]. In addition, inorganic systems can be difficult to modify in a controlled fashion, as chemical doping can often lead to drastic deformations of the underlying crystalline and electronic structures [36].

One particularly fruitful avenue to circumvent these problems has been the pursuit of molecule-based magnetic systems, where coordination polymers present regular arrays of magnetic ions linked via molecular ligands or halogens [37–41]. Often, these molecular linkers have relatively weak exchange energies, typically ~ 10 K [40, 42], such that the magnetism within these systems can be probed using conventional laboratory magnetic fields, $\mu_0 H \lesssim 10$ T. The rich variety of structures available within organic chemistry also makes these systems highly tunable, opening up the possiblity for the spatial exchange anisotropy, and thus the dimensionality of the system, to be chemically tailored [17, 41, 43]. Additionally, the 'softer' nature of molecular crystals, compared to ionic solids, makes them ideal candidates for pressure studies, as the application of hydrostatic pressure more easily modifies the length of the exchange pathways, or geometry of the magnetic-ions local environment, within the material [44].

1.4 Thesis scope

Much of today's most interesting and potentially useful materials exhibit states of matter that can only be explained by quantum mechanical models which are at the limits of our present understanding; such as superconducting Josephson Junctions, which stand at the forefront of quantum computation [45]; graphene, which has potential applications in next generation wearable medical devices [46]; and future solar-cell materials which seek to solve the world's energy crisis [47].

These *quantum materials* play host to an intricate array of many-body interactions between spins, electrons and phonons. As such, the ground states that emerge often host collective behaviour (BEC [23], superconductivity [48], multiferroicity [49]) and exotic excitations (skyrmions [50], Majorana fermions [51], magnetic monopoles [52]) providing the opportunity to study a rich medley of physics. Often, magnetic materials which exhibit such properties interact in reduced dimensions where quantum effects are more prevalent. Hence, for the above reasons, deciphering what causes these quantum states is of pressing concern to modern physics.

This thesis outlines research which attempts to reconcile how various factors, such as crystal architectures, can give rise to a selection of ordered or disordered magnetic ground states, as well as understand the physics which underpins the excitations that develop from them, in order to advance the knowledge of the presented novel magnetic states, and help understand the building blocks of quantum systems. I will present studies on five magnetic insulators with structures rooted in coordination polymer chemistry (for reasons outlined in section 1.3). This avenue of study aims to move toward the construction of designer magnetic materials with specific properties which can be 'made-to-order' for use in physical applications, or, to allow experimental tests of theoretical predictions for research in this area to be performed.

The materials NiI_2(3,5-lut)$_4$ (3,5-lut = 3,5-lutidine = C_7H_9N), $Ni(NCS)_2$(thiourea)$_2$, $S = 1$, and $Co(NCS)_2$(thiourea)$_2$, $S = 3/2$, [thiourea = $SC(NH_2)_2$] show that molecular building blocks can be used to construct highly one-dimensional (1D) systems. The latter is also a promising candidate to physically realise the transverse-field Ising chain, the 'textbook' model of quantum-criticality, due to similarities between its magnetic properties and those of $CoNb_2O_6$, which is the archetypal system for this model [31, 32]. (Presently, $CoNb_2O_6$ is the only known realisation of this model, so identifying other candidate materials would allow the applicability and limitations of the theory to be tested.) Within this model, a chain of N $S = 1/2$ Ising spins are connected in 1D with the ground state being one of FM order with spins aligned colinear to the Ising-axis. If a magnetic field is applied perpendicular to the Ising-axis, the Zeeman interaction attempts to orientate the spins parallel to the field direction (perpendicular to the Ising axis). This results in the spins existing in a superposition of spin-up and spin-down where for N spins there now exist 2^N coupled states, a fact which could be put to good use in quantum computation [53]. $Ni(NCS)_2$(thiourea)$_2$ and $Co(NCS)_2$(thiourea)$_2$ therefore provide an avenue to study the factors, such as choice of bridging ligand and substitution of the spin-species, which affect the formation of 1D FM Ising chains.

The compound NiI_2(3,5-lut)$_4$ is a near-ideal physical realisation of a Haldane $S = 1$ chain. The Haldane state is an exotic, disordered gapped ground-state that is characterised by a topological order-parameter with emergent, fractional spin-half end-chain degrees of freedom which exist at the edges of the chains [25, 34]. The behaviour of a Haldane system with SIA in fields close to the critical values is described by two quantum-field-theoretical models [54], which disagree in their predicted critical field values for field perpendicular to the chain direction (see section 4.1 for details). The low energy scale of the gap in NiI_2(3,5-lut)$_4$ ($\Delta \approx 7$ K) means it can be readily closed in laboratory magnetic fields. The minimal SIA ($D \sim -1$ K) means both critical fields reside in close proximity but remain readily distinguishable from each other. Combined with the vanishingly small interchain coupling, which can lead to a departure from idealised 1D behaviour, means that the experimental data can be easily compared with the critical fields predicted by the two models. This may help further the understanding of the limitations of the two models in describing various Haldane systems.

Often, inorganic Haldane systems have large energy-gaps which makes probing how the edge-state $S = 1/2$ end-chain excitations evolve upon the field-induced closure of the gap difficult [55, 56]. Of the organic Haldane systems where the field-induced closure of the gap can be readily observed, such as the molecule-based Haldane system NDMAP [57], sizable interchain interactions often exist which promote 3D AFM order above the closure of the gap [58, 59]. This negates the possible formation of a gapless Tomonaga-Luttinger liquid (TLL) state proposed to exist in Haldane systems at fields above the closure of the gap [60]. The vanishingly small interchain coupling and minimal SIA present within NiI_2(3,5-lut)$_4$ mitigate the onset of 3D order at fields above the critical values, such that it may be a good candidate to exhibit TLL behaviour. Furthermore, the organic structure of this near-ideal system make it an excellent parent compound to investigate the effect of introducing non-magnetic defects at the transition-metal sites, where the controlled introduction of disorder can lead to exotic quantum states, such as the Bose-glass state found in the quantum-magnet DTN [61]. Hence, characterising the properties of the parent compound is paramount for future studies aimed at investigating the effects of doping.

It is well known that $S = 1/2$ AFM dimers exhibit a field-induced phase-transition from a ground-state of quantum-disorder (QD) to an XY-AFM ordered state that, provided the rotational symmetry of the system is preserved, can be described as a BEC of magnons [23, 62]. As such, these dimer systems are excellent playgrounds to study how quantum fluctuations can drive a system through a QCP. The two AFM coupled $S = 1/2$ dimers $CuVOF_4(H_2O)_6 \cdot H_2O$ and $[Cu(pyz)_{0.5}(gly)]ClO_4$ (pyz = pyrazine = $C_4H_4N_2$; gly = glycine = $C_2H_5NO_2$) are dimers on the verge of phase instability. Hence, their magnetic and structural properties are measured as the external tuning parameters of pressure and magnetic field (which both permit continuous, clean and reversible tuning of the systems quantum interactions) are used to breach the tipping point. Providing an opportunity for these systems to potentially shed light on the role quantum fluctuations play in driving quantum-phase-transitions (QPTs).

1.5 Thesis outline

In Chapter 2, the experimental techniques used to characterise the various magnetic ground-states, and investigate any magnetic excitations, are outlined. The primary probe of the magnetic properties of the materials in this thesis is the application of an external magnetic field, which forces spins to align with the applied field. The field at which all the spins align, the saturation field, encompasses the energies of all the magnetic interactions in a system, whilst various features in the field-sweep provide information about the exchange, or single-ion, anisotropy present in the system. Additionally, techniques such as muon-spin-relaxation, heat capacity, electron-spin resonance, inelastic neutron scattering, density functional theory, as well as high-pressure magnetometry and crystallography measurements are discussed. All provide valuable information about the magnetism within the systems studied in this thesis.

Chapter 3 investigates the magnetic properties of the two isostructural molecule-based magnets $\mathrm{Ni(NCS)_2(thiourea)_2}$ and $\mathrm{Co(NCS)_2(thiourea)_2}$. The are characterised using several techniques in order to rationalise with structural parameters and ascertain magnetic changes cause by substitution of the spin. Both species are compared to the similar, molecule-based, magnetic compounds $M\mathrm{Cl_2(thiourea)_4}$, $M = \mathrm{Ni(II)}$ (DTN) and Co(II) (DTC), where DTN is known to harbour two magnetic field-induced quantum critical points, the first of which belongs to the Bose-Einstein condensate of magnons universality regime [63].

Within Chapter 4, the coordination complex $\mathrm{NiI_2(3,5\text{-}lut)_4}$ is characterised using a variety of measurement techniques. The ground-state of the system is shown to be well within the Haldane phase for Q1D $S = 1$ Heisenberg AFM chains, where a weak axial anisotropy gives rise to two anisotropic Haldane-gaps in zero-field of $\Delta^{\parallel} = 5.3$ K and $\Delta^{\perp} = 7.7$ K. These anisotropic gaps are closed at critical fields of $\mu_0 H_c^{\parallel} = 5.3$ T and $\mu_0 H_c^{\perp} = 4.3$ T. In-field inelastic neutron scattering experiments reveal the emergence of a new feature within the excitation spectrum, whilst high-pressure magnetometry measurements indicate that the system is highly amenable to pressure being used as an external tuning parameter for the magnetic exchange interactions.

Chapter 5 outlines a study of the magnetic properties of the lambda-shaped antiferromagnetically coupled $S = 1/2$ dimer material $CuVOF_4(H_2O)_6{\cdot}H_2O$. The dimer-unit itself is composed of two unlike $S = 1/2$ species, Cu(II) and V(IV), such that the rotational symmetry of the system is broken not only by the non-centrosymmetric structure, but also by the spins which make up the dimer-unit itself. It is found that Jahn-Teller distortions of the Cu site is responsible for not only the unique structure of the system, but also the rare form of exchange coupling present in this system. Further to this, the pressure-evolution of the magnetic and structural properties of $CuVOF_4(H_2O)_6{\cdot}H_2O$ are presented and compared with a parallel pressure study on the symmetric dimer compound $[Cu(pyz)_{0.5}(gly)]ClO_4$.

The last Chapter presents an overview of the results obtained in this thesis, and follows on from this with an outlook as to future experiments on the compounds discussed in the work.

Chapter 2

Experimental Techniques

2.1 Magnetometry techniques

2.1.1 Pulsed-field magnetometry

Pulsed-field magnetometry measurements were performed in collaboration with J. Singleton at the National High Magnetic Field Laboratory in Los Alamos, USA. Powder samples were packed tight into polychlorotrifluoroethylene [PCTFE = $(\mathrm{C_2ClF_3})_\mathrm{n}$] ampoules with inner diameter of 1.3 mm and the open end sealed with Apiezon vacuum M-grease. Fields of up to 65 T with typical rise times of ≈ 10 ms and pulse time of ≈ 50 ms were used. If both the up and down sweeps were clean, the resultant signal is an average of the two. If one sweep was deemed unusable, the cleaner of the two was used. A helium-3 (^{3}He) cryostat provides access to temperatures down to $T \approx 0.5$ K. A schematic of the pulsed-field magnetometry cryostat set-up is shown in Figure 2.1.

The ampoule is attached to a probe which contains a 1500 turn, 1.5 mm bore, 1.5 mm long compensated-coil susceptometer constructed from 50-gauge high-purity copper wire. When the sample is centered within the coil and the field is pulsed, the voltage V induced in the coil is proportional to the rate of change of magnetisation with time,

$$V \propto \frac{\mathrm{d}M}{\mathrm{d}t} = \frac{\mathrm{d}M}{\mathrm{d}H}\frac{\mathrm{d}H}{\mathrm{d}t}. \tag{2.1}$$

Two measurements are required to isolate the sample $\mathrm{d}M/\mathrm{d}H$ response. Firstly, the field is pulsed for the 'sample-in' measurement where the sample is centred within the coil, secondly the 'sample-out' measurement is performed where the sample is translated vertically upward to reside just above the coil. As V and $\mathrm{d}H/\mathrm{d}t$ are measured during each pulse, subtracting the 'sample-out' from the 'sample-in' measurement and numerically integrating the result returns the magnetisation of the sample. The magnetic field is measured via the signal induced within a coaxial ten-turn coil and calibrated using de Haas–van Alphen oscillations within the copper coils of the susceptometer [65]. Whilst pulsed magnetic fields are an invaluable tool for reaching what can be high saturation fields in low-dimensional magnets [39], the rapidly changing field pulse (10-50 ms) can induce a large magnetocaloric effect (MCE) within some materials, which can lead to the shifting of in-field features to higher or lower fields. (For example, within spin-half antiferromagnetic dimers a large MCE can shift the first critical field to lower fields and the second critical field to higher fields, as well as lead to the erroneous observation of both critical fields at elevated temperatures [37]). Here, steady magnetic field measurements,

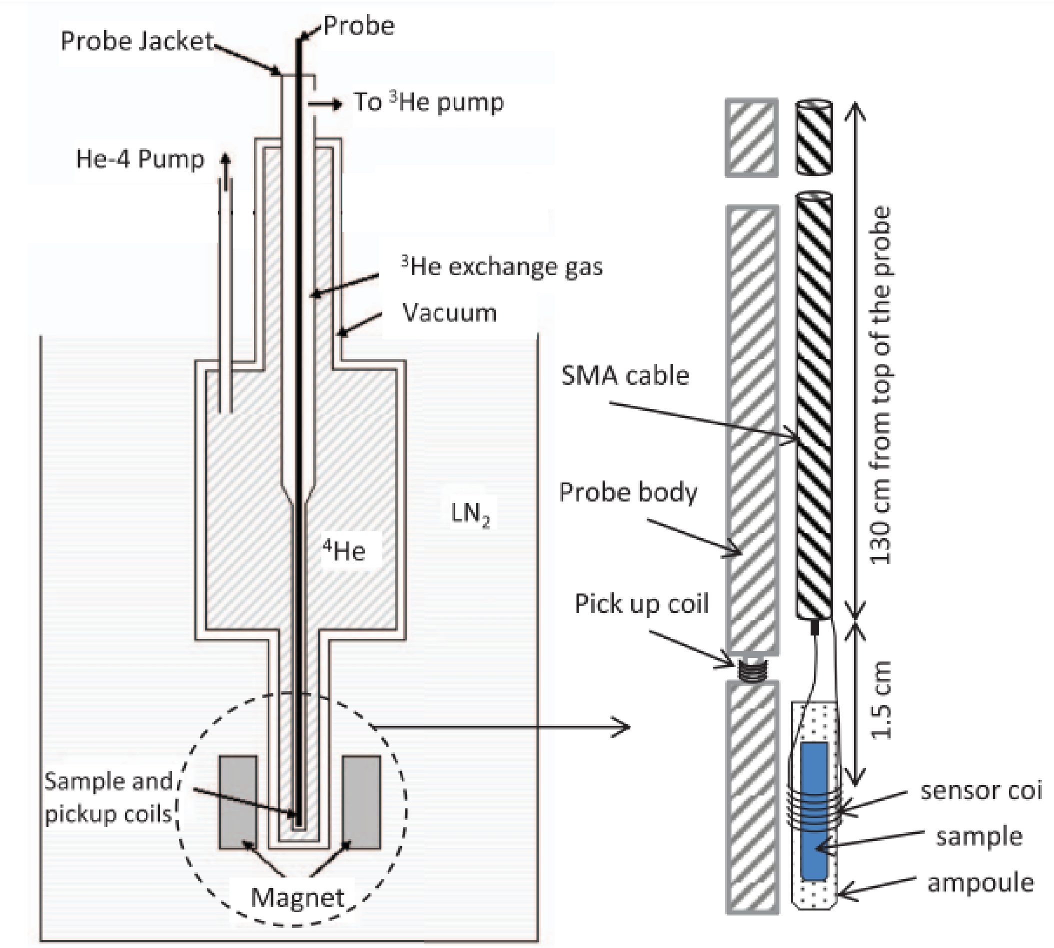

Figure 2.1: Schematic diagram of the pulsed field magnetometer crysostat and radio-frequency susceptometry set up adapted from Ref. [64].

with controllable and often substantially lower field ramp rates, are preferable.

2.1.2 Quasi-static magnetometry

Magnetometry measurements were made using a Superconducting Quantum Interferometer Device (SQUID) insert for a Quantum Design Magnetic Property Measurement System (QD-MPMS) [66]. The MPMS can access a temperature range of $1.8 \leq T \leq 300$ K in standard operating mode. Temperatures down to $T \approx 0.5$ K are possible with the use of a *i*-Quantum ^{3}He insert [67].

The magnetic field is generated by passing a persistent current through a Nb-based superconducting wire wound into a closed loop solenoid, the solenoid is submerged in liquid ^{4}He to keep the wire in the superconducting state [68]. As power does not need to be continuously supplied to the superconducting wire to sustain the current, and therefore the magnetic field, superconducting magnets are often cheaper to run and thus more favourable than their resistive magnet counterparts. The MPMS SQUID magnetometer can access fields $\mu_0 H \leq 7$ T. Fields $\mu_0 H \leq 19$ T can be accessed using superconducting magnets [68], however, the shielding required

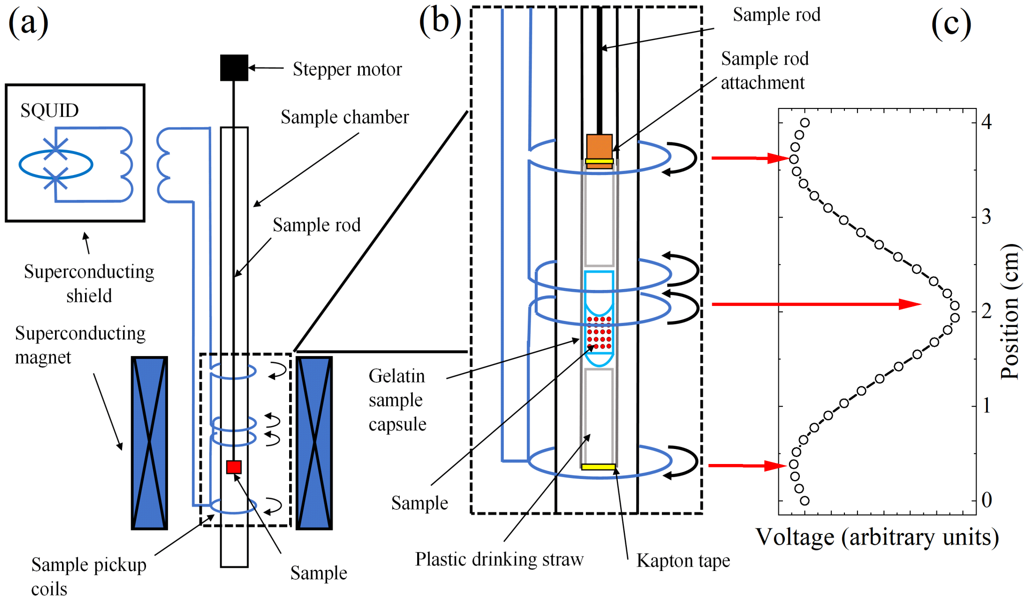

Figure 2.2: (a) Schematic of the QD-MPMS SQUID magnetometer. (b) Enlargement of the MPMS pickup coils highlighting the clockwise winding of the upper and lower coils and anticlockwise winding of the centre coils. (c) Example dipole voltage response measured as the sample moves through the pickup coils. Units here are arbitrary and the shown response simply demonstrates the signal profile, in reality the magnitude of the voltage is directly proportional to the size of the magnetic moment (in electromagnetic units) which is calculated by fitting the response to a dipole model [66].

to make measurements with a SQUID magnetometer in such large fields makes these measurements impractical.

The SQUID circuit itself is highly sensitive to fluctuations in the magnetic field and must therefore be shielded from stray fields generated by the superconducting magnet and from those within the laboratory environment. The SQUID circuit is inductively coupled to the detection coils, such that as the sample passes through the detection coils small changes induced in the detection coil current are converted to a small voltage change in the SQUID circuit. This allows the detection of magnetic moments down to 10^{-11} Am^2 in low fields ($\mu_0 H \leq 2.5$ T). The detection coils are three sets of superconducting wire with the upper and lower coils wound in a clockwise direction and the centre coil in an anticlockwise direction as in Figures 2.2(a) and 2.2(b). This set-up helps to reduce background noise due to fluctuations in the magnetic field. A stepper motor incrementally moves the sample through the three coil set-up which changes the local magnetic flux density between the coils. As the coils are inductively coupled to the SQUID circuit, this directly induces a change in the voltage profile across the SQUID circuit; an example of the induced response is shown in Figure 2.2(c). The response can be fit to a dipole function which allows the size of the measured magnetic moment M to be extracted. The SQUID measures the magnetic moment (M) versus applied field (H) and against changes in temperature (T) to plot both the magnetisation $M(H)$ and magnetic susceptibility curves $\chi(T) = M/H$, respectively.

Samples typically come as either single-crystals approximately 125 mm^3 (5 x 5 x 5 mm) in size or as polycrystalline powders. The former can be mounted within a gelatin capsule and secured via Apiezon vacuum M-grease to allow the magnetic field to be applied along the desired crystallographic direction. For samples where appropriately sized single-crystals could not be grown, the sample is crushed into a fine powder using a pestle and mortar to allow a good powder-average, encompassing all crystallographic orientations, to be measured. The powder is then packed tight into a gelatin capsule. (If the powder-sample is known to have strong magnetic anisotropy, it can be mixed with M-grease to prevent grain motion in strong fields.) The loaded gelatin capsule is then mounted into a low magnetic background drinking straw and secured in the centre using offcuts from a second straw, Kapton tape binds the straw to the sample rod, it is then ready to be loaded into the MPMS for measurements.

Often, to achieve static magnetic fields $\mu_0 H \gtrsim 19$ T, resistive Cu magnets are employed. Measurements involving steady-field resistive Cu magnets were performed at the National High Magnetic Field Laboratory (NHMFL), Tallahassee,

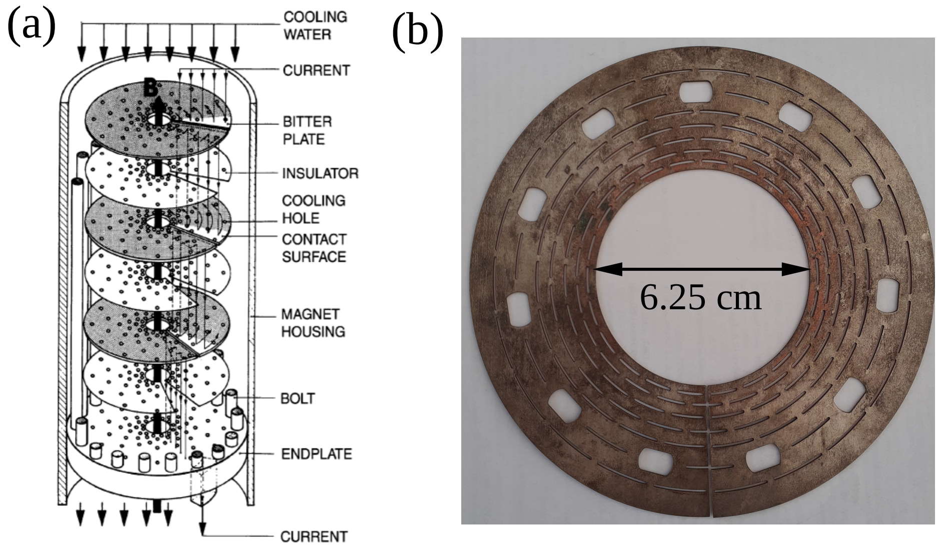

Figure 2.3: (a) Sketch of the arrangement of a Florida-Bitter solenoid as in [69]. (b) Image of a spent Florida-Bitter magnet disc which stack to comprise the solenoid within the DC-Field resistive magnets.

Florida, USA. To achieve fields of up to 35 T without melting the Cu, the magnets are comprised of hundreds of Florida-Bitter coils [69] stacked to form a solenoid as in Figure 2.3(a). The discs are sputter coated with an insulating layer to ensure the current travels along the solenoid path and doesn't jump between adjacent discs. Each disc contains dozens of holes and azimuthal slits to allow deionised water to run the length of the magnet, parallel to the field direction, as can be seen in Figure 2.3(b). This cools the Cu coils enough to allow an extremely high dc-current ($\sim$ 20 MW) to pass through the coil and continuous magnetic fields of $\mu_0 H \leq 35$ T to be generated. Of course, the trade-off with this technique is that the high-current combined with the cooling equipment and materials make this method of generating magnetic fields extremely costly to perform. The sizable field strength and large field gradients within these systems also means passing the sample through a series of counter-wound pickup coils, as in the MPMS, is impractical. In order to extract the magnetic moment of a sample when employing resistive magnets, one typically uses a radio-frequency susceptometry technique.

2.1.3 Radio-frequency susceptometry

The dynamic magnetic susceptibility ($\mathrm{d}M/\mathrm{d}H$) of a material can be measured using a radio-frequency (RF) oscillator circuit technique. The set-up involves an RF tank circuit powered by a tunnel or proximity diode oscillator (TDO or PDO) and is based on an LCR circuit. Being an LCR circuit, the angular resonant frequency of the circuit ω, which typically oscillates in the kHz−MHz range, is, to a good approximation,

$$\omega \approx \frac{1}{\sqrt{LC}} \tag{2.2}$$

where L is the inductance of the sample-coil and C the capacitance of the circuit [70, 71]. If a magnetic sample is placed within the sample-coil of the circuit, as in Figure 2.1, the inductance of the circuit will change by an amount ΔL. This change in inductance is directly proportional to the dynamic magnetic susceptibility of the sample $\Delta L \propto \mathrm{d}M/\mathrm{d}H$. In the case where the change in the inductance is small, such that $\Delta L/L << 1$, then from Eq. 2.2 the change in frequency of the circuit $\Delta\omega$ can be approximated as,

$$\frac{\Delta\omega}{\omega} \approx -\frac{\Delta L}{2L} = -2\pi f \frac{\mathrm{d}M}{\mathrm{d}H} \tag{2.3}$$

where f is the filling factor of the sample within the inductor coil [71, 72]. Therefore, $\mathrm{d}M/\mathrm{d}H$ of a magnetic material can be measured at various values of magnetic field and temperature by tracking changes in the frequency of the adapted LCR circuit. The low spatial footprint and lack of moving parts in this measurement technique also lends itself for use in high-pressure studies, where available space within the pressure-cell for loading measurement devices and samples is at a premium [64].

2.1.4 High-pressure magnetometry

For high-pressure magnetometry experiments, pressure was attained using piston-cylinder cells (PCCs). Two PCCs were employed to achieve high pressures within this thesis. A QD-MPMS 1.3 GPa piston-cylinder pressure-cell for use with the SQUID magnetometer described in section 2.1.2, and a Guertin PCC for use with cryostats in resistive magnets. For the latter. measurements were performed at the University of Warwick by myself or at the NHMFL with the assistance of local contact D. Graf.

QD-MPMS pressure-cell

For high-pressure measurements using a conventional MPMS SQUID magnetometer, a commercially available QD-MPMS 1.3 GPa piston-cylinder pressure-cell (QD-PCC) was employed. This pressure-cell can attain pressures of up to 10 kbar and used a 7373 Daphne-oil as a hydrostatic pressure medium. The QD-PCC is built of a high-tensile, low magnetic background CuBe alloy and is symmetric about the sample chamber in order to provide an integrable background response [74]. A pow-

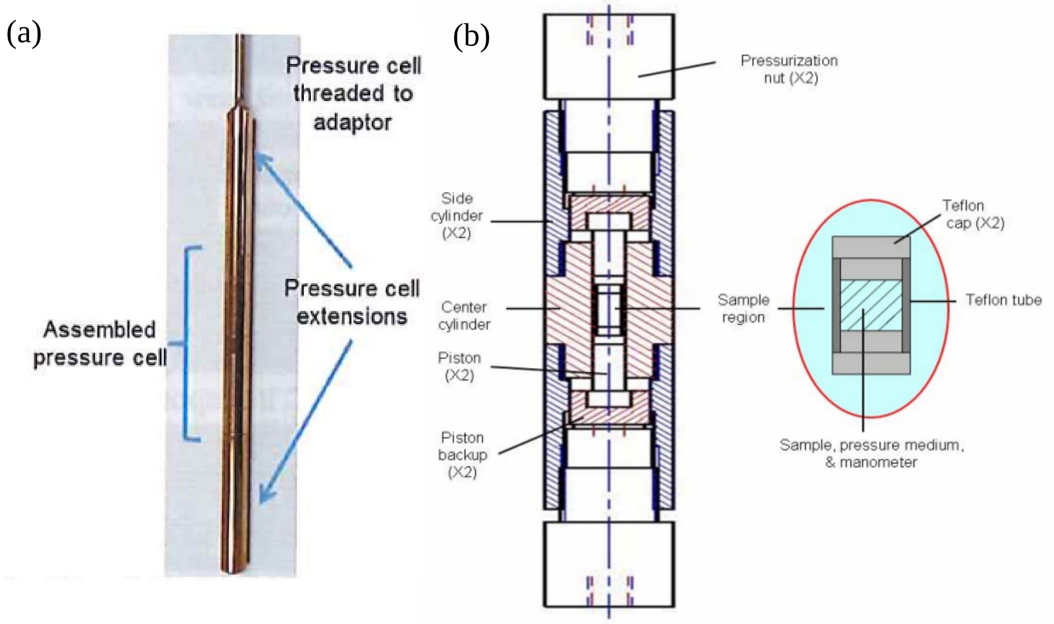

Figure 2.4: (a) Image of a fully assembled Quantum Design MPMS pressure-cell and (b) a schematic of the pressure-cell body and sample space as seen in [73].

der or single-crystal sample is loaded into a teflon cup sealed with a teflon plug at one end. The cup is then filled with an appropriate pressure medium, typically 7373 Daphne-oil or glycerol, to provide a hydrostatic pressure environment for the sample. A second teflon plug is then inserted into the open end of the teflon cup to seal it before sliding the sealed-cup down the central bore of the cell to reside in the very middle of the QD-PCC body. CuBe pistons are placed at either end of the sealed teflon cup and secured in place by two pressurisation nuts screwed finger-tight onto either end of the PCC. Tightening the pressurisation nuts at each end of the cell in equal increments symmetrically drives the two pistons into the ends of the teflon cup, compressing the cup along its length. As the cup is sealed and cannot deform radially due to the cell body, the pressure medium has nowhere to go and is thus pressurised. The hydrostatic pressure-medium transfers this pressure to the sample. Once the system is loaded to the desired pressure, estimated via a load-compression curve, the cell is attached to the end of a sample rod and a measurement performed in the same manner as for standard QD-MPMS SQUID operation (described in section 2.1.2). The cell must be cooled slowly (a max temperature sweep rate of $\sim$1 K/min) to mitigate damage to the cell due to differential contraction of the QD-PCC components upon cooling.

Pressure is calibrated in-situ by tracking the known pressure dependence of the superconducting transition temperature of a Sn manometer [76, 77]. A measurement must first be performed with an empty cell compressed to the same length as the sample measurement. This empty-cell measurement is then used as a background response to be subtracted from the sample measurement, using the SquidLab background subtraction software [78], in order to isolate the sample moment.

Guertin pressure-cell

For measurements made using RF-susceptometry, a Guertin PCC was used which operates in a similar way to the QD-MPMS pressure cell. This pressure-cell can attain pressures of up to 25 kbar and glycerol was used as a hydrostatic pressure-medium (7373 Daphne oil would also be appropriate but it is more costly). The Guertin cell body is made of high tensile MP35N, which is a non-magnetic nickel-cobalt-chromium-molybdenum alloy. The sample resides within a 10-15 turn sample-coil (inductor coil in the LCR circuit) attached to one of a pair of Cu leads emanating

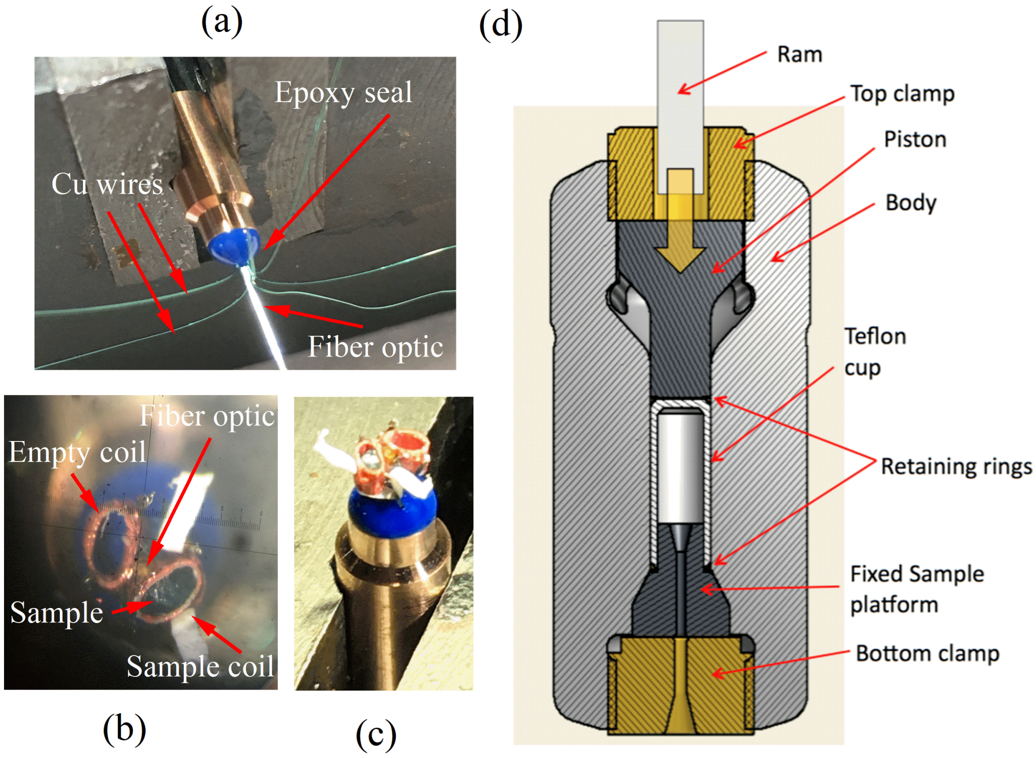

Figure 2.5: (a) Guertin PCC sample platform before attaching the sample and background coils. (b) Sample platform showing the sample and background coils for RF susceptometry with the sample mounted within the measurement coil as viewed from seen (b) and the side (c). A ruby chip is attached to the end of the fiber optic to measure the pressure in vitro but is too small to seen. (d) Schematic cross section of the Guertin PCC as in [75].

from the the Stycast 2850 FT epoxy sample platform, Figures 2.5(a-c). The second Cu lead attaches to an empty coil which provides a measurement of the background signal from the circuit at each pressure. The epoxy platform is placed under vacuum for at least 30 minutes in order to prevent the formation of air bubbles. These air bubbles can collapse under pressure and lead to the failure of the epoxy-seal in the pressure-cell. The coils are soldered to feed-through leads and attached using epoxy resin to the end of an aluminium sheathed fiber optic cable. A small piece of ruby chip is placed on the end of the fiber-optic to measure the in-situ pressure in the cell. A teflon cup is then placed over the sample platform and held in place with a sealing ring before the cup is filled with an appropriate pressure-transmitting medium. A piston is then placed into the open end of the cup and a second sealing ring holds the piston in place before placing the end-cap on. The cell is then placed on a hydraulic press and an appropriate force applied to achieve the desired pressure using a calibrated load-pressure curve. Again, the pressure medium is trapped leading to the pressurisation of the sample chamber. Once the appropriate force is applied, the top threaded end-cap is tightened to hold the system at the desired pressure. The cell is then removed from the press and mounted onto a sample probe before being loaded into a crystostat for measurement. Again, the cell is cooled slowly in order to avoid damaging the cell components due to differential thermal contraction. The low-temperature pressure is calibrated using the fluorescence spectrum from the ruby chip.

2.2 Heat Capacity

Heat capacity measurements were made on a Quantum Design Physical Property Measurement System (PPMS) instrument capable of operating within the temperature range $1.8 \leq T \leq 395$ K and applying magnetic fields $\mu_0 H \leq 9$ T. If suitable plate-like single-crystals were unavailable then polycrystalline powder samples were pressed into pellets. Samples were mounted onto the sample stage with a small

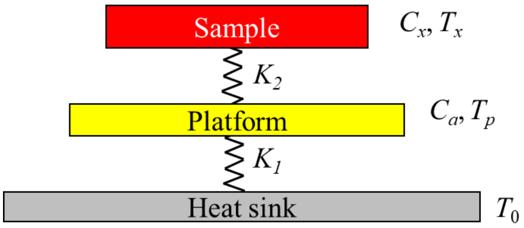

Figure 2.6: Heat flow diagram for heat-capacity measurements as adapted from [79].

amount of Apiezon vacuum M-grease to provide good thermal conductance between the sample and sample platform (K_2). Addenda measurements were performed to correct for the heat capacity of the sample platform and M-grease.

Figure 2.6 shows the heat flow diagram for a standard heat capacity measurement. The sample temperature T_x is initially equal to the platform temperature T_p, such that the two sit in thermal equilibrium. Four Cu wires thermally link the sample platform to the heat-sink which is held at a constant temperature T_0. These wires also create good thermal conductivity between the heat-sink and platform K_1. Upon application of a small heat pulse of power P the temperature of the sample platform is typically raised by $\sim 1\%$ from T_p to $T_p + \Delta T$, where $\Delta T = P/K_1$, with the relaxation of T_p back to equilibrium being governed by the heat-balance equations [79],

$$P = C_a \frac{dT_p}{dt} + K_2(T_p - T_x) + K_1(T_p - T_0), \tag{2.4}$$

$$0 = C_x \frac{dT_x}{dt} + K_2(T_x - T_p). \tag{2.5}$$

with C_a being the heat capacity of the addenda measurement and C_x the heat capacity of the sample. The heat pulse causes the sample platform temperature T_p to relax with the general form,

$$T_p(t) = T_0 + Ae^{-t/\tau_1} + Be^{-t/\tau_2} \tag{2.6}$$

where A, B and $\tau_{1,2}$ are functions of $C_{a,x}$ and $K_{1,2}$. The relaxation time constant τ_1 is the slow relaxing component and models the time for the sample to reach thermal equilibrium with the heat-sink whilst τ_2 models the faster relaxation between the sample and sample-platform. If there is good thermal coupling between the sample and the sample platform then $T_p \simeq T_x$ and, given that τ_2 is typically small and omissible, Eq. 2.6 simplifies to,

$$T_p(t) = T_0 + \Delta T e^{-t/\tau} \tag{2.7}$$

with $\tau = (C_x + C_a)/K_1$. By measuring these relaxation rates and fitting the resultant relaxation curves, the heat capacity of the sample can be reliably extracted [79].

2.3 Inelastic neutron scattering

Inelastic neutron scattering (INS) studies were performed to provide information about the scattered neutron intensity as a function of the energy-transfer $\hbar\omega$ to the sample and the change in the neutron scattering vector $|\mathbf{Q}|$. All INS measurements were performed by myself with the assistance of beamline scientist D. Voneshen on the direct geometry time-of-flight LET spectrometer at the ISIS facility, UK.

Neutrons are hadronic particles with $S = 1/2$ and hence carry a nuclear magnetic moment. Therefore, they are not only scattered by atomic nuclei but also by electrons residing in partially filled shells via a dipole-dipole interaction. This makes them an invaluable tool for investigating magnetic ordering and excitations. The neutrons at the ISIS facility are produced by bombarding high-energy protons into a carbon target through the use of a linear accelerator. To cool the neutrons to the appropriate energy ranges, near those of spin excitations, needed to probe condensed matter systems a solid methane moderator is used. The neutrons are funneled to the sample chamber using a supermirror waveguide. Five mechanical disc-choppers are set along the length of the supermirror guide and are used to select appropriate energy-ranges of neutrons for the experiment in question, as seen in Figure 2.7.

In an inelastic collision, the wavevector of the incident neutron $\mathbf{k}_{\mathrm{i}}$ is not equal to the final wavevector of the scattered neutron $\mathbf{k}_{\mathrm{f}}$, resulting in a non-zero scattering wavevector $\mathbf{Q} = \mathbf{k}_{\mathrm{i}} - \mathbf{k}_{\mathrm{f}} \neq \mathbf{0}$. This change in wavevector accompanies a change in the kinetic energy of the neutron,

$$\Delta E_{\mathrm{k}} = \frac{\hbar^2}{2m_n}(\mathbf{k}_{\mathrm{i}}^2 - \mathbf{k}_{\mathrm{f}}^2) \tag{2.8}$$

where m_n is the rest mass of the neutron and $\mathbf{k}_{\mathrm{i}} > \mathbf{k}_{\mathrm{f}}$ is the neutron losing energy to the sample whilst $\mathbf{k}_{\mathrm{i}} < \mathbf{k}_{\mathrm{f}}$ is the neutron gaining energy from interacting with the sample. The change in the neutron energy is measured using the time-of-flight technique, where the difference in the arrival times of the neutrons at the ^{3}He detector banks can be used to determine the energy-transfer to the sample [80]. The intensity of the scattered neutrons is detected using 3 m long ^{3}He detector tubes which are bunched into packs of 32, with 12 of these packs being capable of covering a full 180° horizontal-range and ±30° vertically [81]. The measured intensity can be used to determine the energy-transfer to the sample and, as the angular position of each detector is known, the momentum-transfer $|\mathbf{Q}|$ can be inferred being that $\mathbf{k}_{\mathrm{i}}$ is known; ultimately this allows the excitation spectrum of a magnetic system to be mapped.

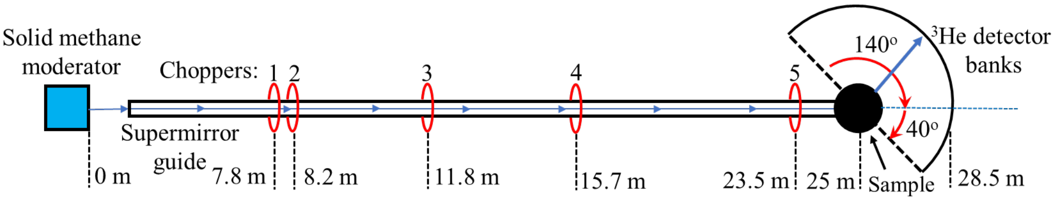

Figure 2.7: Schematic of the direct-geometry cold-neutron multi-disk chopper spectrometer LET as adapted from [81]. Blue arrows highlight the path of the neutrons.

2.4 Muon-spin relaxation

Positive muon-spin relaxation (μ^+SR) measurements were performed in collaboration with T. Lancaster, B. Huddart, T. Hicken, S. Blundell and F. Xiao. Measurements were made on LTF and GPS instruments at the Swiss Muon Source, Paul Scherrer Institut, Switzerland and the HiFi spectrometer at the ISIS facility, Rutherford Appleton Laboratory, UK. In each case, powder samples were packed into a silver or gold foil packet and mounted on the end of a fork into a Cryostat. Data analysis was performed using both WiMDA [82] and a custom built software developed for global fitting.

Similar to the creation of neutrons, in all the above facilities high-energy protons collide with a carbon target creating pions. The pion lifetime is short, at only 26 ns, and it quickly decays into a muon and a neutrino. In the rest frame of the pion, the muon is produced with a relatively slow velocity and a polarised spin which is aligned antiparallel to momentum vector of the muon [6]. The positive charge on the muon leads to it typically being implanted at interstitial sites in the system where it is sensitive to local magnetic moments. The muon then undergoes a series of rapid electron loss and capture reactions and decays in a characteristic time of 2.2 μs. These processes do not interact with the muon-spin, such that the muon is thermalised in the sample without any appreciable loss in its polarisation. The muon decay is a three body process where one of the decay products is a positron,

$$\mu^+ \longrightarrow e^+ + \nu_e + \overline{\nu}_\mu. \tag{2.9}$$

The positron is preferentially emitted along the direction of the muon spin at the time of decay [83]. By measuring the number of positrons emitted along the forward direction of the muon beam as a function of time $N_\mathrm{F}(t)$ and those emitted antiparallel to the direction of the beam as a function of time $N_\mathrm{B}(t)$, it is possible to trace the time evolution of the muon polarisation. This is paramaterised by the asymmetry

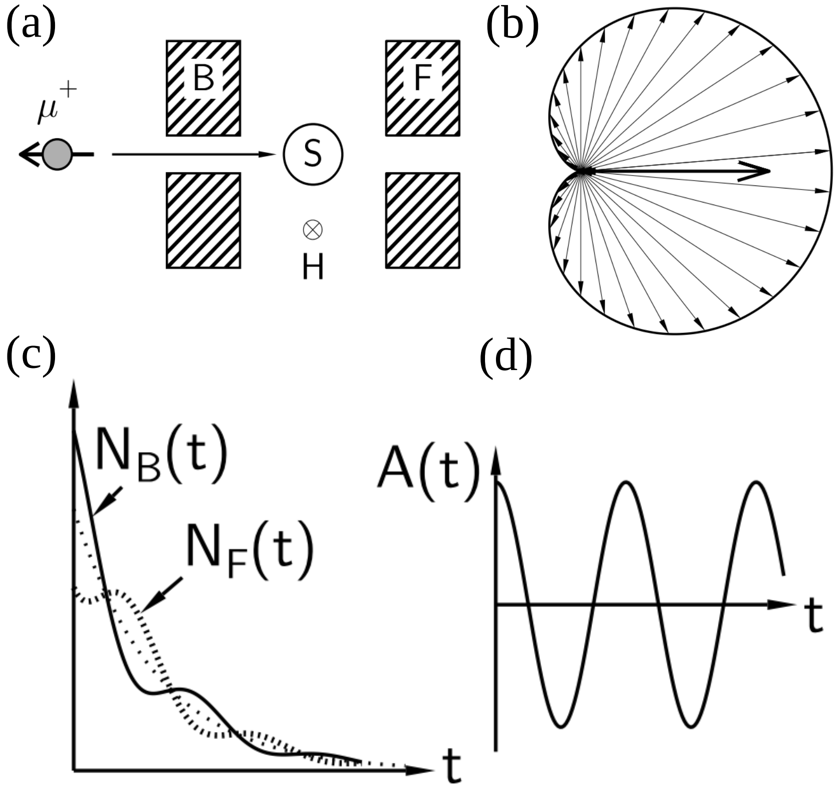

Figure 2.8: Schematic of a μ^+SR experiment as adapted from [84]. (a) A spin-polarised muon beam enters the detector and muons are implanted within the sample (S). As the muons decay, positrons are emitted preferentially along the direction of the muon spin to be detected at either the forward (F) or backward (B) detector. A magnetic field (H) will cause the muon spin to presses about the field direction, such that the positron will be preferentially emitted along this direction. (b) Schematic diagram showing the angular distribution of the emitted positrons with respect to the initial muon-spin direction. (c) Schematic cartoon of the number of positrons detected at the forward and backward detectors and (d) the measured asymmetry function.

function [83]

$$A(t) = \frac{N_{\mathrm{F}}(t) - \alpha N_{\mathrm{B}}(t)}{N_{\mathrm{F}}(t) + \alpha N_{\mathrm{B}}(t)}, \tag{2.10}$$

where α is a correction factor accounting for differences between the two detectors.

In a magnetic field, both external and within the sample, the muon spin will undergo Larmor precession with angular frequency $\omega_\mu = \gamma_\mu B$, where $\gamma_\mu = 2\pi \times 135.5$ MHz T^{-1} is the muon gyromagnetic ratio and B is the local field at the muon site, which is a sum of the internal field arising due to the spin configuration, and any external field $\mu_0 H$. Therefore, the oscillating signals detected from the implanted muon, via Eq. 2.10, relay details about the frequency of the precession of the implanted muon, which in turn reveals information about the strength of the local magnetic field in the sample. The relatively large magnetic moment on the muon compared to other fundamental particles (three times that of the proton [85]) mean it is very sensitive to small magnetic fields ($\sim 10^{-5}$ T), making μ^+SR a demonstrably suitable technique to probe ordering in low-dimensional magnets [86].

2.5 Density functional theory calculations

In order to determine the spin-density distributions and any significant exchange pathways within some of the systems discussed in this work, density functional theory (DFT) calculations were carried out in collaboration with T. Lancaster, B. Huddart, R. Scatena and P. Macchi.

For many-body systems, the effect of coulombic and magnetic exchange interactions between electrons inevitably has an effect on their behaviour. As it is typical for many particles to be involved in real systems, the interactions between electrons are often complex and difficult to describe [6]. DFT is a tool to deal with these complex interactions by recognising that the ground state of an electronic system can be described in terms of a functional of the electron density. This functional contains three contributions: a kinetic-energy term, a coulombic interaction term between electrons and an exchange-correlation term capturing the many-body interactions in the system [6]. The use of this functional of the electron density simplifies calculations considerably.

To calculate the ground-state magnetic structure of a material, the electronic structure of a system is initially set in various spin configurations. The energy functional for each configuration is then minimised to the nearest local minima with each energy minimum corresponding to a different magnetic ground-state [17]. The lowest energy spin configuration is then selected as the magnetic ground-state. To calculate the sign and strength of the magnetic exchange, the energy cost to flip pairs of spins along various crystallographic directions when the system resides in the lowest-energy configuration is calculated. This energy cost can then be converted to an exchange energy by considering the spin quantum number of the magnetic ions in the system [87]. Further to this, one can also calculate the spin-density distribution of the system and map this onto the lattice, in order to better visualise the likely magnetic exchange pathways in a material [88].

2.6 Electron-spin resonance

Electron-spin resonance (ESR) measurements were performed in collaboration with A. Ozarowski at the EMR facility, National High Magnetic Field Laboratory (NHMFL), Tallahassee, Florida, USA and with D. Kamenskyi at Augsburg University. Measurements at the NHMFL were performed on a home-built spectrometer whilst experiments at Augsburg University were carried out using commercially available X-Band Bruker ESR spectrometer operating at 9.35 GHz. High-frequency ESR experiments were done using a multi-frequency spectrometer operated in combination with a 16 T pulsed magnet (5 msec pulse) at Kobe University (Japan). Backward wave oscillators and Gunn diodes were employed as sources of mm- and submm-wavelength radiation. 2,2-Diphenyl-1-picrylhydrazyl (DPPH) was used as a standard magnetic field marker with g-factor $g = 2.0036$.

In an ESR experiment, the sample sits in a resonant cavity and microwave radiation of frequency ν is pumped in via a waveguide, see Figure 2.9(a). Microwave radiation ($\nu \sim 10^9 - 10^{11}$ Hz) is needed to match the precession frequency of the electron [6]. In ESR, the selection rule for transitions between electronic energy levels is $\Delta m_s = \pm 1$ [9]. Whenever the incident energy of the microwave radiation $h\nu$ matches the energy separating two adjacent energy-levels ΔE, an electron transitions between the two states and a resonance is observed in the radiation spectrum of the microwave cavity. Therefore, as $\Delta E = h\nu = g\mu_{\mathrm{B}}\mu_0 H \Delta m_s$, varying the magnetic field and incident radiation can excite transitions between adjacent energy levels. Often it is more convenient to keep the frequency of the incident radiation constant and sweep the magnetic field.

An example transmission spectrum is shown in Figure 2.9(b) for a powder-sample of a $S = 1$ ion with easy-plane single-ion anisotropy $D > 0$. Here, the transitions for field parallel to the unique-axis z adopt a peak-like lineshape whilst transitions for field $\perp z$ have a peak-derivative lineshape. The corresponding energy-level diagrams are shown in Figures 2.9(c) and 2.9(d), with transitions between the energy-levels labelled. At low-fields, and if the system contains a Dzyaloshinskii–Moriya interaction and/or a staggered g-tensor [89], the ground-state energy-levels can mix, which permits what are known as 'half-field' transitions [9], $\Delta m_s = \pm 2$, labelled α and δ in Figures 2.9(c) and 2.9(d), respectively. In addition, such transitions may be observed when the Zeeman energy is comparable to $|D|$ or due to 'off-axis' resonances where the field is not orientated directly along a principle Cartesian axis [17].

By tracking the field-dependence of the various transmissions in the ESR

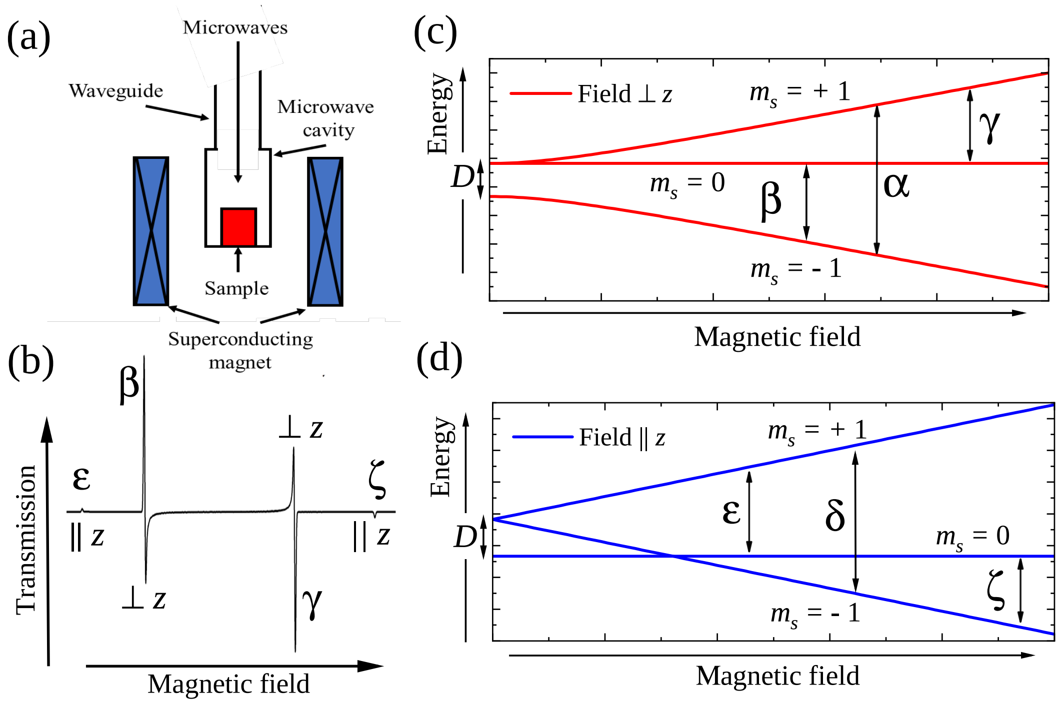

Figure 2.9: (a) Schematic of an electron-spin resonance experiment. (b) Resonances observed in a $S = 1$ powder sample with non-zero single-ion anisotropy as adapted from [9]. Energy-level diagram for $S = 1$ powder sample with easy-plane anisotropy ($D > 0$) for field perpendicular to the unique-axis z (c) and field parallel to z (d). Transitions between $\Delta m_s = \pm 1$ are labelled β, γ, ϵ and ζ [as in (b)] and $\Delta m_s = \pm 2$ transitions are labelled α and δ.

spectra as a function of ν, the measured resonances can be fit to sets of simultaneous equations which describe the field dependence of the energy-levels of the system [9, 17], as in Figures 2.9(c) and 2.9(d), allowing precise values of $|D|$ and g-factors to be obtained. Whilst this method can determine the magnitude of the single-ion anisotropy it cannot ascertain the sign of D, as only the magnitude of the single-ion anisotropy has an effect on the in-field location of the observed resonance. A study of the intensities of the various peaks against temperature is required to determine the sign of D.

Transitions within the excited states will have a low-intensity at low-temperature as most electrons will occupy the ground state. As temperature increases, the intensity of these excitations will increase as the excited state becomes thermally populated. In contrast, at low-temperatures transitions between the ground-state and excited-state will have much higher intensities. As temperature increases the ground-state population reduces and the intensity of transitions between the ground and excited state diminishes. For the picture of a $S = 1$ ion in an octahedral environment, the ground-state is a doublet for $D < 0$ and singlet for $D > 0$, such that tracking the increase or decrease in the intensity of a particular resonance with changing temperature allows the sign of D to be determined [17].

2.7 High-pressure crystallography

High-pressure x-ray diffraction experiments were performed using a Tozer Diamond Anvil Cell (DAC) mounted onto a Rigaku Oxford Diffraction Synergy S diffractometer [92] equipped with a HyPix-6000HE Hybrid Photon Counting detector which allows rapid data collection across the entire Ewald sphere. Measurements were performed using Mo K_α as an incident x-ray source which, due to its small wavelength $\lambda = 0.71\,\text{Å}$, allowed higher-resolution data collection compared to a Cu K_α x-ray source. Additionally, of the two materials subject to high-pressure structural studies in this thesis both contain Cu, meaning a Cu K_α x-ray source was to be avoided to prevent damage to the sample (due to the photoelectric absorption of incident K_α

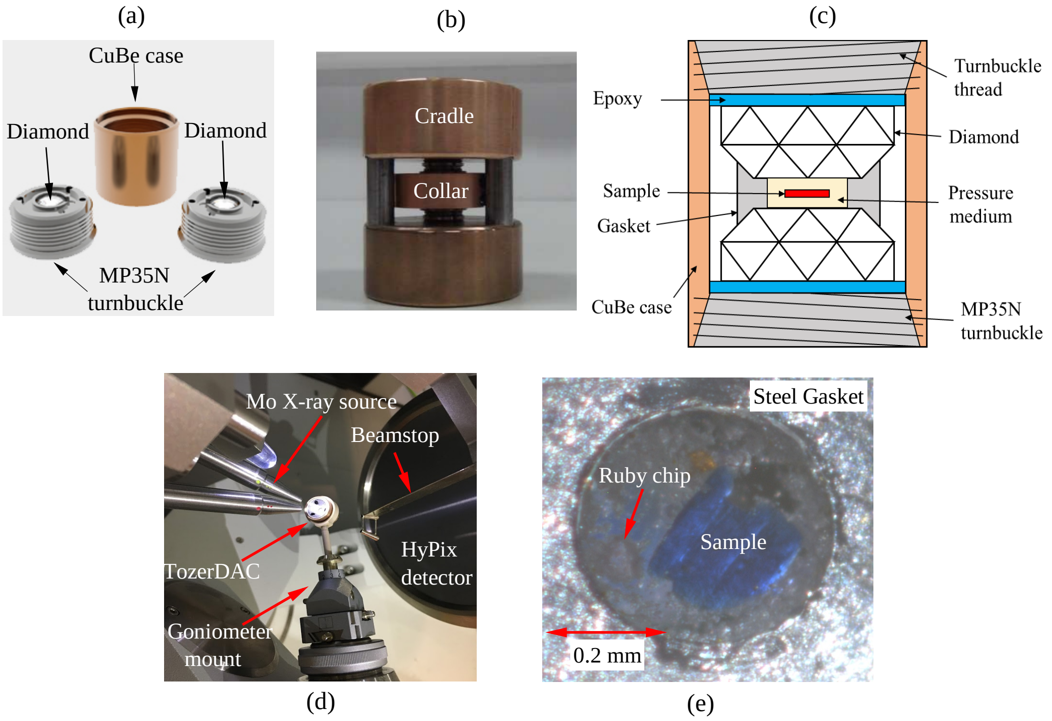

Figure 2.10: (a) Main components of the TozerDAC body as in [90]. (b) TozerDAC residing in the cradle and with collar affixed ready to be pressurised as in [91]. (c) Schematic of the cross section of a pressurised TozerDAC. (d) TozerDAC mounted onto a Rigaku Oxford Diffraction Synergy S diffractometer ready for a measurement. (e) DAC sample chamber viewed through the diamond cutlets.

x-rays by the sample and subsequent heating this would cause).

The Tozer DAC is a compact (11.5 mm in height and 12 mm in width) pressure-cell with the outer casing composed of a high strength CuBe alloy and the inner anvil support plate made of high-tensile MP35N alloy. Two turnbuckle ends made of MP35N with counter-wound threads each contain a 1 mm diameter diamond cutlet held in place by epoxy resin, as seen in Figure 2.10(a), which form the anvils of the cell. A 0.5 mm hole is mechanically drilled into the central region of a steel gasket to form the pressure region, this is then adhered centrally onto the face of one diamond cutlet using epoxy resin. An appropriately sized single-crystal is selected to fill the sample region alongside several smaller ruby spheres to act as pressure markers by tracking the pressure-dependence of the ruby fluorescence spectrum [93]. An appropriate pressure-transmitting medium (7373 Daphne-oil for the experiment presented in this thesis) is then added to the sample region and the two MP35N turnbuckles screwed finger-tight into the CuBe case to seal the sample chamber.

Pressure is attained by placing a collar around the belly of the sealed pressure-cell and mounting the cell into a cradle, see Figure 2.10(b). Load is applied to the cell by placing the cell, mounted in the collar and cradle jig, on a hydraulic ram. The ram drives the two diamond anvils together which begins to indent the steel gasket. As the cutlet faces are smaller than the gasket hole the pressure-medium cannot escape and becomes pressurised, see Figure 2.10(c). The pressure-medium transfers pressure to the sample without the anvils contacting the sample. The load is applied slowly and incrementally to avoid crashing the two diamond anvils into each other, which would destroy the sample and the diamonds. At each increment, the collar is tightened in order to transfer the load from the ram to the MP35N turnbuckles by rotating the CuBe case relative to the MP35N turnbuckles, this 'locks-in' the pressure. One the desired load is reached the cell is removed from the ram and the jig. The pressure is then determined in-situ using a ruby spectrometer.

The cell is then ready to be mounted onto a goniometer which affixes to the Synergy S diffractometer, as in Figure 2.10(d), and a measurement performed. It is important to note that a large part of the Ewald sphere is obscured by the pressure-cell body, with the DAC opening angle being $\approx 38^\circ$. In order to compensate for this, long data collection times (typically $1 - 3$ days) are required to obtain enough data to determine an accurate structural solution. Resultant diffraction data was reduced using CrysalisPro software [94]. Structures were solved using Olex2 [95] and conventional structural refinement carried out with SHELXL [96].

Chapter 3

Magnetic ground-state of the ferromagnetic chains compounds $M(\mathrm{NCS})_2(\mathrm{thiourea})_2$ (M = Ni, Co)

3.1 Introduction

Several classes of low-dimensional magnetic materials can exhibit an order to disorder phase-transition driven by an external tuning parameter, such as magnetic field, that pushes the system though a QCP [53, 62, 97, 98]. The reduced dimensionality of the system typically promotes quantum fluctuations, as the greater spatial localisation of the electron in lower dimensions causes an increase in the uncertainty of the spin component, which can lead to the material hosting an array of exotic quantum ground-states or potentially exhibiting QCP behaviour.

Considering the case of 1D materials, a notable system that exhibits QCP behaviour is the ferromagnetically coupled effective Ising-like $S = 1/2$ chain material $\mathrm{CoNb_2O_6}$. Applying a magnetic field transverse to the Co(II) Ising-axis pushes the system through a QCP, as it moves from a ferromagnetic (FM) ordered ground-state to a disordered quantum paramagnetic phase [31, 32]. The existence of QCPs in 1D chains is not exclusive to the case of FM coupling. The $S = 1$ easy-plane chain material $\mathrm{NiCl_2(thiourea)_4}$ (DTN), where thiourea = $\mathrm{SC(NH_2)_2}$, passes through two field induced QCPs, at least one of which belongs to the universality class of a Bose-Einstein condensate (BEC) [99, 100].

In terms of physically realising such systems, the use of organic ligands has proven highly effective in constructing crystal architectures that readily promote low-dimensional magnetic behaviour [41, 65, 101–103]. With a selection of recently published materials showcasing the ability to test the limits of the theoretical understanding of $S = 1/2$ and $S = 1$ chain materials [38, 39, 42].

To achieve quasi-one-dimensional behaviour, as no real material is truly 1D, the choice of intrachain bridging-ligand is a decisive one, as it ultimately determines the sign and strength of the intrachain exchange interaction (J). Non-bridging ligands also play an important role in promoting Q1D behaviour, keeping adjacent chains well separated and mitigating interactions due to interchain exchange (J') [41, 65]. Characterising both J and J' is therefore paramount to establish how the crystal structure influences the magnetism, and possible emergence of QCP behaviour, in Q1D systems. The ultimate goal being to move toward the construction of bespoke magnetic materials, where the magnetic properties can be chemically tuned at the point of synthesis.

This chapter will outline a study of the magnetic properties of the two isostructural AFM chain coordination polymers $\mathrm{Co(NCS)_2(thiourea)_2}$, $S = 3/2$, and the $S = 1$ analogue $\mathrm{Ni(NCS)_2(thiourea)_2}$. The isostructural nature of the two compounds provides an opportunity to study the effect substitution of the spin species has on the magnitude and strength of J and J'. The two compounds are compared to other known, chemically similar, quantum magnets, such as the 1D chain DTN [104], providing an avenue to study how structural properties influence the observed magnetic ground-state and possible QCP behaviour in low-dimensional magnets. The magnetic properties of both compounds within an applied magnetic field ($\mu_0 H$) can be summarised by the following Hamiltonian,

$$\begin{aligned}\mathcal{H} = -J \sum_{<i,j>} \hat{\mathbf{S}}_i \cdot \hat{\mathbf{S}}_j - J' \sum_{<i,j'>} \hat{\mathbf{S}}_i \cdot \hat{\mathbf{S}}_{j'} + D \sum_i (\hat{\mathbf{S}}_i^z)^2 \\ + E \sum_i [(\hat{\mathbf{S}}_i^x)^2 - (\hat{\mathbf{S}}_i^y)^2] + \mu_\mathrm{B}\mu_0 \sum_i \mathbf{H} \cdot \mathbf{g} \cdot \hat{\mathbf{S}}_i,\end{aligned} \tag{3.1}$$

where $\hat{\mathbf{S}}_i$ is the spin of each ion i, $< i, j >$ denotes a sum over nearest neighbours and a primed index in the summation describes the interaction with a nearest neighbour in an adjacent chain; $J > 0$ corresponds to FM interactions. Here, $\mathbf{g} = \mathrm{diag}(\mathrm{g_x}, \mathrm{g_y}, \mathrm{g_z})$ is a tensor of g-factors where diagonal components are not necessarily equal.

DC-field SQUID magnetometry measurements, in combination with heat-capacity data and DFT calculations, are used to investigate the electronic and magnetic properties of the two compounds and ascertain the sign and strength of the dominant terms in Eq. 5.1: J, J', and the single-ion anisotropy D. The parameter E in Eq. 5.1 corresponds to a rhombic anisotropy term and, in the materials in this chapter, is expected to be minimal due to the small structural distortion of the equatorial $M\mathrm{S}_4$ environment, where M = Co(II) or Ni(II) (discussed in detail in section 3.2.1). Studying both the crystal and electronic structures determines likely magnetic exchange pathways in the materials whilst spin density maps highlight the role of the magnetic ions in mediating J. Positive-muon-spin-relaxation measurements also serve to reveal magnetic ordering in both materials and illustrate a coherent picture of the magnetic ground state.

3.2 $M(\mathrm{NCS})_2(\mathrm{thiourea})_2$ (M = Ni, Co)

3.2.1 Structure

Single-crystal x-ray diffraction measurements were performed by P. Macchi and R. Scatena at The University of Bern, Switzerland. Measurements on the $\mathrm{Co(NCS)_2(thiourea)_2}$ and $\mathrm{Ni(NCS)_2(thiourea)_2}$ coordination polymers revealed twinning in both. However, $\mathrm{Co(NCS)_2(thiourea)_2}$ could be obtained with a thin-sheet morphology, which exhibited clean diffraction frames, and thus permitted the experimental Hansen-Coppens multipolar model (MM) [105] refinement of the d-orbital occupancies. Single-crystals of $\mathrm{Ni(NCS)_2(thiourea)_2}$ was irremediably affected by twinning [27.7(1)%] and thus data of high enough quality for MM refinement could not be obtained.

Both species crystallise into a triclinic structure with the space group $P\bar{1}$, with the structure of both compounds outlined in Figure 3.1. $\mathrm{Co(NCS)_2(thiourea)_2}$ single-crystals were of high enough quality to collect x-ray diffraction data up to d_{min} = 0.50 Å, which allowed the refinement of both the crystal structure and the aspherical electron-charge density distribution; discussed in section 3.2.6. The Co(II) atom resides on an inversion centre in the middle of an octahedral environment constructed of pairs of Co—N [2.0226(4) Å], Co—S [2.5523(1) Å], and Co—S [2.5972(1) Å] coordination bonds. Due to these bond lengths, the octahedral environment is compressed along the axial N—Co—N bond. The S—Co—S bond-angles within the equatorial plane are 84.19(1)° and 95.81(1)°, with the angle between the axial N—Co—N bond and equatorial plane being 96.56(1)°, indicating that the Co(II) octahedra are slightly distorted. A Co—S—Co angle of 95.81(1)° defines the geometry of the Co—S—Co bibridges that make up the polymeric chain. The chains are packed together within the bc-plane by H-bonds in the range 3.43 − 3.47 Å and classify as weakly interacting.

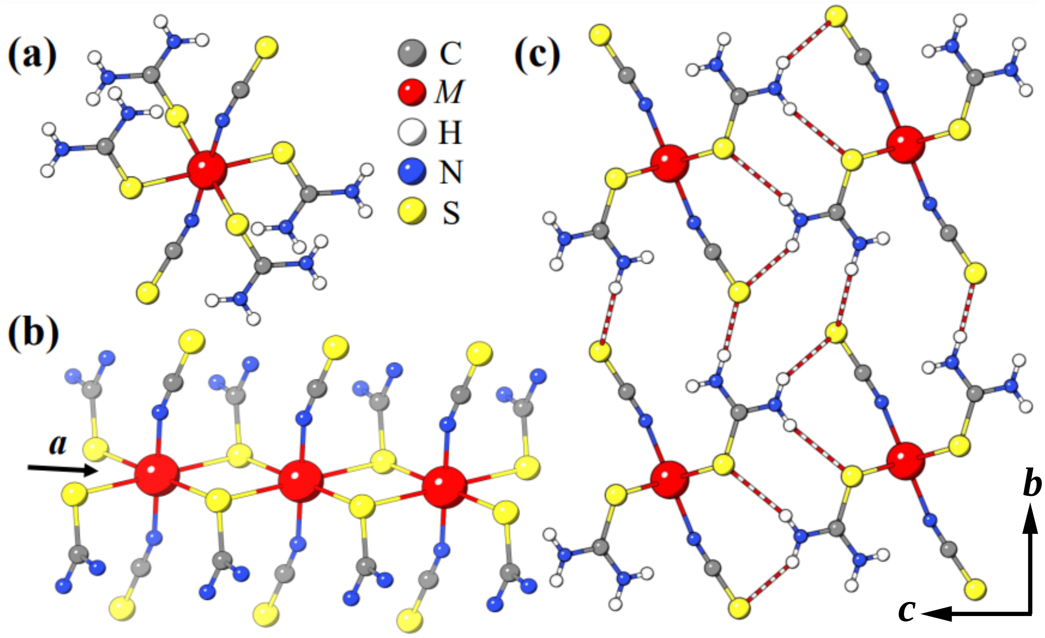

Figure 3.1: Structure of $M(\mathrm{NCS})_2(\mathrm{thiourea})_2$ where M = Ni(II), Co(II). (a) Local M(II) octahedral environment. (b) Two M—S—M bonds form bibridge chains that propagate along the crystallographic a-axis. (c) H-bonding (striped-bonds) between adjacent chains within the bc-plane. The structure is shown for M = Co(II) measured at $T = 100$ K.

Single-crystal x-ray diffraction data for $\mathrm{Ni(NCS)_2(thiourea)_2}$ was measured up to $d_{\mathrm{min}} = 0.70$ Å with a second twinning component of 27.7(1)% observed in the crystal. Analogous to the structure of $\mathrm{Co(NCS)_2(thiourea)_2}$, the Ni atom resides on an inversion centre in the middle an octahedron built by pairs of Ni—N [1.997(2) Å], Ni—S [2.5069(6) Å], and Ni—S [2.5517(6) Å] coordination bonds. The S—Ni—S angles within the equatorial plane [83.93(2)° and 96.07(2)°] and the angle between the octahedron axis and equatorial plane [97.20(7)°] show the Ni(II) octahedra are also slightly distorted. A Ni—S—Ni bond-angle of 96.07(2)° defines the geometry of two Ni—S—Ni bridges along the polymeric chain. H-bonds pack the chains in the bc-plane with distances between the donor and acceptor within the range 3.43-3.45 Å, which again classify as weakly bonded.

In both compounds, along the crystallographic a-axis, adjacent M-ions form chains through the sulphur ions on two thiourea molecules, building two S-bridge pathways as shown in Figure 3.1(b). As the M—S—M bond angles are close to 90° in both, the Goodenough-Kanamori rules [106, 107] suggest these chain compounds represent promising platforms to investigate Q1D FM behaviour. Whilst the triclinic structure of both materials is permissive of an E-term, it is clear that the equatorial $M\mathrm{S}_4$ environments are only slightly distorted. Thus, as the departure from octahedral symmetry is limited, any E-term is expected to be small, as observed in similar Ni(II) and Co(II) complexes [14, 16, 108].

3.2.2 Muon-spin relaxation

Zero-field positive-muon-spin-relaxation measurements were performed in collaboration with T. Hicken, B. Huddart, T. Lancaster, S. Blundell and F. Xiao. Measurements were made using the GPS instrument at Swiss Muon Source, Paul Scherrer Institut. Data analysis was performed using both WiMDA [82] and software developed by T. Lancaster for global fitting of the data.

Figure 3.2(a) shows oscillations observed in the asymmetry spectra for $Ni(NCS)_2(thiourea)_2$ for temperatures $T \lesssim 10.4$ K, indicative of coherent muon-spin precession consistent with long-range magnetic order. Spectra in the magnetically

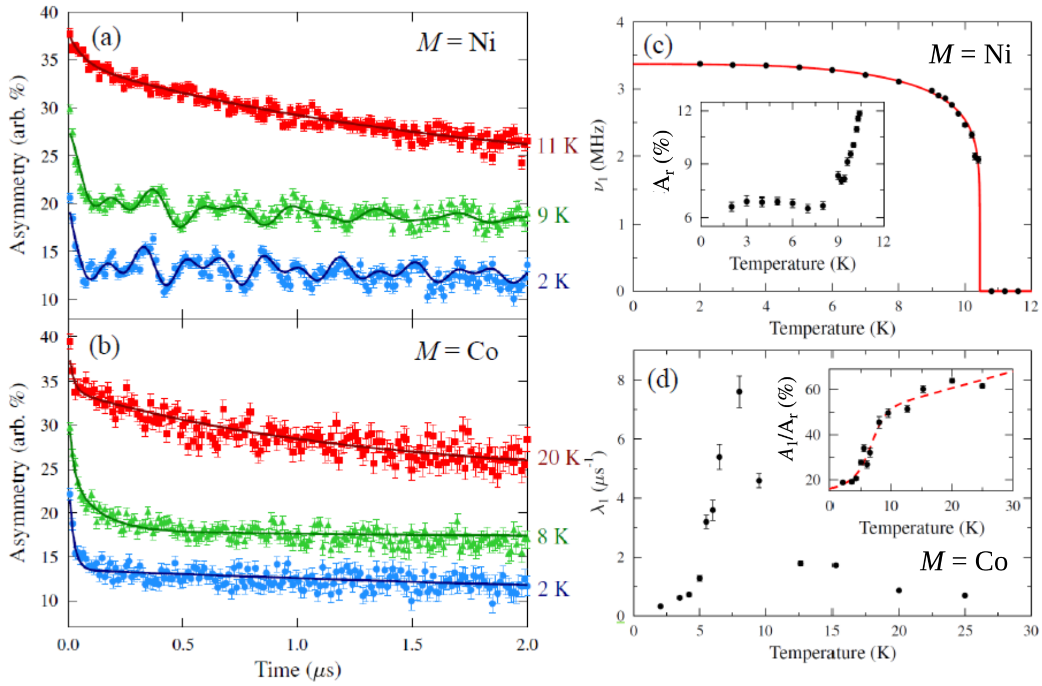

Figure 3.2: ZF μ^+SR spectra measured on (a) $Ni(NCS)_2(thiourea)_2$ and (b) $Co(NCS)_2(thiourea)_2$. Data is presented with a vertical offset where needed for clarity. Fits shown as detailed in the text. (c) Temperature evolution of the smallest oscillation frequency (ν_1) observable in the ZF μ^+SR asymmetry spectra measured on $Ni(NCS)_2(thiourea)_2$, with a fit to Eq. 3.4. Inset shows the temperature evolution of the total relaxing asymmetry (A_{rel}) from the same measurements. (d) Temperature evolution of the small relaxation rate (λ_1) extracted through fitting ZF μ^+SR asymmetry spectra measured on $Co(NCS)_2(thiourea)_2$. Inset shows the temperature evolution of the ratio of the amplitude of the component with small relaxation rate to the total relaxing asymmetry (A_1/A_r). Line is a guide to the eye.

ordered regime were fit to,

$$A(t) = \sum_{i=1}^{2} A_i e^{-\lambda_i t}\cos(2\pi\nu_i t + \phi_i) + A_3 e^{-\lambda_3 t} + A_{\mathrm{bsln}} e^{-\lambda_{\mathrm{bsln}} t}, \tag{3.2}$$

where A_i are the relaxing asymmetry of each component with corresponding relaxation rate λ_i, oscillation frequency ν_i, and the phase ϕ_i. The amplitude of the baseline asymmetry A_{bsln} accounts for muons that stop outside of the sample and those that stop within the sample that only have a component of their spin along the local field direction; A_{bsln} has relaxation rate λ_{bsln}. Each component of the model accounts for muons that stop in different local environments. The exact site at which the muon stops in the sample is difficult to discern, however, recent DFT work has made inroads in narrowing down the precise location at which the implanted muon precesses within the crystal structure [109, 110].

The two oscillatory components accounting for muons that stop in two different local magnetic fields that lead to coherent precession [with a constant ratio of $\nu_2/\nu_1 = 1.754(1)$], indicative of long range magnetic order. A third frequency $\nu_3 \simeq 3\nu_1$ is only observable for $T \lesssim 7$ K which was fit using a purely relaxing component to account for the rapid depolarisation of the initial muon-spin due to this third precession rate. The relaxation rate of this component λ_3 is large at low temperatures and drops for $T \gtrsim 7$ K, again indicating a broad transition region. The three distinct frequencies correspond to three distinct muon stopping sites in this material. Above T_{N}, where oscillations are not resolvable in the spectra, the data are well described by a model comprising of two relaxing components,

$$A(t) = \sum_{i=1}^{2} A_i e^{-\lambda_i t} + A_{\mathrm{bsln}} e^{-\lambda_{\mathrm{bsln}} t}. \tag{3.3}$$

The background relaxation rate λ_{bsln} was set to be equal to that found from fitting below T_{N}, and all other parameters were globally refined to be constant over the entire temperature range, except for the small relaxation rate λ_1, which was found to decrease on increasing temperature.

The smallest frequency was fitted to

$$\nu_1(T) = \nu_1(0)\left[1 - \left(\frac{T}{T_{\mathrm{N}}}\right)^{\delta}\right]^{\beta}, \tag{3.4}$$

as seen in Figure 3.2(c). It was found that $\nu_1(0) = 3.37(2)$ MHz [corresponding to a local magnetic field of 24.1(1) mT at the muon-spin site at zero-temperature], $\delta = 3.2(3)$, $\beta = 0.14(3)$ and $T_{\mathrm{N}} = 10.4(1)$ K. This value of β is consistent with a system dominated by 2D magnetic fluctuations, being very close to the value for the 2D Ising model, $\beta = 1/8$ [111].

The disappearance of the third frequency, in combination with the increase in the relaxing asymmetry (A_{rel}) for $T \gtrsim 7$ K seen in the inset of Figure 3.2(c), is evidence for the onset of the magnetic transition, suggesting a broad transition for $7 \text{ K} \lesssim T \lesssim 10.4$ K. For $T \gtrsim 10.4$ K no oscillations are observable in the asymmetry spectra, consistent with the system being magnetically disordered.

Figure 3.2(b) shows the ZF-μ^+SR asymmetry spectra measured for $\mathrm{Co(NCS)_2(thiourea)_2}$ where no oscillations in the asymmetry are observed down to 2 K. Data were fit to Eq. 3.3 over the entire temperature range where the background relaxation rate λ_{bsln} and the large relaxation rate λ_2 were globally refined over all the datasets to obtain the best fits. The spectra consist of two exponentially relaxing components, one with a large relaxation rate which is constant over the entire temperature range, and one with a smaller relaxation rate that dominates at later times. The large relaxation rate is often observed in coordination polymers of this type and has been ascribed to a class of muon sites that are not well coupled to the magnetism (hence its temperature independence) that are realized close to electron density (e.g., double bonds, aromatic rings, etc.) [112, 113].

The temperature evolution of this small relaxation rate (λ_1) is shown in Figure 3.2(d). It exhibits a large peak around 8 K, typical of a phase transition from a magnetically ordered to disordered state, in good agreement with heat-capacity and magnetometry measurements below. The lack of oscillations suggests that the system is dominated by dynamic effects on the muon timescale, such that coherent precession of the muon-spin does not occur. This has been noted in several coordination polymer magnets containing $\mathrm{Fe^{2+}}$ [114], $\mathrm{Mn^{2+}}$ [115] and (occasionally) $\mathrm{Ni^{2+}}$ [43], where the sizeable magnetic moment leads to a large, fluctuating distribution of local magnetic fields. (In contrast, coordination polymer magnets containing $\mathrm{Cu^{2+}}$ often show oscillations in the ordered regime owing to the smaller relative moment size [112].) Further evidence for a transition to a regime of magnetic order around 8 K comes from the rapid change in amplitude of the small relaxation rate component (A_1), as shown in the inset of Figure 3.2(d), which indicates an increase size of λ_1. As λ_1 is proportional the size of the local magnetic field, its increase indicates increasing local moments due to the onset of magnetic order. The rapid drop in the amplitude of the component with a large relaxation rate has been observed in similar materials close to the transition temperature [43, 114, 115], suggesting that the correlations corresponding to the third frequency die out as temperatures approach 7 K.

3.2.3 Heat capacity

Heat capacity data on polycrystalline pressed pellets of $\mathrm{Ni(NCS)_2(thiourea)_2}$ were collected by myself using a commercially available Quantum-Design Physical Property Measurement System at the University of Warwick. Measurements on single-crystals of $\mathrm{Co(NCS)_2(thiourea)_2}$ were performed by J. Eckert and E. Krenkel of Harvey-Mudd College, CA, USA. All data was processed and analysed by myself. Onsager 2D Ising magnetic heat capacity simulations calculated with R. Williams.

Figure 3.3(a) shows zero-field heat capacity (C) plotted as a function of T for both compounds. To isolate the low-temperature magnetic contribution to the heat capacity, the high-temperature ($T \geq 40$ K, Co; $T \geq 35$ K, Ni) contribution ($C_{\mathrm{high}T}$) can be reproduced by a model containing two Einstein and one Debye phonon mode, with the resultant fit subtracted as a background ($C_{\mathrm{mag}} = C - C_{\mathrm{high}T}$) as described in [17]. The black lines in Figure 3.3(a) are fits to $C_{\mathrm{high}T}$, the resultant fit parameters are shown in Table 3.1. The resultant magnetic heat capacity divided by temperature (C_{mag}/T) is plotted in Figure 3.3(b). Both C_{mag}/T datasets show sharp peaks at $T_c = 6.82(5)$ K and 10.5(1) K for the Co(II) and Ni(II) respectively, indicative of long-range ordering and in excellent agreement with ZF μ^+SR. Whilst the fit parameters for the two isotructural materials are different, the model used to fit the high-temperature heat capacity is purely phenomenological and is not intended to provide an accurate parameterisation of the lattice dynamics. Similar differences have been seen in the heat capacities of the isostructural molecule-based materials $[M\mathrm{(pyz)_2(HF_2)]SbF6}$ with M = Cu(II), Ni(II), Co(II) [101].

$\mathrm{Co(NCS)_2(thiourea)_2}$ C_{mag} data possesses a notably sharper λ-peak compared to $\mathrm{Ni(NCS)_2(thiourea)_2}$. Single-crystal magnetometry for the Co species, section 3.2.4, provides the reason for this. The magnetometry data indicate an AFM ground-state, where the spins possess a strong Ising-like single-ion anisotropy. For a

Table 3.1: Fitted high-temperature contribution to the heat capacity for $\mathrm{Co(NCS)_2(thiourea)_2}$ and $\mathrm{Ni(NCS)_2(thiourea)_2}$. A_i is the amplitude of mode i, whilst θ_i is the characteristic temperature of the mode i (i = D, Debye; i = E, Einstein).

Parameter	$\mathrm{Co(NCS)_2(thiourea)_2}$	$\mathrm{Ni(NCS)_2(thiourea)_2}$
A_{D} (J/K.mol)	94(4)	172(5)
θ_{D} (K)	172(3)	443(28)
$A_{\mathrm{E_1}}$ (J/K.mol)	105(3)	96(8)
$\theta_{\mathrm{E_1}}$ (K)	285(7)	126(5)
$A_{\mathrm{E_2}}$ (J/K.mol)	172(3)	185(6)
$\theta_{\mathrm{E_2}}$ (K)	816(13)	941(46)

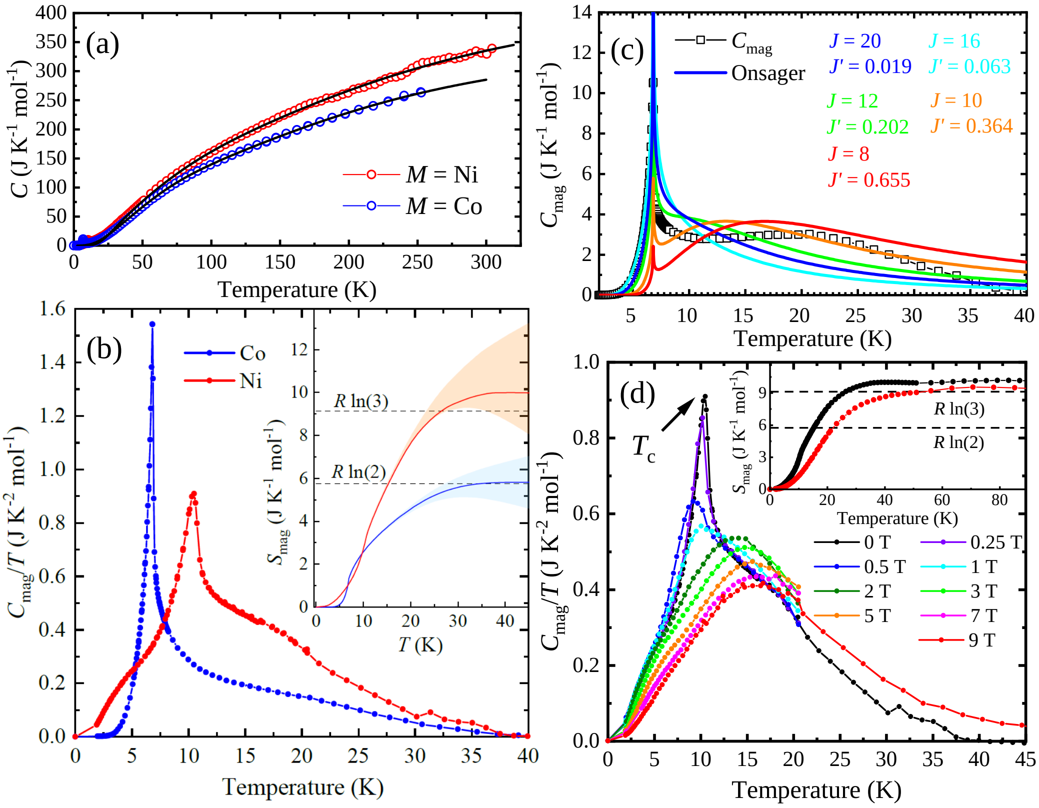

Figure 3.3: (a) Heat capacity (C) measured in zero-field and plotted as a function of temperature for Co(NCS)$_2$(thiourea)$_2$ and Ni(NCS)$_2$(thiourea)$_2$, solid lines are fits to two Einstein and one Debye mode for the temperature range $T > 30$ K and $T > 37$ K, respectively. Fit parameters are shown in Table 3.1. (b) Zero-field magnetic heat capacity (C_{mag}) divided by temperature and plotted as a function of T. Inset shows the resultant magnetic entropy (S_{mag}), where the shaded regions are representative of errors introduced by the uncertainty in the amplitudes of the lattice fit components. (c) Magnetic heat-capacity C_{mag} for the Co compound (squares) plotted as a function of temperature T. Simulated $C_{\text{mag}}(T)$ curves (solid lines) are plotted for a selection of exchange values $\{J, J'\}$ which obey the Onsager relation (Eq. 3.5) for a 2D lattice of Ising spins. (d) Magnetic heat capacity (C_{mag}) divided by temperature and plotted as a function of T for a polycrystalline pressed pellet of Ni(NCS)$_2$(thiourea)$_2$ measured in applied fields up to 9 T. The zero-field transition temperature to a magnetically ordered state is indicated at T_c. Inset shows magnetic entropy (S_{mag}) recover to $R\ln(3)$ at 0 and 9 T, as expected for a $S = 1$ ion.

Q1D chain of Ising spins, a broad-hump in C_{mag} is expected, as the reduced dimensionality causes the build up of spin-spin correlations at temperatures well above the transition temperature [116, 117]. The sharp nature of the peak points to Q2D or 3D Ising-like long-range ordering within the lattice. For a 2D square lattice of Ising-spins with anisotropic exchange interactions (J, J'), C_{mag} can be simulated by considering Eq. 3.5, as derived by Onsager [118, 119], where J and J' obey:

$$\sinh(\frac{2J}{T_\mathrm{c}})\sinh(\frac{2J'}{T_\mathrm{c}}) = 1 \tag{3.5}$$

Here, J and J' are the magnetic exchange interactions along two different directions within the 2D lattice. Taking $T_c = 6.82(5)$ K, $C_\mathrm{mag}(T)$ can be simulated for various sets of $\{J, J'\}$ which obey Eq. 3.5 and compared to the measured response, with the results shown in Figure 3.3(c). The simulated curves do not capture the data convincingly, leading to the conclusion that C_mag cannot be well described by the 2D Ising model. This result is interpreted as evidence to support 3D Ising long-range ordering within the Co compound. The two classes of interchain exchange interaction are therefore expected to be comparable in magnitude, and the number of next nearest neighbours expected to be $n' = 4$.

The magnetic entropy (S_mag) for both compounds can be determined using,

$$S_\mathrm{mag}(T) = \int_0^T \mathrm{d}T' \, \frac{C_\mathrm{mag}(T')}{T'}, \tag{3.6}$$

where it is assumed $C_\mathrm{mag} = 0$ at $T = 0$ K. The results are shown in the inset of Figure 3.3(b). For Ni(NCS)$_2$(thiourea)$_2$, S_mag fully recovers to $R\ln(3)$ (R is the ideal gas constant) as expected for a $S = 1$ ion. In contrast, Co(NCS)$_2$(thiourea)$_2$ shows a initial sharp upturn before a broad rise to a plateau at $R\ln(2)$ around 30 K. Electronic structure calculations reveal the Co ion sits in the high-spin Co^{2+} state. For a $S = 3/2$ ion, one would expect S_mag to recover to $R\ln(4)$ in accordance with $R\ln(2S+1)$ [120]. A recovery to $R\ln(2)$ is indicative of a $S = 3/2$ system consisting of a large SIA which keeps the two $S = \pm3/2$ and $S = \pm1/2$ Kramer-doublets well separated, as shown in Figure 3.4(a). This suggests that the system can be well approximated using an effective spin-half approach within the low-temperature regime as, at low-temperatures, the thermal energy is not enough to allow the ground-state electrons to populate the excited $S = \pm1/2$ Kramer doublet; $k_\mathrm{B}T < 2D$. It is therefore expected that $D \sim -100$ K, as seen in similar easy-axis Co(II) complexes [16].

The behaviour of the Ni-species was investigated further by measuring C_mag in applied magnetic fields up to 9 T as shown in Figure 3.3(d). The λ-peak is initially suppressed in field, suggesting the ground-state is AFM in nature. At higher fields, the ordering peak ceases to be resolvable and the broad hump shifts to higher temperatures reflecting the Schottky-like response to the field induced Zeeman splitting of the ground-state energy levels [6]. (The Schottky-like response occurs when the thermal energy is comparable in magnitude to the size of the energy-gap between the excited and ground-state energy levels, $k_\mathrm{B}T \sim D$ for the Ni system here, such that both the states have a near equal probability of being populated, manifesting as a broad maximum in C_mag.) The inset of Figure 3.3(d) shows S_mag fully recovers

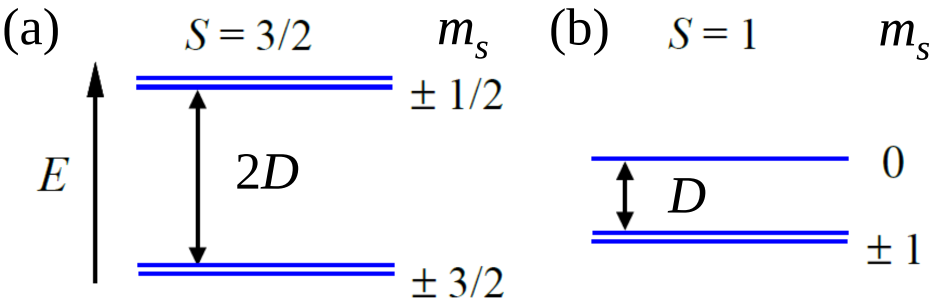

Figure 3.4: Energy (E) level diagrams for (a) $S = 3/2$ and (b) $S = 1$ moments within octahedral environments with easy-axis single-ion anisotropy ($D < 0$) where m_s is the eigenvalue of the spin operator S_z.

to $R\ln(3)$ on warming above about 30 K in zero field and 40 K at 9 T, indicating the level splitting is completely overcome by these temperatures. This is consistent with $|D| \sim 10$ K, which is typical for Ni^{2+} ions in similar local environments [15, 121].

3.2.4 Magnetometry

Single-crystal magnetometry measurements were performed on $\mathrm{Co(NCS)_2(thiourea)_2}$ with the external magnetic-field applied along three unique crystal axes: parallel to the chain axis a, perpendicular to a within the ab-plane denoted b' and normal to the ab-plane denoted c'. The angle between the magnetic field and the unique N—Co—N axis is 84° for $\mu_0 H \parallel a$, 73° for $\mu_0 H \parallel b'$ and 18° for $\mu_0 H \parallel c'$.

Figure 3.5(a) shows that upon decreasing temperature, the magnetic susceptibility [$\chi(T)$] for field along all three axes rises to a sharp peak before plateauing at low-temperatures, behaviour indicative of an AFM ground state. The Fisher relation [122] estimates a transition temperature $T_c = 6.7(1)$ K, in excellent agreement with heat capacity and μ^+SR data. The $\chi(T)$ with field parallel to c', red circles Figure 3.5(a), is an order of magnitude greater than measurements made with the field along a or b', verifying a strong Ising-like ($D < 0$) SIA. Due to the close proximity of c' to the unique axial N—Co—N bond, it is highly likely that the magnetic moments on the Co ions are co-linear with the N—Co—N axis.

The $\chi^{-1}(T)$ data for all three field directions, inset Figure 3.5(a), shows curvature persisting up to the highest measured temperature ($T = 300$ K). This non-Curie-like behaviour suggests that the leading energy term in the Hamiltonian is similar in size to the thermal energy in this temperature range. On the basis of the heat capacity measurements, this is expected to be around the energy scale of the gap between the two Kramer doublets, such that $k_{\mathrm{B}}T \sim 2|D|$. This estimates

$|D| \sim 100$ K in agreement with heat capacity data and similar Co(II) complexes [16].

The large negative SIA (zero-field splitting $= 2|D| \sim 200$ K) suggests that as temperature is lowered below 100 K, a vanishingly small proportion of the spins will populate the excited doublet and the magnetic properties can be accounted for within an effective spin-half ($S_{\mathrm{eff}} = 1/2$) Ising model. This means that over the temperature range $10 \leq T \leq 100$ K, the susceptibility for $H \parallel c'$ (which is close to parallel to the expected Ising axis) can be approximated by that of the ideal 1D $S = 1/2$ Ising chain $[\chi^{||}_{\mathrm{1D}}(T)]$ and parameterised by J_{eff}, the primary exchange energy in the effective $S_{\mathrm{eff}} = 1/2$ picture [123, 124]. Deviations from strictly 1D behaviour can be accounted for by introducing a mean-field correction to the susceptibility given by the expression [124],

$$\chi_{\mathrm{mf}} = \frac{\chi^{||}_{\mathrm{1D}}(T)}{[1 - (n' J'_{\mathrm{eff}})\chi^{||}_{\mathrm{1D}}(T)/C_{\mathrm{1D}}]}, \tag{3.7}$$

where C_{1D} is the easy-axis Curie constant for the idealised 1D picture and J'_{eff} is the interchain exchange in the effective $S_{\mathrm{eff}} = 1/2$ picture arising from n' interchain nearest neighbours where $n' = 4$ for this material.

Following the analysis by Greeney *et al.* [124] in Figure 3.5(b) a semi-logarithmic plot of $\chi T(T)$ against T^{-1} for $H \parallel c$ is shown. In this diagram $\chi^{||}_{\mathrm{1D}}(T)$ is a straight line with gradient given by the effective intrachain exchange J_{eff} and intercept related to C_{1D}. A positive slope is indicative of FM intrachain exchange ($J_{\mathrm{eff}} > 0$). The sharp kink at T_{c} indicates the onset of long-range order. The data near T_{c} deviates from the linear response predicted by the ideal 1D Ising model (dashed line). A fit to Eq. 3.7 within the temperature range $10 \leq T \leq 100$ K ($T < 2|D|$, well within the $S_{\mathrm{eff}} = 1/2$ regime) is found to more accurately track the data [solid line, Figure 3.5 (a-b)], indicating the importance of the interchain exchange interactions. The fit to Eq. 3.7 returned parameters of $g_{\mathrm{eff}} = 8.0(1)$, $J_{\mathrm{eff}} = 10.4(2)$ K and $J'_{\mathrm{eff}} = -0.31(2)$ K. The fit parameters are consistent with the effective $S = 1/2$ model, in which the full Co(II) moment of the ground state doublet is absorbed into the effective g-factor and exchange energies. The real exchange, J, is related to the effective value via $J = (3/5)^2 J_{\mathrm{eff}}$ [125, 126], hence the values extracted are $J = 3.62(7)$ K and $J' = -0.12(1)$ K. The fit to Eq. 3.7 deviates from the data near the onset of long-range order. The departure at high temperatures is caused by the breakdown of the Ising model as temperatures approach $2|D| \sim 200$ K. The difference between $\chi(T)$ for the field along b' and a may be due to either the existence of a small E-term, a slight misalignment of the magnetic field or different

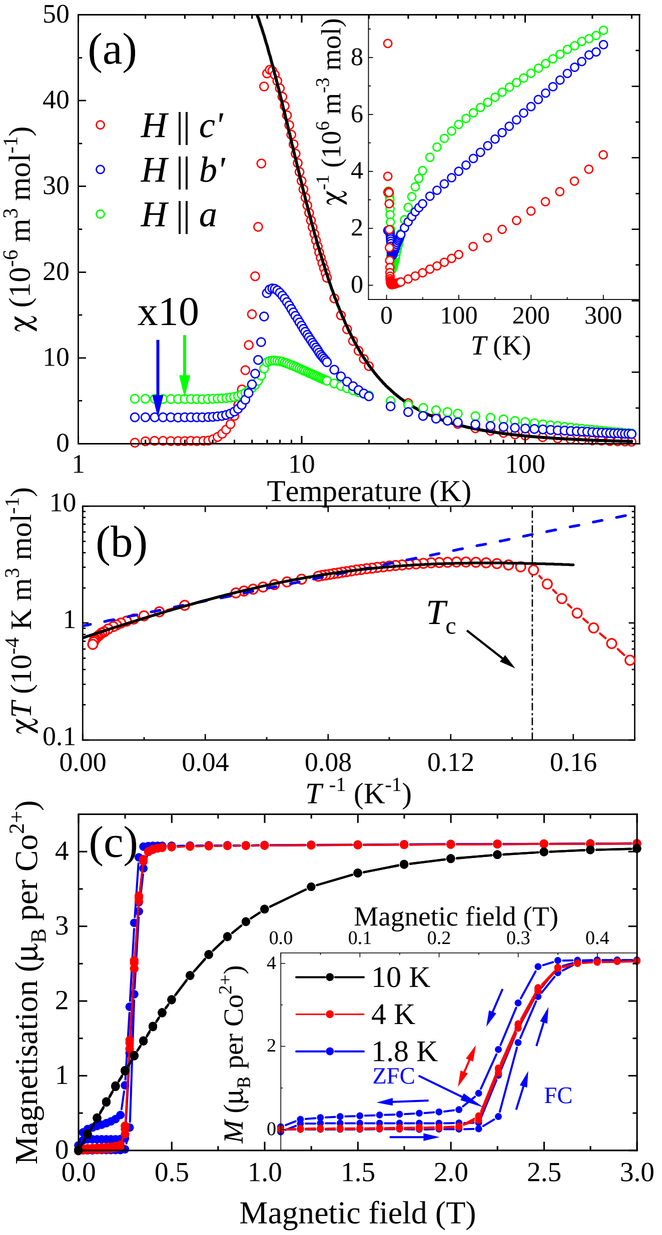

Figure 3.5: (a) Single-crystal magnetic susceptibility $\chi(T)$ data for $\mathrm{Co(NCS)_2(thiourea)_2}$ measured at $\mu_0 H = 0.1$ T. (a) $\chi(T)$ for different field directions where data for $H \parallel b'$ and a are multiplied by a factor of 10. Inset shows a plot of $\chi^{-1}(T)$ with no scaling. (b) Semi-logarithmic plot of χT against T^{-1} (discussed in text) for field parallel to c'. Dashed line is a fit to $\chi_{1\mathrm{D}}^{||}$ (see text). Solid line in (a-b) is a fit to Eq. 3.7 within the temperature range $10 \leq T \leq 100$ K. (c) Single-crystal DC-field magnetisation $M(H)$ data for $\mathrm{Co(NCS)_2(thiourea)_2}$ with the field parallel to c'. Inset highlights the low-field hysteretic behaviour seen at the lowest temperature. Zero-field cooled (ZFC) and field cooled (FC) sweeps are indicated with arrows.

temperature dependencies of the effective magnetic moment along b' and a.

The magnetisation $M(H)$ of Co(NCS)$_2$(thiourea)$_2$ with field parallel to c' is shown in Figure 3.5(c). At $T \leq 4$ K, the induced moment is approximately zero at low fields before rapidly rising to a saturation moment of $M_{\rm sat} = 4.1(1)$ $\mu_{\rm B}$ per Co^{2+} ion at $\mu_0 H_{\rm sf} = 0.29(5)$ T. This feature is attributed to spin-flip behaviour, where the spins are rapidly polarised from their AFM ground-state to an FM saturated state as the interchain AFM bonds are overcome by the Zeeman interaction [6]. The step broadens and disappears at $T > 4$ K.

Within the $S_{\rm eff} = 1/2$ model $M_{\rm sat}$ yields $g_{\rm eff} = 8.2(1)$, in excellent agreement with the result from fitting $\chi(T)$. The field at which the spin-flip occurs can be related to the AFM interaction strength by equating the energy of the magnetic field to the energy of the interchain AFM bonds via $g_{\rm eff}\mu_{\rm B}\mu_0 H_{\rm sf} = Sn'J'_{\rm eff}$. Assuming $n' = 4$, a $J' = -0.3(1)$ K is obtained which is in reasonable agreement with the value extracted from $\chi(T)$. As $M(H)$ directly probes the AFM interchain bonds at low-temperature, during the spin-reversal process, we expect $M(H)$ to provide us with the more trustworthy estimate of J'. The inset to Figure 3.5(c) shows hysteresis in $M(H)$ for $T < 4$ K, expected for FM coupled Ising spins and observed in the similar FM Ising chain compound Co(NCS)$_2$(4-benzoylpyridine)2 (4-benzoylpyridine = $C_{12}H_9NO$) [127].

Figure 3.6(a) shows powder $\chi(T)$ for Ni(NCS)$_2$(thiourea)$_2$. Upon decreasing temperature, $\chi(T)$ rises to a peak before dropping and plateauing at low-temperatures. $\chi T(T)$ data, Figure 3.6(b), are found to increase on cooling from room temperature, reach a broad maximum and then drop towards zero at $T < 10$ K. All this is consistent with large FM primary exchange interactions and a considerably smaller secondary AFM exchange, leading to an AFM ground state. The Fisher method [122] determines $T_c = 10.4(4)$ K, in excellent agreement with heat capacity and μ^+SR measurements. The inset of Figure 3.6(a) shows $\chi^{-1}(T)$ approaching a straight line for $T \geq 100$ K, which gives an approximate energy scale of the large FM exchange interactions. This is consistent with the fitted value of the Curie-Weiss temperature, $\Theta_{\rm CW} = +42(1)$ K, in this quasi-one-dimensional system.

Figure 3.6(b) shows $M(H)$ for a powder sample of Ni(NCS)$_2$(thiourea)$_2$. At low-fields, $M(H)$ is approximately zero prior to exhibiting a sharp upturn at $\mu_0 H_{\rm sf}$ = 0.65(5) T which can be ascribed to spin-flip behaviour. The rise of $M(H)$ slows at fields ~ 1 T before increasing monotonically above 3 T, approaching $M(H) \sim 2$ $\mu_{\rm B}$ per Ni^{2+} ion at the maximum experimentally accessible field of 7 T. The field at which the spin-flip occurs can be used to estimate the interchain magnetic exchange J' via $g\mu_{\rm B}\mu_0 H_{\rm sf} = 2Sn'J'$ where n' is the number of nearest interchain neighbours

[17]. Taking $g = 2.29(1)$, from $\chi^{-1}(T)$, and $n' = 4$ to be the number of next nearest neighbours, the interchain exchange interaction can be estimated at $J' = 0.13(1)$ K.

The behaviour of $M(H)$ above $\mu_0 H_{\text{sf}}$ can be explained by considering the polycrystalline nature of the sample. Grains with their easy-axis parallel to the applied field are those that contribute to the spin-flip. At $\mu_0 H_{\text{sf}}$, their spins are rapidly polarised along the field direction. In contrast, grains not orientated with their easy-axis parallel to the field have their spins more slowly polarised along the field direction as the applied field increases. These spins contribute to the slow rise of $M(H)$ after $\mu_0 H_{\text{sf}}$. By 7 T, $M(H)$ approaches $\approx 2\ \mu_{\text{B}}$ per Ni^{2+} ion. This is consistent with $M_{\text{sat}} \approx 2.29\ \mu_{\text{B}}$ per Ni^{2+} ion as expected from the g-factor extracted from the fit to $\chi^{-1}(T)$. The inset of Figure 3.6(b) shows hysteretic behaviour in $M(H)$ for $T < 4$ K similar to that observed in $\text{Co(NCS)}_2\text{(thiourea)}_2$.

3.2.5 Calculated exchange coupling constants

In order to help validate the sign and strength of J and J' determined from the magnetometry, DFT calculations were performed by R. Scatena and P. Macchi whilst at the University of Bern to calculate the magnetic superexchange coupling constants.

Along each axis, the energy difference (ΔE) between ferromagnetic (FM) and antiferromagnetic (AFM) coupling was calculated for adjacent M ions and used to obtain the sign and magnitude of the magnetic exchange interaction. As $\Delta E = E_{\text{FM}} - E_{\text{AFM}}$, $\Delta E < 0$ is representative of AFM exchange. Values of ΔE were converted to exchange coupling by considering a single J convention in the Hamiltonian (sum over unique exchange pathways), the results of these calculations are shown in Table 3.2.

It was found that the primary exchange is FM in both materials, with $J = 4.22$ K for the Co species and $J = 78.13$ K for the Ni compound. Interchain exchange interactions in both compounds are on the order of $|J'| \sim 0.1$ K. Weak AFM interchain exchange along b is predicted in both compounds with FM exchange along c predicted in the Ni species. Such a discrete change in sign of the exchange is difficult to verify experimentally. Due to the small magnitude of J', and the convergence criterion used for the energy calculations, the calculated J' parameters are less reliable than those calculated for J. In addition, small changes in the lattice geometry can have statistically significant effects on such small energy differences. The calculated J is roughly two and four orders of magnitude greater than J' for $\text{Co(NCS)}_2\text{(thiourea)}_2$ and $\text{Ni(NCS)}_2\text{(thiourea)}_2$ respectively; supporting the argument of Q1D behaviour.

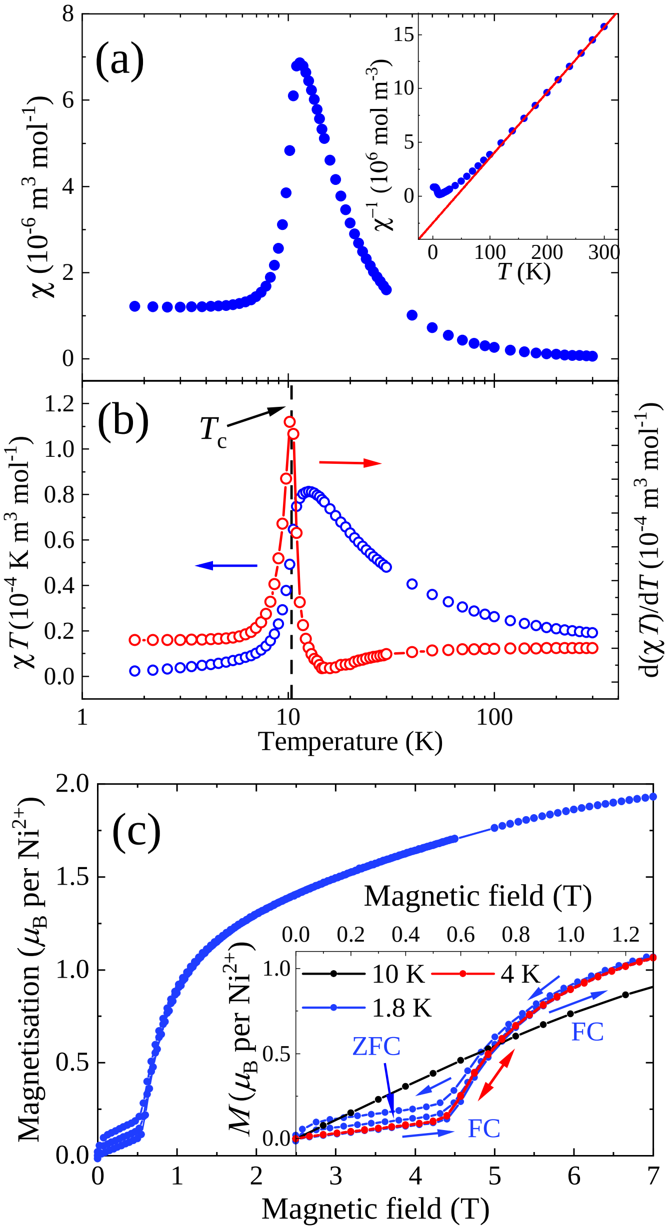

Figure 3.6: (a) Powder magnetic susceptibility $\chi(T)$ data for Ni(NCS)$_2$(thiourea)$_2$ measured at $\mu_0 H = 0.1$ T. Inset shows $\chi^{-1}(T)$ fit to the Curie-Weiss model over the temperature range $100 \leq T \leq 300$ K. (b) $\chi(T)$ multiplied by temperature $[\chi T(T)]$ (blue, left-axis) and its derivative (red, right-axis) with critical temperature T_c marked with a dashed line. (c) Powder DC-field magnetisation $M(H)$ for Ni(NCS)$_2$(thiourea)$_2$. Inset shows hysteretic behaviour for $T < 4$ K with zero-field cooled (ZFC) and field-cooled (FC) sweeps marked.

3.2.6 Charge and spin density

DFT calculations and magnetometry data both suggest that the intrachain exchange in the Co species is significantly weaker than in the Ni species. To investigate

Table 3.2: Energy differences (ΔE) and calculated magnetic superexchange coupling constants (J) between nearest neighbour transition-metal ions along the principle crystallographic axes. Conversion from ΔE to J is done by considering a single J convention. Negative values describe antiferromagnetic interactions.

	$Co(NCS)_2(thiourea)_2$		$Ni(NCS)_2(thiourea)_2$	
Axis	ΔE (K)	J (K)	ΔE (K)	J (K)
a	25.31	4.22	234.38	78.13
b	-0.61	-0.10	-0.34	-0.11
c	-0.51	-0.08	0.20	0.07

the underlying mechanism responsible for the large difference in the values of J, electronic configurations of the M sites, charge-density maps, and calculated spin-density distributions were performed by R. Scatena and P. Macchi whilst at the University of Bern, Switzerland.

The Hansen-Coppens MM [105] was refined against high-resolution single-crystal x-ray diffraction data allowing the electronic configuration of the M sites to be obtained. The population of the fitted multipolar functions is used to estimate the occupancy of the d-orbitals [128] with the results shown in Table 3.3. For the Co material, the results are indicative of the ion residing in the high-spin [t_{2g}^5, e_g^2] electronic configuration; in the Co(II) ($S = 3/2$) oxidation state. The experimental electronic configuration for Co(II) in $Co(NCS)_2(thiourea)_2$ was validated by comparison with the MM refinement determined from DFT calculations, as seen in Table 3.3. In addition, DFT allowed the electronic configuration of the Ni ion in $Ni(NCS)_2(thiourea)_2$ to be determined (Table 3.3), as high-resolution x-ray data was not available. The occupancy of the d-orbital functions suggests that the Ni ion is in the [t_{2g}^6, e_g^2] electronic configuration; in the Ni(II) ($S = 1$) oxidation state. In this case, the abundant occupancy of the $d_{x^2-y^2}$ and d_{z^2} orbital functions (an occupancy of ≈ 1.45 in each) is due to the electron-spin density being partially delocalised along Ni(II) ion ligands. It should be noted that occupancy values slightly exceeding the formal number of one or two electrons is not unusual in MM refinement [129], and that occupancy values tending to two electrons represent fully occupied orbitals.

The valence electron-charge density, responsible for chemical bonding, is shown by deformation density maps as regions of charge density excess and depletion, obtained from differences between the multipolar and spherical charge density. The different electronic configurations retrieved for $Co(NCS)_2(thiourea)_2$ and $Ni(NCS)_2(thiourea)_2$ are thus reflected in their respective deformation density maps. Figure 3.7 shows the deformation density within the equatorial plane, which is relevant for the intrachain magnetic exchange coupling J. In both coordination poly-

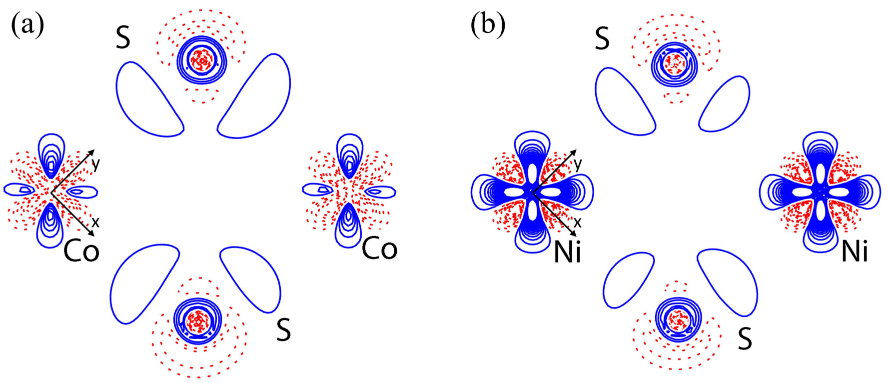

Figure 3.7: Deformation electron-density maps for (a) $Co(NCS)_2(thiourea)_2$ and (b) $Ni(NCS)_2(thiourea)_2$. Blue and red contours (0.2 e Å^{-3}) represent regions of electron charge density excess and depletion, respectively.

mers, the electron density is clearly depleted (dotted red contours) towards the S-ligands, with the $d_{x^2-y^2}$ being singularly occupied in both materials. There is a clear excess of electron-charge density located around the Ni ion in regions between S-ligands (blue contours), depicting the fully occupied d_{xy} orbital. The Co ion has a third semi-occupied orbital pointing between the ligands (d_{xz}), which leads to a reduction in the electron density along this direction, shown in Figure 3.7(a) as a diminished blue contoured region along the Co $\cdots$ Co direction.

Electronic configurations and deformation density maps can be used to infer possible magnetic superexchange pathways in the materials. The results here establish that in $Co(NCS)_2(thiourea)_2$, a through-space magnetic interaction is available, whereas in $Ni(NCS)_2(thiourea)_2$, this exchange pathway is absent. The calculated electron spin-density distributions for the two compounds explicitly follow the dif-

Table 3.3: Experimentally (Exp. MM) and calculated (Calc. MM) d-orbitals occupancy for $M(NCS)_2(thiourea)_2$ as estimated from the multipolar model (MM). The z-axis was set along the unique M—N bond whilst the x- and y-axis were set along M—S bonds in the equatorial plane.

	M = Co		M = Ni
d-orbital	Exp. MM	Calc. MM	Calc. MM
z^2	1.06(2)	1.29	1.46
xz	1.34(2)	1.59	2.04
yz	1.87(2)	1.64	2.06
$x^2 - y^2$	1.42(2)	1.30	1.44
xy	1.87(2)	1.63	2.04
tot	7.45(10)	7.47	9.05

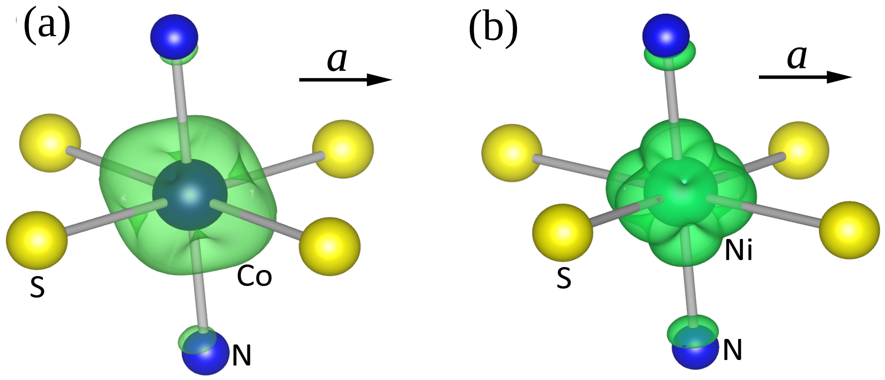

Figure 3.8: Calculated spin-density maps for (a) Co(NCS)$_2$(thiourea)$_2$ and (b) Ni(NCS)$_2$(thiourea)$_2$ plotted at the isovalue of 0.005 e per ^{3}. Spin-density regions are outlined as 3D green contours.

ferences in their electronic configurations. In Co(NCS)$_2$(thiourea)$_2$, the calculated spin-density distribution, centred around the Co ion, is quite spherical as shown in Figure 3.8(a). Here, the spin-density is concentrated not only towards the ligands but also directly along the a-axis, permitting two possible exchange pathways between adjacent Co ions: a through-bond interaction along the two Co—S—Co bridges and a through-space Co $\cdots$ Co exchange interaction. The latter must be AFM in nature, as it is a result of bond-formation which is subject to the Pauli exclusion principle. In contrast, the spin-density at the Ni sites is polarised along the ligands, see Figure 3.8(b). In this case, the spin-density is concentrated exclusively along the Ni—S—Ni pathways and towards the Ni—N bond. Therefore, Ni(NCS)$_2$(thiourea)$_2$ can only exploit the Ni—S—Ni through-bond interactions and, unlike Co(NCS)$_2$(thiourea)$_2$, has no through-space magnetic exchange.

3.2.7 Discussion

Table 3.4 shows the values of J, J' and D determined experimentally for both the Ni and Co compounds. An axial compression of the MS$_4$N$_2$ octahedra results in Ising-like anisotropy in both materials. As is typical [13], the anisotropy energy in the Co material is found to be considerably larger than in the Ni system.

Both compounds exhibit FM intrachain exchange, which is an order of magnitude greater in the Ni than in the Co system. The electronic configurations, by identifying the semi-occupied (magnetic) orbitals shown in Table 3.3, determine that in Ni(NCS)$_2$(thiourea)$_2$ only a through-bond M—S—M exchange is possible, whereas in Co(NCS)$_2$(thiourea)$_2$, both through-bond M—S—M and through-space $M \cdots M$ magnetic interactions are available. The spin-density extending along the

	$\mathrm{Co(NCS)_2(thiourea)_2}$			$\mathrm{Ni(NCS)_2(thiourea)_2}$		
	J (K)	J' (K)	D (K)	J (K)	J' (K)	D (K)
Exp.	$3.62(7)^a$	$-0.3(1)^b$	$\sim -100^a$	$\sim 100^a$	$-0.13(1)^b$	$\sim -10^c$
DFT	4.22	-0.1	—	78.13	-0.1	—

Table 3.4: Comparison of the intrachain J, interchain J', and SIA D determined experimentally [$a = \chi(T)$, $b = M(H)$, $c = C_{\mathrm{mag}}(T)$] and via DFT calculations. Negative exchange values indicate AFM interactions and negative D values indicate easy-axis behaviour. DFT values were calculated by considering a single J convention in the Hamiltonian where summations are made over unique exchange pathways.

thiourea bibridges, Figure 3.8, in both compounds gives rise to strong FM exchange along the M—S—M pathways. However, the spin-density in the Co compound also extends directly along the a-axis, which leads to an additional AFM through-space interaction between Co ions. Competition between the two exchange pathways reduces the resultant intrachain exchange and explains the lower FM J in the Co system. DFT calculations estimate the average interchain exchange to be around -0.1 K in both compounds, in good agreement with magnetometry measurements.

$\mathrm{Ni(NCS)_2(thiourea)_2}$ can be compared to the related material $\mathrm{NiCl_2(thiourea)_4}$ (DTN), an AFM-coupled spin chain that contains two field-induced phase transitions, between which a BEC of magnons is observed [99]; both compounds are obtained by similar wet chemistry synthesis methods [130]. Exchanging the $\mathrm{Cl^-}$ ion for the pseudohalide $\mathrm{NCS^-}$ ion causes a structural change from $I4$ for DTN [104] to $P\overline{1}$ in the present case, and the change in the local Ni(II) environment, from $\mathrm{NiS_4Cl_2}$ to $\mathrm{NiS_4N_2}$, has a strong effect on the SIA. The equatorial Ni—S bond lengths are similar in both systems: 2.46 Å for DTN and an average value of 2.57(3) Å for $\mathrm{Ni(NCS)_2(thiourea)_2}$. However, the octahedra in DTN have a slight axial elongation with an equatorial to axial bond-length ratio of 0.98, while in $\mathrm{Ni(NCS)_2(thiourea)_2}$ the octahedra are axially compressed with a bond-length ratio of 1.26. This results in the Ising-like SIA of $D \sim -10$ K, compared to the easy-plane SIA of $+8.12(4)$ K observed in DTN [99].

The lack of spatial-inversion-symmetry in DTN results in a net electric polarisation along the c direction [131]. In contrast, $\mathrm{Ni(NCS)_2(thiourea)_2}$ does possess a centre of inversion symmetry, so no net electric polarisation is expected.

The structure and SIA of DTN is such that the intrachain AFM exchange is mediated along linear through-space Ni—Cl $\cdots$ Cl—Ni pathways [J = -1.74(3) K] that propagate along the c-axis. Within the ab-plane, non-bridging thiourea ligands keep the magnetic ions well separated (adjacent Ni sites are 9.595 Å apart), which results in weak AFM J' = -0.17(1) K.

For $Ni(NCS)_2(thiourea)_2$, the thiourea ligands are no longer terminal but now connect adjacent Ni sites along a via Ni—S—Ni bibridges which mediate the large FM exchange along a. The thioureas still keep adjacent Ni sites well separated along b at 7.527 Å, and H-bonding between the ligands mediates weak AFM J'. Although Ni—NCS—Ni bond pathways have been shown to effectively mediate magnetic exchange interactions in similar compounds [132], the NCS ligands in $Ni(NCS)_2(thiourea)_2$ are terminal and support only weak AFM J' via H-bonds along c.

Similarly, $Co(NCS)_2(thiourea)_2$ can be compared to the $S = 3/2$ analogue of DTN, $CoCl_2(thiourea)_4$ (DTC) [133]. DTC displays antiferromagnetic order below approximately 1 K that can be suppressed by magnetic fields of around 2 T, and somewhat surprisingly, the observed susceptibility and magnetisation are largely isotropic [131, 134]. Swapping the Cl^- for NCS^- ion again results in a structural change, now from $P4_2/n$ to $P\overline{1}$. Average Co—S bond lengths in DTC and $Co(NCS)_2(thiourea)_2$ are the same within errors at 2.53(3) and 2.57(3) Å, respectively. The local CoS_4N_2 environment in $Co(NCS)_2(thiourea)_2$ is compressed along the axial N—Co—N bond such that the ratio of the equatorial Co—S to axial Co—N bond is 1.28, leading to a large Ising-like SIA $D \sim -100$ K. This contrasts with the isotropic behaviour seen in DTC which also possesses a slight axial compression, with a bond-length bond ratio of 1.02. Analogous to the comparison of the Ni species and DTN above, thiourea ligands form Co—S—Co bibridges in $Co(NCS)_2(thiourea)_2$ that mediate strong FM exchange along the a-axis, while the chains are well separated along b. Again NCS ligands are terminal and mediate weak AFM exchange via H-bond networks along the c-axis.

$Co(NCS)_2(thiourea)_2$ can also be compared to the archetype transverse-field Ising chain material $CoNb_2O_6$, with both possessing strong Ising-like SIA with FM J and weak AFM J' [31]. Interchain exchange interactions induce a transition to long-range AFM order in both, at $T_N = 2.9$ K in $CoNb_2O_6$ [135] and $T_N = 6.82(5)$ K in $Co(NCS)_2(thiourea)_2$. The lower T_c for $CoNb_2O_6$ indicates a more ideal 1D system, with $J' \sim 0.01$ K [136] compared to 0.1 K for $Co(NCS)_2(thiourea)_2$. In $CoNb_2O_6$, a critical field applied perpendicular to the Ising-axis breaks the 3D-AFM order, pushing it through a QCP as the material enters a quantum paramagnetic state [31, 32]. Because application of a transverse field consistently shattered $Co(NCS)_2(thiourea)_2$ single-crystals, the experiments performed here are unable to provide evidence of similar quantum-critical behaviour in $Co(NCS)_2(thiourea)_2$.

3.3 Summary

The isostructural compounds Ni(NCS)$_2$(thiourea)$_2$ and Co(NCS)$_2$(thioruea)$_2$ both exhibit long-range AFM ordering as determined from heat-capacity, magnetisation and μ^+SR data, with respective ordering temperatures of $T_{\text{N}} = 6.82(5)$ K and $T_{\text{N}} = 10.5(1)$ K. This ordering results from weak AFM exchange interactions between adjacent chains, $|J'| \sim 0.1$ K in both. Simulations of the magnetic heat capacity for the Co compound are not compatible with 2D Ising-like long-range order, suggesting 3D ordering in the system. Whilst μ^+SR data for the Ni species suggests 2D Ising-like long-range order. Heat-capacity data, in combination with magnetometry, estimates the magnitude of the Ising-like SIA in both compounds to be on the order of $D_{\text{Co}} \sim -100$ K and $D_{\text{Ni}} \sim -10$ K. The large magnitude of D_{Co} suggests that, at low-temperatures, only the ground-state $S = \pm 3/2$ energy-levels are populated, and thus, the system can be treated using an effective spin-half approximation.

This permits $\chi(T)$ of the Co species to be modelled using an effective spin-half Ising model to extract $J_{\text{Co}} \approx +4$ K, which is notably smaller in magnitude than $J_{\text{Ni}} \sim +100$ K determined from $\chi^{-1}(T)$. The large difference between the magnitude of J_{Co} and J_{Ni} is due to the differing electronic structure in each compound. For the Ni species, the spin-density is localised along the Ni—S bond direction and depleted along the through-space direction. Within the Co compound, spin-density extends both along the through-space direction and along the Co—S bonds. The competition between the FM through-bond and AFM through-space exchange interactions leads to a reduction in the overall intrachain magnetic exchange interaction in the Co compound, resulting in $J_{\text{Ni}} \approx 10 J_{\text{Co}}$

In order to establish a connection between the compounds studied here and known, chemically similar, quantum magnets, both species were compared to the chemically similar compounds MCl$_2$(thiourea)$_4$, M = Ni(II) (DTN) and Co(II) (DTC); where DTN is know to harbour two magnetic field-induced QCPs. Comparing DTN to Ni(NCS)$_2$(thiourea)$_2$, it is seen that substitution of Cl$^-$ for NCS$^-$ results in a radical structural transition from the $I4$ to $P\bar{1}$. Here, the previously non-bridging thiourea ligands in DTN now link via bisulphide bridges along the crystallographic a-axis. In addition, a radical change in the SIA, from easy-plane $D = +8.12(4)$ K in DTN to $D \sim -10$ K, in the Ni compound studied here. Comparing DTC to Co(NCS)$_2$(thiourea)$_2$, the structural transition is from $P4_2/n$ to $P\bar{1}$. Again, the Co compound studied here forms S bibridges along a, but the behaviour moves from an isotropic weakly interacting AFM, DTC, to a Q1D FM Ising chain compound for the Co reported in this chapter.

Chapter 4

A near-ideal Haldane spin chain

4.1 Introduction

This chapter will characterise the magnetic properties of the quasi-one-dimensional $S = 1$ antiferromagnet $\mathrm{NiI_2(3,5\text{-}lut)_4}$ [38].

For Q1D $S = 1$ AFM Heisenberg chain materials where the chains are well isolated and there is minimal single-ion anisotropy, the ground-state is that of a degenerate $S = 1$ triplet-state above a non-magnetic $S = 0$ singlet ground-state, where the singlet-triplet energy gap is denoted Δ_0. This gapped ground-state, which is distinct from the gapless ground-state observed in Q1D $S = 1/2$ AFMs [137], was first identified by Duncan Haldane [138, 139] for which he was jointly awarded the 2016 Nobel Prize in Physics.

The phase diagram for $S = 1$ AFM chain materials with Heisenberg-like exchange interactions is outlined in Figure 4.1 as adapted from reference [34]. At low-temperatures and zero-field, the ground state of the system is determined by both the strength of the interchain magnetic exchange interactions (J'), and sign and strength of the single-ion anisotropy parameter (D), relative to the magnitude of the intrachain exchange (J). Chains with sizable interchain exchange interactions will, at sufficiently low-temperatures, undergo a transition to 3D long-range order. For sizable SIA relative to the strength of the intrachain exchange, the system will exhibit Ising-like order ($D < 0$) or XY-like order ($D > 0$) at low temperatures, dependent upon the sign of D.

In an applied magnetic field ($\mu_0 \boldsymbol{H}$), the Hamiltonian describing $S = 1$ AFM

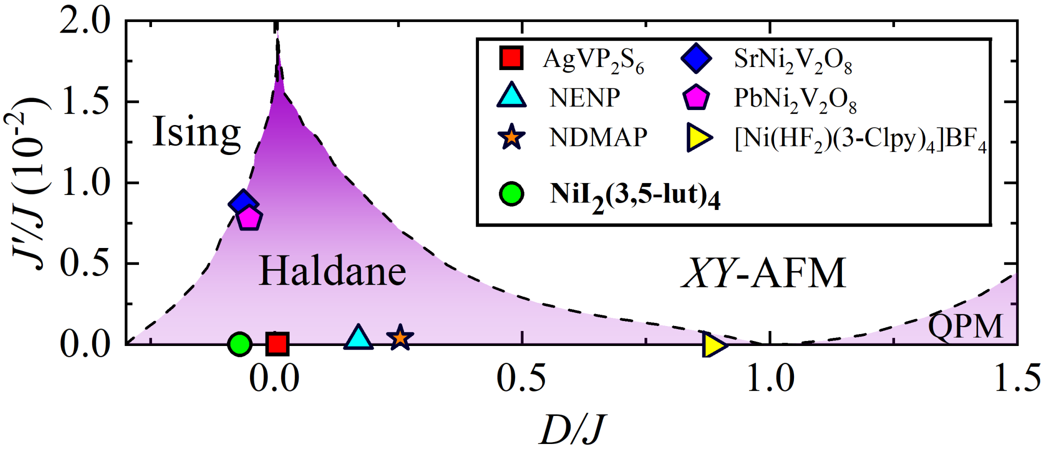

Figure 4.1: The zero-field phase-diagram for quasi-one-dimensional (Q1D) $S = 1$ antiferromagnets (AFMs) reproduced from [34]. Dashed lines are quantum-Monte-Carlo simulations outlining the phase-boundaries between the different ground-states for Q1D $S = 1$ AFM systems. The position of a system on the phase-diagram is dictated by the ratio of the interchain to intrachain exchange J'/J and the ratio of the single-ion anisotropy to the intrachain exchange D/J. The positions of several Haldane systems, reported in [34], are plotted and compared to NiI_2(3,5-lut)$_4$ (green circle). QPM denotes the quantum-paramagnetic region of the phase diagram.

chains, inclusive of SIA and interchain interactions, is;

$$\hat{\mathcal{H}} = J\sum_{\langle i,j\rangle}\hat{\boldsymbol{S}}_i\cdot\hat{\boldsymbol{S}}_j + D\sum_i(\hat{\boldsymbol{S}}_i^z)^2 + J'\sum_{\langle i,j'\rangle}\hat{\boldsymbol{S}}_i\cdot\hat{\boldsymbol{S}}_{j'} + \mu_\text{B}\mu_0\sum_i\boldsymbol{H}\cdot\boldsymbol{g}\cdot\hat{\boldsymbol{S}}_i, \tag{4.1}$$

where angular brackets denote sums over adjacent spins within the chain and primed indices are interactions with between spins in adjacent chains; $\mathbf{g} = \text{diag}(\text{g}_\text{x}, \text{g}_\text{y}, \text{g}_\text{z})$ is a tensor of g-factors. The Hamiltonian in Eq. 4.1 has been extended to include the effects of a rhombic anisotropy term (E) [140], however, the tetragonal structure of NiI_2(3,5-lut)$_4$ (described in detail in Section 4.2.1) precludes the existence of any E-term.

The presence of SIA, described in more detail later in this chapter, serves to lift the degeneracy of the excited triplet state. For Ising-like anisotropy, the triplet-state is subsequently split into a singlet $S_z = 0$ state, which determines the magnitude of the energy-gap along the unique chain-axis $\Delta^{\parallel}$, and an $S_z = \pm 1$ doublet, which determines the magnitude of the energy-gap perpendicular to the chain-axis $\Delta^{\perp}$ [141]. The two anisotropic gaps relate to Δ_0 via;

$$\Delta^{\parallel} = \Delta_0 + 1.41D, \qquad \Delta^{\perp} = \Delta_0 - 0.57D, \tag{4.2}$$

where the size of Δ_0 is dictated by the magnitude of the intrachain coupling $\Delta_0 = 0.41J$ [142, 143]. The energy-level splitting outlined by Eqs. 4.2 is comparable to that of a $S = 1$ ion subject to Ising-like SIA and can be modelled as such by using an effective SIA D_{eff} as a model parameter (note: positive D_{eff} constitutes a negative D and therefore Ising-like anisotropy, and vice versa for positive D), which is given by,

$$D_{\text{eff}} = \Delta^{\perp} - \Delta^{\parallel} = -1.98D. \tag{4.3}$$

In an applied magnetic field, the Zeeman interaction serves to lower the energy of one of the SIA split triplet energy-levels below that of the Haldane ground-state. The point at which the external field closes the anisotropic Haldane gaps ($H = H_{\text{c}}$) is quantified by two different quantum-field-theoretical models, the "fermion" model [54, 141, 144] and the "boson" model [54, 145]. The fermion model derives from a pertubative approach where the field-evolution of the triplet is modelled as three massive, free, majorana fermion modes [54]. The model appears to become exact when J' is minimal [144]. The boson model describes the triplet as a three-component magnon system which, in some cases, appears to become exact when the system is close to 3D order [54, 145]. The two models differ in their predicted values for the critical field perpendicular to the chain axis.

The fermion model predicts the following critical fields,

$$g_{\parallel}\mu_{\text{B}}\mu_0 H_{\text{c}}^{\parallel} = \Delta^{\perp}, \qquad g_{\perp}\mu_{\text{B}}\mu_0 H_{\text{c}}^{\perp} = \sqrt{\Delta^{\parallel}\Delta^{\perp}}, \tag{4.4}$$

for fields parallel and perpendicular to the unique chain-axis c. Whilst the boson model predicts anisotropic critical fields of:

$$g_{\parallel}\mu_{\text{B}}\mu_0 H_{\text{c}}^{\parallel} = \Delta^{\perp}, \qquad g_{\perp}\mu_{\text{B}}\mu_0 H_{\text{c}}^{\perp} = \Delta^{\parallel}. \tag{4.5}$$

It is clear that whilst both models predict the same critical field value for field applied parallel to the chain axis, they differ in their prediction for H_{c} perpendicular to the chain axis. Additionally, Eq. 4.3 shows that for easy-axis systems it is the case that $\Delta^{\parallel} < \Delta^{\perp}$. Therefore, both the fermion and boson model predict $H_{\text{c}}^{\parallel} > H_{\text{c}}^{\perp}$ in Ising systems. This situation is reversed in the easy-plane scenario, $D > 0$, where one would then expect $H_{\text{c}}^{\perp} > H_{\text{c}}^{\parallel}$.

The anisotropic critical fields for easy-plane Haldane compounds, such as NENP [144] and NDMAP [146], are well accounted for by the fermion model. In contrast, the critical field values for easy-axis Haldane chains, such as $\text{PbNi}_2\text{V}_2\text{O}_8$ and $\text{SrNi}_2\text{V}_2\text{O}_8$ [147–149], are readily described by the boson model. Therefore, it is thought that the boson model is able to describe easy-axis Haldane systems well whilst the fermion model accounts for the behaviour of easy-plane systems. The success of the boson model in describing the vanadate family of Haldane spin-chains is believed to be due to their easy-axis anisotropy and larger interchain coupling, locating them near the phase boundary separating the Haldane and Ising AFM ground states.

4.2 $\mathrm{NiI_2(3,5\text{-}lut)_4}$

4.2.1 Structure

Single-crystal and polycrystalline powder samples of $\mathrm{NiI_2(3,5\text{-}lut)_4}$ were synthesised by J. Manson and D. Villa at Eastern Washington University, USA. Collection and refinement of the structure from synchotron single-crystal x-ray diffraction data was completed by D. Villa, J. Schlueter and J. Manson at ChemMatCARS 15-ID-B beamline of the Advanced Photon Source at Argonne National Laboratory.

Single-crystals of $\mathrm{NiI_2(3,5\text{-}lut)_4}$ crystallise into a tetragonal structure with space group $P4/nnc$. The Ni(II) ion resides at the centre of an axially elongated octahedral environment, composed of four equal Ni—N bonds (2.1232 Å) and two equal Ni—I bonds (2.8327 Å) as in Figure 4.2(a). All equatorial N—Ni—N bonds and axial I—Ni—N bond angles are 90°, such that the octahedral environment can be considered close to ideal. The slight axial elongation of the octahedra, axial to equatorial bond-ratio of 1.33, suggests $\mathrm{NiI_2(3,5\text{-}lut)_4}$ may possess a small Ising-like single-ion anisotropy (SIA) term ($D < 0$), as observed in similar Ni(II) complexes [13–15, 108], whilst the tetragonal symmetry of the system precludes the existence of any rhombic-anisotropy term.

Figure 4.2(b) shows that along the *c*-axis, adjacent octahedra form linear Ni—I ⋯ I—Ni through-space pathways, such that any magnetic exchange occurring along this pathway is expected to be antiferromagnetic in accordance with the Goodenough-Kanamori rules [106, 107]. Within the *ab*-plane, adjacent Ni sites are offset from each other and kept well separated by the bulky lutidine ligands, which arrange themselves in a propeller-like fashion around the Ni(II) ion, as seen in Figure 4.2. The packing of adjacent Ni sites within the *ab*-plane is such that there are no obvious exchange pathways between adjacent Ni sites within the *ab*-plane. Due to this, each individual Ni—I ⋯ I—Ni chain-like pathway can be considered to be well isolated and, as such, the interchain exchange interactions J' are likely very small, suggesting that the system is a promising platform to exhibit quasi-one-dimensional (Q1D) behaviour. Inspection of the structure of $\mathrm{NiI_2(3,5\text{-}lut)_4}$ therefore indicates

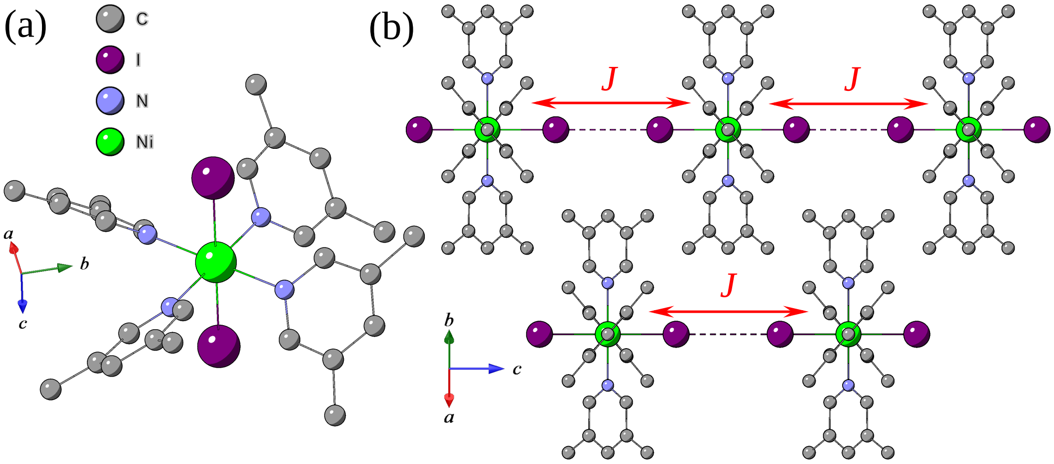

Figure 4.2: Crystal structure for $NiI_2(3,5\text{-lut})_4$ measured at 100 K, hydrogen atoms are omitted for clarity. (a) Local Ni(II) octahedral environment. (b) Chain-like structure of the Ni—I···I—Ni pathways (dashed lines) viewed along the [110] direction. J indicates through-space magnetic exchange pathways between adjacent Ni(II) ions along the c-axis. Dashed lines show through-space I···I paths.

that $NiI_2(3,5\text{-lut})_4$ will likely behave like a Q1D chain with AFM coupling along the Ni—I···I—Ni through-space pathways.

4.2.2 Magnetometry

SQUID magnetometry data on powdered samples of $NiI_2(3,5\text{-lut})_4$ was collected by W. Blackmore at The University of Warwick whilst powder pulsed-field data were collected in collaboration with J. Singleton at The National High Magnetic Field Laboratory (NHMFL-LANL), USA. Single-crystal magnetometry experiments were performed by myself at The University of Warwick.

Magnetic susceptibility data [$\chi(T)$] for powdered $NiI_2(3,5\text{-lut})_4$ is shown in Figure 4.3(a). Upon decreasing temperature, $\chi(T)$ rises to a broad hump centred around 20 K before decreasing in magnitude as temperatures approach ≈ 3 K, a slight upturn is observed at the lowest measured temperatures $T \lesssim 2.5$ K. The measured response can be well captured by a model for an idealised isotropic Haldane spin-chain $\chi_{\text{Law}}(T)$ [150] of the form,

$$\chi = \rho\chi_{\text{Law}}(T) + (1-\rho)\chi_{\text{pm}} \tag{4.6}$$

where χ_{pm} models the low-temperature paramagnetic upturn in the sample and ρ estimates the % of the sample attributable to those paramagnetic moments. The fit [solid line Figure 4.3(a)] captures $\chi(T)$ well over the entire measured temperature

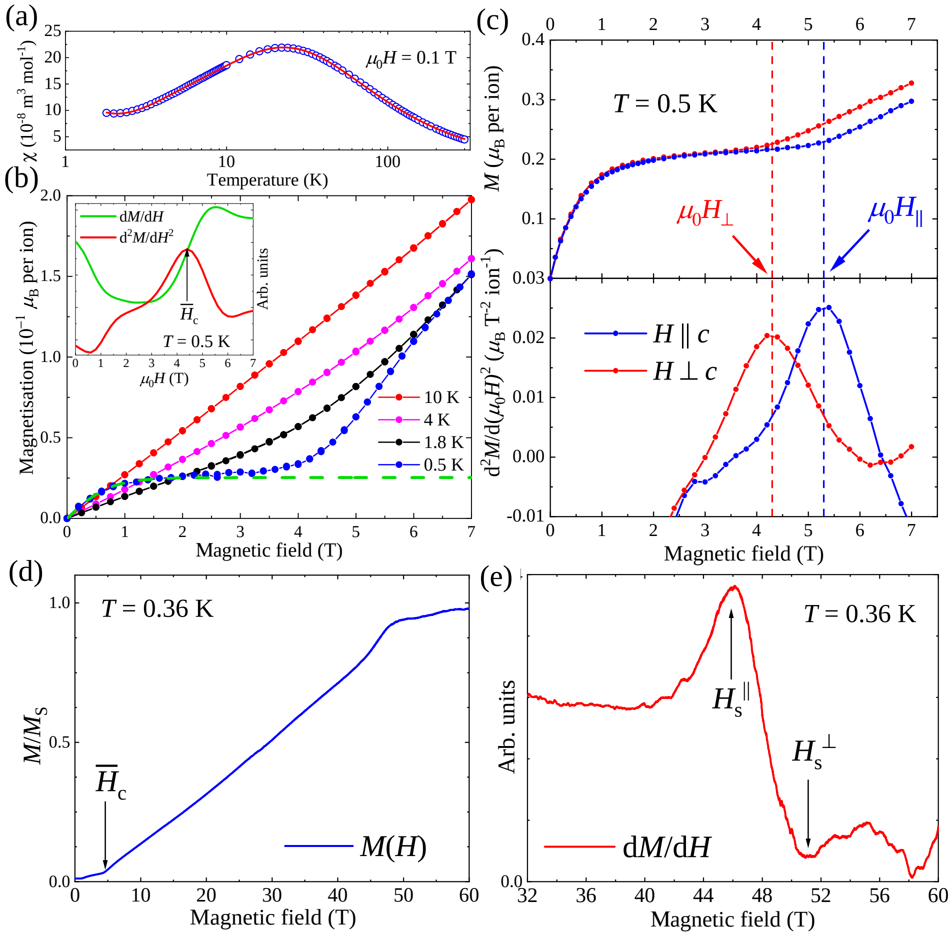

Figure 4.3: Magnetometry data for $\mathrm{NiI_2(3,5\text{-}lut)_4}$ powder and single-crystal samples. (a) Powder magnetic susceptibility (χ) measured as a function of temperature. Solid line is a fit to Eq. 4.6. (b) Powder DC-field magnetisation $M(H)$ with 0.5 K data fit to a Brillouin function for fields $\mu_0 H \leq 2$ T. Inset shows the first and second differential of $M(H)$ with the powder-average critical-field $\overline{H}_\mathrm{c}$ indicated with an arrow. (c) Single-crystal magnetisation data (top-panel) and its second derivative (bottom-panel) for field parallel and perpendicular to the c axis. Positions of the anisotropic critical fields are indicated with arrows and dashed lines. (d) Powder pulsed field magnetisation and its derivative (e) with critical fields, as described in text, indicated with arrows.

range, $1.8 \leq T \leq 300$ K, estimating the intrachain exchange to be $J = 18.27(4)$ K, the size of the powder-average Haldane-gap to be $\Delta_0 = 7.26(1)$ K and a powder-average g-factor of $g = 2.2(1)$.

In the Haldane system NENP [151], the low-temperature paramagnetic upturn in $\chi(T)$ is attributed to the existence of $S = 1/2$ end-chains predicted to exist in Haldane spin-chains by the AKLT model [34, 152]. The number of end-chain spins is expected to be greater in powder samples as grain boundaries lead to more breaks in the chains. In the present case, a slight upturn does exist in the low-temperature $\chi(T)$ which is modelled by the parameter χ_{pm}. Electron-spin resonance measurements on powdered $\mathrm{NiI_2(3,5\text{-}lut)_4}$, discussed in section 4.2.5, indicate the presence of $S = 1/2$ end-chains in this material. However, as the parameter χ_{pm} captures the low-temperature behaviour of the sample equally well when considering a $S = 1$ and $S = 1/2$ paramagnetic response, the powder $\chi(T)$ data here cannot be used to estimate the % of end-chain spins in $\mathrm{NiI_2(3,5\text{-}lut)_4}$. It can only estimate that $\approx 1 - 3\%$ of the sample contributes to the low-temperature paramagnetic response, likely due to a combination of spin-half end-chains and free Ni(II) ions distributed throughout the sample.

Powder DC-field SQUID magnetisation $M(H)$ is shown in Figure 4.3(b). At the lowest measured temperature ($T = 0.5$ K), $M(H)$ initially increases (likely due to a combination of paramagnetic spin-half end chains, ^{3}He sample holder and free impurity spins; see Appendix) then reaches a plateau between $1 \leq \mu_0 H \lesssim 3.5$ T before exhibiting a sharp upturn around 4.5 T. The data then increase linearly with field up to 7 T. Whilst these features are sharp at low-temperatures, they are smeared out as temperature is increased and are completely extinguished by 10 K.

The existence of the sharp upturn in $M(H)$ is ascribed to the field-induced closing of the Haldane energy-gap Δ_0 as the Zeeman interaction pushes the energy of a triplet-state below that of the Haldane ground-state. The field at which this upturn occurs can be estimated by determining the location of the peak in $\mathrm{d}^2M/\mathrm{d}H^2$, inset Figure 4.3(b), and provides a value for the powder-average critical-field of $\mu_0\overline{H}_{\mathrm{c}} = 4.4(2)$ T.

The low-field response, $\mu_0 H < 2$ T, at 0.5 K can be modelled by a $S = 1/2$ Brillouin function [6] [dashed line, Figure 4.3(b)], such that the data resemble a collection of $S = 1/2$ paramagnetic ions. In order to achieve $T \gtrsim 0.5$ K, an *i*-Quantum ^{3}He insert was employed. Attempts to isolate the sample response using background subtraction software [78] proved problematic, hence the low-temperature low-field $M(H)$ response was attributed to a combination of background from the *i*-Quantum ^{3}He insert, $S = 1/2$ end chains and paramagnetic free spins within the sample. The background subtraction process is discussed in detail in the Appendix.

Single-crystal $M(H)$ data also exhibits an isotropic paramagnetic response at low-temperatures and fields, top-panel Figure 4.3(c), consistent with the signal in this regime being due to a combination of background plus $S = 1/2$ end-chains. The single-crystal $M(H)$ measurements were performed in order to check for any orientation dependence of the critical-field, which in turn provides information about the SIA of the system. Figure 4.3(c) shows a clear distinction between $M(H)$ data for field applied parallel and perpendicular to the crystallographic c-axis. For $H \perp c$, $M(H)$ exhibits an upturn at approximately 1 T lower in field than for $H \parallel c$. The field at which these upturns occur is ascertained by observing a peak in $\mathrm{d}^2M/\mathrm{d}H^2$ of both orientations, bottom-panel of Figure 4.3(c), giving $\mu_0 H_\mathrm{c}^\perp = 4.3(1)$ T and $\mu_0 H_\mathrm{c}^\parallel = 5.3(1)$ T. The fact $\mu_0 H_\mathrm{c}^\parallel > \mu_0 H_\mathrm{c}^\perp$ constitutes unambiguous evidence for Ising-like SIA ($D < 0$) in the system, see Eq. 4.3.

In order to reach the saturation magnetisation M_S for $\mathrm{NiI_2(3{,}5\text{-}lut)_4}$, powder pulsed-field magnetisation measurements were performed with the results shown in Figure 4.3(d). An upturn in $M(H)$ around 4 T corresponds to $\overline{H}_\mathrm{c}$, also observed in the DC-field magnetisation in Figure 4.3(b). $M(H)$ then continues to rise monotonically before exhibiting a slight upward curve and reaching a plateau around 50 T.

A peak in $\mathrm{d}^2M/\mathrm{d}H^2$ at 4.3(1) T agrees well with the value of $\overline{H}_\mathrm{c}$ extracted from SQUID magnetometry measurements. By using the fact $D < 0$, as determined from single-crystal $M(H)$, the below relations [153] can be employed to estimate J and D,

$$g_\parallel \mu_\mathrm{B} \mu_0 H_\mathrm{s}^\parallel = 2(2J - |D|), \qquad g_\perp \mu_\mathrm{B} \mu_0 H_\mathrm{s}^\perp = 2(2J + |D|), \tag{4.7}$$

where it is assumed J' is small (this is in line with μ^+SR measurements in section 4.2.4) such that $J >> J'$. Figure 4.3(e) shows $\mu_0 H_\mathrm{s}^\parallel = 46.0(4)$ T and $\mu_0 H_\mathrm{s}^\perp = 50.7(8)$ T. Using Eqs. 4.7, and the anisotropic g-factors $g_{\parallel,\perp} = 2.13(1), 2.19(1)$ determined from ESR, it is estimated $D = -1.2(3)$ K and $J = 17.5(2)$ K, where J in in good agreement with the value determined from fitting $\chi(T)$.

4.2.3 Zero-field inelastic neutron scattering

Inelastic neutron scattering measurements were performed on powder samples of $\mathrm{NiI_2(3{,}5\text{-}lut)_4}$ in order to investigate the magnetic excitations in the sample as well as probe the zero-field splitting of the Haldane energy-gaps, the results of which are shown in Figure 4.4. INS data was collected with assistance of D. Voneshen on the direct geometry time-of-flight spectrometer LET, ISIS, UK.

Representative INS spectra collected at $T = 1.8$ K and $T = 12$ K are plotted in Figures 4.4(a) and (b). Data were collected at an incident energy of $E_i = 2.19$ meV and plotted as a $(|Q|, E)$ heat-map where $|Q|$ and E are the momentum and energy transfer, respectively. In order to isolate the features in the spectrum attributable to the Haldane phase, the $T = 12$ K data (a temperature where $k_\mathrm{B}T > \Delta_0$) was used as a background for all measurements. The results of the background subtraction for the $T = 1.8$ K data is shown in Figure 4.4(c).

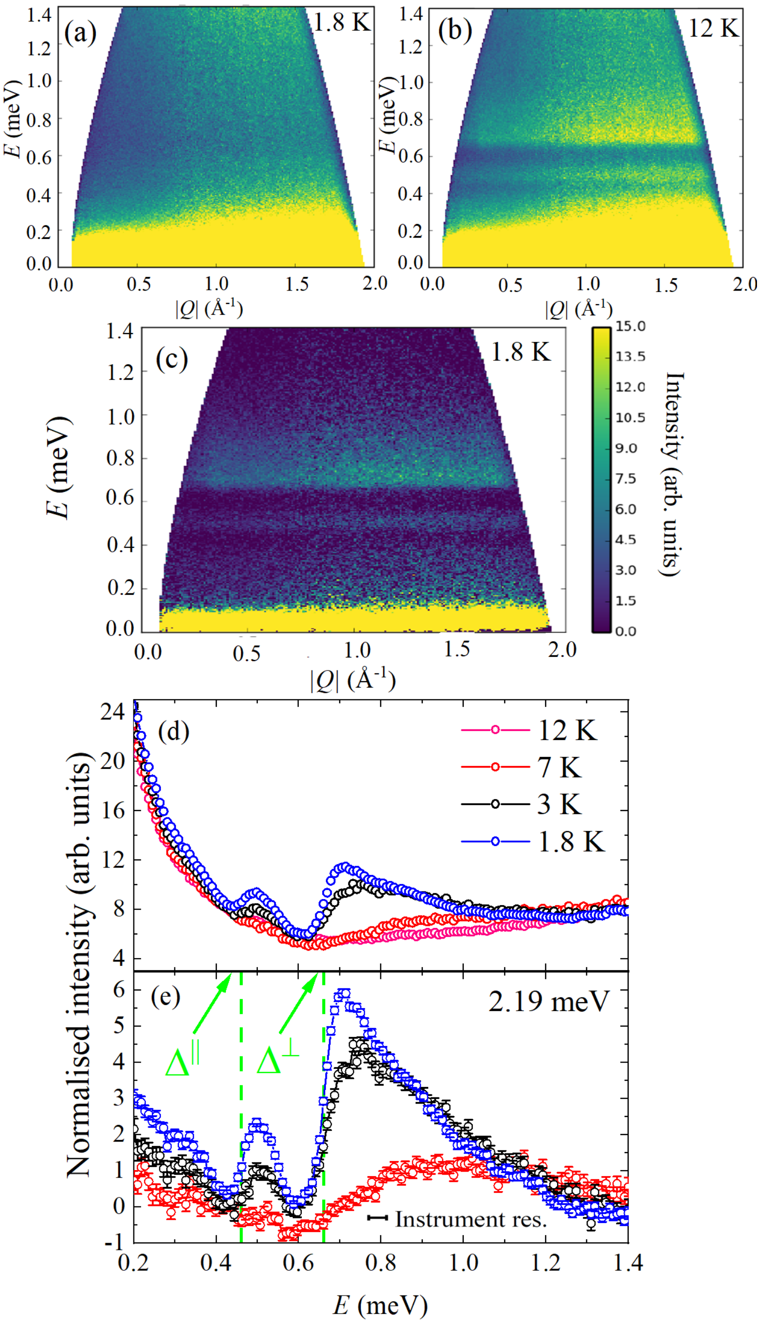

Figure 4.4: Time of flight inelastic neutron scattering spectrum presented as a $(|Q|, E)$ heat-map for powder $\mathrm{NiI_2(3{,}5\text{-}lut)_4}$ measured at (a) 1.8 K, (b) 12 K and (c) 1.8 K after subtraction of the 12 K data as a background. Intensity scale-bar to the right of (c) also holds for plots (a) and (b). Energy cuts, obtained by integrating data over the full measured $|Q|$-range, for all measured temperatures (d) and after subtracting the 12 K data as a background (e). Positions of the SIA-split Haldane energy-gaps are indicated with dashed lines and arrows in (e).

The background subtracted data in Figure 4.4(c) exhibit two minima at energies of ≈ 0.4 and ≈ 0.6 meV, attributable to gaps in the excitation spectra. This measurement *directly* images the zero-field SIA-split Haldane energy-gaps. Below $E < 0.3$ meV, there is significant intensity in the spectrum due to remnant elastic scattering and quasi-elastic scattering off of atomic nuclei. The intensity of these low energy excitations grows with decreasing temperature, best seen in Figure 4.4(e), possibly due to the build up of spin-spin correlations between end-chain magnetic moments.

The values of the Haldane energy gaps can be more readily quantified by integrating the spectrum over the full measured momentum range of $0 \leq |Q| \leq 2.0$ Å^{-1} with the results for all measured temperatures shown in Figure 4.4(d). The data after subtracting the 12 K background are seen in Figure 4.4(e). Two distinct peaks are seen in the data in Figure 4.4(e) corresponding to excitations within the SIA split triplet-states. In ZF, the higher energy peak has approximately twice the intensity of the lower energy feature. This difference is due to the high energy mode resulting from neutrons scattering from two degenerate energy-levels, $S_z = \pm 1$, whilst the lower energy mode corresponds to scattering from just a single energy-level, $S_z = 0$, as outlined by the energy-level diagram in Figure 4.7. This constitutes further evidence for Ising-like SIA in the system, in agreement with single-crystal $M(H)$ data.

As such, in accordance with Eq. 4.3, the high energy mode is attributed to $\Delta^{\perp}$ and the low energy mode to $\Delta^{\parallel}$. Taking the onset of these excitations estimates the anisotropic Haldane-gap energies of $\Delta^{\parallel} = 0.46(1)$ meV $= 5.3(1)$ K and $\Delta^{\perp} = 0.66(1)$ meV $= 7.7(1)$ K. Using Eq. 4.3 this returns $D = -1.2(1)$ K, in excellent agreement with the value of $D = -1.2(3)$ K determined using pulsed-field magnetometry. The intrinsic Haldane gap $\Delta_0 = 0.60(1)$ meV $= 7.0(1)$ K, found using the expression for an ideal Haldane chain (Eq. 4.2), results in a $J = 17.0(2)$ K, which is in good agreement with the value of $J = 17.5(2)$ K and $\Delta_0 = 7.2(1)$ K determined from magnetometry measurements in Figure 4.3. The data in Figure 4.4(e) also highlights the increase in the low-energy, $E \leq 0.3$ meV, intensity with decreasing temperature, which may be attributable to spin-spin correlations between spin-half end-chains.

4.2.4 Muon-spin relaxation

Positive-muon-spin-relaxation measurements were carried out by T. Lancaster, B. Huddart, T. Hicken, S. Blundell and F. Xiao with measurements carried out on the LTF and GPS instruments at the Swiss Muon Source, Paul Scherrer Institut, Switzerland. Data analysis was carried out using the WiMDA analysis program [154].

ZF μ^+SR measurements were performed on a powder sample of NiI$_2$(3,5-lut)$_4$ where no oscillations in the muon asymmetry were observed down to the lowest measured temperature of $T = 20$ mK as seen in Figure 4.5(a). The data in Figure 4.5(a) were fit to two exponentially relaxing components and one constant background component (A_{bkd}) of the form,

$$A(t) = A_1 e^{-\lambda_1 t} + A_2 e^{-\lambda_2 t} + A_{\text{bkd}} \tag{4.8}$$

where λ_i models the slow and fast exponentially relaxing response of the muon. The fast relaxing response is typically due to the muon forming a bound state with an electron where the muon loses energy very quickly as it undergoes a series of rapid electron capture and loss reactions [84]. The slow relaxing component results from the muon occupying diamagnetic regions in the sample, which makes the muon sensitive to the local magnetic field [83].

It was found that the values of A_1 and A_2 were relatively unchanged when fitting to all temperatures and therefore both A_1 and A_2 were fixed. In addition, the values of the fast relaxing exponent related to the bound muon-states was not expected to change with temperature and, as the value remained constant $\lambda_2 \approx$ 38 MHz over the measured temperature range, the value was fixed for all fits.

The value of the slow-relaxing exponent λ_1 remained roughly constant down to the lowest measured temperature, $T = 0.02$ K, as seen in Figure 4.5(b). The

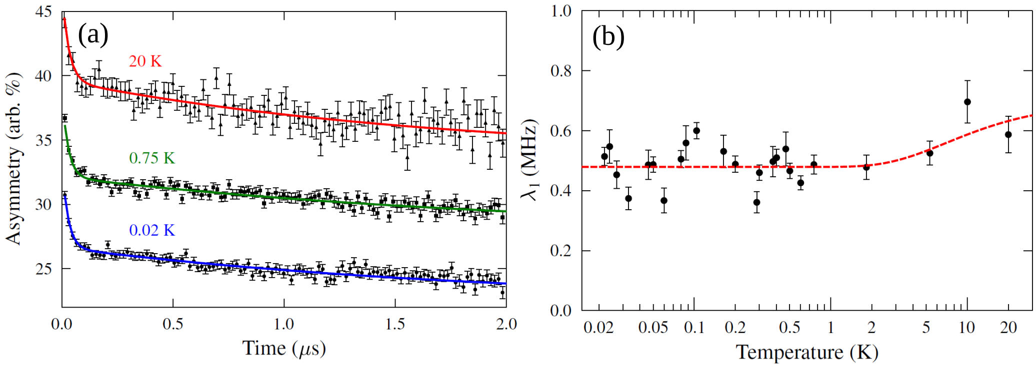

Figure 4.5: Zero-field μ^+SR results for powder NiI$_2$(3,5-lut)$_4$ (a) Temperature dependence of the relaxing asymmetry where solid lines are fits to two exponential relaxing components and one constant background component as described in the main text. (b) Temperature dependence of the first exponential relaxing exponent λ_1 where dashed line is a fit to $\lambda_1 \propto \exp -\Delta_0/k_B T$ with $\Delta_0 = 7$ K.

slight upturn around 5 K is predicted for Haldane chain systems where the relaxing exponent should vary as $\exp(-\Delta_0/k_\mathrm{B}T)$ [155]. The data in Figure 4.5(b) is well captured by this model (red-dashed line) where the gap-value is set to $\Delta_0 = 7$ K, in good agreement with the value of Δ_0 determined from other techniques.

A sharp change in λ_1 is indicative of the onset of magnetic ordering in the system. Figure 4.5(b) shows that there is no such sharp jump in λ_1 in the data here. As λ_1 is approximately constant over the entire measured temperature range, it suggest a lack of long-range magnetic ordering in the system down to 20 mK. This result is a strong indicator that the interchain magnetic exchange interactions (J') are exceedingly small in $\mathrm{NiI_2}$(3,5-lut)$_4$, such that the chains can be considered to be very well isolated. Transverse field μ^+SR studies determined a value of the powder-average critical field of $\overline{H}_\mathrm{c} \approx 4.4(2)$ T, see reference [38], in excellent agreement with magnetometry data.

4.2.5 Electron spin resonance

Electron-spin resonance measurements data was collected by A. Ozarowski on powdered samples of $\mathrm{NiI_2}$(3,5-lut)$_4$ using a home built spectrometer at the EMR facility, National High Magnetic Field Laboratory, Tallahassee, Florida, USA. I participated in the analysis of the data.

At high-temperatures ($T = 30$ K) there is a single exchange-narrowed [156] transmission shown in Figure 4.6(a). At $T = 30$ K the thermal energy of the system is well above that of Δ_0 and J, such that the system can be considered to be in the thermally disordered phase. This single transition is similar to that seen in the easy-axis Haldane system $\mathrm{PbNi_2V_2O_8}$ [147] which was also ascribed to an exchange-narrowed resonance originating from the local Ni(II) environment in the thermally disordered phase. The frequency-dependence of this resonance tracks linearly with field, such that it can be fit to a free $S = 1$ ion model shown as a dashed-line in Figure 4.6(a). This fit, where the gradient of the line is equal to $g\mu_\mathrm{B}$, extracts a powder average $g = 2.19(1)$, in excellent agreement with $g = 2.2(1)$ determined from fitting $\chi(T)$ in Figure 4.3(a).

At low-temperatures ($T = 3$ K) and fields below $\overline{H}_\mathrm{c}$ the ground-state is that of the Haldane $S = 0$ singlet. Transitions between the $S = 0$ singlet and $S = 1$ triplet are forbidden by momentum conservation [157] and are not observed in the ESR spectrum of $\mathrm{NiI_2}$(3,5-lut)$_4$. The dominant feature of the low-temperature data is indicated by the green arrows in Figure 4.6(b). This feature is ascribed to $S = 1/2$ end-chains, similar to that observed in the Haldane chain system NENB [158], which form due to dislocations and grain boundaries within the polycrytalline powder. The

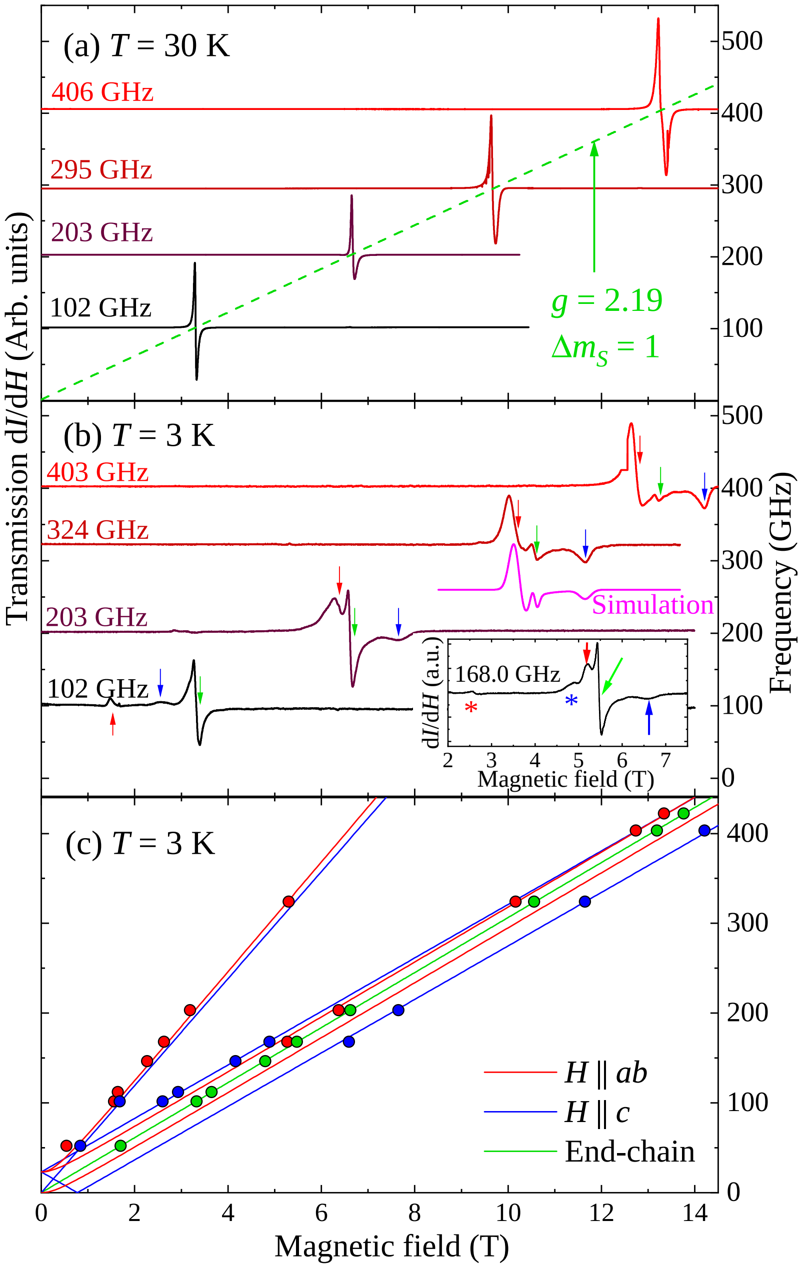

Figure 4.6: Frequency dependence of the electron-spin resonances for powder $NiI_2(3,5\text{-lut})_4$ at 30 K (a) and 3 K (b) with the inset of (b) showing the 168.0 GHz transmission spectra. (c) Position of the resonance observed at 3 K upon increasing field. Half-field transitions ($\Delta m_s = \pm 2$), which are denoted as asterisked peaks in the inset of (b), are seen to increase rapidly in frequency with increasing field. Resonances corresponding to transitions within the triplet-state, outlined within Figure 4.7, are denoted with red and blue arrows whilst the central branch, which corresponds to spin-half end-chain resonances, is denoted with green arrows. Solid lines are fits as described in main text.

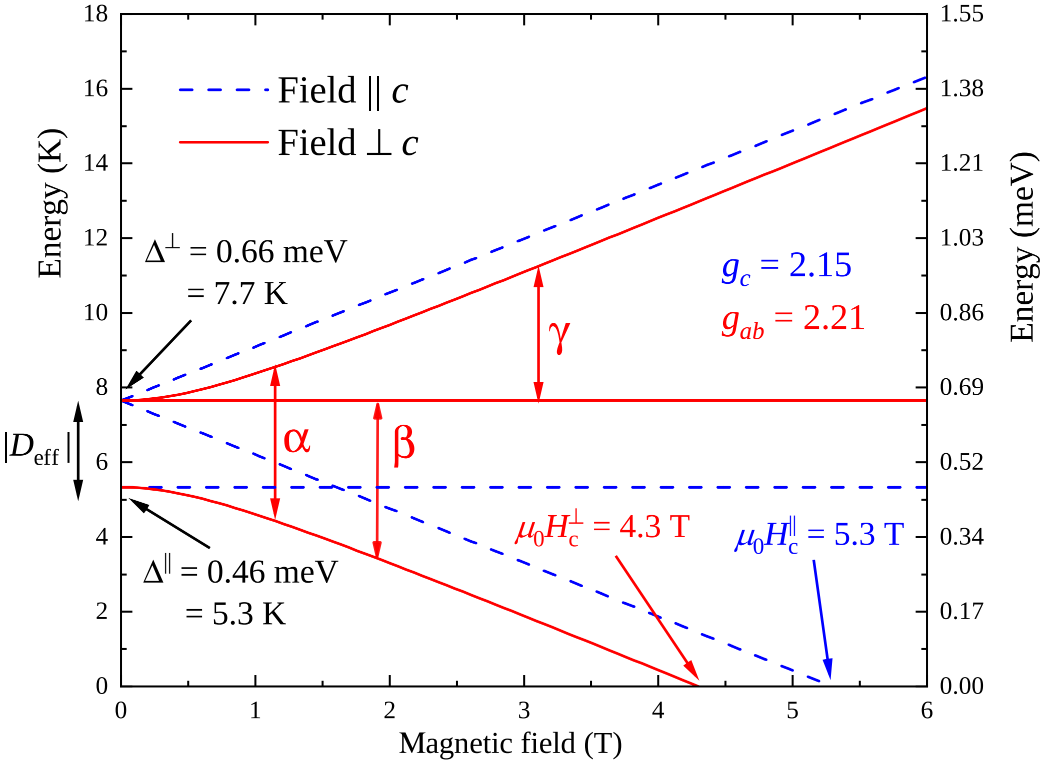

Figure 4.7: Field dependence of the SIA split Haldane energy-levels modelled within the fermion picture. The values of the anisotropic critical fields and Haldane-gaps are derived from the single-crystal magnetometry and INS, respectively. The g-factors used are those determined within the fermion picture in Table 4.1 which satisfy Eq. 4.3 and Eqs. 4.4. Transitions between the SIA split triplet energy-levels are labelled α, β and γ. The value of the effective SIA $D_{\mathrm{eff}} = +2.4(2)$ K, determined from Eq. 4.3, is also labelled.

magnitude of this resonance decreases for fields above $\overline{H}_{\mathrm{c}}$ due to the depopulation of the Haldane ground-state as the Zeeman interaction brings the energy of a triplet-state below that of the $S = 0$ singlet. The decrease in magnitude of this feature upon closure of the Haldane gap precludes it originating from free impurity $\mathrm{S} = 1$ spins, which would be unaffected by the closure of the Haldane gap. In addition, if the resonance were attributable to isolated axially-elongated Ni(II) octahedra, the resonance would not extrapolate through the origin due to the presence of the Ising SIA. Figure 4.6(c) tracks the linear field dependence of this resonance (green circles). Modelling this resonance as an isotropic $S = 1/2$ moment returns $g = 2.191(4)$ which is in excellent agreement with the bulk value determined for $S = 1$ Ni(II) moments at high temperature of $g = 2.19(1)$.

Either side of the central spin-half resonance are two satellite resonances, indicated in Figures 4.6(b) and 4.6(c) by blue and red arrows and circles. To understand these satellite resonances, it is useful to consider the field-dependence of the transitions within the triplet $S = 1$ state above the Haldane $S = 0$ ground state. For field applied within the ab-plane ($\perp c$) the energy-transitions within the triplet are labelled β and γ within Figure 4.7. Additionally the half-field transitions which are also observed in the ESR spectra, $\Delta m_s = \pm 2$ [159], are denoted with an α in Figure 4.7.

Below the critical field, the excitations between the triplet states are minimal such that the satellite peaks they correspond to are small in amplitude in Figure 4.6(b). Above the critical field, the Zeeman interaction forces the triplet-state lower in energy than the singlet state such that it becomes the ground-state of the system. This leads to a drastic increase in the amplitude of these satellite resonances due to the population of the triplet state. By considering the characteristic line shapes for powder ESR spectra [160] (i.e., a peak-like line shape is characteristic of resonances with field parallel to the unique-axis, $H \parallel z$, whilst a peak derivative line shape is characteristic of resonances with $H \perp z$; see section 2.6) the resonances for field along c, denoted with blue arrows, and transitions for the field within the ab-plane, denoted with red arrows, in Figure 4.6(b) can be identified.

The frequency-field dependencies for these transitions are seen Figure 4.6(c) with the same colour coding scheme as used in Figure 4.6(b). As expected, the half-field transitions, denoted with α in Figure 4.7, have twice the gradient of the $\Delta m_s = \pm 1$ transitions. The frequency dependence for the resonances can be fit using the fermion model, solid blue and red lines Figure 4.6(c), which within an Ising system reduces to the model of a free $S = 1$ ion with D_{eff} [159]. The fit returned parameters of $g_{\parallel} = g_c = 2.13(1)$ and $g_{\perp} = g_{ab} = 2.19(1)$, and an easy-plane effective SIA parameter $D_{\text{eff}} = +1.11(6)$ K, which, by looking at Eq. 4.3, results in a easy-axis anisotropy of $D = -0.56(1)$ K, of the same order as determined from INS. Using the parameters determined from the fitting, a simulated spectrum at $\nu = 324$ GHz is shown in Figure 4.6(b), where it can be seen that the simulation captures the measured response very well.

4.2.6 Discussion

INS and single-crystal $M(H)$ measurements directly measure the size of the anisotropic Haldane gaps ($\Delta^{\parallel}, \Delta^{\perp}$) and critical-fields ($H_c^{\parallel}$, $H_c^{\perp}$), respectively. In order to test the validity of the boson and fermion models in describing these anisotropic parameters in NiI_2(3,5-lut)$_4$, Eqs. 4.4 and 4.5 can be used to estimate g-factors and then compare the results with g-factor values determined using ESR and $\chi(T)$ measurements, as shown in Table 4.1.

Both the fermion and boson model predict identical values of $g_{\parallel} = 2.15(5)$, which is the measured g-factor with field parallel to the crystallographic c-axis. However, they differ in their predicted values for $g_{\perp}$, with field applied perpendicular to the Ni—I $\cdots$ I—Ni chain. The fermion model returns $g_{\perp} = 2.21(6)$, which is close to what is expected for a Ni(II) ion [13, 15] and in line with other techniques, whilst the boson model returns a much reduced $g_{\perp} = 1.85(6)$. Therefore, the fermion model is found to most aptly describe the behaviour of $\mathrm{NiI_2(3,5\text{-}lut)_4}$ within the Haldane-phase, implying that this model need not exclusively describe easy-plane Haldane systems, as has been posited in previous literature [148, 149].

Magnetometry measurements are able to determine the value of the intrachain magnetic exchange to be $J = 17.5(2)$ K, whilst INS measurements estimate an isotropic Haldane-gap value of $\Delta_0 = 7.0(1)$ K. This gives a ratio of $\Delta_0/J = 0.40(1)$ which is exceedingly close to the idealised value of 0.41 [34]. A value of $D/J = -0.07(1)$ also makes $\mathrm{NiI_2(3,5\text{-}lut)_4}$ relatively close to isotropic compared to other Haldane systems, whilst the lack of long-range ordering down to $T = 20$ mK suggests negligible interchain interactions, such that the chains must be very well isolated due to the bulky lutidine ligands. This places $\mathrm{NiI_2(3,5\text{-}lut)_4}$ deep within the Haldane-phase for $S = 1$ Q1D AFM systems [34] as seen in Figure 4.1. In addition, ESR and INS data both indicate the existence of $S = 1/2$ end-chain excitations, predicted to exist in Haldane spin-chains by the AKLT model [152].

As can be seen for the selected materials in Figure 4.1, only the compound $\mathrm{AgVP_2S_6}$ is closer to the origin, and therefore resides deeper in the Haldane phase, than $\mathrm{NiI_2(3,5\text{-}lut)_4}$ as a result of a minimal $D/J = 0.006$; where $J = 780$ K and $D = 4.5$ K [55]. However, the large J within $\mathrm{AgVP_2S_6}$ results in critical fields which are estimated to be on the order of $H_\mathrm{c} \sim 200$ T, far beyond what is considered experimentally accessible. The critical fields for $\mathrm{NiI_2(3,5\text{-}lut)_4}$ are, however, well within the experimentally accessible regime for more standard measurement

Theory/Measurement	$g_{\parallel} = g_c$	$g_{\perp} = g_{ab}$	g_powder
Fermion model	2.15(5)	2.21(6)	2.19(4)
Boson model	2.15(5)	1.85(6)	1.95(4)
ESR	2.13(1)	2.19(1)	2.191(4)
$\chi(T)$	-	-	2.2(1)

Table 4.1: Comparison of g-factors determined within the fermion, Eqs. 4.4, and boson, Eqs. 4.5, pictures as derived from $\Delta^{\parallel,\perp}$ and $H_\mathrm{c}^{\parallel,\perp}$ measured directly using INS and single-crystal magnetisation, respectively. The calculated powder-average value, $g_\mathrm{powder} = (g_{\parallel} + 2g_{\perp})/3$, for each model is compared to the values extracted from electron-spin resonance (ESR) and magnetic susceptibility $\chi(T)$ data.

techniques; i.e., $\overline{H}_{\mathrm{c}} \approx 4.4(2)$ T, well within the regime of laboratory-based superconducting magnets, whilst the upper critical of $H_{\mathrm{s}}^{\perp} = 50.7(8)$ T is readily accessed by pulsed magnetic fields. This, alongside the highly tunable nature of molecular systems, make $\mathrm{NiI_2(3,5\text{-}lut)_4}$ an ideal testing ground to study the effect bond disorder has on Haldane systems, something that, to date, has been primarily investigated theoretically due to the dearth of suitable materials [161, 162].

Furthermore, as the Haldane gap is closed at relatively low fields, $\overline{H}_{\mathrm{c}} \approx 4.4(2)$ T, $\mathrm{NiI_2(3,5\text{-}lut)_4}$ is a prime candidate for investigating field-induced excitations present in Haldane systems upon closure of the gap. In addition, the low-energy scales of the magnetic parameters, coupled with compressible nature of the molecule-based systems, open up the possibility of traversing the $S = 1$ AFM phase-diagram by introducing pressure as an external tuning parameter. The following sections explore both of these intriguing possibilities.

4.2.7 In-field inelastic neutron scattering

Powder INS measurements were performed on $\mathrm{NiI_2(3,5\text{-}lut)_4}$ in an applied magnetic-field in order to directly observe the field-induced closing of the Haldane-gap and the possible emergence of any in-field excitations in the system, the results of which are shown in Figure 4.8. INS data collection was performed by myself with the assistance of beamline scientist D. Voneshen on the direct geometry time-of-flight spectrometer LET, ISIS, UK. Magnetic fields were attained using an 8.8 T wide-angle cryomagnet.

Selected INS spectra are plotted in Figure 4.8(a) as a $(|Q|, E)$ heat-map after subtracting a ZF background measured at 10.5 K with the 8.8 T wide-angle cryomagnet in place. At ZF, an excitation at $E \approx 0.7$ meV, corresponding to neutrons scattering from two degenerate energy bands $\Delta^{\perp}$, is again observed as in Figure 4.4(c). Upon increasing field the intensity of this band decreases and is extinguished by 4.3 T, close to $\overline{H}_{\mathrm{c}} = 4.4(2)$ T determined from magnetometry measurements. In addition, a new excitation band emerges at an applied field of ≈ 2 T, which arises from the quasi-elastic line and moves linearly to higher energies upon increasing field. Of note, is the apparent absence of the ZF excitation observed at $E \approx 0.5$ meV, which originates from neutrons scattering from the single energy mode $\Delta^{\parallel}$; see Figure 4.4(c).

Figure 4.8(b) shows an energy-cut of both ZF measurements with and without the wide-angle cryomagnet in place, where the peak centred around ≈ 0.5 meV cannot be resolved for the measurement with the magnet in place (green data). Both INS measurements were performed on the same sample approximately one year apart, with the ZF measurements performed first and the in-field measurements performed second. As such, sample degradation is considered a possible cause for the difference in the two ZF spectra.

To investigate this, powder $\chi(T)$ measurements, performed just prior to the first and second INS experiment, were analysed. INS and $\chi(T)$ measurements were not performed on the very same sample, but the sample used in each measurement did originate from the same batch [samples used in $\chi(T)$ measurements had not been exposed to neutrons]. The inset of Figure 4.8(b) shows $\chi(T)$ data collected just before the first INS measurement (blue) exhibits a reduced low-temperature upturn compared to $\chi(T)$ data measured just before the second (green) INS measurement. This suggests a $\sim 1\%$ increase in the number of end-chain and free spins in the system, determined by fitting the data to Eq. 4.6 (solid red lines).

The effect of introducing end-chains into a Haldane systems has been studied in the Mn-doped Ising-like Haldane chain $Y_2BaNi_{x-1}Mg_xO_5$ [56]. Here, doping serves to introduce more chain breaks in the sample which leads to a greater distribution in the chain-lengths, the consequence of which is an attenuation of the INS spectrum and a lengthening of the high-energy tail. Looking at Figure 4.8(b), the 2.0 K data, measured second with the magnet in place, is attenuated and exhibits a longer high-energy tail compared to the 1.8 K data, measured first without the magnet in place; this is consistent with the observations made in [56]. Therefore, it is possible that the difference in the two spectra is due to an increase in the distribution of chain lengths, owing to the sample batch having degraded slightly between the two INS measurements. A plot of the attenuated spectra for NiI_2(3,5-lut)$_4$ and $Y_2BaNi_{x-1}Mg_xO_5$, taken from [56], is shown in Figure 4.9 for comparison.

Another possibility is that the in-field measurement was in fact performed at a temperature much higher than 2.0 K, due to miscalibrated instrument thermometry, leading to thermal fluctuations smearing out the excitation spectrum. Comparing the temperature dependence of the ZF spectra in Figure 4.8(b), the data would be consistent with the measurement actually being performed at ≈ 4 K. Investigations are underway to ascertain the likeliness of this scenario, however, the in-field behaviour of the spectra can still be examined despite the lower resolution of the in-field dataset compared to the data in Figure 4.4.

Figure 4.8(c) shows that upon increasing field, the excitation corresponding to the higher energy Haldane-gap $\Delta^{\perp}$ appears to be suppressed in intensity, being completely extinguished by $H = 4.3$ T in agreement with the $\overline{H}_{\mathrm{c}} = 4.4(2)$ T. In similar field-dependent INS studies on the Haldane compounds NDMAP, NDMAZ and NENP [57–59, 163], the Zeeman interaction serves to drive the SIA-split triplet-states further apart in energy. Similar results might be expected for NiI_2(3,5-lut)$_4$,

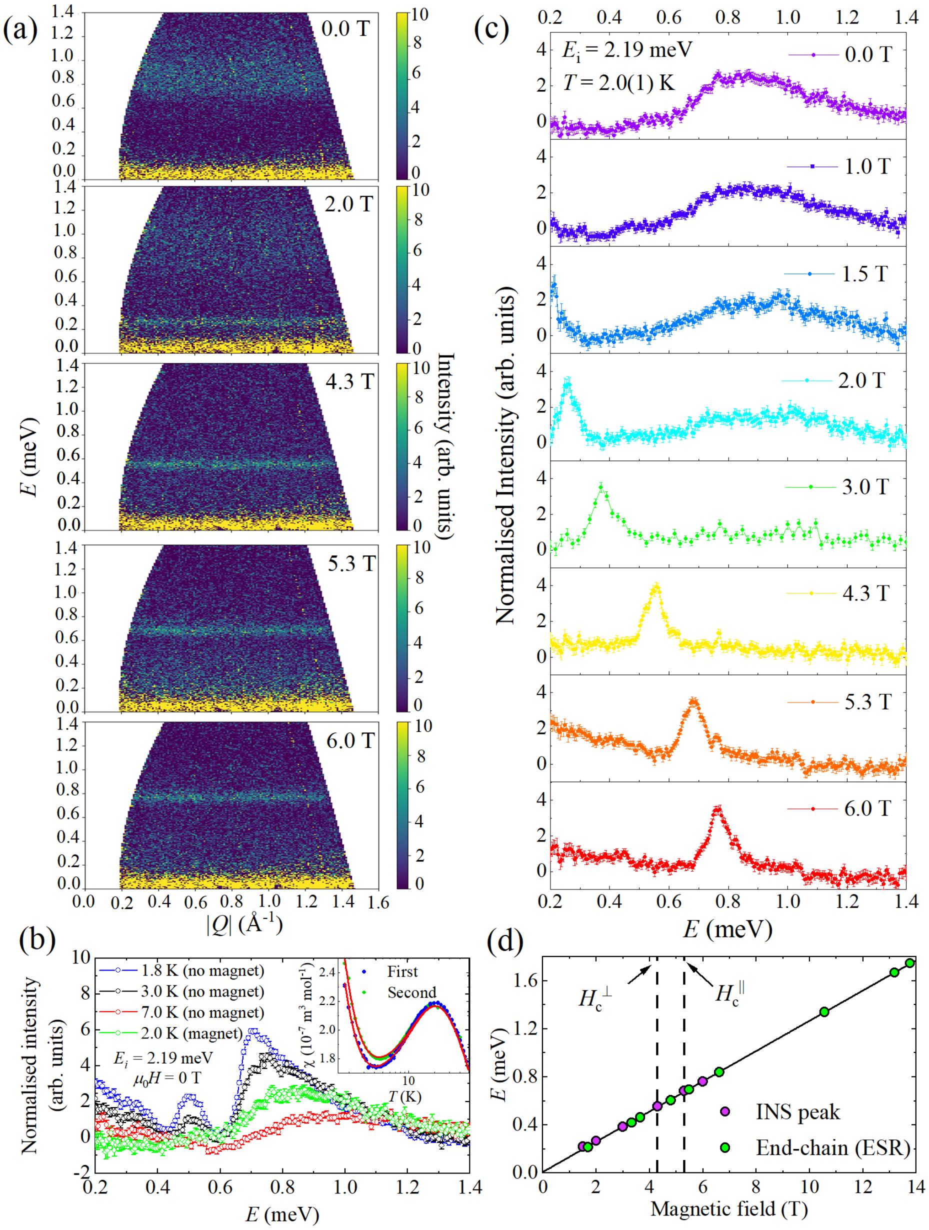

Figure 4.8: INS spectrum for powder $\mathrm{NiI_2(3,5\text{-}lut)_4}$ in an applied magnetic field with data presented as $|Q|, E$ heat-maps (a) and energy cuts obtained by integrating data over the full measured $|Q|$-range with incident neutron energy $E_i = 2.19$ meV in (a), (b) and (c). (b) Comparison of ZF energy-cuts with and without the presence of a wide-angle cryomagnet. Inset compares low-temperature upturns in the magnetic susceptibility for the same batch of sample measured one year apart, as discussed in text. Solid lines are fits to Eq. 4.6. (d) Comparison of in-field position of INS excitation observed in (c) and end-chain excitations as determined by ESR (see section 4.2.5). Solid line is a linear fit of both datasets to an isotropic $S = 1/2$ model, position of the anisotropic critical fields are marked with dashed-lines and arrows.

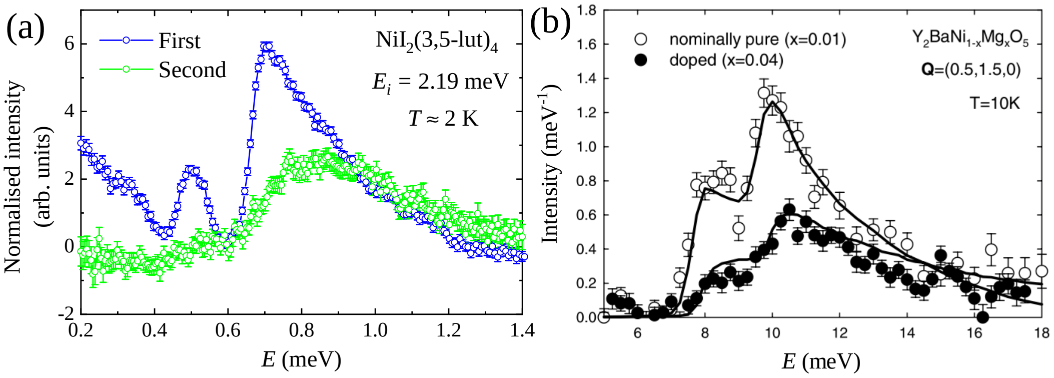

Figure 4.9: Comparison of the attenuation of the INS spectrum observed in NiI$_2$(3,5-lut)$_4$ with the 'first' measurement taken one year prior to the 'second' in (a), with that observed in the doped Haldane chain material Y$_2$BaNi$_{x-1}$Mg$_x$O$_5$ (b) extracted from reference [56]; see main text for details.

with the triplet-states varying in accordance with the field-dependence of the energy-levels outlined in Figure 4.7. The powder nature of the sample implies a greater statistical weight is given to excitations occurring with $H \parallel ab$. At 2 T, Eqs. 4.4 would imply that, for $H \parallel ab$, the triplet energy-levels within $\Delta^{\perp}$ are split by $\approx$ 0.17 meV. Inspecting the 2 T spectra in Figure 4.8(c), it is clear the intensity of the hump is greatly diminished, likely due to the field-induced splitting of the triplet-states within $\Delta^{\perp}$, with the feature now spreading over an approximately 0.2 meV energy range. Whilst the data do qualitatively show the apparent diminishing of the $\Delta^{\perp}$ excitation, the attenuation of the spectrum (owing to the introduction of end-chains or for experimental reasons) and powder nature of the sample both limit the resolution of the measurement, such that the field-dependence of the SIA split energy-levels cannot be easily quantified.

A new excitation emerges in the spectrum for $H \geq 1.5$ T, see third panel of Figure 4.8(c). Upon increasing field, this excitation moves linearly to higher energies and is still present for fields above $\overline{H}_{\rm c}$. The appearance of an excitation in an applied field has also been observed in NDMAP [58], however, in NDMAP this feature is due to a new magnetic Bragg-peak arising as the system enters a long-range AFM ordered phase upon closure of the Haldane-gap. For NiI$_2$(3,5-lut)$_4$, the existence of this feature below the gap, where the system lacks long-range magnetic order, means this feature cannot be ascribed to a new magnetic Bragg-peak. An excitation with similar field dependence for $H < \overline{H}_{\rm c}$ is observed in the Haldane system Y$_2$BaNi$_{x-1}$Mg$_x$O$_5$ [56], and is attributed to the excitation of end-chain spins.

Tracking the position of the excitation with increasing magnetic field, the feature is found to agree exceedingly well with ESR resonances attributed to $S = 1/2$

end-chains as shown in Figure 4.8(d). A linear fit to both datasets using an isolated $S = 1/2$ moment model returns $g = 2.173(1)$ in excellent agreement with other techniques. Therefore, the peak is ascribed to excitations of $S = 1/2$ end-chains in the system observed through 'neutron ESR' measurements as in [56] and similar to excitations observed in the Haldane system NENB [158].

4.2.8 High-pressure magnetometry

Quasistatic magnetometry measurements were performed on powder samples of $\mathrm{NiI_2(3,5\text{-}lut)_4}$ under increasing hydrostatic pressure at the University of Warwick by myself. Pressure was attained using a Quantum-Design MPMS high-pressure cell with pressure determined by tracking the pressure dependence of the superconducting transition temperature of a Sn manometer.

Figure 4.10(a) shows the pressure dependence of the magnetisation for powder $\mathrm{NiI_2(3,5\text{-}lut)_4}$ measured at $T = 1.8$ K; the lowest accessible temperature for this experimental set up. Upon increasing pressure, the low-field $M(H)$ response is qualitatively unchanged from the ambient data [see also Figure 4.3(b)], rising smoothly before beginning to flatten for fields $1 \leq \mu_0 H \lesssim 2.5$ T, such that the data still resemble a paramagnetic response from an ensemble of $S = 1/2$ ions. This low-temperature low-field $M(H)$ is due to a combination of paramagnetic $S = 1/2$ end-chains plus background signal originating from the pressure-cell, however, the sizable increase in the sample moment near $\overline{H}_\mathrm{c}$ (see Appendix) indicates the upturns in $M(H)$ can be attributed solely to the sample.

For fields $\mu_0 H > 2.5$ T, the characteristic upturn in $M(H)$, attributed to the closing of the Haldane energy-gap Δ_0 at $\overline{H}_\mathrm{c}$, is seen to move to higher fields upon increasing pressure. This upturn becomes hard to distinguish above 4.4 kbar and moves well beyond 7 T by ≈ 6.9 kbar. At 1.8 K, a peak in $\mathrm{d}^2M/\mathrm{d}H^2$ could not be readily distinguished for $M(H)$ data in Figure 4.10(a). However, the pressure dependence of $\overline{H}_\mathrm{c}$ can be determined via linear extrapolation of the data near the upturn feature in $M(H)$, a method used to ascertain critical field values in similar Haldane systems [89, 147], as seen in the inset of Figure 4.10(a). At 4.4 kbar this method estimates $\overline{H}_\mathrm{c} = 5.9(5)$ T. Beyond this pressure the paucity of data points above the upturn in $M(H)$ means $\overline{H}_\mathrm{c}$ could not be reliably extracted. However, the continued motion of the upturn to higher fields above 4.4 kbar qualitatively indicates that the magnitude of $\overline{H}_\mathrm{c}$ (and by extension Δ_0 and J as $\Delta_0 = 0.41J$) increases. Whilst it is possible increasing pressure may have an affect on the sign and strength of D (or indeed introduce an E-term) within the system, Eqs. 4.4 and Eq. 4.3 dictate that the sizable increase in $\overline{H}_\mathrm{c}$ cannot be accomplished by changing D alone, and

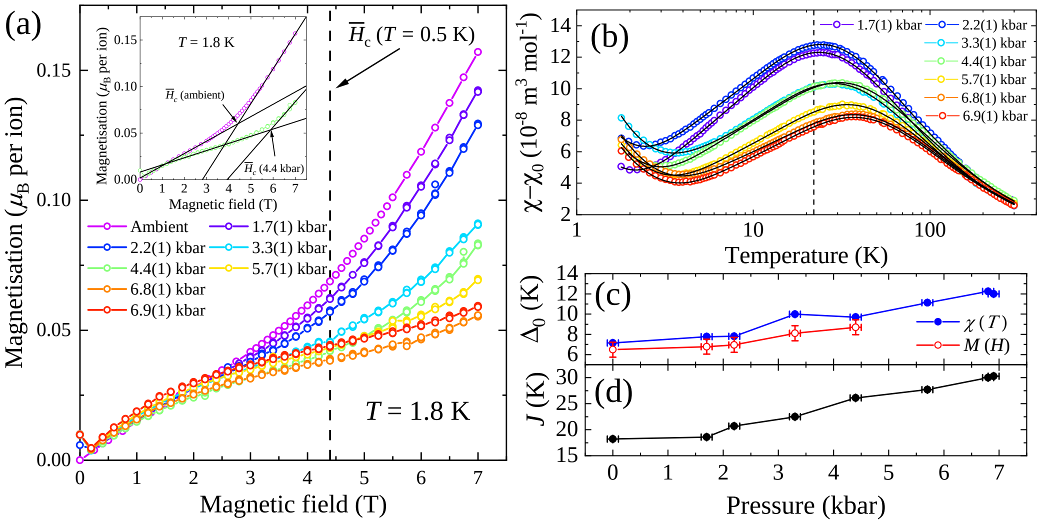

Figure 4.10: Quasistatic magnetometry of powder $\mathrm{NiI_2(3,5\text{-}lut)_4}$ measured under increasing hydrostatic pressure. (a) Magnetisation $M(H)$ up to 6.9(1) kbar, powder-average critical-field $\overline{H}_{\mathrm{c}} = 4.4(2)$ T extracted from inset Figure 4.3(b) indicated with dashed line. Inset shows $\overline{H}_{\mathrm{c}}$ extracted by linear extrapolation method (see text). (b) Powder magnetic susceptibility $\chi(T)$, after subtracting temperature-independent χ_0 term (see text) measured at $\mu_0 H = 0.1$ T. Solid lines are fits to Eq. 4.6 and dashed line marks the position of the hump in ambient $\chi(T)$. (c) Pressure dependence of powder-average Haldane-gap (Δ_0) extracted from $\chi(T)$ (filled circles) and $M(H)$ (open circles). (d) Pressure dependence of the intrachain exchange J extracted from fitting $\chi(T)$ data.

must therefore be primarily a result of an increase in the magnitude of J.

Figure 4.10(b) shows the effect of increasing pressure on the magnetic susceptibility $\chi(T)$ of $\mathrm{NiI_2(3,5\text{-}lut)_4}$. At each pressure, $\chi(T)$ can be well modelled using Eq. 4.6 with the addition of a small temperature-independent χ_0 term. The g-factors extracted from the fit (for $P > 0$ kbar) are well below what is typical for Ni(II) [14], with an average $g = 1.7(3)$ over all pressures. This is likely due to imperfect background subtraction within $\chi(T)$ data, as a small component of the background signal leaches into the measured response, reducing the magnitude of $\chi(T)$, and by extension g, see Figure A.1(b) located in the Appendix. Subtracting χ_0, which models this small remnant component of the background from pressure-cell, from $\chi(T)$ data and refitting, data in Figure 4.10(b), leaves the fit parameters Δ_0 and J unchanged. However, it does permit the resultant $\chi(T)$ curves to converge at high temperatures, as expected within the paramagnetic regime. An average $\rho = 0.9(1)\%$ over all pressures (modelling the low-temperature upturn as a spin-half paramagnetic response) is in reasonable agreement with ambient $\chi(T)$ data where $\rho = 1 - 3\%$; see section 4.2.2.

Whilst g-factors could not be reliably extracted, Figure 4.10(b) clearly shows the hump in $\chi(T)$ move to higher temperatures upon increasing pressure; parameterised by J and Δ_0 in Eq. 4.6. The extracted values of J and Δ_0 are shown in Figures 4.10(c) and 4.10(d) with both parameters seen to increase upon increasing pressure, in good agreement with $M(H)$ data. At 5.7 kbar, the fit returns $\Delta_0 = 11.1(1)$ K, equivalent to $\overline{H}_\mathrm{c} = 7.5(1)$ T found using the powder-average g-factor from ESR. Again this agrees with $M(H)$, which indicates that by 5.7 kbar $\overline{H}_\mathrm{c}$ moves beyond the maximum experimentally accessible field of 7 T.

4.2.9 Discussion

Powder in-field INS data show the closure of the Haldane-gap around 4.3 T, close to $\overline{H}_\mathrm{c}$ determined from other techniques. The powder nature of the sample, in addition to possible sample degradation and some uncertainty in the thermometry, makes quantifying the exact field-dependence of the SIA-split energy levels difficult. However, the emergent excitation for fields ≥ 1.5 T can be ascribed to end-chain excitations, where the field dependence of this excitation is in excellent agreement with resonances observed in ESR data also attributable to $S = 1/2$ end chains.

The observation of this $S = 1/2$ resonance for $H \geq \overline{H}_\mathrm{c}$, also observed in an ESR study of the Haldane compound NENB [158], is not necessarily expected. As the singlet-triplet energy gap closes at $\overline{H}_\mathrm{c}$, the Haldane ground-state is quickly depopulated for $H > \overline{H}_\mathrm{c}$, and, as such, one might expect the $S = 1/2$ end-chains associated with this phase to also vanish, as the system enters a gapless Tomonaga-Luttinger liquid (TLL) phase [60] for $\overline{H}_\mathrm{c} < H < H_\mathrm{s}$. A similar resonance is seen in the ESR spectra of the Q1D strong-leg spin-ladder system DIMPY [164], which also enters a TLL phase above a critical field $H_\mathrm{c} = 2.8$ T. The resonance in DIMPY originates from transitions within an excited triplet state and, like the spin-half resonance observed in $\mathrm{NiI_2(3,5\text{-}lut)_4}$, intercepts the frequency-field plane at the origin indicating negligible ZFS. Therefore, it is possible that the emergent resonance in $\mathrm{NiI_2(3,5\text{-}lut)_4}$ also originates from excitations within a triplet (possibly due to interacting $S = 1/2$ end-chains). To investigate this, further measurements, such as temperature dependent ESR, are planned. However, for now, the question of whether $\mathrm{NiI_2(3,5\text{-}lut)_4}$ exhibits spin-half excitations that survive above the closure of the Haldane-gap remains tantalisingly open.

Initial pressure studies on $\mathrm{NiI_2(3,5\text{-}lut)_4}$ indicate that increasing hydrostatic pressure, up to 6.9(1) kbar, serves to push the compound deeper into the Haldane phase due to an increase in the size of Δ_0, as outlined in Figure 4.10(c). The rate of change of J with pressure ($\mathrm{d}J/\mathrm{d}P$) observed in $\mathrm{NiI_2(3,5\text{-}lut)_4}$ is $\mathrm{d}J/\mathrm{d}P \approx$

2.1(1) K/kbar, with the magnitude of J increasing by $\approx 64\%$ when moving from ambient pressure to $P = 6.9(1)$ kbar. This pressure dependence is very close to that observed in the similar, molecule-based, Haldane chain NDMAP where $\mathrm{d}J/\mathrm{d}P \approx$ 2 K/kbar [165]. NDMAP is composed of Ni—N—N—N—Ni chains where the N—N—N bond angles close to 180°. It is suspected that the increase in J in NDMAP is due to a decrease in the N—N—N bond angles. Comparatively, for $\mathrm{NiI_2(3,5\text{-}lut)_4}$ it would be expected that the through-space distance between adjacent I-ions $\mathrm{I} \cdots \mathrm{I}$ is the most compressible section of the structure. As such, the increase in J is most likely due to an increased overlap of the magnetic orbitals along the $\mathrm{Ni—I} \cdots \mathrm{I—Ni}$ direction, as the increasing pressure reduces the $\mathrm{I} \cdots \mathrm{I}$ distance.

It is possible that increasing pressure may also increase J'. However, given that no magnetic ordering is observed in ambient ZF μ^+SR data down to 20 mK, the energy-scale of J' should remain well below that of J even at 6.9(1) kbar, such that $J'/J << 1$ and the system remains firmly within the Haldane phase. Additionally, there is the possibility increasing pressure also alters the local $\mathrm{NiI_2N_4}$ octahedral environment. This change may be accompanied by a change in the sign and strength of D as well as an introduction of an E-term in Eq. 4.1. However, as outlined in section 4.2.8, the observed increase in $\overline{H}_\mathrm{c}$ cannot be accounted for changing D exclusively, such that the Haldane state is expected to be preserved at 6.9(1) kbar. Verifying the above hypothesis would of course require a detailed study of the structural changes induced by increasing hydrostatic pressure.

4.3 Summary

The compound $\mathrm{NiI_2(3,5\text{-}lut)_4}$ has been characterised using a variety of measurement techniques and found to be a near-ideal Haldane spin-chain, with intrachain exchange mediated along linear $\mathrm{Ni—I} \cdots \mathrm{I—Ni}$ through-space pathways which propagate along the c-axis. By comparing the measured values of the anisotropic Haldane-gaps and critical fields to two quantum-field-theoretical models, $\mathrm{NiI_2(3,5\text{-}lut)_4}$ shows that the fermion model, previously posited to exclusively describe easy-plane Haldane spin chains, is also applicable to easy-axis Haldane systems. This is in contrast to previous literature [148, 149], where J' is critically large (the system is close to 3D AFM order) and the boson model appears more consistent with experiment. Hence, the work suggests it is not the nature of the anisotropy that determines the applicability of the boson or fermion model, but J'. However, the influence J' has on the critical field scaling is yet to be quantified.

In-field INS studies show the emergence of a new excitation for fields above

1.5 T, the field dependence of which agrees extremely well with resonances within the ESR spectrum ascribed to $S = 1/2$ end-chains. The existence of this feature for $H > \overline{H}_{\mathrm{c}}$ may suggest the surprising survival of end-chain spins upon the closure of the Haldane gap. Whilst some work is still required to uncover the exact nature of the excitation, ESR and current INS data are compelling that the excitation is attributable to isotropic $S = 1/2$ moments. Further theoretical modelling of the data are planned in order to elucidate the origin of this novel excitation.

Additionally, the low-energy scales of the J and Δ_0 make $\mathrm{NiI_2(3,5\text{-}lut)_4}$ a prime candidate to study the effect pressure has on Haldane spin-chains, demonstrated by the large increase in J of $\mathrm{d}J/\mathrm{d}P \approx 2.1(1)$ K/kbar; similar to $\mathrm{d}J/\mathrm{d}P \approx 2$ K/kbar in the known molecule-based Haldane chain NDMAP. This increase in J is accompanied by a corresponding increase in the Haldane-gap by ≈ 5 K from ambient at 6.9 kbar, indicative that increasing pressure serves to make the Haldane ground-state more robust. This is likely due to a decrease in the $\mathrm{I}\cdots\mathrm{I}$ distance, however, single-crystal x-ray diffraction measurements under pressure are needed to confirm this hypothesis. Further application of pressure may serve to increase or decrease D and introduce a sizable J' within $\mathrm{NiI_2(3,5\text{-}lut)_4}$. An increase in D and J' is suspected to be the cause of the introduction of a paramagnetic moment orientated within the easy-plane of NDMAP above ≈ 9 kbar of pressure [165]. Therefore, if similar could be observed in $\mathrm{NiI_2(3,5\text{-}lut)_4}$ it may indicate that the system is amenable to pressure tuning the sign and strength of D and J', allowing $\mathrm{NiI_2(3,5\text{-}lut)_4}$ to traverse the Q1D $S = 1$ AFM phase diagram.

Chapter 5

Quantum phase transitions in spin-half dimers

5.1 Introduction

This chapter will outline the magnetic properties of the antiferromagnetically coupled, asymmetric spin-half dimer material $\mathrm{CuVOF_4(H_2O)_6{\cdot}H_2O}$ [Cu(II) ($3d^9$) and V(IV) ($3d^1$)] at ambient pressure. Alongside this, the pressure-evolution of the structural and magnetic properties of both $\mathrm{CuVOF_4(H_2O)_6{\cdot}H_2O}$ and the symmetric dimer system $\mathrm{[Cu(pyz)_{0.5}(gly)]ClO_4}$ are tracked.

Cooperative phenomena in materials known to exhibit QCPs have been the subject of consistent interest in condensed matter systems [23, 166, 167]. In particular, systems of AFM coupled $S = 1/2$ dimers have been known to exhibit two magnetic-field induced phase-transitions; the first of which, at least, involves the system passing through a QCP which, should the rotational symmetry of the system be preserved, belongs to the BEC universality class [23]. (As the second transition involves the dimer system moving from XY-AFM to FM order, there is some debate in the community as to whether it can be classified as a true QPT as it does not involve an order to disorder transition.) The dimer system $\mathrm{[Cu(pyz)_{0.5}(gly)]ClO_4}$ studied in this chapter is one such system where the first QCP appears to belong to the BEC universality class [37, 168].

In ZF, AFM dimer systems exist in a state of quantum-disorder, the ground-state being composed of a sea of spin-singlets ($S = 0$) situated against a backdrop of quantum fluctuations. Above this singlet ground-state resides a degenerate excited triplet-state ($S = 1$), where the size of the singlet-triplet energy gap is dictated by the strength of the intradimer AFM Heisenberg exchange interaction, $J_0 > 0$. The

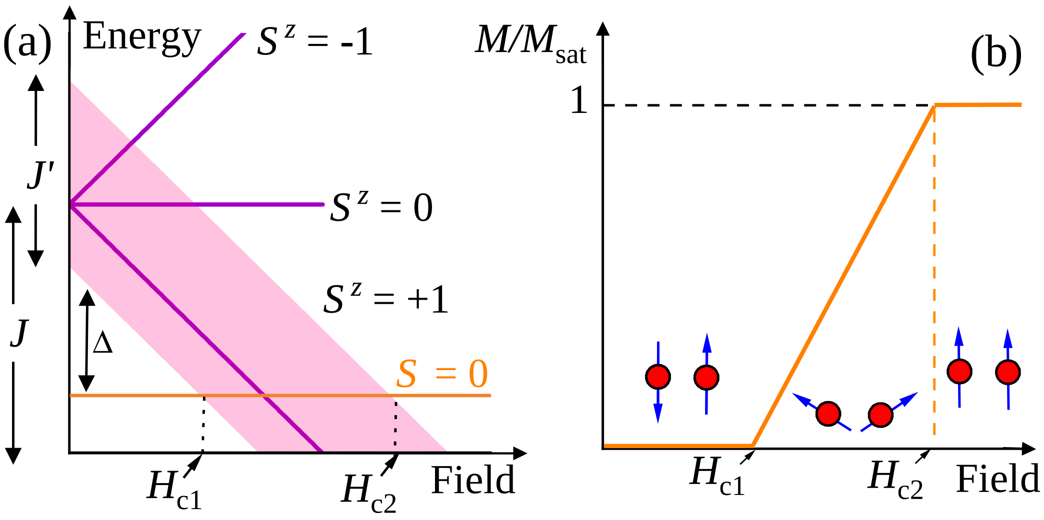

Figure 5.1: (a) Cartoon energy-level diagram for a system of weakly coupled $S = 1/2$ AFM dimers. (b) Cartoon magnetisation, at zero-temperature, of such a system as adapted from [62]. Inset of (b) presents a simplified cartoon of the orientation of dimer spins throughout the magnetisation process.

presence of any interdimer exchange J' serves to disperse the excited triplet, giving a band of excitations and reducing the size of the singlet-triplet energy gap relative to the case for an isolated dimer [see energy-level diagram in Figure 5.1(a)].

Upon application of an external field, the system moves through the first QCP, at H_{c1}, as the Zeeman interaction splits the degenerate triplet, lowering the energy of the excited $S_z = +1$ triplet-state below that of the $S = 0$ singlet ground-state, such that at H_{c1} the system undergoes a transition to a long-range XY-AFM ordered state. Further application of field eventually fully polarises the spins along the field direction, as the system enters a ferromagnetic (FM) saturated state above H_{c2}. The evolution of the energy-levels and magnetisation for a system of weakly coupled AFM dimers at zero temperature is outlined in Figure 5.1.

In order for the excited triplet-state to effectively map onto the BEC of magnons picture, the transverse component of the spins must spontaneously break the rotational $O(2)$ symmetry of the system at H_{c1} [36, 62]. Therefore, any term in the spin Hamiltonian that breaks the rotational symmetry of the system in ZF prohibits the dimer from being described within the BEC universality class [36]. Dimer systems which exhibit an excited triplet-state where the crystal structure breaks the $O(2)$ symmetry have been previously reported [169, 170], however, $CuVOF_4(H_2O)_6{\cdot}H_2O$ [171] is a dimer where the rotational symmetry is broken by the spin-species which make up the dimer-unit itself. Additionally, as detailed in reference [171], $CuVOF_4(H_2O)_6{\cdot}H_2O$ is composed of the two unlike $S = 1/2$ ions, Cu(II) and V(IV), linked via a lambda-shaped Cu—O—V bond. The formation of this Cu—O—V bond relies on the Jahn-Teller distortion of the Cu(II) octahedra, as replacing Cu(II) with other M(II) transition-metal ions (M = Ni, Zn, Co) results in the M(II) and V(IV) ions forming isolated octahedra. This chapter provides a detailed study of the magnetic properties of $CuVOF_4(H_2O)_6{\cdot}H_2O$ and demonstrates that the JT-distortion of the Cu is not only responsible for the novel structure, as outlined in [171], but also the low-dimensional magnetism in this compound.

In addition to magnetic field, the application of pressure can also serve to drive the closure of the singlet-triplet energy gap in $S = 1/2$ AFM dimers. Here, pressure typically closes the gap by increasing the ratio of the interdimer to intradimer exchange interactions, as in the model dimer compound $TlCuCl_3$ [172] and in the organic dimer $(C_4H_{12}N_2)Cu_2Cl_6$ (PHCC) [173]. As pressure closes the gap by lowering not just the $S_z = +1$ level, as is the case for an applied magnetic field, but of all the excited triplet states, the universality class of a pressure-induced QCP differs from that of a field-induced QCP [23]. For example, the pressure-induced QCP within $TlCuCl_3$ breaks the $O(3)$ symmetry of the system as the gap is closed by lowering the energy of the entire triplet, resulting in a critical exponent of 1 (Ising universality class) as opposed to the 2/3 exponent value expected for BEC class systems. To date, few dimer compounds possess a critical pressure P_c low enough to suppress the singlet-triplet energy gap to ZF [174]. In this chapter two parallel pressure-studies on the magnetic and structural properties of the dimer compounds $[Cu(pyz)_{0.5}(gly)]ClO_4$ and $CuVOF_4(H_2O)_6{\cdot}H_2O$ are outlined, where each compound exhibits a notably different response to the application of hydrostatic pressure.

Within an applied magnetic field, both $[Cu(pyz)_{0.5}(gly)]ClO_4$ and $CuVOF_4(H_2O)_6{\cdot}H_2O$ can be modelled as a lattice of weakly coupled $S = 1/2$ AFM dimers interacting via Heisenberg exchange, with the magnetic properties summarised by;

$$\mathcal{H} = J_0 \sum_i \hat{\mathbf{S}}_{1,i} \cdot \hat{\mathbf{S}}_{2,i} + \sum_{<mnij>} J'_{mnij} \hat{\mathbf{S}}_{m,i} \cdot \hat{\mathbf{S}}_{n,j} - g\mu_B\mu_0 H \sum_i \hat{S}^z_{m,i} \tag{5.1}$$

where i and j denote dimers and m, n = 1,2 label magnetic sites [62, 168]. As such, J'_{mnij} is the interdimer exchange between the sites, m and n, on adjacent dimers i and j but it labelled J' for simplicity from henceforth. It should be noted that for $CuVOF_4(H_2O)_6{\cdot}H_2O$, the dimer unit itself lacks a center of inversion symmetry and therefore suggests the possibility of an additional Dzyaloshinskii-Moriya interaction (DMI) term in the Hamiltonian of the form $\boldsymbol{D} \cdot (\mathbf{S}_1 \times \mathbf{S}_2)$. A similar DM term is suspected to emerge in $[Cu(pyz)_{0.5}(gly)]ClO_4$ at sufficiently low temperatures, where

$k_\mathrm{B}T \sim \boldsymbol{D}$, due to the structure of the system, as outlined in detail section 5.3.1 and References [37, 168].

5.2 $CuVOF_4(H_2O)_6{\cdot}H_2O$

5.2.1 Structure

Single-crystal x-ray diffraction data were by collected and refined by myself with the assistance of J. Tidey at the University of Warwick using a Rigaku Oxford Diffraction Synergy S diffractometer equipped with a HyPix-6000HE Hybrid Photon Counting (HPC) detector. Low-temperatures were attained using an Oxford Cryosystems N-Helix cryo cooling system.

Single-crystal x-ray diffraction data indicate $CuVOF_4(H_2O)_6{\cdot}H_2O$ crystallises into an orthorhombic structure with polar space-group $Pna2_1$ in agreement with [171]. The structure of $CuVOF_4(H_2O)_6{\cdot}H_2O$ is based on a lattice of weakly interacting $S = 1/2$ antiferromagneticaly (AFM) coupled dimers. The dimer-unit itself is composed of two unlike $S = 1/2$ ions, V(IV) and Cu(II), both of which reside in octahedral environments of the form VF_4O_2, Figure 5.2(a), and CuO_6, Figure 5.2(b). Figure 5.2(c) shows that the Cu(II) and V(IV) ions are linked via a kinked Cu—O—V bond [3.942(2) Å, 142.87(5)°].

The JT axis of the Cu(II) ion is co-linear with the Cu—O—V bond, such that the valence electron ($3d^9$) resides in the $d_{x^2-y^2}$ orbital orientated perpendicular to the JT-axis of the Cu(II) and therefore the Cu—O—V bond. Density functional theory (DFT) calculations (outlined in section 5.2.4) indicate the V(IV) valence electron ($3d^1$) occupies the d_{xy} orbital, which is also perpendicular to the Cu—O—V bond. It should be noted that JT-active Cu(II) systems often exhibit extreme low-dimensionality, as the reduced orbital overlap along JT direction typically leads to a strong superexchange interaction perpendicular to the JT-axis with only weak superexchange along it, such as in the quasi-two-dimensional $[Cu(HF_2)(pyz)_2]SbF_6$ [40] and quasi-one-dimensional $Cu(NO_3)_2(pyz)_3$ [42] (pyz = pyrazine = $C_4H_4N_2$) molecule-based magnets. As the magnetic orbitals of both the Cu and V lie within the plane of the equatorial ligands of each octahedral environment, one might expect that the minimal orbital overlap along the Cu—O—V bond direction would lead to the intradimer exchange coupling (J_0) being mediated along the intradimer Cu—O—H···F—V H-bond pathway, seen in Figure 5.2(c). H-bonds have previously been shown to be highly effective mediators of superexchange interactions in low-dimensional magnets, such as in $[CuF_2(H_2O)_2(pyz)]$ [175]. However, it is shown later in this chapter, that this is not the case.

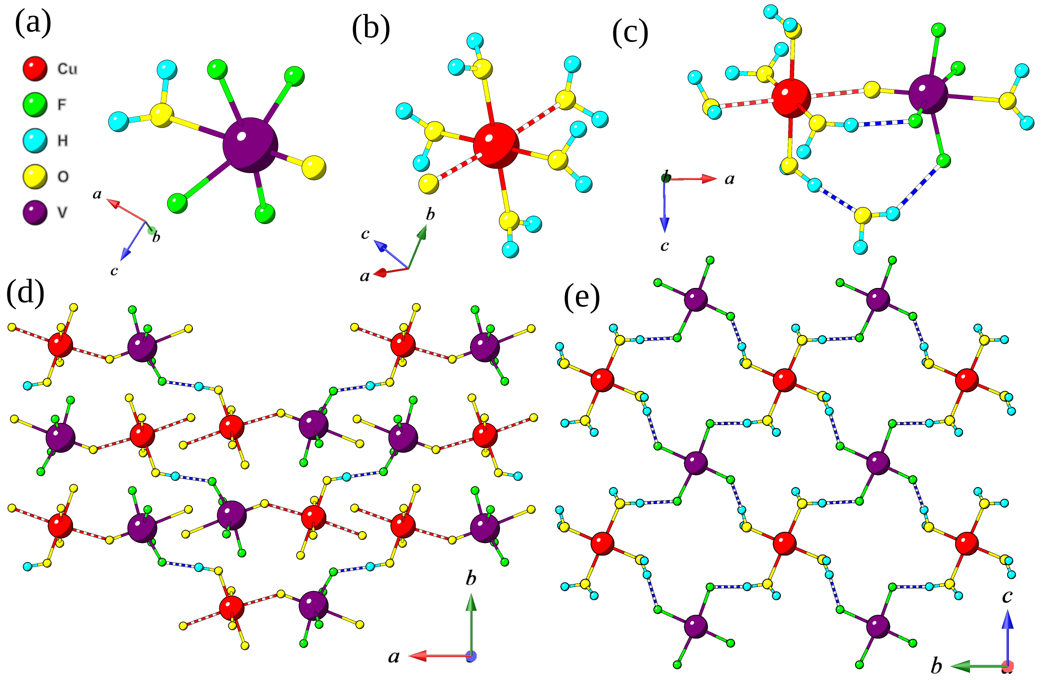

Figure 5.2: Local octahedral environment of (a) V(IV) and (b) Cu(II). Red-striped bonds indicate the Jahn-Teller (JT) axis of Cu(II) octahedra. (c) Dimer unit with intradimer H-bonds (blue-striped bonds), through equatorial ligands and uncoordinated water molecule. (d) Packing of the dimers along a showing equatorial H-bonds expected to mediate secondary interdimer exchange (J''); see text. Axial H-bonds and uncoordinated waters omitted for clarity. (e) Interdimer H-bond network within the bc-plane expected to mediate primary interdimer exchange (J'). Uncoordinated water omitted for clarity. Structure determined from single-crystal x-ray diffraction data collected at 150 K.

Weak H-bonds between the dimers form a complex 3D interdimer network, outlined in detail in [171]. Only the interdimer H-bonds between equatorial ligands are expected to mediate notable magnetic exchange, as the magnetic orbitals of both transition-metal ion species lie within the plane of the equatorial ligands, with no spin-density located on the axial water ligands of either species (see section 5.2.4). As such, the primary interdimer exchange (J') is expected to act within the bc-plane via the H-bond network shown Figure 5.2(e), with potentially weak exchange along a (J'') via the H-bonds highlighted in Figure 5.2(d), resulting in each dimer having four nearest dimer neighbours $n = 4$. It should be noted that adjacent Cu octahedra throughout the lattice are arranged in a staggered fashion (likewise for adjacent V octahedra), as seen in Figure 5.2(d), indicating the possibility of a staggered g-tensor within the system.

5.2.2 Magnetometry

Single-crystal radio-frequency susceptometry data was collected at the National High Magnetic Field laboratory, Florida, USA on the 36 T resistive magnet in Cell 12 with the support of local contact D. Graf.

Figure 5.3(a) shows the static magnetic susceptibility [$\chi(T)$] for a single-crystal of $CuVOF_4(H_2O)_6{\cdot}H_2O$ with field orientated parallel and perpendicular to the crystallographic a-axis (close to parallel with the Cu—O—V bond). Upon decreasing temperature, $\chi(T)$ data in both orientations rises to a broad hump centred around 15 K, decreases down to $T \approx 3$ K, and then exhibits a slight upturn at $T < 3$ K; behaviour typical of AFM coupled spin-half dimers. Over the measured temperature range, $1.8 \leq T \leq 300$ K, $\chi(T)$ can well described using a Bleaney-Bowers model with mean-field interactions $\chi_{\mathrm{b}}(T)$ [176, 177], of the form;

$$\chi = (1-\rho)\chi_{\mathrm{b}}(T) + \rho\chi_{\mathrm{pm}}(T) \tag{5.2}$$

where χ_{pm} models the low-temperature paramagnetic tail and ρ captures the % of the sample attributable to uncoupled $S = 1/2$ spins due to impurities, broken dimers, or, possibly arising from the staggering of the local g-tensor as seen in staggered $S = 1/2$ chains [39, 178]. $\chi(T)$ datasets were fit simultaneously sharing J_0, J' and ρ as global parameters but with g-factors free to vary for each dataset. The resultant fit is shown in Figure 5.3(a) (solid lines) and returns parameters of $J_0 = 21.3(1)$ K, $J' = 1.3(1)$ K (taking $n = 4$ from the structure) and $\rho = 2.5(1)\%$. The extracted g-factors of $g_a = 2.1(1)$ and $g_{bc} = 2.0(1)$ are in excellent agreement with the $g_a = 2.145$ and $g_{bc} = 2.051$ determined from 20 K ESR data in section 5.2.3.

Figure 5.3(b) shows the field dependence of the differential magnetisation ($\mathrm{d}M/\mathrm{d}H$), at various temperatures, for a single-crystal of $CuVOF_4(H_2O)_6{\cdot}H_2O$ with field parallel to a, measured using radio-frequency susceptometry [64, 72, 179]. Measurements were performed using quasistatic fields with sweep rates of 1 T min^{-1} to mitigate magnetocaloric effects known to be present in dimer systems in rapidly changing magnetic fields [37, 64].

At low temperatures, $\mathrm{d}M/\mathrm{d}H$ exhibits two peak-like features centred around 14.5 T and 18.5 T which coalesce and become unresolvable as separate peaks for $1.68 < T \leq 2$ K, akin to behaviour observed in other BEC class dimers [176, 180]. Typically in $S = 1/2$ dimer systems, sharp cusps are observed in $\mathrm{d}M/\mathrm{d}H$ at the critical fields, for example H_{c1} and H_{c2} for the dimer $[Cu(pyz)_{0.5}(gly)]ClO_4$ exist over an ≈ 0.5 T field range [37, 168]. Whilst the reason for the broad nature of the transition features in $\mathrm{d}M/\mathrm{d}H$ here is not fully known, it could arise due to H-bond disorder within the complex interdimer exchange network, giving rise to a

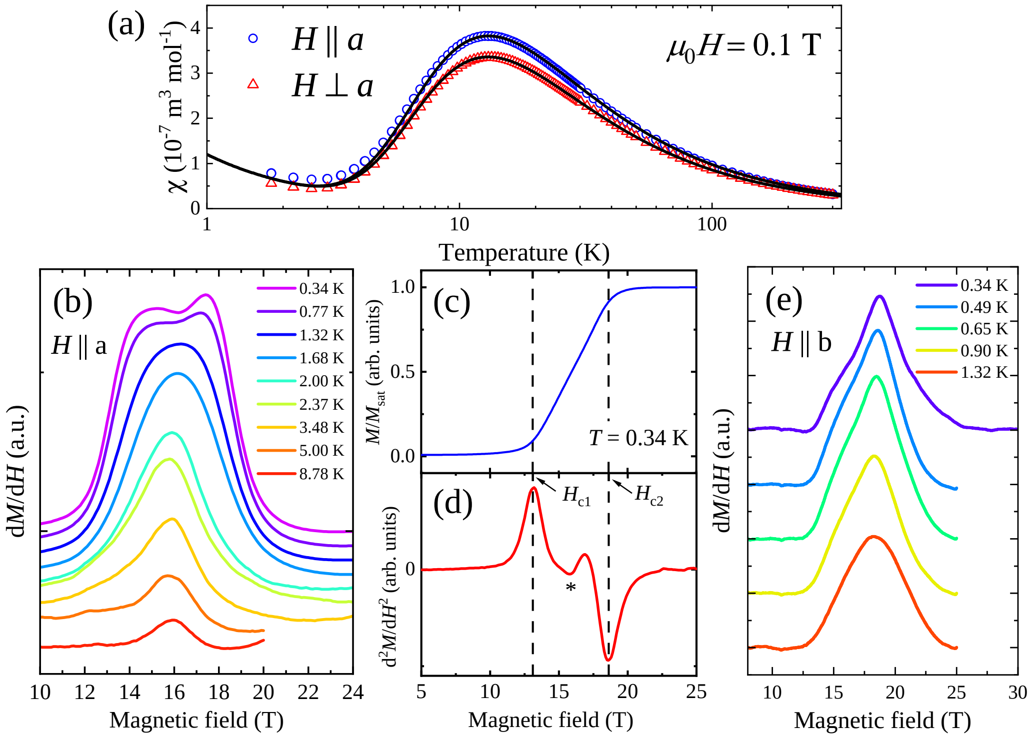

Figure 5.3: (a) DC-field susceptibility $\chi(T)$ for an orientated single-crystal of $\mathrm{CuVOF_4(H_2O)_6{\cdot}H_2O}$. Solid lines are a global fit of Eq. 5.2 to both data sets as described in the text. (b) Dynamic susceptibility $\mathrm{d}M/\mathrm{d}H$ measured at several temperatures, with field along the a-axis, using radio frequency (RF) susceptometry. Data are offset at each temperature for clarity. Magnetisation $M(H)$ (c) and its second differential ($\mathrm{d}^2M/\mathrm{d}H^2$) (d) measured at $T = 0.34$ K with field along a extracted from the RF susceptometry. First and second critical fields, H_{c1} and H_{c2}, extracted from $\mathrm{d}^2M/\mathrm{d}H^2$ are marked with dashed lines in (c) and (d). Minimum feature in $\mathrm{d}^2M/\mathrm{d}H^2$, discussed in text, marked with an asterisk. (e) $\mathrm{d}M/\mathrm{d}H$ measured at several temperatures, with field along the b-axis, using RF susceptometry with data offset for clarity.

distribution in the superexchange between neighbouring transition metal sites and a smearing of the transition features in $\mathrm{d}M/\mathrm{d}H$ [181].

The magnetisation $M(H)$ is extracted by integrating the measured $\mathrm{d}M/\mathrm{d}H$ response and calibrated using similar temperature DC-field SQUID data, with the result for the 0.34 K data shown in Figure 5.3(c). $M(H)$ saturates at $M_{\mathrm{sat}} = 2.7(1)\ \mu_{\mathrm{B}}$ per dimer unit, in excellent agreement with the calculated effective moment of 2.7 μ_{B} per dimer determined in [171]. The low-temperature $M(H)$ response is typical for a system of weakly interacting $S = 1/2$ AFM dimers [168, 180], with a sharp upturn at $H = H_{\mathrm{c1}}$ corresponding to the closing of the single-triplet energy gap and a levelling off at $H = H_{\mathrm{c2}}$ indicating the spins are fully polarised along the field direction at H_{c2}.

Figure 5.3(d) shows the peaks in the second differential of the $M(H)$ ($\mathrm{d}^2M/\mathrm{d}H^2$) used to track the positions of $H_{\mathrm{c}1}$ and $H_{\mathrm{c}2}$, as done previously for other dimer systems such as $Ba_3Cr_2O_8$ where $H_{\mathrm{c}1}$ and $H_{\mathrm{c}2}$ exist over ~ 1 T regions [182], similar to $CuVOF_4(H_2O)_6{\cdot}H_2O$. The minimum in $\mathrm{d}^2M/\mathrm{d}H^2$ between the two critical fields, marked with an asterisk, disappears for $1.68 < T \leq 2$ K. This is the same temperature range where the two peak features in $\mathrm{d}M/\mathrm{d}H$ coalesce [Figure 5.3(b)] and provides a consistent estimate for the temperature limit beyond which the two critical fields can no longer be resolved. For field along the b axis, $\mathrm{d}M/\mathrm{d}H$ data exhibits similar features as $H \parallel a$ but with the features shifted to higher fields owing to g-factor anisotropy as seen in Figure 5.3(e).

5.2.3 Electron-spin resonance

Electron-spin resonance (ESR) measurements were performed in collaboration with D. Kamenskyi using a commercially available X-band Bruker ESR spectrometer operating at 9.35 GHz at Augsburg University. High-frequency ESR experiments were done using a multi-frequency spectrometer operated in combination with a 16 T pulsed magnet (5 msec pulse) at Kobe University (Japan). Backward wave oscillators and Gunn diodes were employed as sources of mm- and submm-wavelength radiation. 2,2-Diphenyl-1-picrylhydrazyl (DPPH) was used as a standard magnetic field marker with g-factor $g = 2.0036$.

ESR measurements are capable of directly observing the closure of the singlet-triplet energy gap in $CuVOF_4(H_2O)_6{\cdot}H_2O$. The exceptional energy resolution and relevant frequency range of ESR make it one of the most relevant experimental techniques to probe the singlet-triplet excitations, as has been observed in the high-frequency ESR for many AFM spin-dimers, such as: $SrCu_2(BO_3)_2$ [183, 184], $CuTe_2O_5$ [185] based on Cu(II) ($3d^9$, $S = 1/2$) ions, $Ba_3Cr_2O_8$ [186, 187] and $Sr_3Cr_2O_8$ [187, 188] based on Cr^{5+} ($3\mathrm{d}^1$, $S = 1/2$).

X band ESR

Figure 5.4(a) displays the low-temperature ESR spectra for $CuVOF_4(H_2O)_6{\cdot}H_2O$ measured at a frequency of $\nu = 9.35$ GHz. The top panel compares spectra for field along the a- and b-axes. For field along a (black curve) the spectrum consists of four peaks which are indicated with arrows. Upon increasing temperature the magnitude of the three most intense peaks diminishes, as seen in the bottom panel of Figure 5.4(a), indicating these resonances can be attributed to free paramagnetic ions with g-factors: 1.95, originating from V(IV); 2.37, originating from Cu(II); and

2.05, which is likely due to Cu(II) but may contain some V(IV) resonance component. It is possible that there exists an uncompensated moment on the dimer due to the non-identical spins. This would likely manifest in the measured ESR spectra as a g-factor between that of the Cu and V values as seen in the data in Figure 5.4(a). However, the possibility that the $g = 2.05$ transition is due to impurity spins in the sample cannot be conclusively ruled out.

The weak peak marked τ corresponds to transitions ($\Delta S_z = \pm 1$) that occur within the excited triplet states indicated in Figure 5.4(b). For field along b only two peaks can be resolved: that arising from V(IV) with $g = 1.965$ and a very intense absorption with $g = 2.15$ deriving from transitions within the triplet state and Cu(II) impurities. These results are in agreement with the magnetometry, which also suggests the presence of a small component resembling free $S = 1/2$ ions within the sample.

The temperature evolution of the ESR spectra with $H \parallel a$ is shown in the bottom panel of Figure 5.4(a). As expected, upon increasing temperature the intensity of the transitions within the excited triplet (τ-peak) increases rapidly as the population of the triplet-state increases, in accordance with the Boltzmann distribution, whilst the intensity of the other transition peaks decreases.

At 10 K, the g-factor of the τ-mode with $H \parallel a$ is 2.145, the g-factor then grows to 2.155 upon warming to room temperature $T = 295$ K. The orientation dependence of the g-factors corresponding to the τ-transitions is shown in Figure 5.4(c). Along the principle axes the g-factors can therefore be determined to be $g_a = 2.145$, $g_b = 2.046$ and $g_c = 2.055$ at 20 K and $g_a = 2.155$, $g_b = 2.039$ and $g_c = 2.047$ at room temperature. This reflects the structure of the system, where the equatorial VF_4 and CuO_4 environments lie roughly within the bc-plane and g-factors along the unique axis are typically larger for JT-active Cu(II) octahdral environments [168, 175].

High-frequency ESR

Figure 5.4(d) shows the ESR spectra measured at frequencies $\nu = 60$, 105, 130 and 180 GHz with $H \parallel a$. The multiple modes observed in the spectra (labelled τ, G_1, G_2, and G_3) can be separated into two groups based upon their frequency-field dependence. The field position of the τ-mode [excitations within the triplet as in Figure 5.4(b)], and the several satellite peaks which are due to free spin components, increase linearly with the radiation frequency, $h\nu = g\mu_B\mu_0 H$.

The G_n modes have a finite energy in zero-field, Δ_{G_n}, such that Δ_{G_n} decreases upon increasing field. This is typical behaviour of singlet-triplet transitions whose

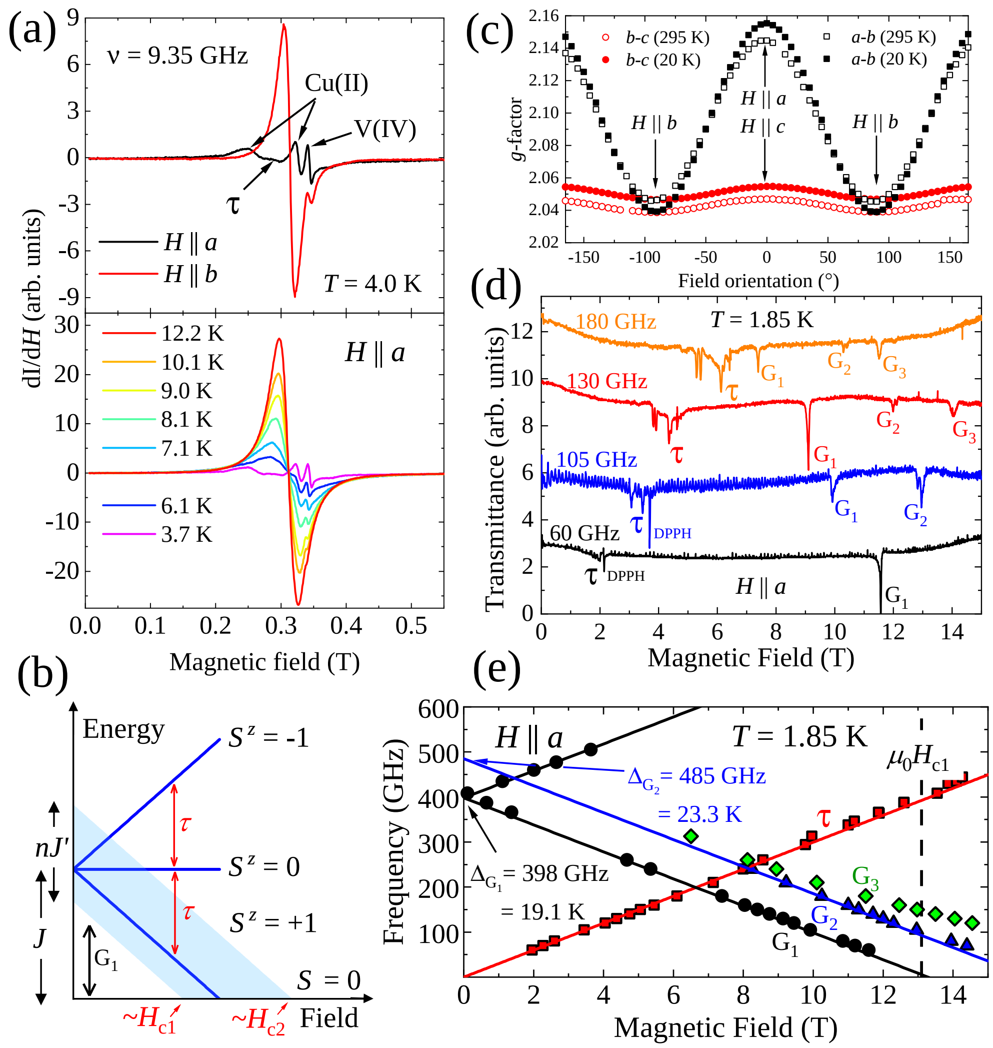

Figure 5.4: (a) Top panel shows X-band ESR spectra of CuVOF$_4$(H$_2$O)$_6$·H$_2$O measured at 4.0 K for $H \parallel a$ (black curve) and $H \parallel b$ (red curve). Bottom panel shows the temperature evolution of ESR spectra for $H \parallel a$. (b) Cartoon energy-level diagram for interacting $S = 1/2$ dimers. (c) Angular dependence of the g-factor determined for τ transitions. (d) ESR spectra at different radiation frequencies measured at 1.85 K and $H \parallel a$. A sharp peak marked "DPPH" corresponds to the absorption by the field marker compound. The peaks labelled τ and G$_{1,2,3}$ are as described in the text. (e) Frequency-field dependence of the ESR transitions in CuVOF$_4$(H$_2$O)$_6$·H$_2$O measured at 1.85 K and $H \parallel a$. Solid lines are the best fit of the data with $g = 2.145$ as obtained from the X-band measurements. Dashed line marks the first critical field, $\mu_0 H_{c1} = 13.1$ T, obtained from dM/dH measurements at $T = 0.34$ K with $H \parallel a$.

frequency follows $h\nu = h\Delta_{\mathrm{G}_n} - g\mu_{\mathrm{B}}\mu_0 H$, where Δ_{G_n} corresponds to the energy-gap between the $S = 0$ singlet ground-state and $S_z = 1$ triplet state. Typically, the observation of singlet-triplet transitions is forbidden in ESR for simple dimers, however, the presence of a non-zero DMI interaction or an alternating g-tensor can serve to mix the wave functions of the spin-singlet ground state and spin-triplet exited states, permitting singlet-triplet transitions [186]. The unlike nature of the constituent spins of the dimer may also allow the observation of singlet-triplet transitions in this system.

Normally, ESR experiments probe transitions at the center of the Brillouin zone (Γ point), at $k = 0$. However, under certain circumstances transitions at non-zero k can be observed due to Brillouin zone folding [186, 187, 189]. Therefore, the most intense mode, G_1, is assigned to singlet-triplet excitations at the Γ point whilst all other modes, G_2 and G_3, are attributed to similar transitions which occur at non-zero k. The transition corresponding to the G_1 modes is shown in the cartoon energy-level diagram in Figure 5.4(b). The nature of the G_3 mode is discussed later in this chapter.

The frequency dependence of the peak positions at 1.85 K is shown in Figure 5.4(e). The solid lines show the best fit of the data obtained using $g = 2.145$ taken from the X-band measurements, the fit returns values of $\Delta_{\mathrm{G}_1} = 398(3)$ GHz [19.1(1) K] and $\Delta_{\mathrm{G}_2} = 485(3)$ GHz [23.3(1) K]).

The gap values Δ_{G_1} and Δ_{G_2} can be used to determine the strength of the intradimer and interdimer couplings as the singlet-triplet ZF-splitting is dictated by the intradimer coupling J_0 whilst the interdimer interaction J' determines the dispersion of the triplet state, such that $h\Delta_{\mathrm{G}_1,\mathrm{G}_2} = J_0 \mp 2J'$ [190]. Values of J_0 and J' are estimated to be $J_0 = 21.0(2)$ K and $J' = 1.0(1)$ K (assuming $n = 4$ nearest neighbours), in excellent agreement with $J_0 = 21.3(1)$ K and $J' = 1.3(1)$ K determined from SQUID magnetometry data in Figure 5.3(a). Extrapolating the G_1 mode to zero-frequency estimates values of $\mu_0 H_{\mathrm{c1}}^{a} = 13.3(2)$ T for field along the a axis, which is in good agreement with the critical field of 13.1 T, for field along a, extracted from RF susceptometry [dashed line Figure 5.4(e)].

The phase transition occurs at H_{c1}, which is the point when the Zeeman interaction closes the singlet-triplet energy gap. Upon increasing field, the singlet-triplet energy gap need not strictly close at the Γ point but may close at another point within the Brillouin zone. Whilst ESR measurements are sensitive to the Γ point, the bulk magnetometry probes the whole of the Brilluoin zone. Therefore, the critical fields extracted using ESR data must fall between the magnetic-field range outlined by the values of $H_{\mathrm{c1,2}}$ determined from magnetometry measurements, as reported in the dimer compound $\mathrm{Ba_3Cr_2O_8}$ [186], and in line with the results here.

The observation of a third mode G_3 in the ESR spectrum is unexpected, as only two modes, corresponding to the resonances originating from the top (optical)

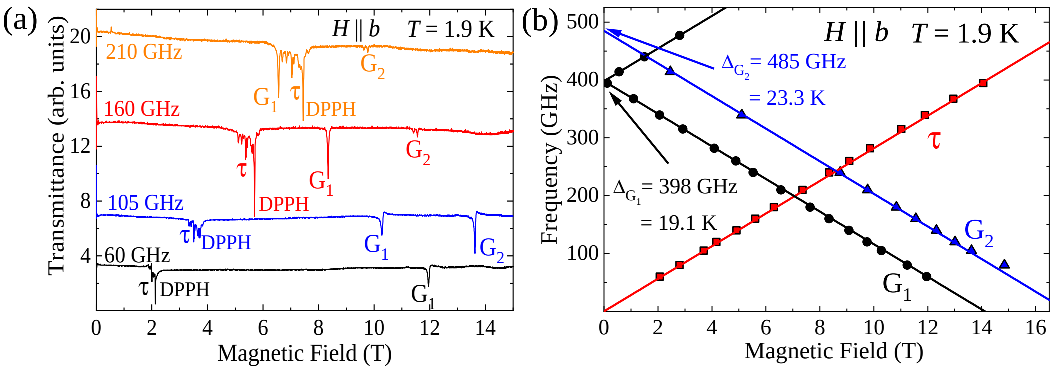

Figure 5.5: (a) ESR spectra at different radiation frequencies measured at 1.9 K and with $H \parallel b$. The sharp peak marked “DPPH” corresponds to the absorption by the field marker compound. The peaks labelled τ and $G_{1,2}$ are as described in the text. (b) Frequency-field dependence of the ESR transitions in $CuVOF_4(H_2O)_6{\cdot}H_2O$ measured at 1.9 K with $H \parallel b$. Solid lines are the best fit of the data with $g = 2.039$ as obtained from the X-band measurements.

and bottom (acoustic) of the dispersion band, are observed in the ESR spectrum of similar dimer materials [186–188]. Whilst the origin of this mode is presently unclear, further orientation dependent single-crystal ESR experiments are planned to investigate the possible existence of a DMI, and to elucidate the effect this may have on the field-dependence of the dimer energy-levels, as the uniformity and direction of the DM vector relative to the applied field (alongside whether the ESR measurement is performed in a Voigt, microwave field perpendicular to the applied field, or Faraday, microwave field parallel to the applied field, configuration) can alter the positions of the critical fields and suppress or promote the amplitude of certain energy level transitions [191]. Some initial evidence of this is seen in Figure 5.5, which shows the transmission spectrum and frequency-field dependence of the ESR transitions for field along b, where the mysterious G_3 mode is absent.

5.2.4 Density functional theory

Spin-polarised density functional theory (DFT) calculations were performed by B. Huddart and T. Lancaster using using CASTEP software [192] in order to calculate the spin-density distribution of the magnetic ground-state of $CuVOF_4(H_2O)_6{\cdot}H_2O$ and highlight the primary magnetic exchange pathways in the material.

Figure 5.6(a) shows the spins of the Cu and V ions within a dimer are aligned antiferromagnetically, as are Cu and V spins on adjacent dimers. Figure 5.6(b) shows the spin-density distribution within the dimer-unit itself. Significant spin-density is found on the Cu and V ions but also on the bridging oxide within the Cu—O—V intradimer bond. The spin density on the central O atom and its antiferromagnetic alignment with the spin of the V ion, with which it shares a short V=O double bond (≈ 1.6 Å), is likely to play a key role in promoting the intradimer exchange, though it is not clear how this exchange continues along the dimer to the Cu ion, given the fact that this O atom lies along the JT axis of Cu.

As expected from the structure, the magnetic orbitals of the Cu ion lie along the equatorial Cu—O bonds, perpendicular to the JT axis, which results in a large spin-density along the equatorial water ligands. In contrast, the axial water ligands on both the Cu and V octahedra possess very little spin-density. For the V ion, the magnetic orbitals lie in-between the V—F bonds with the spin density on the F atoms being relatively small.

Considering the DFT energies corresponding to a variety of spin configurations, the magnitude of the exchange energies along each exchange pathway within the material can be estimated. This results in an intradimer exchange of $J_0 = 20.3(3)$ K and an interdimer exchange within the *bc*-plane of $J' = 7.3(3)$ K. Whilst the strength of the intradimer exchange agrees well with other techniques, the magnitude of J' is much larger than $J' \sim 1$ K from ESR and magnetometry. DFT optimised H-bond geometries and strengths are known to be highly susceptible to the linearity of the H-bond pathway, with the accuracy of the DFT optimised geometries dropping off as the H-bond angle moves away from 180° [193]. As such, the presence of any H-bond disorder, and the known variations in the O—H $\cdots$ F bonds angles within the *bc*-plane ($\approx 160 - 170°$), will likely have an influence on the calculated value of J'.

Calculations also estimate an exchange interaction along the *a*-axis, via the Cu—O—H $\cdots$ F—V pathways outlined in Figure 5.2(d), of $J'' < 0.6$ K which is sufficiently small that its sign cannot be determined accurately within the uncertainties associated with these calculations. These results suggest that each dimer couples antiferromagnetically to its four nearest-neighbours in the *bc* plane, with only very weak, or indeed negligible, coupling between dimers along the *a*-axis direction.

5.2.5 Discussion

The positions of $H_{\mathrm{c}1,2}$ determined using RF-susceptometry, see Figure 5.3, shows some dependence on the orientation of the sample relative to the applied magnetic field, which is ascribed predominantly to *g*-factor anisotropy. The orientation-dependent ESR measurements in Figure 5.4(c) enable the *g*-factors for measurements made with an applied field along all three principle crystallographic axes to be de-

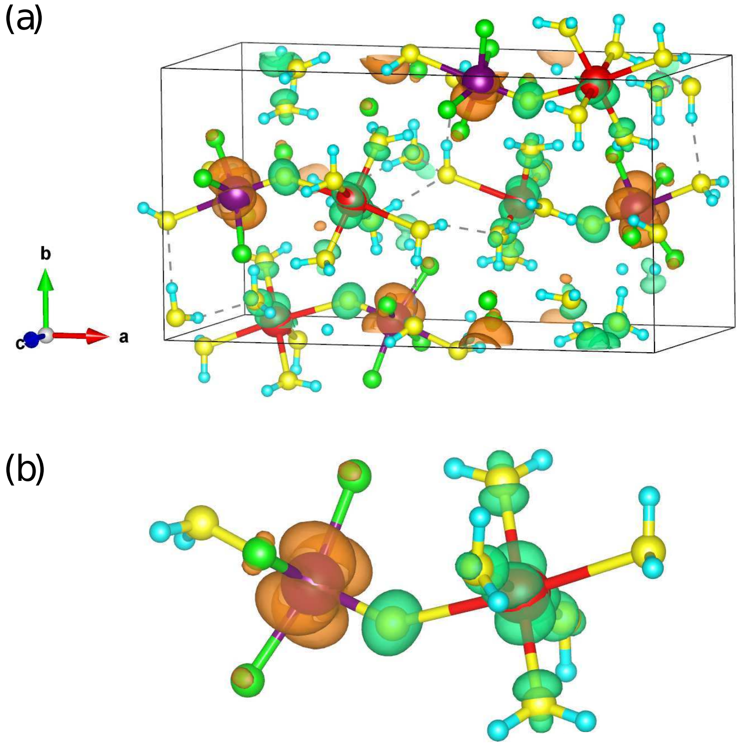

Figure 5.6: Spin density distribution for the ground-state magnetic structure obtained from DFT. Orange and green isosurfaces represent regions with significant positive and negative spin density, respectively. (b) View of a single dimer in an antiferromagnetic configuration.

termined. Scaling the values of $H_{\mathrm{c}1,2}$, measured with $H \perp a$, by using $g_b = 2.046$ and plotting them as $(g_b/g_a)B_{\mathrm{c}1,2}$ (where $B_{\mathrm{c}1,2} = \mu_0 H_{\mathrm{c}1,2}$), results in the values of $H_{\mathrm{c}1,2}$ for both measured orientations closely coinciding with one another as shown in Figure 5.7. The 2 K data-point (red data-point, Figure 5.7) estimates the upper temperature limit for the existence of the triplet excited state, using RF susceptometry data.

Despite correcting for g-factor anisotropy, a slight anisotropy is still observed between similar temperature $H_{\mathrm{c}1,2}$ values determined with $H \parallel a$ and $H \parallel b$. The cause of this may be the smearing out of the positions of $H_{\mathrm{c}1,2}$ due to disorder in the extensive H-bond network, as described above. The lack of an inversion center between the Cu and V ions may also permit the existence of a small DMI, which could lead to an additional orientation dependence of $H_{\mathrm{c}1,2}$ [169, 194].

The temperature-field phase diagram in Figure 5.7 is a result of both the intradimer exchange J_0 and the interdimer exchange J'. As $\chi(T)$, ESR and DFT calculations suggest J' is AFM, at low-temperature the critical fields relate to J_0

and J' via [195],

$$g\mu_B B_{c1} = J_0 - nJ'/2, \qquad g\mu_B B_{c2} = J_0 + nJ' \tag{5.3}$$

where $n = 4$ is the number of nearest dimer neighbours, as determined from DFT calculations.

Using the critical field values at $T = 0.34$ K and g-factors from ESR, Eqs. 5.3 return parameters of $J_0 = 22.1(6)$ K, in excellent agreement with $\chi(T)$, DFT and ESR, and $J' = 1.4(2)$ K ($n = 4$) which also agrees well with $\chi(T)$ and ESR. The system can therefore be well approximated using an isotropic dimer-model with weak interdimer interactions [195]. A comparison of the values of g, J_0 and J' estimated using various methods is shown Table 5.1.

Crystal architectures comprised of JT-active Cu(II) octahedra have previously been shown to promote low-dimensional magnetic behaviour [40, 44, 101, 196],

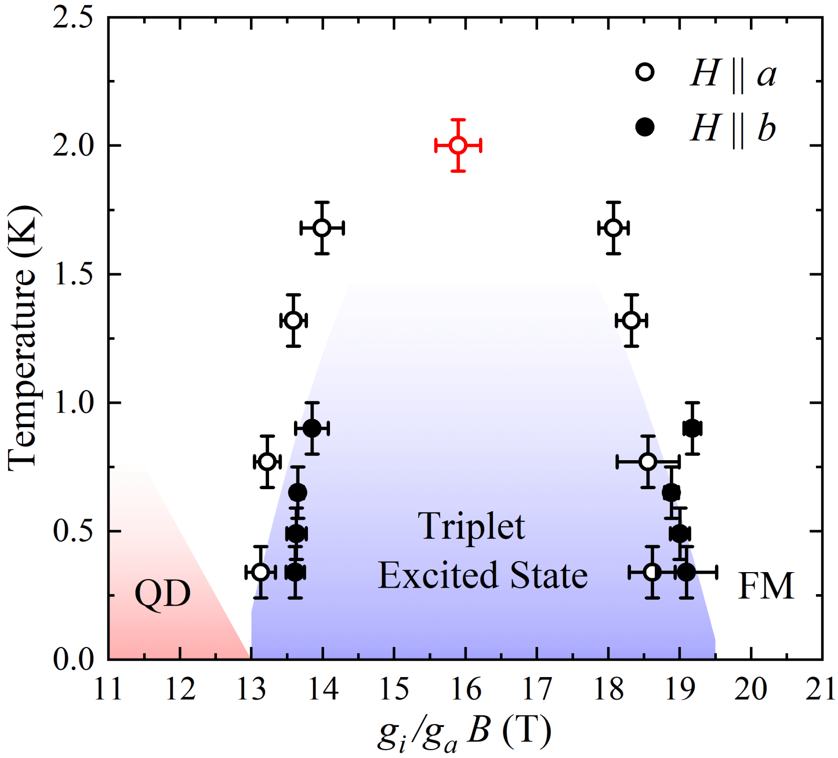

Figure 5.7: Temperature-field phase-diagram for $CuVOF_4(H_2O)_6{\cdot}H_2O$ where g_i denotes g-factors with field along $i = a, b$ as described in the text. Blue shaded region serves as a guide to the eye to highlight phase boundaries that enclose the triplet excited state. Red shaded region indicates the quantum disordered (QD) state at fields below H_{c1} whilst FM indicates the ferromagnetically saturated state above H_{c2}. Upper limit for the dome marked with red circle at $T = 2.0(1)$ K.

Technique	g_a	g_{bc}	J_0(K)	J'(K)
$\chi(T)$	2.1(1)	2.0(0)	21.3(1)	1.3(1)
ESR	2.145	2.051	21.0(2)	1.0(1)
RF-susceptometry	-	-	22.1(6)	1.4(2)
DFT	-	-	20.3(3)	7.3(1)

Table 5.1: Comparison of g-factors and exchange interactions determined using various methods for $CuVOF_4(H_2O)_6{\cdot}H_2O$.

as the $d_{x^2-y^2}$ orbital of the Cu lies within a plane perpendicular to the JT-axis, resulting in minimal orbital overlap between adjacent Cu ions bonded along the JT-axis, and hence very weak magnetic exchange in this direction. This is reflected in the DFT calculations performed for $CuVOF_4(H_2O)_6{\cdot}H_2O$ (see Figure 5.6) which show an increased spin density, arising from the $d_{x^2-y^2}$ orbital, along the equatorial Cu—OH_2 bonds, perpendicular to the axial O—Cu—OH_2 JT bond direction.

Similarly, the presence of a pseudo-JT distortion in six-coordinate V(IV) ($3d^1$) complexes can also facilitate the emergence of low-dimensional magnetic properties [197, 198]. For non-polar octahedra, an axial elongation results in the $3d^1$ electron occupying the degenerate d_{xz} and d_{yz} orbitals, whilst an axial compression leads to the $3d^1$ electron inhabiting the d_{xy} orbital. (Typically, axial compression is favoured in $3d^1$ octahedra because occupying the d_{xy} orbital offers the greater energy saving to the system compared to occupying one of the degenerate d_{xz} or d_{yz} orbitals for the case of axial elongation [199]). In the present case, the shortened V=O double-bond [1.6083(8) Å] and elongated V—OH_2 bond [2.2903(7) Å] of the polar VF_4O_2 octahedra makes it difficult to ascertain which orbital the $3d^1$ electron occupies by inspecting the structure alone. However, DFT calculations in Figure 5.6 show an increased spin-density between the V—F ligands in the bc-plane, indicative that the $3d^1$ electron occupies the d_{xy} orbital.

As anticipated, DFT calculations find negligible spin-density located on the axial water ligand of either the Cu or V octahedra. Therefore, whilst the axial waters do form H-bonds between adjacent dimers along a, the interdimer magnetic exchange is expected to occur primarily within the bc-plane via the H-bond network outlined in Figure 5.2(e). Furthermore, the only H-bond pathway along a which is not via an axial water [blue-striped bonds, Figure 5.2(d)] is found by DFT to mediate an vanishingly weak exchange $J'' = 0.03(6)$ K, such that the system can be considered to be a magnetically 2D network of $S = 1/2$ dimers.

The interdimer exchange within this 2D network (bc-plane) is estimated to be $J' \approx 1$ K, whilst the intradimer exchange is determined to be much greater at

$J_0 \approx 21$ K. Therefore, the exchange pathway which mediates J_0 must be considerably more efficient than the J' exchange pathways. The interdimer Cu—O—H$\cdots$F—V bonds which mediate J' fall within the range 6.51$-$6.656 Å, [Figures 5.2(d) and 5.2(e)] which is very similar in length to the intradimer Cu—O—H$\cdots$F—V bond 6.553 Å [Figure 5.2(c)]. Due to the highly similar length of the interdimer and intradimer Cu—O—H$\cdots$F—V bonds, and large difference in the magnitudes of J_0 and J', it is unlikely the strong intradimer exchange is mediated along the intradimer H-bond pathway. DFT calculations do however show significant spin-density located on the oxygen adjoining the Cu and V ions [Figure 5.6(b)]. It is therefore highly probable that the strong primary intradimer magnetic superexchange occurs along the Cu—O—V bond, via the JT-axis of the Cu. This is corroborated by the high-pressure structural and mangetometry measurements discussed below.

For the reasons outlined above, strong exchange through a JT bond is very rare, however, it has also been observed in the 2D AFM chain compounds CuX$_2$(pyz); where X = Cl, Br, F [200–202]. In this case, however, magnetic exchange is mediated along Cu—X$_2$—Cu bibridges, where only one of the X—Cu—X bridges lies along the JT axial direction, while the other lies in the plane containing the $d_{x^2-y^2}$ magnetic orbital [202]. As such, spin-density is found at the halide ion along the JT X—Cu—X axes, permitting intrachain exchange interactions (J) to be mediated via the JT-axis. Moving down the halide series, the strength of the exchange along the Cu—X$_2$—Cu pathways increases as the size of the halide ion increases ($J_\mathrm{F} \approx 1$ K, $J_\mathrm{Cl} \approx 28$ K, $J_\mathrm{Br} \approx 46$ K) [201]. For the Cl and Br species, these halide bibridges constitute the primary exchange pathways, whilst for X = F the primary exchange occurs along the Cu-pyz-Cu pathways ($J_\mathrm{pyz} \approx 7$ K) with weaker exchange via the halide bibridges ($J_\mathrm{F} \approx 1$ K).

Similarly, in CuVOF$_4$(H$_2$O)$_6$·H$_2$O there is sizable spin-density located on the bridging-oxide ligand along the JT-axis. As outlined in [171], it is the JT distortion of the Cu that allows the vanadyl cation to form a strong covalent bond with the bridging oxide, permitting the formation of the Cu—O—V bond. Guided by DFT calculations, it is hypothesised that it is this strong V=O double-bond which allows the vanadyl species to donate a sizable portion of its spin-density to the bridging oxide. This leads to the Cu and V ions coupling antiferromagnetically to form an AFM spin-half dimer, demonstrating that, surprisingly, the JT distortion is not only responsible for the polar crystal structure, but also the formation of the low-dimensional magnetism of this system.

5.2.6 High-pressure magnetometry

Pressure-dependent RF-susceptomtetry measurements were performed on single-crystals of $CuVOF_4(H_2O)_6{\cdot}H_2O$ using a piston-cylinder cell to attain pressures of up to $\approx$ 25 kbar a with fields attained using a 36 T resistive magnet and 18 T superconducting magnet at the National High Magnetic Field Laboratory, Tallahasee, Fl, USA. Pressure-cell setup was performed with the assistance of local experimental contact D. Graf. In-situ pressure was determined by tracking the pressure-dependence of the fluorescence spectrum of a ruby chip located on the end of a fiber optic cable situated next to the sample.

The top-panel of Figure 5.8(a) shows $\mathrm{d}M/\mathrm{d}H$ for a single-crystal of $CuVOF_4(H_2O)_6{\cdot}H_2O$ measured using RF-susceptometry, at ambient and 19(1) kbar of pressure [pressure of 4(1) kbar, 9(1) kbar and 15(1) kbar were also measured within the 36 T resistive magnets]. Ambient data was measured with $H \parallel a$ and measurements within the cell performed with field approximately along a as potential tumble of the crystal upon closure of the cell, makes know the exact crystal orientation difficult. However, the J_0 values at ambient and 4(1) kbar (s H_{c1} values at this Whilst the profile of the two $\mathrm{d}M/\mathrm{d}H$ curves is qualitatively similar, the two peak-l ike features are both shifted to higher fields at 19 kbar (blue curve). The bottom panel shows the trough and peak features in the second differential of the magnetisation used to determine the positions of H_{c1} and H_{c2}, respectively. At 19 kbar, $H_{\mathrm{c1}} = 16.4(2)$ T and $H_{\mathrm{c2}} = 21.5(2)$ T, an increase of $\approx$ 3 T in both values compared to the ambient data. The difference between the two critical fields ($\Delta H = H_{\mathrm{c2}} - H_{\mathrm{c1}}$) at 19 kbar is $\Delta H = 5.1(3)$ T, which is the same to within error as the ambient value of $\Delta H = 5.5(3)$ T; this is true for all measured pressures. In addition, the two hump-like features become unresolvable as separate features at 2 K for all measured pressures.

Figure 5.8(c) shows RF-susceptometry measurements performed up to 24(1) kbar using an 18 T Oxford Instruments superconducting magnet. At 24 kbar, the position of H_{c1} (midpoint of the downturn in $\mathrm{d}M/\mathrm{d}H$) is seen to continue to increase, being just outside of the field range of the 18 T magnet. As the change in amplitude of $\mathrm{d}M/\mathrm{d}H$ is roughly constant for each measurement (approximated by multiple field sweeps to be $\approx$ 90 a.u.), the value of H_{c1} at 24 kbar can be estimated to be $\approx$ 18.3(2) T. To gain insight into the pressure-induced changes seen in the magnetometry, high-pressure single-crystal measurements were performed.

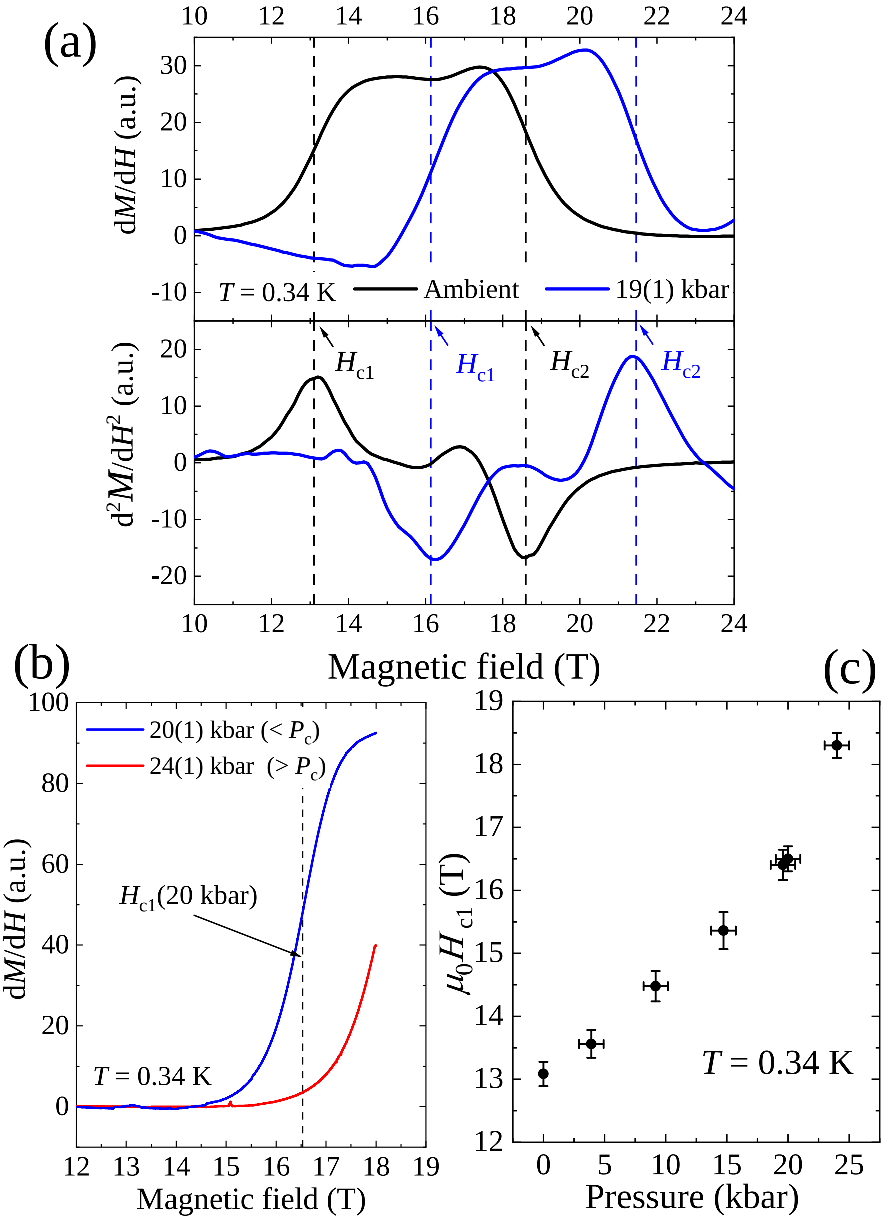

Figure 5.8: Differential susceptibility $\mathrm{d}M/\mathrm{d}H$ measured using radio-frequency susceptometry at ambient ($H \parallel a$) and 19(1) kbar (with field approximately along a, as the possibility of the crystal tumbling slightly upon closure of the cell prevents one knowing the precise orientation) of pressure. Positions of the critical fields at both pressures are indicated with dashed lines and arrows. Measurement performed using resistive DC-field magnet. (b) $\mathrm{d}M/\mathrm{d}H$ at 20 kbar (below the critical pressure of $P_\mathrm{c} \approx 22$ kbar) and 24 kbar ($P > P_\mathrm{c}$) measured using an 18 T quasistatic Oxford superconducting magnet. Pressure was attained using a piston cylinder cell for both measurements. (c) Pressure dependence of the first critical field.

5.2.7 High-pressure crystallography

Pressure dependent single-crystal x-ray diffraction measurements were performed at The University of Warwick by myself with the assistance of J. Tidey using a Tozer Diamond Anvil Cell (DAC) mounted onto a Rigaku Oxford Diffraction Synergy S diffractometer. Measurements were performed using Mo K_α as an incident x-ray source to allow high-resolution data collection. In situ pressure was determined by tracking the pressure-dependence of the fluorescence spectrum of a small ruby chip within the DAC sample chamber.

Figure 5.9 shows the effect increasing hydrostatic pressure has on the unit-cell of $CuVOF_4(H_2O)_6{\cdot}H_2O$ up to 30 kbar. Below 21(1) kbar, the unit-cell volume can be modelled using a cubic polynomial (top-panel, black line) indicating a linear compression of the cell. Within the pressure-region $21 < P \leq 24$ kbar the system undergoes a structural phase-transition from the polar spacegroup $Pna2_1$ to the chiral spacegroup $P2_12_12_1$, confirmed by the measurement of systematic absences in the data at pressures $P \geq 24(1)$ kbar. (The symmetry of a crystal determines the position of the observed Bragg peaks within reciprocal space, as diffracted x-rays

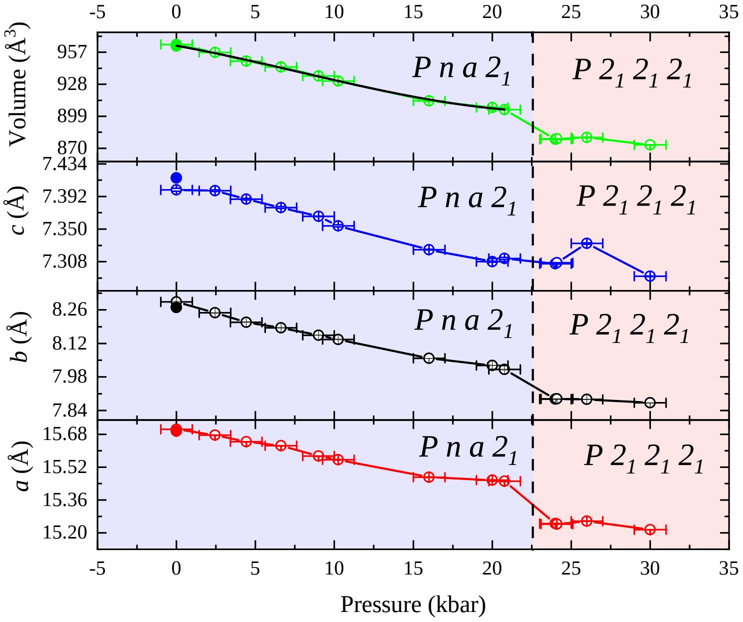

Figure 5.9: Pressure dependence of the unit of cell of $CuVOF_4(H_2O)_6{\cdot}H_2O$ at 300 K with errors plotted at 3σ. Solid circle denotes ambient measurement outside of cell and open circles denote measurements made using a Tozer Diamond Anvil Cell. Shaded regions highlight the low pressure $Pna2_1$ and high-pressure $P2_12_12_1$ phase, with the two regions delineated by a dashed black line. Solid black line in top-panel is a cubic fit to the data for pressures below 24 kbar.

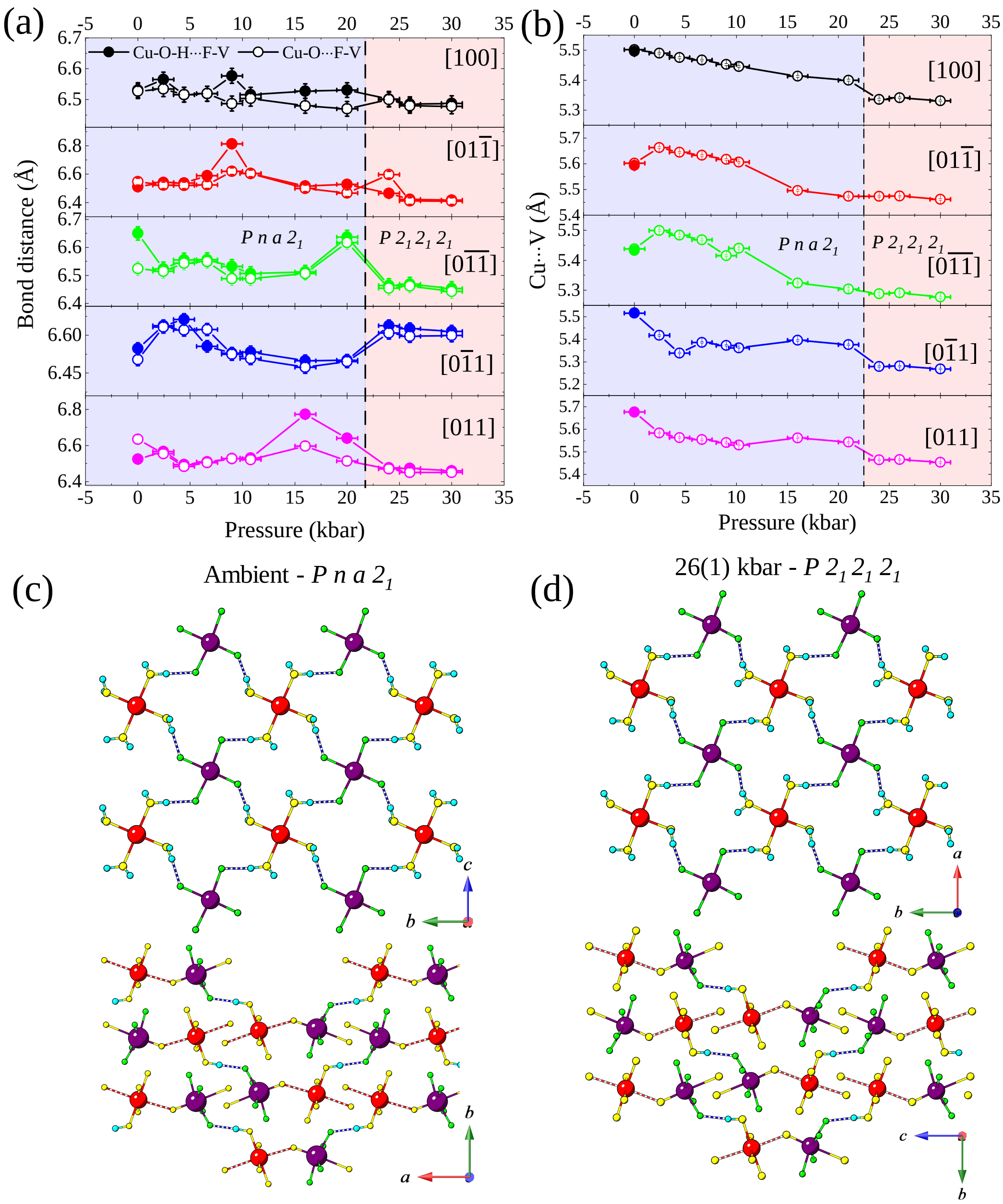

Figure 5.10: (a) Pressure dependence of the interdimer exchange pathways; closed circles are Cu—O—H···F—V and open circles are Cu—O···F—V bond distances. (b) Pressure dependence of the through-space interdimer Cu and V distances. Interdimer H-bond exchange pathway geometry in the low-pressure phase (c) and high-pressure phase (d). Measurements made at 300 K and errors plotted at 3σ.

constructively interfere to give regions of high intensity. In addition, the symmetry of a system also defines positions within reciprocal space that are characterised by regions of zero intensity due to the destructive interference between diffracted

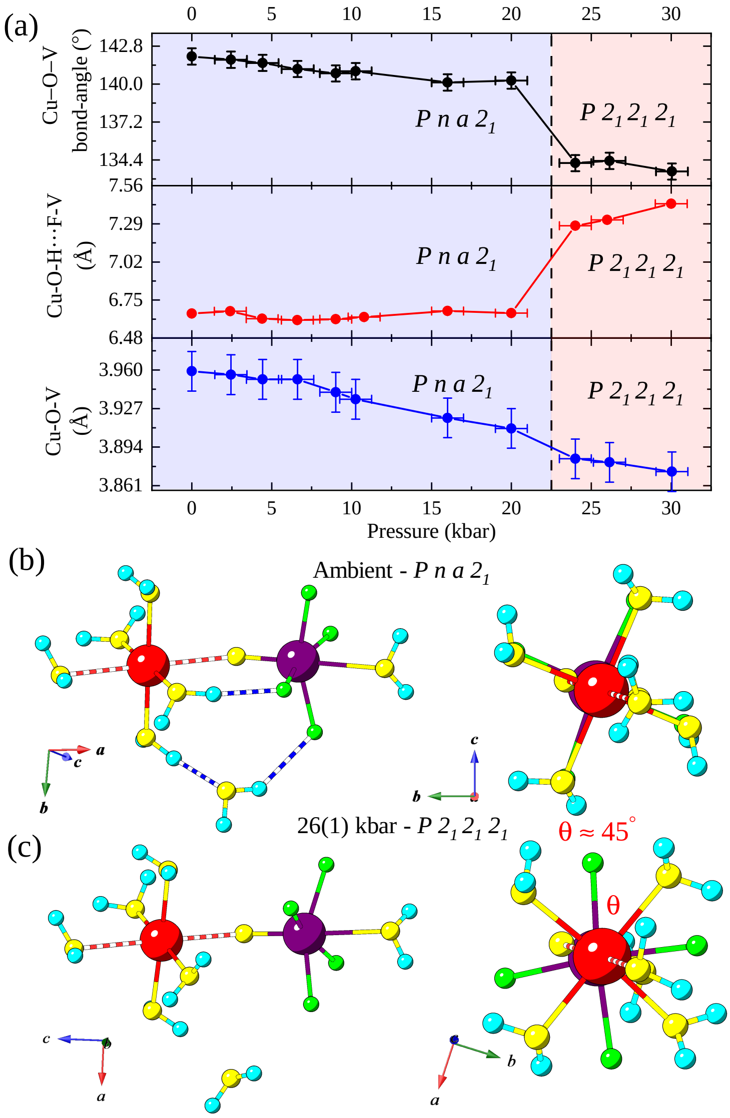

Figure 5.11: (a) Pressure dependence of the intradimer Cu—O—V bond distance (bottom panel), intradimer Cu—O—H · · · F—V bond distance (middle panel) and Cu—O—V bond angle (top panel). Structure of the dimer-unit in the low-pressure (b) and high-pressure (c) phase. Measurements made at 300 K and errors plotted at 3σ.

x-rays. These are known as systematic absences and are used within x-ray crystallography measurements to determine the space-group of a system [80]. Hence, changes within the observed systematic absences can be used to characterise structural phase-transitions.)

In the $Pna2_1$ phase, the interdimer Cu—O—H · · · F—V bond lengths within the bc plane do not exhibit obvious decreases upon increasing pressure as one might expect, see Figure 5.10(a). For example, from 16 to 20 kbar a reduction in the interdimer bond distance along the [011] direction of 0.132 Å is accompanied by an increase in the corresponding interdimer bond distance along the $[0\overline{1}\overline{1}]$ direction by 0.125 Å. Whilst the true position of the electron deficient hydrogens can be poorly defined in x-ray experiments (an issue compounded when using a pressure cell, as a significant portion of reciprocal space is obscured by the cell body), Figure 5.10(a) shows that the Cu—O—H···F—V bond distances (filled circles) overlay well with the Cu—O···F—V bond distances (open circles); indicative that, as expected, O—H bonds point almost directly at the highly electronegative F ligands.

Figure 5.10(b) shows that the through-space distance between Cu and V ions on adjacent dimer-units does decrease upon increasing pressure. Therefore, as pressure brings neighbouring dimer-units into closer proximity, it is likely that the increased electrostatic repulsion between the dimers induces rotations of the water ligands. This leaves the interdimer Cu—O—H···F—V bond distance approximately constant, at an average value of 6.52(6) Å across all interdimer H-bond pathways and pressures. The overall geometry of the interdimer H-bond network is also unchanged up to the highest measured pressure, see Figures 5.10(c) and 5.10(d).

Figure 5.11(a) shows the effect increasing pressure has on the intradimer bonds. Both the Cu—O—V bond angle (top panel) and Cu—O—V through-bond distance (bottom panel) decrease. The intradimer Cu—O—H···F—V bond distance (middle panel) is found to be relatively unchanged up to the point of the structural phase transition; likely due to rotations of the water. At the transition to the high-pressure $P2_12_12_1$ phase, the intradimer Cu—O—H···F—V bond distance (middle panel) increases by $\approx$ 0.5 Å. This is due to an $\approx 45°$ rotation of the equatorial F-ligands on the V, relative to the equatorial H_2O ligands on the Cu, about the Cu—O—V bond, as shown in Figures 5.11(b) and 5.11(c). This is accompanied by an $\approx 5°$ decrease in the Cu—O—V bond angle at the phase-transition, with a continued steady decrease in the Cu—O—V bond distance up to the highest measured pressure.

5.2.8 Discussion

For $CuVOF_4(H_2O)_6{\cdot}H_2O$ the temperature dependence of H_{c1} and H_{c2} at each measured pressure allows the pressure-evolution of the temperature-field phase-diagram to be tracked, with the results shown in Figure 5.12. Up to 19(1) kbar, the area enclosed by the dome-like phase-diagram, dictated by the magnitude of J', is unchanged. The in-field position of the dome, which is determined by the size of J_0, is increased. The inset of Figure 5.12 shows the pressure-evolution of J_0 and J' extracted using Eqs. 5.3. Up to 19(1) kbar, pressure has little effect on the magnitude of the interdimer exchange, which remains approximately constant at $J' \approx 1.3$ K.

This is in line with high-pressure structural measurements, which show that whilst pressure does bring the dimer-units into closer proximity, the overall geometry and length of the interdimer exchange pathways is nearly unchanged up to 30 kbar; see Figure 5.10.

In contrast, the magnitude of J_0 is seen to increase linearly, reaching a maximum measured value of $J_0 = 25.2(3)$ K at 19 kbar for the low-pressure structural phase. This increase is due to a decreases in both the Cu—O—V bond length and angle, Figure 5.11(a), which likely increases the amount of spin-density located on the bridging oxide as the vanadyl group moves into closer proximity to it, thereby increasing J_0. In the high-pressure phase, $P \geq 24(1)$ kbar, the Cu—O—V bond distance continues to decrease, whilst the bond itself buckles as the bond-angle reduces by $\approx 5°$ when moving from 20 to 24 kbar [Figure 5.11(a)]. The structural phase-transition induces a rotation of the equatorial ligands on each ion about the Cu—O—V bond, Figures 5.11(b) and 5.11(c). This in turn causes a drastic increase in the length of the intradimer Cu—O—H$\cdots$F—V bond, by 0.62 Å, at the onset of the phase transition. RF susceptometry data in Figure 5.8(b) indicate H_{c1} continues to increase up to 24(1) kbar ($H_{c1} \approx 18.3$ T), a pressure at which the system is

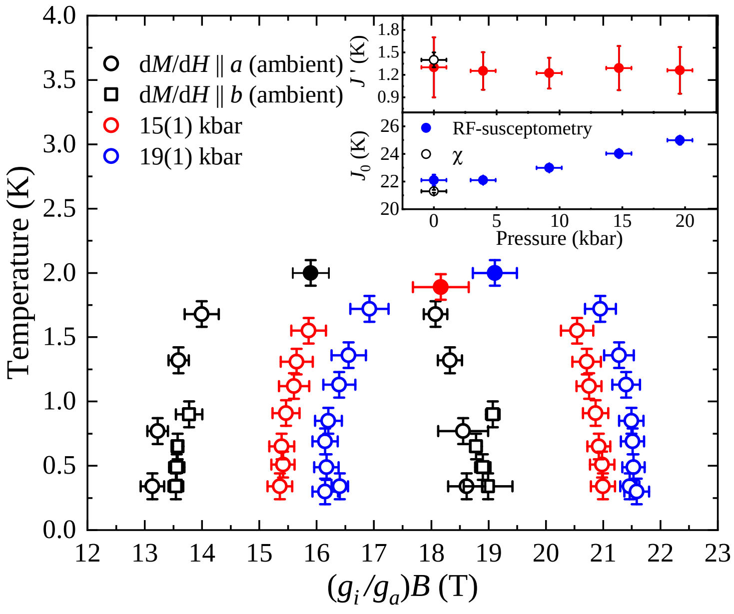

Figure 5.12: Pressure dependence of the temperature-field phase diagram of $CuVOF_4(H_2O)_6{\cdot}H_2O$ measured using DC-field resistive magnet. Filled circles denote the upper temperature limit for the phase diagram at each pressure, as determined from RF susceptometry measurements. Inset shows intradimer (J_0) and interdimer (J') exchange plotted as a function of pressure as determined from Eqs. 5.3.

known to be within the high-pressure $P2_12_12_1$ phase. The increase in H_{c1} can only be accomplished by an increase in J_0 (see Eqs. 5.3). The sharp increase in the intradimer Cu—O—H$\cdots$F—V distance at the structural phase-transition, alongside the continued decrease in the Cu—O—V bond length and angle, provides further strong evidence that the strong J_0 must be mediated along the Cu—O—V bond via the JT-axis of the Cu.

5.3 [Cu(pyz)$_{0.5}$(gly)]ClO$_4$

5.3.1 Structure and prior results

[Cu(pyz)$_{0.5}$(gly)]ClO$_4$ (pyz = pyrazine = $C_4H_4N_2$; gly = glycine = $C_2H_5NO_2$) crystallises into the monoclinic structure with space group $P2_1/n$ [37, 168]. The material is based on a lattice of weakly interacting $S = 1/2$ dimers, with the dimer-unit itself composed of two Cu ions linked by a bridging pyz molecule which mediates the primary intradimer exchange interaction (J_0). The Cu-pyz-Cu dimer-unit is indicated in Figure 5.13 with shaded regions.

Glycine ligands mediate the primary interdimer exchange (J'_{gly}) and bridge each dimer to four nearest dimer neighbours. The dimers are arranged in corrugated sheets which stack along the $[10\overline{1}]$ direction, as shown in Figure 5.13(a). The sheets are separated by ClO$_4$ counter ions, which bond to the dimer along the JT axis of the Cu. Due to this, the $d_{x^2-y^2}$ orbitals on the Cu sites lie within the equatorial CuO$_2$N$_2$ plane, such that the Cu$\cdots$O—Cl—O$\cdots$Cu coordination bond likely mediates only very weak secondary interdimer exchange ($J''_{\mathrm{ClO_4}}$) between the layers, as shown in Figure 5.13(b). Whilst an inversion centre exists between dimers with the same orientation within the ac plane, see Figure 5.13(a), neighbours with different orientations are symmetry related through a glide plane, meaning a small DM term may act within the ab plane [37, 168].

Previous μ^+SR data show a lack of long-range ordering down to $T \approx 32$ mK and the existence of two field-induced phase transitions determined from $\mathrm{d}M/\mathrm{d}H$, μ^+SR and heat capacity measurements [168]. With this data, reference [168] demonstrated that the temperature-field phase-diagram for [Cu(pyz)$_{0.5}$(gly)]ClO$_4$ is reminiscent of that seen in a other BEC dimer material, outlining a dome-like region of XY-AFM order, with an AFM $J_0 = 9.0(2)$ K and FM $J'_{\mathrm{gly}} = -3.3(1)$ K, however, the paucity of data near the QCPs meant the dimensionality of the system could not be determined. A further study from reference [37] demonstrated that $J''_{\mathrm{ClO_4}}$ in the system was small but finite, with the system being well described as a Q2D network of dimers with AFM coupling between the dimers; $J_0 = 5.8(3)$ K

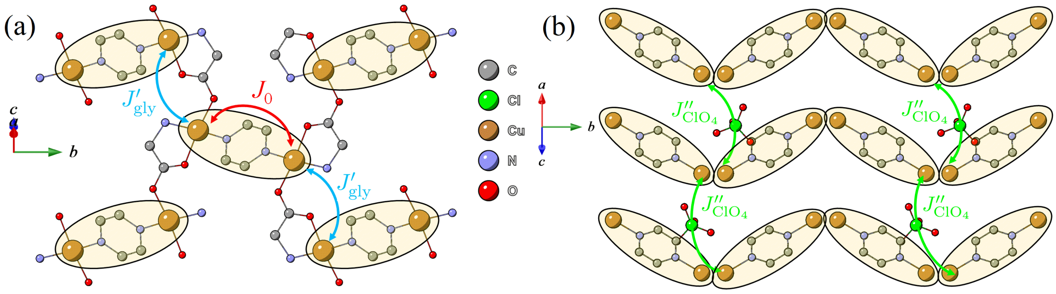

Figure 5.13: Crystal structure of [Cu(pyz)$_{0.5}$(gly)]ClO$_4$ measured at 300 K with dimer-units denoted with shaded regions. (a) Corrugated dimer sheets with intradimer (J_0) and interdimer (J'_{gly}; within the corrugated layers) exchange pathways marked with arrows. (b) Interlayer exchange ($J''_{\mathrm{ClO_4}}$) pathway between Cu(II) ions via ClO$_4$ pathways.

and $J'_{\mathrm{gly}} = 1.6(1)$ K. The FM J'_{gly} in [168] was determined comparing the values of J_0 and J'_{gly} extracted from dM/dH data and a mean-field corrected fit to $\chi(T)$, where the authors note that mean-field fits to $\chi(T)$ are sensitive to the details of the model used. Due to this, and that preliminary DFT calculations (not shown in this thesis) are suggestive of AFM J'_{gly}, the analyses that follows in this thesis chapter will consider the situation for [Cu(pyz)$_{0.5}$(gly)]ClO$_4$ with AFM interdimer interactions, $J'_{\mathrm{gly}} > 0$, as in reference [37].

5.3.2 High-pressure magnetometry

Pressure-dependent RF-susceptometry measurements were performed on single-crystals of [Cu(pyz)$_{0.5}$(gly)]ClO$_4$ using a piston-cylinder cell with field attained using an 18 T superconducting magnet at the National High Magnetic Field Laboratory, Tallahasee, Fl, USA. Pressure-cell setup was performed with the assistance of local experimental contact D. Graf. In-situ pressure was determined by tracking the pressure-dependence of the fluorescence spectrum of a ruby chip located on the end of a fiber-optic cable situated next to the sample.

Figure 5.14(a) shows the temperature dependence of the differential magnetisation (dM/dH) for a single-crystal of [Cu(pyz)$_{0.5}$(gly)]ClO$_4$ measured at 13(1) kbar using RF susceptometry. At the lowest measured temperature (T = 0.3 K), two sharp cusps are seen in the data at H = 0.8 T and H = 6.7 T. These features correspond to the first critical field (H_{c1}), at which the singlet-triplet energy gap is closed, and second critical field (H_{c2}), at which the spins are polarised along the field direction. Upon increasing temperature, H_{c1} and H_{c2} move in closer proximity to each other and cease to be resolvable as separate features for temperatures in the range $1.7 < T \leq 2.7$ K. In contrast, at ambient pressure the highest temperature

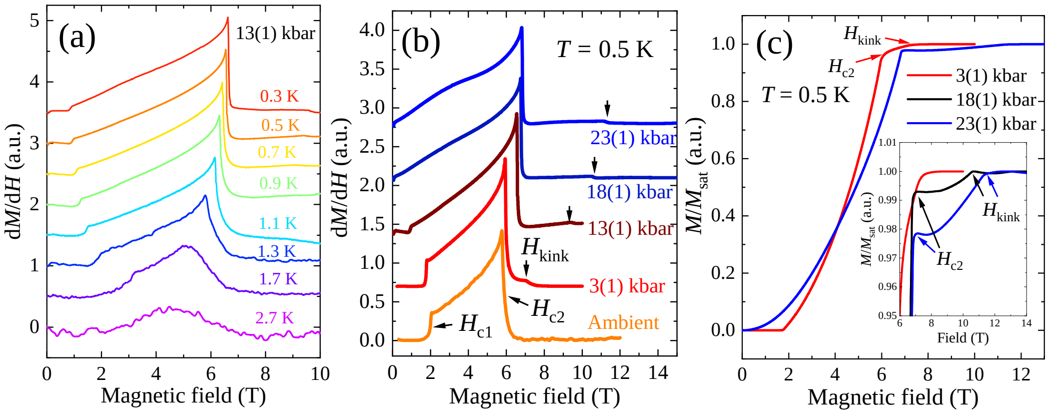

Figure 5.14: (a) Temperature dependence of the dynamic susceptibility ($\mathrm{d}M/\mathrm{d}H$) measured at 13(1) kbar. (b) Pressure evolution of $\mathrm{d}M/\mathrm{d}H$ data measured at 0.5 K. Position of the first critical field (H_{c1}), second critical field (H_{c2}) and kink-like feature (H_{kink}) are marked with arrows. Ambient data from [37]. (c) Pressure evolution of the magnetisation $M(H)$ measured at 0.5 K determined by integrating the data in (b). Inset highlights H_{kink} feature.

H_{c1} and H_{c2} can be resolved is $T \approx 1.3$ K [37, 168].

The profile of $\mathrm{d}M/\mathrm{d}H$ at 13(1) kbar is qualitatively similar to that at ambient pressure, see Figure 5.14(b), however, H_{c1} and H_{c2} are both shifted to lower and higher fields, respectively, by ≈ 1 T. At 18(1) kbar and above, the cusp associated with H_{c1} can no longer be resolved in the data whilst the more dramatic cusp at H_{c2} remains located at $H \approx 7$ T. At $P \geq 3(1)$ kbar, an additional kink in $\mathrm{d}M/\mathrm{d}H$ emerges, marked in Figure 5.14(b) by H_{kink}. This feature tracks to higher fields as pressure is increased up to 23(1) kbar.

By integrating the measured $\mathrm{d}M/\mathrm{d}H$ responses in Figure 5.14(b), one can extract the magnetisation $M(H)$ as shown in Figure 5.14(c). At $P \leq 13(1)$ kbar, the form of $M(H)$ remains typical for a dimer system, with a sharp upturn due to the closing of the singlet-triplet energy gap and a plateau at H_{c2} as the spins are nearly polarised along the field direction. For $P \geq 18(1)$ kbar, the sharp low-field upturn in $M(H)$ at H_{c1} is lost, as $M(H)$ instead exhibits a slightly concave increase up to a sharp plateau at $H = H_{\mathrm{c2}}$. The data then continue to rise before reaching a second plateau at $H = H_{\mathrm{kink}}$, best seen in the inset of Figure 5.14(c). This feature is attributed to the spins slight canting along the field direction at $H = H_{\mathrm{c2}}$, as the field overcomes the primary exchange interactions, and then the full polarisation of the spin along the field direction at $H = H_{\mathrm{kink}}$.

5.3.3 High-pressure crystallography

Pressure dependent single-crystal x-ray diffraction measurements were performed at The University of Warwick by myself using a Tozer Diamond Anvil Cell (DAC) mounted onto a Rigaku Oxford Diffraction Synergy S diffractometer. Measurements were performed using Mo K_α as an incident x-ray source to allow high-resolution data collection. In situ pressure was determined by tracking the pressure-dependence of the fluorescence spectrum of a small ruby chip within the DAC sample chamber.

The top panel of Figure 5.15(a) shows that upon increasing pressure, the unit cell volume of $[\mathrm{Cu(pyz)_{0.5}(gly)}]\mathrm{ClO_4}$ decrease linearly up to 28(1) kbar. The angle between the a and the c axis, β, decreases up to 15 kbar then continues to decrease at a slightly reduced rate up to 28 kbar. Unlike $\mathrm{CuVOF_4(H_2O)_6{\cdot}H_2O}$, no structural phase transition is observed within the measured pressure range for $[\mathrm{Cu(pyz)_{0.5}(gly)}]\mathrm{ClO_4}$.

Figure 5.15(b) highlights the effect pressure has upon the Cu-Cu distances along the various magnetic exchange pathways within the $[\mathrm{Cu(pyz)_{0.5}(gly)}]\mathrm{ClO_4}$. The data in the bottom panel of Figure 5.15(b) show that the primary intradimer Cu-pyz-Cu exchange pathway is relatively unchanged over the measured pressure range, as the Cu-pyz-Cu distance at ambient [6.777(9) Å] and at 28(1) kbar [6.78(2) Å] are the same to within error. The kink-angle of the bridging pyrazine molecule, top-panel Figure 5.15(c), shows a very slight decrease, by $\approx 2^\circ$, when comparing the 28 kbar to the ambient data. (A large kink of the pyrazine ring may lead to an overlap of the d_{xy} or d_{yz} orbital of the Cu and the π-orbital on the pyrazine ring [203], resulting in a π exchange mechanism occurring alongside the σ exchange mechanism [88], increasing the overall exchange coupling within the dimer). The twist angle of the pyrazine ring, third-panel Figure 5.15(c), also shows little change upon increasing pressure. Whilst the pyrazine ring does tilt toward the glycine ligand upon increasing pressure, bottom-panel Figure 5.15(c), the pyrazine tilt-angle has been found to have little influence on the size of the magnetic exchange interactions in other Cu-pyz-Cu based low-dimensional magnets [204, 205]. As such, one might expect the primary intradimer exchange to be unchanged, as the pyrazine ring which dimerizes the two Cu ions is relatively robust over the measured pressure range.

The second panel of Figure 5.15(b) shows that upon increasing pressure, the distance between adjacent Cu ions along the interdimer Cu-gly-Cu direction initially decreases, plateaus in the pressure range $10 \leq P \leq 17$ kbar, then continues to decrease up to 28 kbar; a total reduction in the intralayer distance between Cu ions on adjacent dimers of ≈ 0.12 Å. This is likely followed by an increase in the magnitude of the intralayer coupling (J') between the dimers.

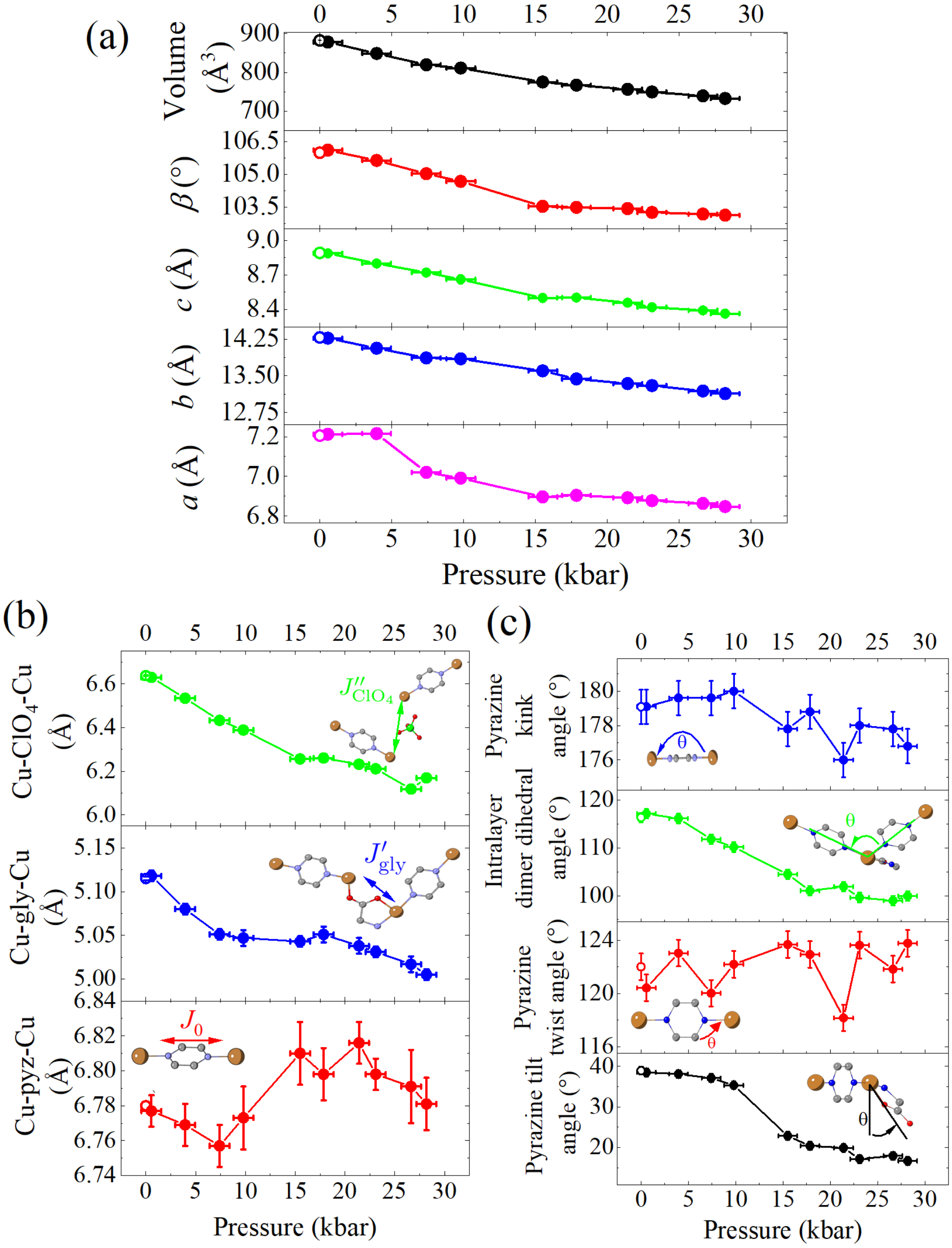

Figure 5.15: (a) Pressure dependence of the unit cell of [Cu(pyz)$_{0.5}$(gly)]ClO$_4$, open circle denotes ambient pressure measurement outside of cell and solid circles denote measurements made using a Tozer Diamond Anvil Cell. Pressure dependence of the distances between adjacent Cu ions (b) and various bond angles (c) along the exchange pathways in [Cu(pyz)$_{0.5}$(gly)]ClO$_4$. The intralayer dimer dihedral angle is measured between the N—Cu—Cu—N atoms and the pyrazine tilt angle is the dihedral angle between O—Cu—N—C atoms. Inset shows a cartoon of the exchange pathway, or bond-angle, being considered. Measurements performed at 300 K and errors plotted at 3σ.

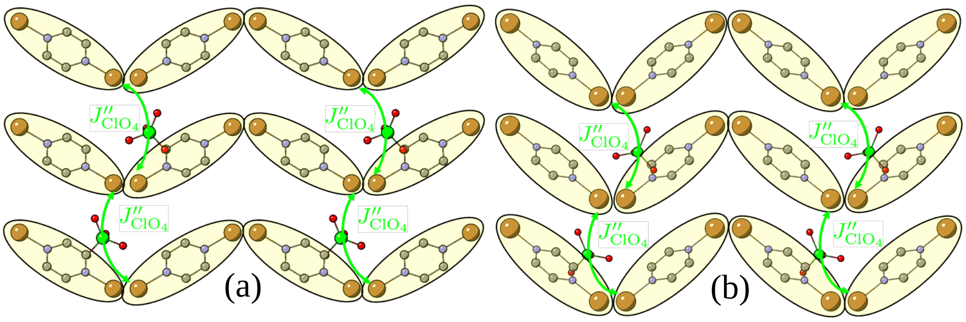

Figure 5.16: Packing of the dimer-units (shaded) at ambient (a) and 28(1) kbar (b) of pressure viewed along [101]. Intralayer glycine and H-atoms omitted for clarity. Data collected at 300 K.

The most dramatic change is seen in the interlayer distance, where dimers are coupled via ClO_4 ions along the $[10\bar{1}]$ direction as shown in the top panel of Figure 5.15(b). The interlayer Cu distance decreases linearly with increasing pressure up to 16 kbar, plateaus slightly up to 18 kbar, then continues to decrease up to 28 kbar. Over the measured pressure range, the interlayer distance between adjacent Cu ions is reduced by ≈ 0.5 Å. This indicates the greatest effect pressure has on the system is to pack the dimer layers more tightly along the $[10\bar{1}]$ direction, with adjacent dimers within the layers becoming more orthogonal to each other as they do so, see second panel of Figure 5.15(c) and Figure 5.16 (the change in structure moving from ambient to high-pressure is subtle, but involves an increased orthogonality between adjacent dimers and a tilting of the pyrazine ring).

5.3.4 Discussion

The temperature dependence of $H_{\mathrm{c}1,2}$ at various pressures for $[\mathrm{Cu(pyz)_{0.5}(gly)}]\mathrm{ClO_4}$ is shown in Figure 5.17(a). The bottom panel shows that up to 13(1) kbar, the dome-shaped phase-diagram remains centred around $H \approx 4$ T whilst the area enclosed by the dome within the temperature-field plane increases as $H_{\mathrm{c}1}$ moves to lower fields and $H_{\mathrm{c}2}$ to higher fields. Alongside this, both $H_{\mathrm{c}1}$ and $H_{\mathrm{c}2}$ remain distinguishable as separate features up to $T = 1.7$ K, compared to $T \approx 1.3$ K at ambient pressure, indicating that the XY-AFM ordered phase survives to higher temperatures upon increasing pressure.

Reference [37] shows that the critical fields within $[\mathrm{Cu(pyz)_{0.5}(gly)}]\mathrm{ClO_4}$ can be well described via [62],

$$g\mu_{\mathrm{B}}\mu_0 H_{\mathrm{c}1} = J_0 - J_{\mathrm{eff}}/2, \qquad g\mu_{\mathrm{B}}\mu_0 H_{\mathrm{c}2} = J_0 + J_{\mathrm{eff}}/2 \tag{5.4}$$

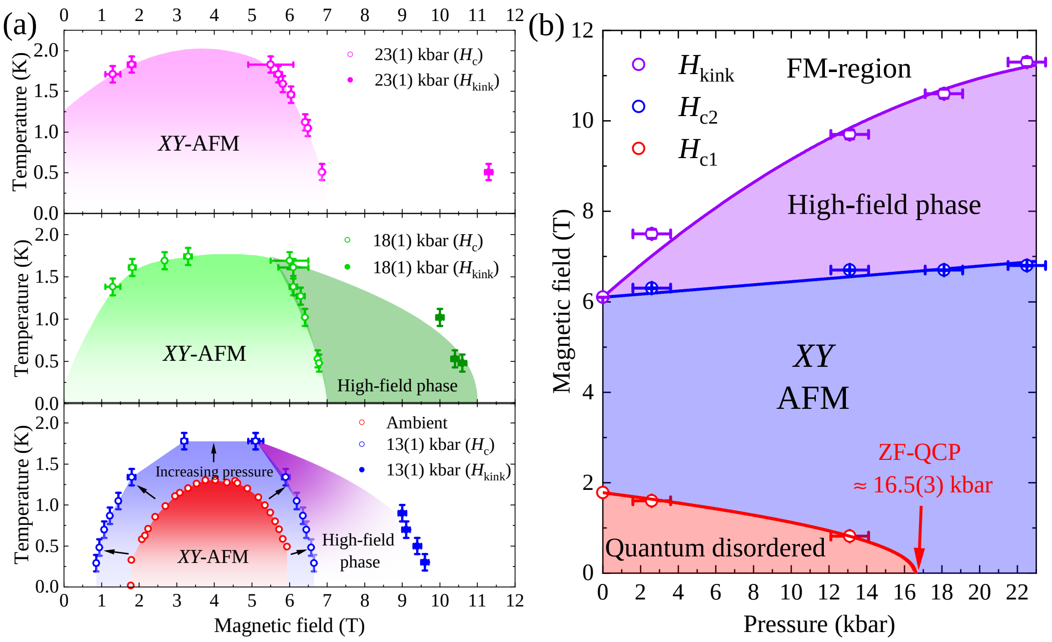

Figure 5.17: (a) Pressure-evolution of the temperature-field phase diagram from the bottom up for $[\mathrm{Cu(pyz)_{0.5}(gly)}]\mathrm{ClO_4}$ determined from $\mathrm{d}M/\mathrm{d}H$ data. Shaded areas denote regions of AFM order (suspected to be XY-AFM order as in other dimers) outlined by $H_{\mathrm{c}1,2}$. Within the centre and bottom panel, a high-field region is outlined $H_{\mathrm{c}2}$ and H_{kink} is also shaded. (b) Pressure-field phase diagram with values of $H_{\mathrm{c}1}$, $H_{\mathrm{c}2}$ and H_{kink} determined from extrapolations to 0 K. Estimated position of zero-field quantum critical point (ZF-QCP) pressure indicated with an arrow.

where J_{eff} is the total interdimer exchange coupling $J_{\mathrm{eff}} = 4(J'_{\mathrm{gly}} + J''_{\mathrm{ClO_4}})$ with $J''_{\mathrm{ClO_4}} \approx 0$ K at ambient pressure. At 13 kbar, Eqs. 5.4 return $J_0 = 5.5(2)$ K, which is within error of the ambient value $J_0 = 5.8(2)$ K and in agreement with the structural data which shows that the Cu-pyz-Cu bond remains relatively sturdy up to 28 kbar, such that one would expect a constant J_0. The value of the total interdimer coupling rises from $J_{\mathrm{eff}} = 6.3(1)$ K at ambient pressure to $J_{\mathrm{eff}} = 8.6(1)$ K at 13 kbar. This is in keeping with the pressure-induced structural changes, where the interdimer distance both within and between the corrugated dimer layers is seen to decrease upon increasing pressure.

Whilst $H_{\mathrm{c}2}$ and H_{kink} are distinguishable up to the highest measured pressure, at low-temperatures $H_{\mathrm{c}1}$ ceases to be resolvable within the pressure range $13 < P \leq 18$ kbar. As $H_{\mathrm{c}1}$ arises due to the closing of the singlet-triplet energy gap Δ, its disappearance indicates increasing pressure acts to reduce and eventually suppress Δ to ZF. A reduction in Δ upon increasing pressure is observed in similar materials, such as the spin-ladder system IPA-CuCl$_3$ [206]; the dimer system $(\mathrm{C_4H_{12}N_2})\mathrm{Cu_2Cl_6}$

(PHCC) [207]; and the archetypal dimer compound $\mathrm{TlCuCl_3}$ [172].

Within $\mathrm{TlCuCl_3}$, pressure serves to increase the ratio between the interdimer and intradimer exchange coupling, which ultimately drives the closure of the singlet-triplet energy gap at 4.4 kbar, as the system is pushed through a pressure-induced QCP and into a long-range AFM ordered state [172, 208, 209]. Similarly, in $[\mathrm{Cu(pyz)_{0.5}(gly)]ClO_4}$, up to 13 kbar, a reduction in the interdimer distances is seen to increase the magnitude of the interdimer exchange whilst intradimer exchange remains relatively unchanged due to the robust nature of Cu-pyz-Cu dimer-unit.Thus, like $\mathrm{TlCuCl_3}$, it is highly likely that between $13 < P \leq 18$ kbar the magnetic ground-state of $[\mathrm{Cu(pyz)_{0.5}(gly)]ClO_4}$ moves from one of quantum-disorder to that of an AFM long-range ordered state (likely XY-AFM order as observed in other dimers), as outlined within the top two panels of Figure 5.17(a).

Magnetometry evidence for an AFM ordered ground-state in $\mathrm{TlCuCl_3}$ is given by the emergence of a spin-flop feature in $M(H)$ at 4.4 kbar. Whilst no spin-flop is observed in $M(H)$ of $[\mathrm{Cu(pyz)_{0.5}(gly)]ClO_4}$ at high pressure, at $P \geq 19(1)$ kbar $M(H)$ lacks the sharp upturn at $H = H_{\mathrm{c1}}$, indicative of the field-induced closing of the singlet-triplet energy gap. The $M(H)$ curve is much alike that of other gapless low-dimensional molecule-based Cu(II) compounds [41, 65], and that predicted by Quantum-Monte-Carlo (QMC) calculations performed on similar dimer lattices which undergo a transition to a 3D AFM ordered state, also driven by an increase in the ratio of J_{eff}/J_0 [210].

Figure 5.17(b) shows the zero-temperature pressure-field phase diagram for $[\mathrm{Cu(pyz)_{0.5}(gly)]ClO_4}$, found by extrapolating the values of H_{c1}, H_{c2} and H_{kink} to 0 K. To more accurately estimate the critical pressure (P_{c}) to close the singlet-triplet energy gap in $[\mathrm{Cu(pyz)_{0.5}(gly)]ClO_4}$, the pressure-dependence of H_{c1} can be fit to a square root power law (as done previously for the dimer material $\mathrm{TlCuCl_3}$ [172]) which estimates a critical pressure of $P_{\mathrm{c}} = 16.5(3)$ kbar. This also gives a rate of change of the gap with pressure of $\mathrm{d}\Delta/\mathrm{d}P \approx 0.2$ K kbar^{-1}, similar to other, molecule-based, gapped systems, with $\mathrm{d}\Delta/\mathrm{d}P \approx 0.6$ K kbar^{-1} for PHCC and $\mathrm{d}\Delta/\mathrm{d}P \approx 0.1$ K kbar^{-1} for IPA-$\mathrm{CuCl_3}$.

As shown in section 5.3.3, the primary effect of pressure on $[\mathrm{Cu(pyz)_{0.5}(gly)]ClO_4}$ is to more tightly pack the corrugated dimer sheets along the $[10\bar{1}]$ direction. This is highlighted by a reduction in the $\mathrm{Cu}\cdots\mathrm{Cu}$ distance along the $\mathrm{ClO_4}$ direction of 0.36 Å, compared to a 0.1 Å reduction along the glycine direction, when moving from ambient to $P \approx P_{\mathrm{c}}$. As such, it is likely that the transition to AFM long-range order is predominantly driven by an increase in the magnitude of $J''_{\mathrm{ClO_4}}$ (where $J''_{\mathrm{ClO_4}} = 0$ K at ambient) upon increasing pressure. Given this, if one assumes a constant J_0 and J'_{gly} up to P_{c}, an estimation of $J''_{\mathrm{ClO_4}} = 0.7(2)$ K at $P = P_{\mathrm{c}}$ can be obtained. This subsequently gives an average interdimer coupling [$\overline{J'} = (J'_{\mathrm{gly}} + J''_{\mathrm{ClO_4}})/2$] to intradimer coupling ratio of $\overline{J'}/J_0 = 0.20(3)$ at $P = P_{\mathrm{c}}$. This value is remarkably close to the critical coupling ratio of $\overline{J'}/J_0 = 0.217$ predicted by QMC calculations to be the point at which similar dimer systems enter a 3D AFM Néel ordered state [210].

Above H_{c2}, the temperature dependence of H_{kink} maps out a high-field region of the phase-diagram, which exists above and below P_{c}, as outlined in Figure 5.17. This region is attributed to the slight canting of the spins along the field at $H = H_{\mathrm{c2}}$ before the spins are fully polarised along the field direction at $H = H_{\mathrm{kink}}$. Whilst the pressure-evolution of $M(H)$ within [Cu(pyz)$_{0.5}$(gly)]ClO$_4$ is akin to that predicted by QMC calculations [210] (suppression of H_{c1} to ZF and H_{c2} tracking to higher fields as $\overline{J'}/J_0$ grows), the existence of H_{kink} is not predicted.

As the model systems in reference [210] deal with equivalent intralayer and interlayer interdimer exchange pathways, the inequivalent interlayer and intralayer exchange pathways in [Cu(pyz)$_{0.5}$(gly)]ClO$_4$ may be the source of the three features seen in $M(H)$ data. Further QMC calculations are underway to verify this hypothesis and to elucidate the nature of the high-field phase. The existence of H_{kink} may also be due to the presence of a small DMI term, suspected to exist between the dimers at sufficiently low-temperatures [37, 168]. One can suppose that the increased orthogonality between adjacent dimers caused by increasing pressure, see Figure 5.16, may serve to increase the strength of any interdimer DMI term [as $\boldsymbol{D} \cdot (\mathbf{S}_1 \times \mathbf{S}_2)$] up to 28(1) kbar, explaining why H_{kink} tracks to higher fields upon increasing pressure.

5.4 Summary

In summary, in this chapter I have shown via multiple measurement techniques that the magnetic ground-state of $\mathrm{CuVOF_4(H_2O)_6{\cdot}H_2O}$ is that of a lattice of $S = 1/2$ AFM coupled dimers with weak AFM interdimer interactions. An applied magnetic field drives the system into an triplet excited state at H_{c1}, whilst further application of field pushes the system into an FM saturated state at H_{c2}. Similar to other dimer systems, the temperature dependence of $H_{\mathrm{c1,2}}$ allows the construction of the temperature-field phase diagram of the system, shown in Figure 5.7, which encloses a region of triplet excitations. However, $\mathrm{CuVOF_4(H_2O)_6{\cdot}H_2O}$ is prohibited from mapping onto the BEC of magnons picture due to the broken rotational symmetry of the system. The crystal structure breaking the rotational symmetry of a dimer system has been previously reported [169, 170], however, $\mathrm{CuVOF_4(H_2O)_6{\cdot}H_2O}$ appears unique in that the $O(2)$ symmetry is also broken by the spin-species that make up the dimer-unit itself. Additionally, J_0 in this material is mediated by a rarely seen form of exchange coupling which seems to act along the JT-axis of the Cu. The underlying mechanism for this is suspected to be due to significant spin-density being donated to the bridging oxide ligand by the neighbouring vanadyl group.

The pressure dependence of the magnetic and structural properties of $CuVOF_4(H_2O)_6{\cdot}H_2O$ both corroborate with the Cu—O—V bond being the primary pathway which mediates J_0. Up to 24(1) kbar, the magnetometry data shows the dimer state is made more robust by increasing pressure, as the increase in the strength of J_0 in turn increases the magnitude of the singlet-triplet energy gap. The pressure-induced changes in the structure indicate this behaviour likely continues up to 28(1) kbar.

The strengthening of the disordered ground-state under pressure in $CuVOF_4(H_2O)_6{\cdot}H_2O$ is in contrast the pressure-evolution of the magnetic properties of $[Cu(pyz)_{0.5}(gly)]ClO_4$. In the latter, pressure reduces the interdimer distances, mostly notably between the corrugated dimer sheets. This serves to increases the interdimer AFM exchange interactions and ultimately pushes the system through a pressure-induced QCP, at $P_c \approx 16.5(3)$ kbar, as the ZF ground-state becomes one of long-range AFM order. In addition, the robust intradimer Cu-pyz-Cu bond leaves J_0 unchanged to within error. In contrast, for $CuVOF_4(H_2O)_6{\cdot}H_2O$ the Cu—O—V J_0 pathway kinks upon increasing hydrostatic pressure, driving J_0 to higher values. (Figure 5.18 shows a comparison of the change in exchange energies with increasing pressure for the two dimers.) Furthermore, whilst pressure does bring adjacent dimers into closer proximity in $CuVOF_4(H_2O)_6{\cdot}H_2O$, rotations of the water ligands within the complex interdimer exchange network leaves J' unchanged, even as the system enters the high-pressure $P2_12_12_1$ phase. One can speculate about the existence of a pressure-induced QCP in $CuVOF_4(H_2O)_6{\cdot}H_2O$ should the Cu—O—V bond continue to kink for $P > 30$ kbar. This may eventually diminish the AFM component of J_0 as the bond-angle moves closer to 90°. A similar process is observed in the dimer $KCuCl_3$, where a reduction in the Cu—Cl—Cu intradimer bond-angle with pressure correspondingly decreases J_0, and is thought to be the primary driver behind the transition to long-range AFM order at ≈ 8.4 kbar [211].

Whilst other dimer systems do exhibit a reduction in the singlet-triplet energy gap with increasing pressure, to date, few compounds have been shown to have values of P_c low enough to suppress the QCP to ZF [174]; namely, $TlCuCl_3$ [172], $KCuCl_3$ [211] and PHCC [212]. Each of these possess large H_{c2} values: ~ 100 T for $TlCuCl_3$; 54.5 T for $KCuCl_3$; and 37 T for PHCC [23]. As such, $[Cu(pyz)_{0.5}(gly)]ClO_4$ is

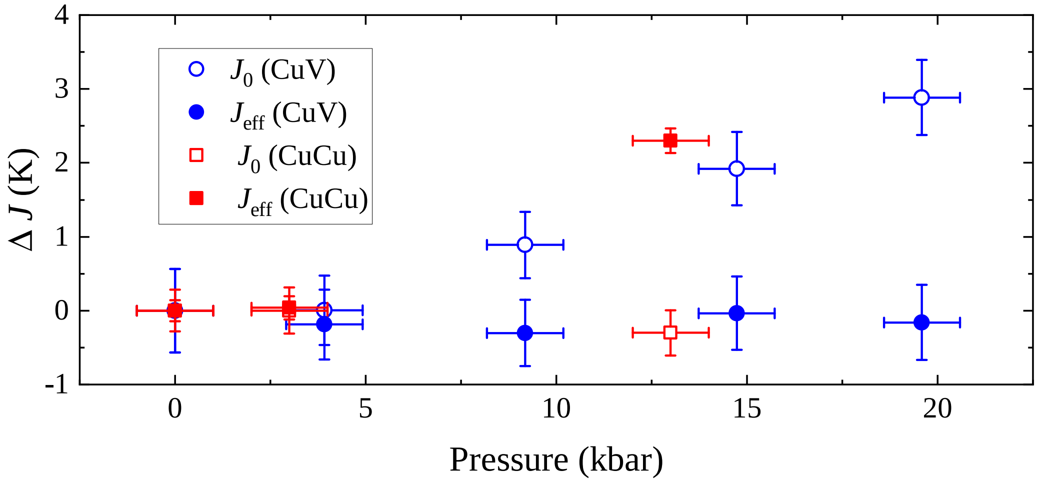

Figure 5.18: Comparison of the change in intradimer J_0 (open shapes) and effective interdimer J_{eff} (filled shapes; equal to the sum of all the interdimer exchange energies) exchange energies for $\mathrm{CuVOF_4(H_2O)_6{\cdot}H_2O}$ (blue circles) and $\mathrm{[Cu(pyz)_{0.5}(gly)]ClO_4}$ (red squares) upon increasing pressure.

uniquely placed, owing to both the low critical field values and P_c, to be a prime candidate for neutron studies, as the full pressure-field phase-diagram can be accessed at user facilities and, as such, the role quantum fluctuations play in driving both field-induced and pressure-induced QCPs can be investigated simultaneously within a single system. Alongside this, neutron and QMC studies would be extremely valuable to help elucidate the nature of the suspected spin-canted phase for $H_{c2} < H < H_{\mathrm{kink}}$.

Chapter 6

Conclusion

Within this thesis, I have presented studies on five quantum magnets, characterising their magnetic properties and investigating how these properties evolve under extreme conditions, such as high magnetic fields, high pressures and low temperatures. This chapter will summarise these studies and present a brief outlook as to possible future experiments.

Within Chapter 3, the magnetic properties of the isostructural ferromagnetic chains compounds $\mathrm{Ni(NCS)_2(thiourea)_2}$ and $\mathrm{Co(NCS)_2(thiourea)_2}$ were characterised. Both compounds present strong platforms to investigate Q1D behaviour due to the weak interchain coupling $|J'|/J_0 \sim 0.01 - 0.1$ K. The Ni compound is chemically similar to the known BEC quantum-magnet DTN [$\mathrm{NiCl_2(thiourea)_4}$], however, the magnetic properties of the two are drastically different, as substitution of the axial Halide ligand results in the ground state changing from a weakly coupled Q1D $S = 1$ XY-AFM chain in DTN ($J \approx 1.7$ K and $J' \approx 0.17$ K) to a Q1D chain with very strong FM intrachain coupling, $|J| \sim 100$ K, in $\mathrm{Ni(NCS)_2(thiourea)_2}$. The intrachain FM coupling within the Co species is approximately an order of magnitude weaker than in the Ni owing to the presence of an AFM through-space intrachain exchange, an interaction absent in the Ni species due to the magnetic orbitals being constrained along the through-bond direction. The competition between the FM through-bond and AFM through-space exchange results in a drastic reduction in J_{Co}, despite the near identical exchange pathways in the two compounds. The work, published in reference [213], represents a notable study in low-dimensional magnetism, and indicates how substitution of the spin species alone can dramatically alter the strength of the magnetic exchange interactions.

Further to this, the effective spin-half FM Ising ground-state within $\mathrm{Co(NCS)_2(thiourea)_2}$ is akin to that of $\mathrm{CoNb_2O_6}$, which is the archetypal system for investigating the transverse-field Ising model, a celebrated ‘textbook example’ of quantum criticality [31]. If an appropriate method to affix $\mathrm{Co(NCS)_2(thiourea)_2}$ single-crystals with field perpendicular to the Ising-axis could be found, then this system may offer the tantalising possibility of a further physical realisation of the transverse-field Ising model. For $\mathrm{CoNb_2O_6}$, inelastic neutron studies revealed the emergence of a rare $E8$ symmetry once the external transverse field breaks the FM order of the ground-state [214], as such, it is possible that $\mathrm{Co(NCS)_2(thiourea)_2}$ may offer similar exotic excitations.

Turning to AFM coupled Q1D systems, Chapter 4 outlines a study of the near-ideal molecule-based Haldane spin-chain $\mathrm{NiI_2(3,5\text{-}lut)_4}$. A combination of pulsed-field magnetometry, single-crystal magnetometry and zero-field inelastic neutron scattering (INS) measurements enable the values of the anisotropic Haldane-gaps, $\Delta^{\parallel} = 5.3(1)$ K and $\Delta^{\perp} = 7.7(1)$ K, and critical fields, $\mu_0 H_{\mathrm{c}}^{\parallel} = 5.3(1)$ T and $\mu_0 H_{\mathrm{c}}^{\perp} = 4.3(1)$ T, to be extracted. These return an intrachain exchange of $J = 17.5(2)$ K. ESR enables the Ising-like SIA parameter to be determined at $D = -1.2(1)$ K. The absence of long-range order down to 20 mK, from μ^{+}SR measurements, suggests a vanishingly small J'. This leads to the system being found to reside deep within the Haldane phase, with only $\mathrm{AgVP_2S_6}$ closer to the origin of the Q1D $S = 1$ AFM phase-diagram due to minute D/J and J'/J ratios. However, the large magnitude of the intrachain exchange, $J = 780$ K [55], in $\mathrm{AgVP_2S_6}$ makes closing the Haldane-gap using an applied magnetic field problematic.

In contrast, the low critical-fields of $\mathrm{NiI_2(3,5\text{-}lut)_4}$ mean that the Haldane-gap can be readily closed using standard laboratory magnetic fields. As such, it is able to test the applicability of two quantum-field-theoretical models which describe the behaviour of Haldane chains in the vicinity of the closure of the gap: the boson model, which has been posited to be applicable to easy-axis Haldane systems; and the fermion model, which was thought to be applicable only to easy-plane Haldane chains. By comparing the predicted g-factors for each of these models against those extracted from various experimental techniques, it was found that the fermion model better accounts for the measured g-factors, providing evidence to possibly overturn the notion that the fermion model describes exclusively easy-plane Haldane systems. This published work [38] therefore evokes the need for the development of a further theoretical framework which, in particular, is able to explain the applicability of the boson model in describing the behaviour of the vanadate Haldane family, $\mathrm{PbNiV_2O_8}$ [147] and $\mathrm{SrNiV_2O_8}$ [215], at fields close to the critical values. Additionally, the highly tunable nature of this molecule-based Haldane system, lends itself to investigations into the effect introducing non-magnetic defect sites has on the

Haldane-phase, something that there is presently a paucity of [36].

As noted above, the critical fields in $\mathrm{NiI_2(3,5\text{-}lut)_4}$ are well within the range of commercially available superconducting magnets being $\mu_0 H < 6$ T. Thus, the system provided an ideal opportunity for in-field INS studies to observe the closure of the Haldane-gap. The in-field INS data in this thesis appears to directly observe the closure of the gap around 4.4 T, in excellent agreement with other techniques, as well as the emergence of a new in-field excitation for $\mu_0 H \geq 2$ T. The new excitation tracks linearly with field and persists up to 6 T, well above the closure of the Haldane-gap. It is attributed to the existence of $S = 1/2$ end-chains, due to the excellent agreement of the INS data with ESR data, and similar excitations observed in the Haldane compounds NENB [158] and $\mathrm{Y_2BaNi_{x-1}Mg_xO_5}$ [56]. The possible existence of $S = 1/2$ end-chains upon the field-induced closure of the Haldane-gap is perhaps surprising. End-chains are predicted features of the Haldane ground-state as described by the AKLT model [34, 152]. Therefore, one might expect their demise as the Haldane ground-state is rapidly depopulated for $H > \overline{H}_\mathrm{c}$, leading to the strength of the end-chain excitation seen in the INS data to rapidly decrease for $H > \overline{H}_\mathrm{c}$, which does not seem to be the case. To understand this, a detailed theoretical modelling of the excitation spectrum of this material is currently underway, in order to ascertain the origin of this exotic excitation. Alongside this, further temperature dependent ESR measurements may also help elucidate the nature of this excitation. Furthermore, the application of hydrostatic pressure shows pressure can readily tune the strength of the intrachain magnetic exchange, driving $\mathrm{NiI_2(3,5\text{-}lut)_4}$ deeper into the Haldane phase. However, high-pressure crystallography studies are planned to verify that this increase in J is indeed due to a decrease in the intrachain $\mathrm{I \cdots I}$ distance, as is suspected. These measurements help to confirm $\mathrm{NiI_2(3,5\text{-}lut)_4}$ is an ideal test-bed for studying Haldane physics in a variety of extreme environments.

The results in Chapter 5 outline a detailed study of the $S = 1/2$ AFM dimer compound $\mathrm{CuVOF_4(H_2O)_6{\cdot}H_2O}$, revealing its ground-state to be that of a disordered sea of spin-singlets, with strong intradimer coupling $J_0 \approx 21$ K and weak AFM coupling between dimers $J' \approx 1$ K. The temperature dependence of the two critical fields, H_c1 and H_c2, encloses a region of triplet excitations, akin to other BEC class dimer systems, but one which cannot be mapped directly onto the BEC of magnons picture, due to the broken rotational symmetry of the system; as in other dimer compounds [169, 170]. What appears to make $\mathrm{CuVOF_4(H_2O)_6{\cdot}H_2O}$ unique is that the rotational symmetry is not only broken by the asymmetric structure, but also by the spin-species that make up the dimer. The effect of the two unlike spin-species may give rise to an uncompensated moment on the dimers, hinted at in the ESR data by the existence of a g-factor between that of the Cu(II) and V(IV) values, however, at present, the ESR data cannot rule out the possibility of this resonance originating from impurity spins. As such, further ESR measurements are planned in an attempt to resolve this, alongside an investigation into the origin of the mysterious G_3 mode which has not been observed in similar AFM dimers.

The ambient work on this compound is a published study [216]. The significance of this work also in the observation of a rare form of strong magnetic exchange which is seemingly mediated along the Jahn-Teller axis of the Cu ion. The mechanism for this is suspected to be primarily due to the antiferromagnetic coupling between the V and the bridging oxygen ligand, which hosts a sizable spin-density donated to it by the vanadyl group. However, the process by which the exchange is further mediated along the Jahn-Teller axis to the Cu ion is not necessarily clear, and warrants additional study. Alongside this, high-pressure studies, which provide further evidence of strong exchange along the Jahn-Teller direction, show that the application of hydrostatic pressure is able to increase the strength of J_0 whilst leaving J' unaffected, enabling the quantum-disordered phase of $\mathrm{CuVOF_4(H_2O)_6{\cdot}H_2O}$ to survive to higher fields upon increasing pressure; even after the compound undergoes a structural phase-transition to the chiral $P2_12_12_1$ spacegroup.

A parallel pressure study on the symmetric dimer compound $[\mathrm{Cu(pyz)_{0.5}(gly)}]\mathrm{ClO_4}$ reveals radically different behaviour, as the application of pressure drives the singlet-triplet energy gap to ZF, with the system passing through a pressure-induced QCP at a critical pressure of $P_\mathrm{c} \approx 16.3(5)$ kbar. This quantum phase transition is driven by increasing pressure forcing closer packing of the corrugated dimer layers along the $[10\overline{1}]$ crystallographic direction, in addition to a decrease in the intradimer Cu-gly-Cu distance. These structural changes correspond to significant increases in the interdimer exchange interactions, to the point where the interdimer exchange becomes strong enough to promote the formation of a long-range AFM ordered state in ZF. Few other dimer compounds have a critical pressure low enough to observe this phenomena [172, 211, 212], and of those that do all have values of $H_{\mathrm{c}2} > 35$ T, which is far above what can be readily accessed at most user facilities. Thus, the fact $H_{\mathrm{c}2}$ remains located at ≈ 7 T for pressures above the critical pressure P_c, and up to at least 24(1) kbar, combined with the relatively low $P_c \approx 16.3$ kbar in $[\mathrm{Cu(pyz)_{0.5}(gly)}]\mathrm{ClO_4}$, make it ripe for neutron studies, as it presents a unique opportunity to observe how quantum fluctuations influence both field- and pressure-induced QCPs, across the entire pressure-field phase-diagram, all within a single compound. The study of the two dimer compounds also highlights the starkly different effect pressure has on tuning the crystal and magnetic structure within low-dimensional quantum magnets.

This work shows that molecular building blocks are excellent starter materials for use in constructing a variety of quantum-magnets which can exhibit extreme low-dimensionality, as well as interesting excited states which emerge due to the collective interactions between the spin and electronic degrees of freedom in the system. Some of the materials in this thesis were found to exist at the edge phase-instability. Therefore, the work also shows that ultra-high magnetic fields and applied pressures can be used to push systems through the critical region, where the state of matter changes and inherently quantum effects dominate. Due to the low energy scale of their magnetic interactions and compressible structure, coordination polymers are exceedingly apt materials to study QPTs, as the magnetic fields and pressures required to push them through the critical region is reduced considerably in comparison to inorganic systems. This allows one to more easily investigate the influence quantum fluctuations have on driving QPTs. The molecule-based systems studied here are also promising candidates for future investigations into the effect disorder has on the stability of quantum states. The work in this thesis is a contribution to the wider effort which aims to shed light on how inherently quantum systems can interact collectively, on the microscopic scale, to exhibit interesting and desirable macroscopic properties. By understanding this, the work aims to move toward building bespoke, functional quantum-materials which could one day find use in next generation medical devices, energy generation, as well as fast and secure data storage and processing. In addition, they can be used to test the limits of theoretical predictions to help provide a better fundamental understanding of quantum mechanics, such as was done for the Haldane chain system in this thesis.

Appendix A

A.1 Background subtraction in SQUID magnetometry measurements

A.1.1 ^{3}He sample holder

One difficulty is reliably reproducing the positioning of the sample and ^{3}He sample insert relative to the measurement coils. It has been noted in similar measurements (such as those involving pressure-cells which also have an inherently large background signal) that a small misalignment between the position of the 'sample-in' (^{3}He sample-insert plus sample) measurement compared to the 'sample-out' (just the ^{3}He sample-insert) background measurement, coupled with small sample signal, can lead to erroneous background subtraction [217–219]. As the Haldane ground-state is inherently non-magnetic and only a small fraction of the sample contributes to the low-field low-temperature paramagnetic response, as determined by $\chi(T)$, $M(H)$ and ESR measurements, a small sample signal relative to the background signal at low-fields and temperatures is intrinsic to this measurement.

The top-panel of Figure A.1(a) highlights this, as at low-temperature and field the background signal is sizable relative to the sample response. However, upon increasing field the sample signal is found to increase significantly, making it the dominant signal at higher fields, especially for $H \geq H_\mathrm{c}$, as can be seen in the centre and bottom panel of Figure A.1(a). In addition, the background response from the sample-insert is found to be nearly field independent above 1.5 T, Figure A.1(b). This leaves no doubt that the measured response at higher fields, especially near the closing of the Haldane-gap $H \geq 4$ T, is dominated by the sample.

A.1.2 QD-MPMS pressure-cell

The SquidLab background subtraction software [78] was used to isolate the sample response from the diamagnetic background of the pressure-cell. The background measurement involves the cell compressing a blank sample chamber (Teflon cup plus

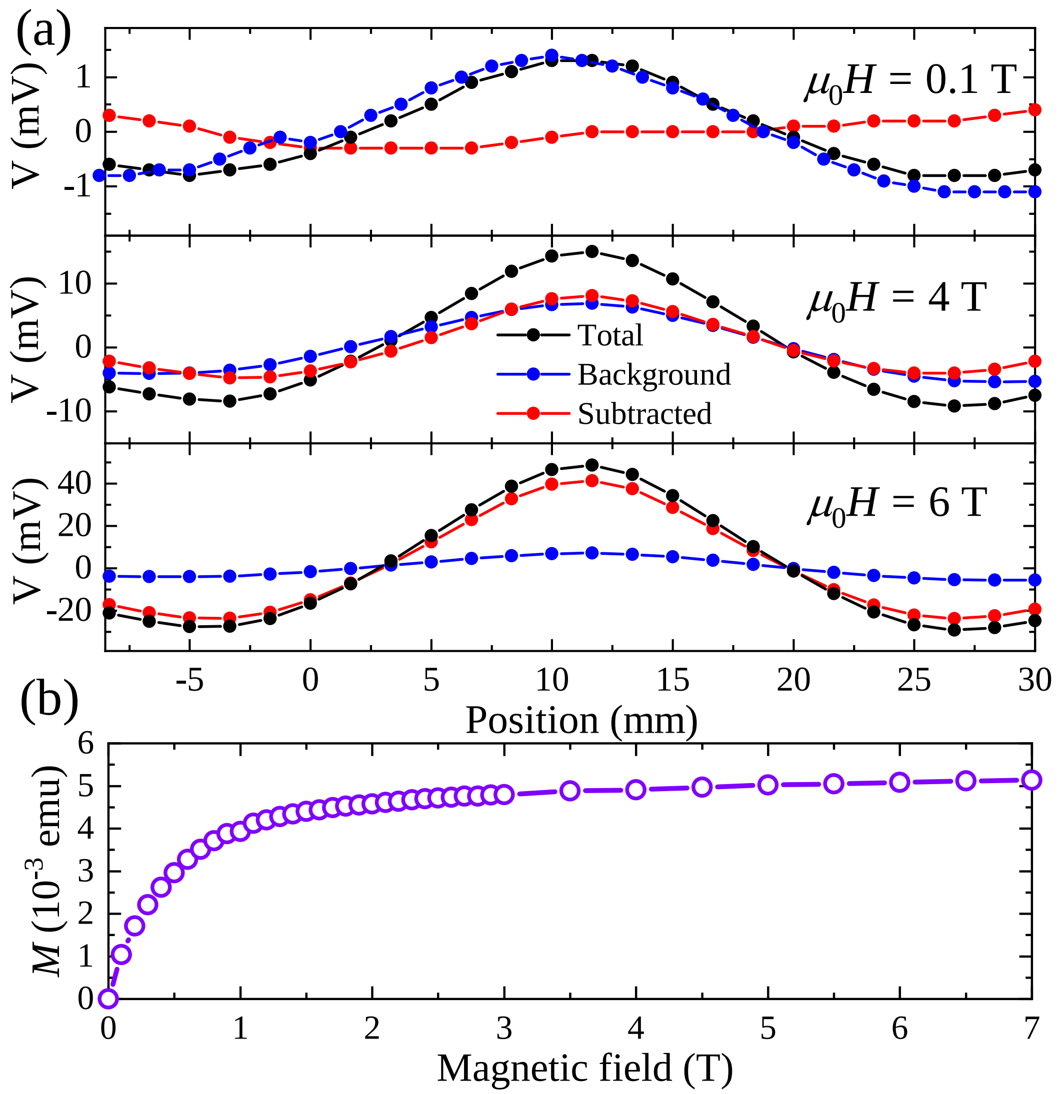

Figure A.1: (a) Raw SQUID dipole signal vs position plots for measurements using the *i*-Quantum ^{3}He insert at 0.5 K, showing the total measured signal (black), background response (blue) and the background-subtracted result (red) at various magnetic field values ($\mu_0 H$) given in the top-right corner of each panel. Background subtraction is performed using the SquidLab program [78]. (b) Measured background only $M(H)$ response at 0.5 K.

pressure-transmitting medium with no sample) to the same length as in the sample measurement (see section 2.1.4). Great care was taken to accurately reproduce the position of the sample measurement (sample plus pressure-cell) and background measurement (pressure-cell only) relative to the MPMS measurement coils, as misalignment can lead to errors in background subtraction [217–219]. For a large sample moment relative to the background signal, see Figure A.2(a), a slight misalignment

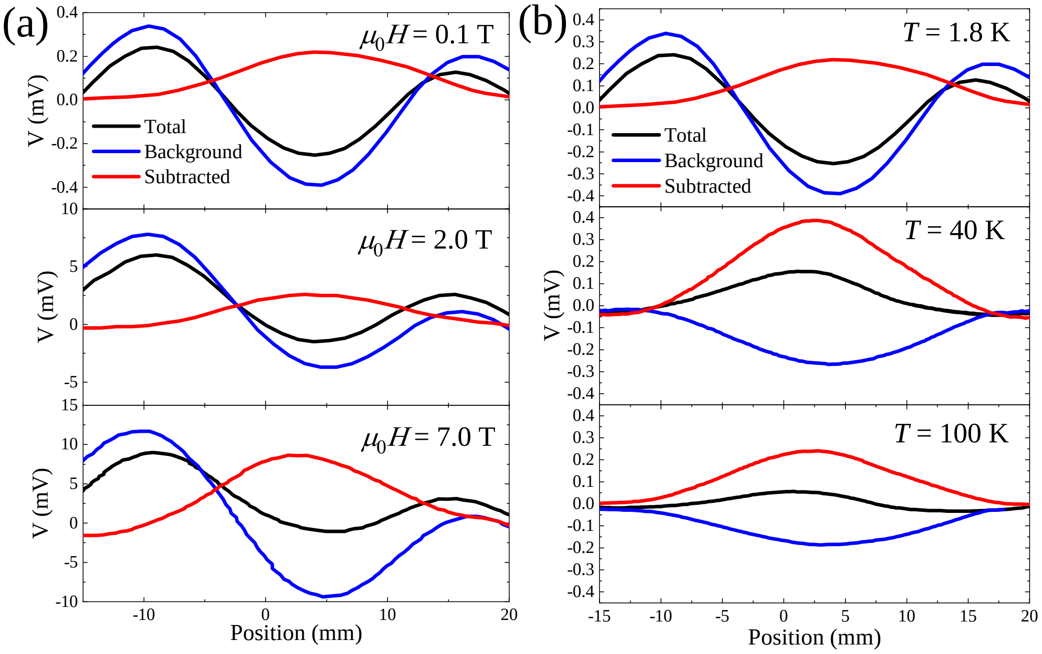

Figure A.2: Raw SQUID dipole signal vs position plots for 4.4 kbar data measured using the Quantum-Design MPMS pressure-cell. The total measured signal (black), background response (blue) and the background-subtracted result (red) are shown for data (a) at a fixed temperature (1.8 K) for various magnetic field values and (b) for a fixed field ($\mu_0 H = 0.1$ T) at various temperatures (changes in the form of the data on cooling are due to thermal contraction of the cell). Background subtraction is performed using the SquidLab program [78].

has little effect on the measured response. This is exemplified in Figure 4.10(a), where $M(H)$ under pressure agrees well with the ambient data for $H < H_c$. At very low-fields, necessary in $\chi(T)$ measurements, a small sample moment relative to the background is inherent, see Figure A.1(b), such that a slight misalignment can lead to a small error in the absolute value of the measured moment. When modelling $\chi(T)$ using Eq. 4.6, this translates to a slightly reduced g-factor (see below). However, the form of $\chi(T)$, parameterised by J and Δ_0 in Eq. 4.6, is unaffected, and thus these parameters can be extracted reliably.

A.2 Structural data

The structural data for all the compounds discussed within this thesis is presented below. For the dimer materials $\mathrm{CuVOF_4(H_2O)_6{\cdot}H_2O}$ and $\mathrm{[Cu(pyz)_{0.5}(gly)]ClO_4}$, where structural properties were tracked as a function of applied hydrostatic pressure, the data are presented at ambient pressure and for one high-pressure data

Table A.1: Single crystal x-ay data and refinements details for Co(NCS)$_2$(thiourea)$_2$ and Ni(NCS)$_2$(thiourea)$_2$ as found in [213]

Parameter (units)	Fit Results (error)	
Formula	$CoS_4N_6C_4H_8$	$NiS_4N_6C_4H_8$
M.W. / g·mol^{-1}	327.34	327.10
Temperature / K	100(2)	173(2)
Crystal system	primitive	primitive
Space group	$P\bar{1}$	$P\bar{1}$
a / Å	3.82030(10)	3.7615(2)
b / Å	7.5341(2)	7.5273(5)
c / Å	10.0847(2)	10.0744(7)
α / °	92.065(2)	92.129(5)
β / °	98.230(2)	98.055(5)
γ / °	104.835(2)	104.080(5)
Volume / Å^3	276.896(2)	273.19(3)
Z	1	1
ρ_{calc} / g·cm^{-3}	1.961	1.988
μ / mm^{-1}	2.275	2.513
2θ range /°	4.1 - 90.7	4.1 - 26.2
h index range	-7 / 7	-4 / 4
k index range	-15 / 14	-9 / 9
l index range	-20 / 20	-13 / 13
Collected/unique	40906 / 4662	4059 / 2315
R$_{int}$	0.040	0.039
R$_\sigma$	0.018	0.049
	Spherical atom refinement	
Data/restr./param.	4527/0/71	2315/0/87
GooF on F^2	1.057	1.028
R indexes [I≥2$_\sigma$]	R1 = 0.022	R1 = 0.030
	wR2 = 0.06	wR2 = 0.08
Residuals /eÅ^{-3}	0.75/-0.95	0.64/-0.32
	Multipole model refinement	
Data/restr./param.	4650/0/279	
GooF on F^2	1.069	
R indexes [all data]	R1 = 0.019	
	wR2 = 0.05	
Residuals / eÅ^{-3}	0.63/-0.75	

collection.

Table A.2: Single crystal X-ray data and refinements details for NiI_2(3,5-lut)$_4$ at ambient pressure as found in [38].

Parameter (units)	Fit Results (error)
Instrument	Huber3-circle fixed-Kappa
Method	Single crystal
Empirical formula	$C_{28}H_{36}I_2N_4Ni$
Formula weight (g mol^{-1})	741.11
Temperature (K)	100
Crystal system	tetragonal
Space group	$P4/ncc$
a (Å)	12.0019(3)
b (Å)	12.0019(3)
c (Å)	9.9783(2)
α (°)	90
β (°)	90
γ (°)	90
Volume (Å^3)	1437.33(8)
Z	2
ρ_{calc} (g cm^{-3})	1.712
μ (mm^{-1})	0.646
/,(Å)	0.41328
Reflections collected	51036
Independent reflections	1272
Parameters	44
Goodness-of-fit	1.184
Final R indexes [$I \geq 2\sigma$ (I)]	$R_1 = 0.0142$
	w$R_2 = 0.0420$

Table A.3: Single crystal X-ray data and refinements details for $CuVOF_4(H_2O)_6{\cdot}H_2O$ at ambient and 26(1) kbar of pressure.

Parameter (units)	Fit Results (error)		
Instrument	Rigaku Oxford Diffraction Synergy S		
Method	Single crystal		
Empirical formula	$Cu\ F_4\ H_{14}\ O_8\ V$		
Formula weight (g mol^{-1})	332.59		
Pressure (kbar)	Ambient	Ambient	26(1)
Temperature (K)	150	300	300
Crystal system	orthorhombic		
Space group	$Pna2_1$	$Pna2_1$	$P2_12_12_1$
a (Å)	15.65164(16)	15.6961(2)	7.3115(9)
b (Å)	8.24054(8)	8.26990(10)	7.8864(14)
c (Å)	7.37877(7)	7.41590(10)	15.2574(7)
α (°)	90	90	90
β (°)	90	90	90
γ (°)	90	90	90
Volume (Å^3)	951.699(16)	962.62(2)	879.76(19)
Z	4		
ρ_{calc} (g cm^{-3})	2.321	2.295	2.503
μ (mm^{-1})	3.301	3.264	3.531
Crystal size (mm^3)	0.479 x 0.320 x 0.143		0.13 x 0.1 x 0.15
Radiation	Mo K_α ($\lambda = 0.71073$)		
Reflections collected	37584	38485	7990
Independent reflections	7743	7850	1511
Parameters	171		140
Goodness-of-fit on F2	1.069	1.016	1.059
Final R indexes [$I \geq 2\sigma\ (I)$]	$R_1 = 0.0226$	$R_1 = 0.0618$	$R_1 = 0.0200$
	w$R_2 = 0.0602$	w$R_2 = 0.1336$	w$R_2 = 0.0510$
Flack parameter	0.012(5)	0.016(6)	0.477(15)

Table A.4: Single crystal X-ray data and refinements details for $[Cu(pyz)_{0.5}(gly)]ClO_4$ at ambient (within a sealed pressure-cell) and 28(1) kbar of pressure.

Parameter (units)	Fit Results (error)	
Instrument	Rigaku Oxford Diffraction Synergy S	
Method	Single crystal	
Empirical formula	C_4 H_7 Cl Cu N_2 O_6	
Formula weight (g mol^{-1})	278.11	
Pressure (kbar)	Ambient	28(1)
Temperature (K)	300	
Crystal system	monoclinic	
Space group	$P2_1/n$	
a (Å)	7.2209(4)	6.8477(9)
b (Å)	14.231(5)	13.137(14)
c (Å)	8.8952(5)	8.3629(11)
α (°)	90	90
β (°)	106.051(5)	103.120(13)
γ (°)	90	90
Volume (Å^3)	951.699(16)	732.7(8)
Z	4	
ρ_{calc} (g cm^{-3})	2.103	2.503
μ (mm^{-1})	2.797	3.353
Radiation	Mo K_α ($\lambda = 0.71073$)	
Reflections collected	11386	10057
Independent reflections	963	753
Parameters	132	
Goodness-of-fit on F2	1.197	1.016
Final R indexes [$I \geq 2\sigma$ (I)]	$R_1 = 0.1089$ w$R_2 = 0.3015$	$R_1 = 0.0618$ w$R_2 = 0.1336$

Bibliography

[1] R. T. Merrill and M. W. McElhinny, *The earth's magnetic field: its history, origin, and planetary perspective*, 2nd ed. (Academic Press; London; New York, 1983).

[2] R. C. Stauffer, Isis **48**, 33 (1957).

[3] J. C. Maxwell, Philosophical Transactions of the Royal Society of London **155**, 459 (1865).

[4] R. Mould, Current Oncology **14**, 74 (2007).

[5] P. Weiss, J. Phys. Theor. Appl. **6**, 661 (1907).

[6] S. Blundell, *Magnetism in condensed matter*, 1st ed. (Oxford University Press, 2001).

[7] C. P. Landee and M. M. Turnbull, J. Coord. Chem. **67**, 375 (2014).

[8] D. P. Zeeman, The London, Edinburgh, and Dublin Philosophical Magazine and Journal of Science **43**, 226 (1897).

[9] N. M. Atherton, *Principles of electron spin resonance* (Ellis Horwood Limited, 1993).

[10] S. J. Blundell, Contemp. Phys. **48**, 275 (2007).

[11] H. A. Jahn, E. Teller, and F. G. Donnan, Proceedings of the Royal Society of London. Series A - Mathematical and Physical Sciences **161**, 220 (1937).

[12] O. Kahn, *Molecular magnetism*, 1st ed. (Wiley-Blackwell, 1994).

[13] R. Boča, Coord. Chem. Rev. **248**, 757 (2004).

[14] J. Titiš, R. Boča, L. Dlháň, T. Ďurčeková, H. Fuess, R. Ivaniková, V. Mrázová, B. Papánková, and I. Svoboda, Polyhedron **26**, 1523 (2007).

[15] J. Titiş and R. Boça, Inorg. Chem. **49**, 3971 (2010).

[16] J. Titiš and R. Boča, Inorg. Chem. **50**, 11838 (2011).

[17] W. J. A. Blackmore, J. Brambleby, T. Lancaster, S. J. Clark, R. D. Johnson, J. Singleton, A. Ozarowski, J. A. Schlueter, Y.-S. Cheng, A. M. Arif, S. Lapidus, F. Xiao, R. C. Williams, S. J. Blundell, M. J. Pearce, M. R. Lees, P. Manuel, D. Y. Villa, J. A. Villa, J. L. Manson, and P. A. Goddard, New J. Phys. **21**, 093025 (2019).

[18] W. Heisenberg, Zeitschrift für Physik **49**, 619 (1928).

[19] P. W. Anderson, Phys. Rev. **115**, 2 (1959).

[20] Néel, L., Ann. Phys. **10**, 5 (1932).

[21] A. Vasiliev, O. Volkova, E. Zvereva, and M. Markina, npj Quantum Materials **3**, 18 (2018).

[22] S. Sachdev, Science **288**, 475 (2000).

[23] V. Zapf, M. Jaime, and C. D. Batista, Rev. Mod. Phys. **86**, 563 (2014).

[24] S. Kimura, M. Hagiwara, H. Tanaka, A. K. Kolezhuk, and K. Kindo, J. Magn. Magn. Mater. **310**, 1218 (2007).

[25] F. D. M. Haldane, Phys. Rev. Lett. **50**, 1153 (1983).

[26] A. Zheludev, Z. Honda, Y. Chen, C. L. Broholm, C. L. Broholm, K. Katsumata, and S. M. Shapiro, Phys. Rev. Lett. **88**, 772061 (2002).

[27] L. P. Regnault, I. Zaliznyak, J. P. Renard, and C. Vettier, Phys. Rev. B **50**, 9174 (1994).

[28] J. M. Kosterlitz and D. J. Thouless, Journal of Physics C: Solid State Physics **5**, L124 (1972).

[29] J. M. Kosterlitz and D. J. Thouless, Journal of Physics C: Solid State Physics **6**, 1181 (1973).

[30] V. L. Berezinsky, Sov. Phys. JETP **32**, 493 (1971).

[31] A. W. Kinross, M. Fu, T. J. Munsie, H. A. Dabkowska, G. M. Luke, S. Sachdev, and T. Imai, Phys. Rev. X **4**, 1 (2014).

[32] R. Coldea, D. A. Tennant, E. M. Wheeler, E. Wawrzynska, D. Prabhakaran, M. Telling, K. Habicht, P. Smeibidl, and K. Kiefer, Science (80-.). **327**, 177 (2010).

[33] M. A. Kastner, R. J. Birgeneau, G. Shirane, and Y. Endoh, Rev. Mod. Phys. **70**, 897 (1998).

[34] K. Wierschem and P. Sengupta, Mod. Phys. Lett. B **28**, 1430017 (2014).

[35] S. J. Blundell and F. L. Pratt, J. Phys. Condens. Matter **16**, 771 (2004).

[36] A. Zheludev and T. Roscilde, Comptes Rendus Phys. **14**, 740 (2013).

[37] J. Brambleby, P. A. Goddard, J. Singleton, M. Jaime, T. Lancaster, L. Huang, J. Wosnitza, C. V. Topping, K. E. Carreiro, H. E. Tran, Z. E. Manson, and J. L. Manson, Phys. Rev. B **95** (2017).

[38] R. C. Williams, W. J. A. Blackmore, S. P. M. Curley, M. R. Lees, S. M. Birnbaum, J. Singleton, B. M. Huddart, T. J. Hicken, T. Lancaster, S. J. Blundell, F. Xiao, A. Ozarowski, F. L. Pratt, D. J. Voneshen, Z. Guguchia, C. Baines, J. A. Schlueter, D. Y. Villa, J. L. Manson, and P. A. Goddard, Phys. Rev. Res. **2**, 1 (2020).

[39] J. Liu, S. Kittaka, R. D. Johnson, T. Lancaster, J. Singleton, T. Sakakibara, Y. Kohama, J. Van Tol, A. Ardavan, B. H. Williams, S. J. Blundell, Z. E. Manson, J. L. Manson, and P. A. Goddard, Phys. Rev. Lett. **122**, 57207 (2019).

[40] J. L. Manson, J. A. Schlueter, K. A. Funk, H. I. Southerland, B. Twamley, T. Lancaster, S. J. Blundell, P. J. Baker, F. L. Pratt, J. Singleton, R. D. McDonald, P. A. Goddard, P. Sengupta, C. D. Batista, L. Ding, C. Lee, M.-H. Whangbo, I. Franke, S. Cox, C. Baines, and D. Trial, Journal of the American Chemical Society **131**, PMID: 19290599, 6733 (2009).

[41] P. A. Goddard, J. L. Manson, J. Singleton, I. Franke, T. Lancaster, A. J. Steele, S. J. Blundell, C. Baines, F. L. Pratt, R. D. McDonald, O. E. Ayala-Valenzuela, J. F. Corbey, H. I. Southerland, P. Sengupta, and J. A. Schlueter, Phys. Rev. Lett. **108**, 077208 (2012).

[42] B. M. Huddart, J. Brambleby, T. Lancaster, P. A. Goddard, F. Xiao, S. J. Blundell, F. L. Pratt, J. Singleton, P. MacChi, R. Scatena, A. M. Barton, and J. L. Manson, Phys. Chem. Chem. Phys. **21**, 1014 (2019).

[43] J. Liu, P. A. Goddard, J. Singleton, J. Brambleby, F. Foronda, J. S. Möller, Y. Kohama, S. Ghannadzadeh, A. Ardavan, S. J. Blundell, T. Lancaster, F. Xiao, R. C. Williams, F. L. Pratt, P. J. Baker, K. Wierschem, S. H. Lapidus, K. H. Stone, P. W. Stephens, J. Bendix, T. J. Woods, K. E. Carreiro, H. E. Tran, C. J. Villa, and J. L. Manson, Inorg. Chem. **55**, 3515 (2016).

[44] S. Ghannadzadeh, J. S. Möller, P. A. Goddard, T. Lancaster, F. Xiao, S. J. Blundell, A. Maisuradze, R. Khasanov, J. L. Manson, S. W. Tozer, D. Graf, and J. A. Schlueter, Phys. Rev. B - Condens. Matter Mater. Phys. **87**, 1 (2013).

[45] H.-L. Huang, D. Wu, D. Fan, and X. Zhu, Science China Information Sciences **63**, 180501 (2020).

[46] H. Huang, S. Su, N. Wu, H. Wan, S. Wan, H. Bi, and L. Sun, Frontiers in Chemistry **7**, 399 (2019).

[47] S. Manzhos, C.-C. Chueh, G. Giorgi, T. Kubo, G. Saianand, J. Lüder, P. Sonar, and M. Ihara, The Journal of Physical Chemistry Letters **12**, PMID: 33974435, 4638 (2021).

[48] X. Zhou, W.-S. Lee, M. Imada, N. Trivedi, P. Phillips, H.-Y. Kee, P. Törmä, and M. Eremets, Nature Reviews Physics **3**, 462 (2021).

[49] M. Fiebig, T. Lottermoser, D. Meier, and M. Trassin, Nature Reviews Materials **1**, 16046 (2016).

[50] A. Fert, N. Reyren, and V. Cros, Nature Reviews Materials **2**, 17031 (2017).

[51] S. D. Sarma, M. Freedman, and C. Nayak, npj Quantum Information **1**, 15001 (2015).

[52] M. J. Pearce, K. Götze, A. Szabó, T. S. Sikkenk, M. R. Lees, A. T. Boothroyd, D. Prabhakaran, C. Castelnovo, and P. A. Goddard, *Monopole density and antiferromagnetic domain control in spin-ice iridates*, 2021.

[53] S. Sachdev, *Quantum phase transitions*, 2nd ed. (Cambridge University Press, 2011).

[54] I. Affleck, Phys. Rev. B **46**, 9002 (1992).

[55] H. Mutka, C. Payen, P. Molinié, J. L. Soubeyroux, P. Colombet, and A. D. Taylor, Phys. Rev. Lett. **67**, 497 (1991).

[56] M. Kenzelmann, G. Xu, I. A. Zaliznyak, C. Broholm, J. F. DiTusa, G. Aeppli, T. Ito, K. Oka, and H. Takagi, Phys. Rev. Lett. **90**, 4 (2003).

[57] M. Hagiwara, Z. Honda, K. Katsumata, A. K. Kolezhuk, and H. J. Mikeska, Phys. Rev. Lett. **91**, 17 (2003).

[58] A. Zheludev, Z. Honda, C. L. Broholm, K. Katsumata, S. M. Shapiro, A. Kolezhuk, S. Park, and Y. Qiu, Phys. Rev. B **68**, 134438 (2003).

[59] A. Zheludev, S. M. Shapiro, Z. Honda, K. Katsumata, B. Grenier, E. Ressouche, L.-P. Regnault, Y. Chen, P. Vorderwisch, H.-J. Mikeska, and A. K. Kolezhuk, Phys. Rev. B **69**, 054414 (2004).

[60] F. H. L. Essler and I. Affleck, Journal of Statistical Mechanics: Theory and Experiment **2004**, P12006 (2004).

[61] R. Yu, L. Yin, N. S. Sullivan, J. S. Xia, C. Huan, A. Paduan-Filho, N. F. Oliveira Jr, S. Haas, A. Steppke, C. F. Miclea, F. Weickert, R. Movshovich, E.-D. Mun, B. L. Scott, V. S. Zapf, and T. Roscilde, Nature **489**, 379 (2012).

[62] T. Giamarchi, C. Rüegg, and O. Tchernyshyov, Nat. Phys. **4**, 198 (2008).

[63] V. S. Zapf, D. Zocco, B. R. Hansen, M. Jaime, N. Harrison, C. D. Batista, M. Kenzelmann, C. Niedermayer, A. Lacerda, and A. Paduan-Filho, Phys. Rev. Lett. **96**, 077204 (2006).

[64] S. Ghannadzadeh, M. Coak, I. Franke, P. A. Goddard, J. Singleton, and J. L. Manson, Review of Scientific Instruments **82**, 113902 (2011).

[65] P. A. Goddard, J. Singleton, P. Sengupta, R. D. McDonald, T. Lancaster, S. J. Blundell, F. L. Pratt, S. Cox, N. Harrison, J. L. Manson, H. I. Southerland, and J. A. Schlueter, New J. Phys. **10**, 83025 (2008).

[66] M. McElfesh, *Fundamentals of Magnetism and Magnetic Measurements*, tech. rep. ((Quantum Design, Inc., San Diego), 1994), pp 1–34.

[67] i-Quantum corporation, *Sub-two-kelvin magnetic measurement system*, http://iquantum.co.jp/image/iHelium3Brochure1.pdf.

[68] F. J. Brown, N. W. Kerley, R. B. Knox, and K. W. Timms, *PHYSICAD Review of high field superconducting magnet development at Oxford Instruments*, tech. rep. (1996), p. 208.

[69] H. Schneider-Muntau, J. Toth, and H. Weijers, IEEE Transactions on Applied Superconductivity **14**, 1245 (2004).

[70] B. Bleaney and B. Bleaney, *Electricity and magnetism* (Oxford University Press, New York, 1976).

[71] R. B. Clover and W. P. Wolf, Rev. Sci. Instrum. **41**, 617 (1970).

[72] T. Coffey, Z. Bayindir, J. F. DeCarolis, M. Bennett, G. Esper, and C. C. Agosta, Rev. Sci. Instrum. **71**, 4600 (2000).

[73] *Quantum design high pressure cell manual*, Quantum Design Japan (July 2016).

[74] K. V. Kamenev, S. Tancharakorn, N. Robertson, and A. Harrison, Review of Scientific Instruments **77**, 073905 (2006).

[75] R. L. Stillwell, “Fermi surface reconstruction in chromium at high pressure and high magnetic fields”, PhD thesis (Florida State University, 2013).

[76] T. F. Smith and C. W. Chu, Phys. Rev. **159**, 353 (1967).

[77] A. Eiling and J. Schilling, Journal of Physics F: Metal Physics **11**, 623 (1981).

[78] M. J. Coak, C. Liu, D. M. Jarvis, S. Park, M. J. Cliffe, and P. A. Goddard, Review of Scientific Instruments **91**, 023901 (2020).

[79] J. Lashley, M. Hundley, A. Migliori, J. Sarrao, P. Pagliuso, T. Darling, M. Jaime, J. Cooley, W. Hults, L. Morales, D. Thoma, J. Smith, J. Boerio-Goates, B. Woodfield, G. Stewart, R. Fisher, and N. Phillips, Cryogenics **43**, 369 (2003).

[80] S. D. Sivia, *Elementary scattering theory* (Oxford University Press, 2011).

[81] R. I. Bewley, J. W. Taylor, and S. M. Bennington., Nucl. Instruments Methods Phys. Res. Sect. A Accel. Spectrometers, Detect. Assoc. Equip. **637**, 128 (2011).

[82] F. Pratt, Physica B: Condensed Matter **289**, 710 (2000).

[83] D. E. Maclaughlin, Hyperfine Interact. **19**, 981 (1984).

[84] S. J. Blundell, Contemp. Phys. **40**, 175 (1999).

[85] S. J. Blundell, Contemporary Physics **40**, 175 (1999).

[86] S. J. Blundell, F. L. Pratt, T. Lancaster, I. M. Marshall, C. A. Steer, S. L. Heath, J. F. Létard, T. Sugano, D. Mihailovic, and A. Omerzu, Polyhedron **22**, 1973 (2003).

[87] I. O. Thomas, S. J. Clark, and T. Lancaster, Phys. Rev. B **96**, 094403 (2017).

[88] L. H. Dos Santos, A. Lanza, A. M. Barton, J. Brambleby, W. J. Blackmore, P. A. Goddard, F. Xiao, R. C. Williams, T. Lancaster, F. L. Pratt, S. J. Blundell, J. Singleton, J. L. Manson, and P. Macchi, J. Am. Chem. Soc. **138**, 2280 (2016).

[89] E. Čižmár, M. Ozerov, O. Ignatchik, T. P. Papageorgiou, J. Wosnitza, S. A. Zvyagin, J. Krzystek, Z. Zhou, C. P. Landee, B. R. Landry, M. M. Turnbull, and J. L. Wikaira, New Journal of Physics **10**, 033008 (2008).

[90] AlmaxEasyLab, https://www.almax-easylab.com/admin/Uploadnew/ML15_02%5C%20TozerDAC.pdfs.

[91] AlmaxEasyLab, https://www.almax-easylab.com/admin/Uploadnew/Brochure%5C%20TozerDAC%5C%20X-ray.pdf.

[92] Rigaku, https://www.rigaku.com/products/crystallography/synergys.

[93] H. K. Mao, J. Xu, and P. M. Bell, Journal of Geophysical Research: Solid Earth **91**, 4673 (1986).

[94] *Crysalispro*, CrysAlisPRO, Oxford Diffraction /Agilent Technologies UK Ltd, Yarnton, England.

[95] O. V. Dolomanov, L. J. Bourhis, R. J. Gildea, J. A. K. Howard, and H. Puschmann, Journal of Applied Crystallography **42**, 339 (2009).

[96] G. M. Sheldrick, Acta Crystallographica Section C **71**, 3 (2015).

[97] J. M. Kosterlitz and D. J. Thouless, Journal of Physics C: Solid State Physics **6**, 1181 (1973).

[98] V. Zapf, M. Jaime, and C. D. Batista, Rev. Mod. Phys. **86**, 563 (2014).

[99] V. S. Zapf, D. Zocco, B. R. Hansen, M. Jaime, N. Harrison, C. D. Batista, M. Kenzelmann, C. Niedermayer, A. Lacerda, and A. Paduan-Filho, Phys. Rev. Lett. **96**, 077204 (2006).

[100] S. A. Zvyagin, J. Wosnitza, C. D. Batista, M. Tsukamoto, N. Kawashima, J. Krzystek, V. S. Zapf, M. Jaime, N. F. Oliveira, and A. Paduan-Filho, Phys. Rev. Lett. **98**, 047205 (2007).

[101] J. Brambleby, P. A. Goddard, R. D. Johnson, J. Liu, D. Kaminski, A. Ardavan, A. J. Steele, S. J. Blundell, T. Lancaster, P. Manuel, P. J. Baker, J. Singleton, S. G. Schwalbe, P. M. Spurgeon, H. E. Tran, P. K. Peterson, J. F. Corbey, and J. L. Manson, Phys. Rev. B **92**, 134406 (2015).

[102] P. R. Hammar, M. B. Stone, D. H. Reich, C. Broholm, P. J. Gibson, M. M. Turnbull, C. P. Landee, and M. Oshikawa, Phys. Rev. B **59**, 1008 (1999).

[103] F. M. Woodward, A. S. Albrecht, C. M. Wynn, C. P. Landee, and M. M. Turnbull, Phys. Rev. B **65**, 144412 (2002).

[104] B. N. Figgis and P. A. Reynolds, J. Chem. Soc., Dalton Trans., 125 (1986).

[105] N. K. Hansen and P. Coppens, Acta Crystallographica Section A **34**, 909 (1978).

[106] J. B. Goodenough, Phys. Rev. **100**, 564 (1955).

[107] J. Kanamori, J. Phys. Chem. Solids **10**, 87 (1959).

[108] R. Ivaniková, R. Boča, L. Dlháň, H. Fuess, A. Mašlejová, V. Mrázová, I. Svoboda, and J. Titiš, Polyhedron **25**, 3261 (2006).

[109] T. Lancaster, F. Xiao, B. M. Huddart, R. C. Williams, F. L. Pratt, S. J. Blundell, S. J. Clark, R. Scheuermann, T. Goko, S. Ward, J. L. Manson, C. Rüegg, and K. W. Krämer, New Journal of Physics **20**, 103002 (2018).

[110] B. M. Huddart, A. Hernández-Melián, T. J. Hicken, M. Gomilšek, Z. Hawkhead, S. J. Clark, F. L. Pratt, and T. Lancaster, *Mufinder: a program to determine and analyse muon stopping sites*, 2021.

[111] J. J. Binney, N. J. Dowrick, A. J. Fisher, and M. E. Newman, *The theory of critical phenomena: an introduction to the renormalization group* (Oxford University Press, Oxford, 1992).

[112] A. J. Steele, T. Lancaster, S. J. Blundell, P. J. Baker, F. L. Pratt, C. Baines, M. M. Conner, H. I. Southerland, J. L. Manson, and J. A. Schlueter, Physical Review B **84**, 064412 (2011).

[113] F. Xiao, J. S. Möller, T. Lancaster, R. C. Williams, F. L. Pratt, S. J. Blundell, D. Ceresoli, A. M. Barton, and J. L. Manson, Phys. Rev. B **91**, 144417 (2015).

[114] T. Lancaster, S. Blundell, M. Brooks, F. Pratt, and J. Manson, Physica B: Condensed Matter **374**, 118 (2006).

[115] J. L. Manson, C. M. Brown, Q. Huang, J. A. Schlueter, T. Lancaster, S. J. Blundell, J. Singleton, J. W. Lynn, and F. L. Pratt, Polyhedron **52**, 679 (2013).

[116] R. Honmura, Phys. Rev. B **30**, 348 (1984).

[117] X. Feng and H. W. Blöte, Phys. Rev. E - Stat. Nonlinear, Soft Matter Phys. **81** (2010).

[118] L. Onsager, Phys. Rev. **65**, 117 (1944).

[119] B. M. McCoy and T. T. Wu, *The two-dimensional ising model* (Harvard University Press, Cambridge MA, 1973).

[120] S. Blundell and K. Blundell, *Concepts in thermal physics*, 2nd ed. (Oxford University Press, 2009).

[121] P. Baran, M. Boča, R. Boča, A. Krutošíková, J. Miklovič, J. Pelikán, and J. Titiš, Polyhedron **24**, 1510 (2005).

[122] M. E. Fisher, Philos. Mag. **7**, 1731 (1962).

[123] M. E. Fisher, J. Math. Phys. **4**, 124 (1963).

[124] R. E. Greeney, C. P. Landee, J. H. Zhang, and W. M. Reiff, Phys. Rev. B **39**, 12200 (1989).

[125] M. E. Lines, J. Chem. Phys. **55**, 2977 (1971).

[126] F. Lloret, M. Julve, J. Cano, R. Ruiz-García, and E. Pardo, Inorganica Chim. Acta **361**, 3432 (2008).

[127] M. Rams, Z. Tomkowicz, M. Böhme, W. Plass, S. Suckert, J. Werner, I. Jess, and C. Näther, Phys. Chem. Chem. Phys. **19**, 3232 (2017).

[128] A. Holladay, P. Leung, and P. Coppens, Acta Crystallographica Section A **39**, 377 (1983).

[129] P. MacChi, Crystallogr. Rev. **19**, 58 (2013).

[130] A. Paduan-Filho, R. D. Chirico, K. O. Joung, and R. L. Carlin, J. Chem. Phys. **74**, 4103 (1981).

[131] E. Mun, J. Wilcox, J. L. Manson, B. Scott, P. Tobash, and V. S. Zapf, Adv. Condens. Matter Phys. **2014**, 512621 (2014).

[132] J. Palion-Gazda, B. Machura, F. Lloret, and M. Julve, Cryst. Growth Des. **15**, 2380 (2015).

[133] J. E. O'Connor and E. L. Amma, Inorganic Chemistry **8**, 2367 (1969).

[134] H. Forstat, N. D. Love, J. McElearney, and H. Weinstock, Phys. Rev. **145**, 406 (1966).

[135] W. Scharf, H. Weitzel, I. Yaeger, I. Maartense, and B. M. Wanklyn, J. Magn. Magn. Mater. **13**, 121 (1979).

[136] T. Kunimoto, K. Nagasaka, H. Noriji, S. Luther, M. Motokawa, H. Ohta, T. Goto, S. M. Okubo, and K. Kohn, J. Phys. Soc. Japan **68**, 1703 (1999).

[137] M. Oshikawa, M. M. Turnbull, and C. P. Landee, Phys. Rev. B - Condens. Matter Mater. Phys. **59**, 1008 (1999).

[138] F. Haldane, Physics Letters A **93**, 464 (1983).

[139] F. D. M. Haldane, Phys. Rev. Lett. **50**, 1153 (1983).

[140] Y. C. Tzeng, H. Onishi, T. Okubo, and Y. J. Kao, Phys. Rev. B **96**, 60404 (2017).

[141] O. Golinelli, T. Jolicoeur, and R. Lacaze, Phys. Rev. B **45**, 9798 (1992).

[142] S. R. White and D. A. Huse, Phys. Rev. B **48**, 3844 (1993).

[143] M. P. Nightingale and H. W. J. Blöte, Phys. Rev. B **33**, 659 (1986).

[144] L. P. Regnault, I. Zaliznyak, J. P. Renard, and C. Vettier, Phys. Rev. B **50**, 9174 (1994).

[145] A. M. Farutin and V. I. Marchenko, J. Exp. Theor. Phys. **104**, 751 (2007).

[146] A. Zheludev, Z. Honda, C. L. Broholm, K. Katsumata, S. M. Shapiro, A. Kolezhuk, S. Park, and Y. Qiu, Phys. Rev. B **68**, 134438 (2003).

[147] A. I. Smirnov, V. N. Glazkov, T. Kashiwagi, S. Kimura, M. Hagiwara, K. Kindo, A. Y. Shapiro, and L. N. Demianets, Phys. Rev. B **77**, 100401 (2008).

[148] A. K. Bera, B. Lake, A. T. M. N. Islam, O. Janson, H. Rosner, A. Schneidewind, J. T. Park, E. Wheeler, and S. Zander, Phys. Rev. B **91**, 144414 (2015).

[149] A. K. Bera, B. Lake, A. T. M. N. Islam, and A. Schneidewind, Phys. Rev. B **92**, 060412 (2015).

[150] J. M. Law, H. Benner, and R. K. Kremer, Journal of Physics: Condensed Matter **25**, 065601 (2013).

[151] O. Avenel, J. Xu, J. S. Xia, M. F. Xu, B. Andraka, T. Lang, P. L. Moyland, W. Ni, P. J. Signore, C. M. Van Woerkens, E. D. Adams, G. G. Ihas, M. W. Meisel, S. E. Nagler, N. S. Sullivan, Y. Takano, D. R. Talham, T. Goto, and N. Fujiwara, Phys. Rev. B **46**, 8655 (1992).

[152] I. Affleck, T. Kennedy, E. H. Lieb, and H. Tasaki, Phys. Rev. Lett. **59**, 799 (1987).

[153] J. Brambleby, J. L. Manson, P. A. Goddard, M. B. Stone, R. D. Johnson, P. Manuel, J. A. Villa, C. M. Brown, H. Lu, S. Chikara, V. Zapf, S. H. Lapidus, R. Scatena, P. Macchi, Y.-s. Chen, L.-C. Wu, and J. Singleton, Phys. Rev. B **95**, 134435 (2017).

[154] F. L. Pratt, Physica B: Condensed Matter **289-290**, 710 (2000).

[155] S. Capponi, M. Dupont, A. W. Sandvik, and P. Sengupta, Phys. Rev. B **100**, 094411 (2019).

[156] R. Calvo, V. T. Santana, and O. R. Nascimento, Phys. Rev. B **96**, 64424 (2017).

[157] H. Shiba, T. Sakai, B. Lüthi, W. Palme, and M. Sieling, J. Magn. Magn. Mater. **140-144**, 1590 (1995).

[158] E. Čižmár, M. Ozerov, O. Ignatchik, T. P. Papageorgiou, J. Wosnitza, S. A. Zvyagin, J. Krzystek, Z. Zhou, C. P. Landee, B. R. Landry, M. M. Turnbull, and J. L. Wikaira, New Journal of Physics **10**, 033008 (2008).

[159] J. Bolton and J. Weil, *Basic principles of paramagnetic resonance* (John Wiley Sons, Ltd, 2006) Chap. 1, pp. 1–35.

[160] N. M. Atherton, *Principles of Electron Spin Resonance* (Ellis Horwood Limited, 1993).

[161] E. S. Sørensen and I. Affleck, Phys. Rev. B **51**, 16115 (1995).

[162] X. Wang and S. Mallwitz, Phys. Rev. B **53**, R492 (1996).

[163] Y. Koike, N. Metoki, Y. Morii, T. Kobayashi, T. Ishii, and M. Yamashita, J. Phys. Soc. Japan **69**, 4034 (2000).

[164] M. Ozerov, M. Maksymenko, J. Wosnitza, A. Honecker, C. P. Landee, M. M. Turnbull, S. C. Furuya, T. Giamarchi, and S. A. Zvyagin, RAPID Commun. Phys. Rev. B **92**, 241113 (2015).

[165] M. Mito, H. Akama, H. Deguchi, S. Takagi, T. Kawae, K. Takeda, T. Ishii, M. Yamashita, H. Nakao, Y. Murakami, and S. Yamamoto, J. Phys. Soc. Japan **72**, 399 (2003).

[166] P. Gegenwart, Q. Si, and F. Steglich, Nat. Phys. **4**, 186 (2008).

[167] O. Stockert and F. Steglich, Annual Review of Condensed Matter Physics **2**, 79 (2011).

[168] T. Lancaster, P. A. Goddard, S. J. Blundell, F. R. Foronda, S. Ghannadzadeh, J. S. Möller, P. J. Baker, F. L. Pratt, C. Baines, L. Huang, J. Wosnitza, R. D. McDonald, K. A. Modic, J. Singleton, C. V. Topping, T. A. W. Beale, F. Xiao, J. A. Schlueter, A. M. Barton, R. D. Cabrera, K. E. Carreiro, H. E. Tran, and J. L. Manson, Phys. Rev. Lett. **112**, 207201 (2014).

[169] K. Nawa, C. Michioka, K. Yoshimura, A. Matsuo, and K. Kindo, J. Phys. Soc. Japan **80**, 034710 (2011).

[170] S. E. Sebastian, P. Tanedo, P. A. Goddard, S.-C. Lee, A. Wilson, S. Kim, S. Cox, R. D. McDonald, S. Hill, N. Harrison, C. D. Batista, and I. R. Fisher, Phys. Rev. B **74**, 180401 (2006).

[171] M. D. Donakowski, R. Gautier, J. Yeon, D. T. Moore, J. C. Nino, P. S. Halasyamani, and K. R. Poeppelmeier, J. Am. Chem. Soc. **134**, 7679 (2012).

[172] C. Rüegg, A. Furrer, D. Sheptyakov, T. Strässle, K. W. Krämer, H.-U. Güdel, and L. Mélési, Phys. Rev. Lett. **93**, 257201 (2004).

[173] G. Perren, J. S. Möller, D. Hüvonen, A. A. Podlesnyak, and A. Zheludev, Phys. Rev. B - Condens. Matter Mater. Phys. **92**, 2 (2015).

[174] S. Bettler, G. Simutis, G. Perren, D. Blosser, S. Gvasaliya, and A. Zheludev, Phys. Rev. B **96**, 174431 (2017).

[175] A. Lanza, C. Fiolka, M. Fisch, N. Casati, M. Skoulatos, C. Rüegg, K. W. Krämer, and P. Macchi, Chem. Commun. **50**, 14504 (2014).

[176] A. A. Aczel, Y. Kohama, M. Jaime, K. Ninios, H. B. Chan, L. Balicas, H. A. Dabkowska, and G. M. Luke, Phys. Rev. B **79**, 100409 (2009).

[177] A. A. Aczel, Y. Kohama, C. Marcenat, F. Weickert, M. Jaime, O. E. Ayala-Valenzuela, R. D. McDonald, S. D. Selesnic, H. A. Dabkowska, and G. M. Luke, Phys. Rev. Lett. **103**, 207203 (2009).

[178] R. Feyerherm and S. Abens, J. Phys. Condens. Matter **12**, 8495 (2000).

[179] G. J. Athas, J. S. Brooks, S. J. Klepper, S. Uji, and M. Tokumoto, Rev. Sci. Instrum. **64**, 3248 (1993).

[180] M. Jaime, V. F. Correa, N. Harrison, C. D. Batista, N. Kawashima, Y. Kazuma, G. A. Jorge, R. Stern, I. Heinmaa, S. A. Zvyagin, Y. Sasago, and K. Uchinokura, Phys. Rev. Lett. **93**, 087203 (2004).

[181] J. L. Manson, J. Brambleby, P. A. Goddard, P. M. Spurgeon, J. A. Villa, J. Liu, S. Ghannadzadeh, F. Foronda, J. Singleton, T. Lancaster, S. J. Clark, I. O. Thomas, F. Xiao, R. C. Williams, F. L. Pratt, S. J. Blundell, C. V. Topping, C. Baines, C. Campana, and B. Noll, Sci. Rep. **8**, 4745 (2018).

[182] T. Nakajima, H. Mitamura, and Y. Ueda, Journal of the Physical Society of Japan **75**, 054706 (2006).

[183] H. Nojiri, H. Kageyama, K. Onizuka, Y. Ueda, and M. Motokawa, Journal of the Physical Society of Japan **68**, 2906 (1999).

[184] T. Rõõm, D. Hüvonen, U. Nagel, J. Hwang, T. Timusk, and H. Kageyama, Phys. Rev. B **70**, 144417 (2004).

[185] Z. Wang, M. Schmidt, Y. Goncharov, Y. Skourski, J. Wosnitza, H. Berger, H.-A. Krug von Nidda, A. Loidl, and J. Deisenhofer, Journal of the Physical Society of Japan **80**, 124707 (2011).

[186] D. Kamenskyi, J. Wosnitza, J. Krzystek, A. A. Aczel, H. A. Dabkowska, A. B. Dabkowski, G. M. Luke, and S. A. Zvyagin, J. Low Temp. Phys. **170**, 231 (2013).

[187] Z. Wang, D. Kamenskyi, O. Cépas, M. Schmidt, D. L. Quintero-Castro, A. T. M. N. Islam, B. Lake, A. A. Aczel, H. A. Dabkowska, A. B. Dabkowski, G. M. Luke, Y. Wan, A. Loidl, M. Ozerov, J. Wosnitza, S. A. Zvyagin, and J. Deisenhofer, Phys. Rev. B **89**, 174406 (2014).

[188] Z. Wang, M. Schmidt, A. Günther, F. Mayr, Y. Wan, S.-H. Lee, H. Ueda, Y. Ueda, A. Loidl, and J. Deisenhofer, Phys. Rev. B **85**, 224304 (2012).

[189] S. A. Zvyagin, M. Ozerov, D. Kamenskyi, J. Wosnitza, J. Krzystek, D. Yoshizawa, M. Hagiwara, R. Hu, H. Ryu, C. Petrovic, and M. E. Zhitomirsky, New Journal of Physics **17**, 113059 (2015).

[190] A. Ceulemans, L. F. Chibotaru, G. A. Heylen, K. Pierloot, and L. G. Vanquickenborne, Chemical Reviews **100**, PMID: 11749251, 787 (2000).

[191] M. Matsumoto, T. Shoji, and M. Koga, J. Phys. Soc. Japan **77**, 1 (2008).

[192] S. J. Clark, M. D. Segall, C. J. Pickard, P. J. Hasnip, M. I. Probert, K. Refson, and M. C. Payne, Zeitschrift fur Krist. **220**, 567 (2005).

[193] J. Ireta, J. Neugebauer, and M. Scheffler, The Journal of Physical Chemistry A **108**, 5692 (2004).

[194] M. Kofu, J.-H. Kim, S. Ji, S.-H. Lee, H. Ueda, Y. Qiu, H.-J. Kang, M. A. Green, and Y. Ueda, Phys. Rev. Lett. **102**, 037206 (2009).

[195] M. Tachiki and T. Yamada, J. Phys. Soc. Japan **28**, 1413 (1970).

[196] Z. Wang, P. Jain, K.-Y. Choi, J. van Tol, A. K. Cheetham, H. W. Kroto, H.-J. Koo, H. Zhou, J. Hwang, E. S. Choi, M.-H. Whangbo, and N. S. Dalal, Phys. Rev. B **87**, 224406 (2013).

[197] T. Waki, M. Kato, Y. Itoh, C. Michioka, K. Yoshimura, and T. Goto, Journal of Physics and Chemistry of Solids **66**, 1432 (2005).

[198] O. Mentré, A. C. Dhaussy, F. Abraham, E. Suard, and H. Steinfink, Chemistry of Materials **11**, 2408 (1999).

[199] M. Dalal, *A textbook of inorganic chemistry – volume 1* (Amazon Digital Services LLC - KDP Print US, 2017), pp. 312–321.

[200] R. T. Butcher, C. P. Landee, M. M. Turnbull, and F. Xiao, Inorganica Chim. Acta **361**, 3654 (2008).

[201] S. H. Lapidus, J. L. Manson, J. Liu, M. J. Smith, P. Goddard, J. Bendix, C. V. Topping, J. Singleton, C. Dunmars, J. F. Mitchell, and J. A. Schlueter, Chem. Commun. **49**, 3558 (2013).

[202] T. Lancaster, B. M. Huddart, R. C. Williams, F. Xiao, K. J. A. Franke, P. J. Baker, F. L. Pratt, S. J. Blundell, J. A. Schlueter, M. B. Mills, A. C. Maahs, and K. E. Preuss, Journal of Physics: Condensed Matter **31**, 394002 (2019).

[203] R. T. Butcher, PhD thesis (Clark University; Worcester, 2008).

[204] S. Vela, J. Jornet-Somoza, M. M. Turnbull, R. Feyerherm, J. J. Novoa, and M. Deumal, Inorg. Chem. **52**, 12923 (2013).

[205] E. P. Kenny, A. C. Jacko, and B. J. Powell, arXiv (2021).

[206] T. Hong, V. O. Garlea, A. Zheludev, J. A. Fernandez-Baca, H. Manaka, S. Chang, J. B. Leao, and S. J. Poulton, Phys. Rev. B **78**, 224409 (2008).

[207] T. Hong, C. Stock, I. Cabrera, C. Broholm, Y. Qiu, J. B. Leao, S. J. Poulton, and J. R. D. Copley, Phys. Rev. B **82**, 184424 (2010).

[208] C. Rüegg, B. Normand, M. Matsumoto, A. Furrer, D. F. McMorrow, K. W. Krämer, H. .-.-U. Güdel, S. N. Gvasaliya, H. Mutka, and M. Boehm, Phys. Rev. Lett. **100**, 205701 (2008).

[209] H. Tanaka, K. Goto, M. Fujisawa, T. Ono, and Y. Uwatoko, Physica B: Condensed Matter **329-333**, 697 (2003).

[210] O. Nohadani, S. Wessel, and S. Haas, Phys. Rev. B **72**, 024440 (2005).

[211] K. Goto, M. Fujisawa, H. Tanaka, Y. Uwatoko, A. Oosawa, T. Osakabe, and K. Kakurai, Journal of the Physical Society of Japan **75**, 064703 (2006).

[212] M. Thede, A. Mannig, M. Månsson, D. Hüvonen, R. Khasanov, E. Morenzoni, and A. Zheludev, Phys. Rev. Lett. **112**, 087204 (2014).

[213] S. P. M. Curley, R. Scatena, R. C. Williams, P. A. Goddard, P. Macchi, T. J. Hicken, T. Lancaster, F. Xiao, S. J. Blundell, V. Zapf, J. C. Eckert, E. H. Krenkel, J. A. Villa, M. L. Rhodehouse, and J. L. Manson, Phys. Rev. Mater. **5**, 34401 (2021).

[214] R. Coldea, D. A. Tennant, E. M. Wheeler, E. Wawrzynska, D. Prabhakaran, M. Telling, K. Habicht, P. Smeibidl, and K. Kiefer, Science (80-.). **327**, 177 (2010).

[215] A. K. Bera, B. Lake, A. T. M. N. Islam, B. Klemke, E. Faulhaber, and J. M. Law, Phys. Rev. B **87**, 224423 (2013).

[216] S. P. M. Curley, B. M. Huddart, D. Kamenskyi, M. J. Coak, R. C. Williams, S. Ghannadzadeh, A. Schneider, S. Okubo, T. Sakurai, H. Ohta, J. P. Tidey, D. Graf, S. J. Clark, S. J. Blundell, F. L. Pratt, M. T. F. Telling, T. Lancaster, J. L. Manson, and P. A. Goddard, Phys. Rev. B **104**, 214435 (2021).

[217] K. V. Kamenev, S. Tancharakorn, N. Robertson, and A. Harrison, Review of Scientific Instruments **77**, 073905 (2006).

[218] M. Sawicki, W. Stefanowicz, and A. Ney, Semiconductor Science and Technology **26**, 064006 (2011).

[219] P. Stamenov and J. M. D. Coey, Review of Scientific Instruments **77**, 015106 (2006).